

**FAST TRANSFER PATH ANALYSIS USING
CONTROLLED ELECTRIC MOTORS AS IN-SITU
BLOCKED FORCE VIBRATION SOURCES**

KEVIN WIENEN

Fast Transfer Path Analysis Using Controlled Electric Motors as In-Situ Blocked Force Vibration Sources



University of
Salford
MANCHESTER

Acoustics Research Centre
School of Science, Engineering and Environment

Author

Kevin Wienen

Supervisory team

Prof. Andy T. Moorhouse

Dr. Joshua W.R. Meggitt

Dr. Andy S. Elliott

Dr. Michael Sturm

Doctorate of Philosophy in Acoustics and Audio Engineering

Contents

List of Figures	iv
List of Tables	xii
Acknowledgements	xiii
Author Publications	xiv
Nomenclature	xv
Abstract	xviii

PART I. Introduction, Literature Review and Theory 1

1 Introduction	2
1.1 Background and Motivation	2
1.2 Concepts for Reliable and Fast TPA	6
1.3 Thesis Aims and Objectives	8
1.4 Thesis Outline	10
2 Review of Structure-Borne Sound Characterisation	11
2.1 Passive System Properties	11
2.1.1 Mobility and Related Frequency Response Functions	12
2.1.2 Impedance and Inverse Frequency Response Functions	15
2.2 Independent Source Characterisation	16
2.2.1 Direct Measurement of the Blocked Force	18
2.2.2 In-Situ Blocked Force Approach (ISO 20270)	18
2.2.3 Direct Measurement of the Free Velocity (ISO 9611)	21
2.3 Rotational Degrees of Freedom	22
2.3.1 Equivalent Multi-Point Connection	24
2.3.2 Finite Difference Approximation	26
2.3.3 Virtual Point Transformation	29
2.4 Uncertainty in the Interface Description	33
2.4.1 On-Board and Transferability Validation	34
2.4.2 Transformation Consistency of Indicator DoFs	36
2.4.3 ICC – Interface Completeness Criterion	40
2.5 Introduction to Transfer Path Analysis	42
2.5.1 Source-Interface-Receiver Model	43
2.5.2 TPA Categories and Workflow	44
2.5.3 History and Classification of FastTPA	48

PART II. Theoretical Concept of System Identification 51

3 Framework for Round-Trip Identity 52

- 3.1 Introduction to Indirect FRF Determination Using Ideal Excitations . 53
- 3.2 Single Interface Round-Trip Identity 54
- 3.3 Dual Interface Round-Trip Identity 56
- 3.4 Generalised Round-Trip Identity 58
 - 3.4.1 Alternative Derivation of the Generalised Round-Trip Identity 62
 - 3.4.2 Application I: Obtaining Inaccessible Transfer FRFs from Indirect Measurements 63
 - 3.4.3 Application II: Improving Long Distance Transfer FRFs by Sectioned Measurements 65
- 3.5 Sub-Structure Round-Trip Identity 68
- 3.6 Controllability and Observability of the Round-Trip Relations 72
- 3.7 Summary and Concluding Remarks 76

4 Operational System Identification and Concept of FastTPA 78

- 4.1 Introduction to the Transmissibility Concept 79
 - 4.1.1 Transmissibility Concept for Single-DoF Systems 80
 - 4.1.2 Generalised Transmissibility for Multi-DoF Systems 82
- 4.2 Round-Trip System Identification Using Operational Transmissibilities 86
- 4.3 Two-Stage MIMO System Identification Using a Controlled Blocked Force Exciter 93
 - 4.3.1 FastTPA – Inverse Force Identification 100
 - 4.3.2 FastTPA – Forward Prediction, Validation and FastVAP 103
 - 4.3.3 Controllability and Observability in FastTPA 106
- 4.4 Summary and Concluding Remarks 110

PART III. Concept Testing and Simulations 112

5 System Identification and Validation 113

- 5.1 Generalised Round-Trip Identity for a Single Contact Assembly 113
 - 5.1.1 Free-Free Rod Model – Analytical Verification 115
 - 5.1.2 Force Excited Rod – Experimental Validation 118
- 5.2 Indirect System Identification for MIMO Systems 123
 - 5.2.1 Beam-Plate Assembly – Generalised Round-Trip Identity for Inaccessible Assembly FRFs 124
 - 5.2.2 Plate Receiver – Sub-Structure Round-Trip Identity for Receiver FRFs 129
 - 5.2.3 Beam-Plate Assemblies – Controlled Blocked Force Exciter Concept 134
- 5.3 Steering Setup – Characterisation of Long Distance Transfer Functions 139
- 5.4 Summary and Concluding Remarks 144

PART IV. Application to Steering Gear Vibration	146
6 Calibration of a Steering System as a Blocked Force Exciter	147
6.1 Introduction to Electric Powered Steering	147
6.2 Calibration of the Controlled Exciter	149
6.3 Excitation Strategy	154
6.3.1 Roving Shaker Excitation	155
6.3.2 Operational Excitation Using the Electric Motor	157
6.4 Summary and Concluding Remarks	162
7 Vehicle Identification and Steering Noise Prediction	163
7.1 Introduction and Outline	164
7.2 Vehicle Subsystem Description	164
7.2.1 Source – Calibrated Steering System	165
7.2.2 Receiver – Front Subframe and Vehicle Cabin	165
7.2.3 Interface – Subsystem Connectivity and Completeness	168
7.3 In-Situ TPA Benchmark Study	171
7.3.1 Prediction and On-Board Validation of Steering Noise	173
7.3.2 Partial Path Analysis and Contribution Ranking	176
7.4 System Identification with the Controlled Exciter	180
7.4.1 Roving Shaker Excitation	181
7.4.2 Operational Excitation Using the Electric Motor	184
7.5 Case Study I: FastTPA for Vehicle Troubleshooting	190
7.5.1 FastTPA – Remote Blocked Force Relation	191
7.5.2 FastTPA – Interface Blocked Force Relation	196
7.5.3 FastTPA – Extension to the Flexible Modal Regime	198
7.6 Case Study II: FastVAP for Pro-Active Development	202
7.7 Case Study III: System Identification under Realistic Mounting Con- ditions	206
7.7.1 Virtual Point Transformation at the REPS Mounts	207
7.7.2 Repeated Vehicle Identification	209
7.8 Summary and Concluding Remarks	212
PART V. Conclusions, Bibliography and Appendices	214
8 Conclusions and Future Work	215
A Appendices	222
A.1 Local Flexibilities at the Adapter	222
Bibliography	225

List of Figures

1.1	Structure-borne (SB) vibrations induced by the REPS system (source) are propagated through the passive vehicle body (receiver) to the target response at the driver’s ear.	4
2.1	Equivalent multi-point connection by considering 9-DoFs translational coupling at 3 indicator points ($c_1 - c_3$) in the proximity of the interface. The source-receiver setup contains: REPS - source (A); mounting fixture - receiver (B); multi-point tri-axial sensor array - coupling interface (c).	25
2.2	Finite difference configuration for the approximation of the interface dynamics at the REPS mount (c_0) from response and excitation measurements at the indicator DoFs (c_1) and (c_2). The source-receiver setup contains: REPS - source (A); mounting fixture - receiver (B); cross-like element - coupling interfaces (c).	27
2.3	Virtual point transformation to map user-chosen response (blue arrows) and excitation (red arrows) measurements onto the virtual point DoFs (c_0). The source-receiver setup contains: REPS - source (A); mounting fixture - receiver (B); virtual point (c_0) with the coupling interface centred in the REPS mount.	30
2.4	Source-receiver model used in component-based TPA to identify dominant source contributions to a particular response (d).	43
2.5	Stepwise workflow for the three TPA categories and the proposed concepts of fastTPA and fastVAP used as diagnostic and predictive tools, respectively [4].	44
3.1	Transfer paths forming a ‘round-trip’ relationship for the indirect identification of driving-point FRFs, $\mathbf{Y}_{C,cc} = \mathbf{Y}_{C,ca} \mathbf{Y}_{C,ba}^{-1} \mathbf{Y}_{C,cb}^T$ (see Eq. (3.1)), at the coupling interface (c) using excitations with a known input force at source-side locations (a) and receiver-side remote points (b).	54
3.2	Transfer paths of the dual interface round-trip identity for the indirect measurement of transfer FRFs, $\mathbf{Y}_{C,c_2c_1} = \mathbf{Y}_{C,c_2a} \mathbf{Y}_{C,ba}^{-1} \mathbf{Y}_{C,c_1b}^T$ (see Eq. (3.3)), between interfaces (c_1) and (c_2) of a source-isolator-receiver system.	56
3.3	Measurement steps to obtain the path segments forming the generalised round-trip identity for the indirect characterisation of structural, $\mathbf{Y}_{C,dc} = \mathbf{Y}_{C,da} \mathbf{Y}_{C,ba}^{-1} \mathbf{Y}_{C,cb}^T$ (see Eq.(3.19)), and vibro-acoustic, $\mathbf{H}_{C,dc} = \mathbf{H}_{C,da} \mathbf{Y}_{C,ba}^{-1} \mathbf{Y}_{C,cb}^T$, transfer functions.	59
3.4	Re-arranged transfer path segments of the generalised round-trip identity to improve measurement quality of long distance transfer FRFs, $\mathbf{Y}_{C,ab} = \mathbf{Y}_{C,ad} \mathbf{Y}_{C,cd}^{-1} \mathbf{Y}_{C,cb}$ (see Eq. (3.21)), due to poor SNR or a high noise environment.	66

3.5	Path segments of the long distance FRF, $\mathbf{Y}_{C,ab} = \mathbf{Y}_{C,ad} \mathbf{Y}_{C,cd}^{-1} \mathbf{Y}_{C,cf} \mathbf{Y}_{C,ef}^{-1} \mathbf{Y}_{C,eb}$ (see Eq. (3.24)), using a nested generalised round-trip identity with 3 receiver-side excitation locations. The source-receiver model contains: target source DoFs (a); coupling interface (c); virtual coupling interface (e); and remote DoFs (d), (f), and (b) accessible for direct excitation.	66
3.6	Transfer paths forming the sub-structure round-trip identity for indirect identification of $\mathbf{Y}_{A,gc} = \mathbf{Y}_{C,gb} \mathbf{Y}_{C,ab}^{-1} \mathbf{Y}_{A,ca}^T$ (see Eq. (3.32)). The two-step procedure is partly conducted on the coupled assembly (C) and the decoupled source (A).	68
3.7	Transfer paths forming the sub-structure round-trip identity for indirect identification of $\mathbf{Y}_{B,dc} = \mathbf{Y}_{C,da} \mathbf{Y}_{C,ba}^{-1} \mathbf{Y}_{B,cb}^T$ (see Eq. (3.40)). For generality, the target sound pressure probe (d) may be replaced by an accelerometer.	71
3.8	Concept of controllability and observability effectively limiting the independent modes of vibration transmitted across the interface (bottleneck effect).	73
4.1	Transfer paths forming the generalised round-trip identity via ideal excitations or operational forces generated by an embedded source. The generalised transmissibility term may replace the highlighted paths requiring ideal remote excitation.	79
4.2	Two-stage procedure of Eq. (4.32) to characterise the source component (A) as a controlled blocked force exciter and subsequent MIMO system identification of $\mathbf{Y}_{C_2,dc}$ and/or $\mathbf{H}_{C_2,dc}$ in a different assembly (C_2).	96
4.3	Different scenarios of controllability and observability encountered in the inverse force and forward prediction step of fastTPA. Vibrations from the controlled source (A) are channelled through the interface (bottleneck) and transmitted onto the receiver-side [10].	107
5.1	Coupled rods joined end-to-end at (c), discretised using 3D quadratic tetrahedron elements. In this single contact case, the accessible DoFs (a) and (b) at the free end, as well as the internal target location (d) and the interface (c) are defined in the x-direction.	114
5.2	Experimental setup of two virtually coupled rods for indirect identification of the structural properties using the generalised round-trip identity. Four surface-mounted accelerometers characterise the inaccessible coupling interface (c) and target DoF (d).	119
5.3	Validation of the generalised round-trip identity for the interface driving-point mobility and the transfer FRF from (c) to the target DoF (d) of the single contact assembly. Narrowband representation of amplitude (top) and phase spectra (bottom): experimental round-trip data (—); analytically modelled (—); and FE simulation (—).	121
5.4	Representation of the real \Re and imaginary \Im part of the experimentally determined driving-point mobility $Y_{C,cc}$ (—) and the transfer mobility $Y_{C,dc}$ (—) using the generalised round-trip identity.	123

5.5	Test structure for indirect determination of \mathbf{Y}_{C,dc_1} and \mathbf{Y}_{C,dc_2} . Arrows indicate the excitation (red) and response (blue) measurements utilised in the FRF reconstruction using the generalised round-trip concept, whilst excitations depicted in the close-up inset are required for the reference measurements. The source-receiver setup contains: beam - source (A); plate - receiver (B); cross-like elements with the coupling interfaces (c_1, c_2) being positioned exactly in its center plane; inaccessible target DoFs (d).	125
5.6	Validation of inaccessible transfer functions $\mathbf{Y}_{C,dc}$ using a determined system of equations ($n_a = n_b = n_c = 12$). Narrowband representation of amplitude (top) and phase spectra (bottom): reference measurement (—); compared to the indirect generalised round-trip identity (—). . .	126
5.7	Validation of the inaccessible FRF $\mathbf{Y}_{C,dc}$ for an over-determined solution ($n_a \geq n_b \geq n_c = 12$) of the generalised round-trip identity and results for the determined system (as in Fig. 5.6b) subject to singular value rejection. Narrowband representation of amplitude (top) and phase spectra (bottom): reference measurement (—); over-determined generalised round-trip identity (—); and round-trip result using TSVD (—).	128
5.8	Receiver (B) for indirect measurement of $\mathbf{Y}_{B,dc}$ using the sub-structure round-trip identity. Arrows indicate the excitation (red) and response (blue) measurements utilised in the FRF reconstruction, whilst excitations depicted in the close-up inset are required for the reference measurement.	130
5.9	Validation of the receiver FRF $\mathbf{Y}_{B,dc}$ for a determined ($n_a = n_b = n_c = 12$) and over-determined ($n_a > n_b > n_c$) solution of the sub-structure round-trip identity. Narrowband representation of amplitude (top) and phase spectra (bottom): reference measurement (—); compared to the determined (—); and over-determined (—) sub-structure round-trip result.	131
5.10	Transmissibilities for the receiver (—) and the assembly (C), with excitations applied on the source (—) or at the interface (—), assuming full controllability/observability. An incomplete subset of interface excitations, e.g. discarding rotations in $\mathbf{T}_{C,dc}^{(c)}$ (—), leads to a not invariant matrix.	133
5.11	Test structures (C_1) and (C_2) for the two-stage system identification using the source (A) as a blocked force exciter. Controlled roving excitation (red arrows) are applied with a shaker, as shown in the close-up inserts. The source-receiver setups contain: beam - source (A); aluminium plate - receiver (B_1); plastic plate - receiver (B_2). . .	135
5.12	Element of the transmissibility matrix relating responses between the DoFs (d) and (b) of two different assemblies. $\mathbf{T}_{C_{1,2},db} \in \mathbb{C}^{3 \times 21}$ is determined via conventional mobility measurements (—) and phase referenced velocity matrices (—).	137

5.13	Validation of $Y_{C_2,dc}$ using controlled electro-dynamic shakers (see close-up inset in Fig. 5.11b) to turn the source (A) into a blocked force vibration source. Narrowband representation of amplitude (top) and phase spectra (bottom): reference measurement (—); compared to the two-stage estimates using the mobility (—) and velocity approach (—).	138
5.14	Test structure forming a long distance transfer function $Y_{C,ab}$ from the remote position (b) on the beam to the motor mount (a). Arrows indicate the excitation (red) and response (blue) measurements of the conventional FRF characterisation, whilst the shaker excitation at (d), depicted in the left close-up inset, is part of the generalised round-trip identity. The source-receiver setup contains: REPS - source (A); plate-beam assembly - receiver (B); cross-like elements - coupling interfaces (c_1, c_2); remote locations (d) accessible for direct excitation.	140
5.15	Acceleration response (—) at the motor mount (a) with poor SNR, close to the sensor's noise floor (—), due to 'low/insufficient' shaker excitation at (b). The directly measured long distance FRF $Y_{C,ba}$ (—) (Fig. 5.15b) is clearly influenced by noise, whilst the generalised round-trip concept (—) improves measurement quality.	142
5.16	Validation of the long distance FRF $Y_{C,ab}$ based on a complete description of the coupling interface (c) (same as in Fig. 5.15b), including rotations and translations ($n_c = 12$; finite-difference approximation) and simplified translational coupling only ($n_c = 6$; e.g. tri-axial sensor). Narrowband representation of amplitude (top) and phase spectra (bottom): measured reference at 'high' shaker output (—); generalised round-trip identity with fully described interface (—); and using an incomplete interface description (—).	143
6.1	Steering system in its intended vehicle installation. The close-up insets show the replaced stepper motor and the ball nut assembly to transform the motor torque into a (side-to-side) rack force [source: bosch-mediaspace.com].	148
6.2	Calibration setup (C_1) to turn the REPS system into a controlled blocked force vibration exciter. Arrows indicate excitation (red) and response (blue) measurements as utilised in the FRF measurements. The calibration setup contains: REPS - source (A); plate - receiver (B_1); adapters with the coupling interfaces (c_1, c_2) being positioned exactly in its centre.	150
6.3	Evaluation of the overall and specific excitation consistency for the finite difference approximation of 8 excitations at each coupling point: (c_1) motor-side (—); and (c_2) pinion-side (—).	152
6.4	ICC for the calibration bench using a 'complete' interface description (—) with translational and rotational coupling DoFs and reduced incomplete connectivity accounting for translational-DoFs (—) at (c_1, c_2) only (i.e. x, y, z coupling).	154

6.5	Singular values of the bench assembly matrix $\mathbf{Y}_{C_1,ba}$ for 36 roving excitations on the REPS system and 24 remote DoFs (b). The first 8 values (—) are dominant, representing 96 % (■) of the energy, indicating a bottleneck effect at the interfaces.	156
6.6	Variation in the driving-point FRFs of the calibration setup (C_1) for different steering angles: centre position (—); left end stop (—); and right end stop (--).	159
6.7	Singular values of the bench assembly matrix $\hat{\mathbf{V}}_{C_1,ba}$ for operational excitation of the controlled REPS system and 24 remote DoFs (b). The first 8 values (—) are dominant, representing 96 % (■) of the energy, indicating a bottleneck effect at the interfaces.	161
7.1	Bottom view: Scan of the front subframe, including the target accelerometer (d_1) and the adapters to facilitate access at the coupling interfaces (c_1, c_2). Blue arrows indicate response measurements at the interfaces, the remote DoFs (b) and the target (d).	166
7.2	Scan of the vehicle cockpit with the target microphones at the driver's ear positions and a windscreen accelerometer at (d_3). The sound pressure probes at (d_2) may be replaced by a volume-velocity source for reciprocal measurements, as shown in the close-up.	167
7.3	ICC for the calibration bench (—) and the vehicle assembly (—), alongside changes between the full (i.e. 3 translations and 3 rotations) and an incomplete interface description (—) using translational DoFs (x, y, z) at each connection point.	169
7.4	Evaluation of the response and excitation consistency for the finite difference approximation of 8 responses/excitations at each coupling point: (c_1) motor-side (—); and (c_2) pinion-side (—).	170
7.5	Vehicle assembly for in-situ TPA benchmarking and prediction of steering noise. The source-receiver setup contains: REPS - source (A); subframe - receiver (B_2); adapters - coupling interfaces (c_1, c_2); target DoF (d_1).	171
7.6	SNR at the target accelerometer/sound pressure probe (d_1, d_2) for the operated REPS (constant speed). Narrowband representation: measured operational response (—); measured noise floor (—); and predicted noise (—) for the vehicle assembly (C_3).	173
7.7	On-board validation at the target accelerometer/microphone (d_1, d_2) for the operated REPS (steering cycle). Narrowband representation: measured operational response (—); predicted velocity/sound pressure response (—) of the vehicle assembly (C_2).	175
7.8	Narrowband contribution analysis for the total predicted sum and the partial paths from the coupling DoFs (c_1, c_2) to a target sound pressure probe (left driver's ear) for the operational REPS (constant speed).	177

7.9	Measured and predicted sound pressure at the left driver's ear (d_2), including a contribution ranking of the partial paths. Sound pressure levels: measured (■); predicted sum (■); and rank ordered partial contributions (■) for the operational REPS system.	178
7.10	On-board validation for an incomplete interface description (x , y , z and β) and ICC for the corresponding full 12 DoF (—) and simplified 8 DoF (—) interface coupling.	179
7.11	Validation of the predicted transfer FRFs $\mathbf{Y}_{C_2,dc}$ between the coupling interface (c_1) and the vibration response on the subframe (d_1). Narrowband representation for force excitation (top) and moment excitation (bottom): shaker measurement (—); and prediction using a roving shaker approach (—).	182
7.12	Validation of the predicted vibro-acoustic FRFs compared to shaker and volume-velocity source measurements of $\mathbf{H}_{C_2,dc}$ and $\mathbf{H}_{C_2,cd}^T$, respectively. Narrowband representation: direct measurement (—); reciprocal characterisation (—); and prediction using a roving shaker approach (—).	183
7.13	Validation of the predicted driving-point FRFs $\mathbf{Y}_{C_2,cc}$ at the coupling interface (c_1). Narrowband representation of amplitude (top) and phase spectra (bottom): reference measurement (—); and prediction using a roving shaker approach (—).	184
7.14	Validation of the transfer FRFs between the coupling interface (c_1) and the vibration response on the subframe (d_1). Narrowband representation of amplitude (top) and phase spectra (bottom): reference measurement (—); and prediction using a controlled motor excitation (—).	186
7.15	Blocked load excitation of the operated REPS system (white noise) in the calibration setup (C_1) (—) and reproduced in the vehicle (C_2) (—). The blocked load noise (—) allows evaluating the effect of noise in the reproduced excitations.	187
7.16	Validation of the vibro-acoustic transfer FRFs between the coupling interface (c_1) and the sound pressure probe (d_2). Narrowband representation: reference (shaker) measurement (—); and prediction using a controlled motor excitation (—).	189
7.17	Spread (■) between direct (shaker) and reciprocal (volume-velocity source) vibro-acoustic measurements compared to the predicted (—) FRF obtained with the controlled motor approach between the motor-side interface DoF (c_{1y}) to the target microphone (d_2) (see Fig. 7.16a).	190
7.18	Blocked loads at the interface (c_1) for the operated REPS system. Narrowband representation of forces (top) and moments (bottom): results of the benchmark in-situ TPA study (Sec. 7.3) (—); fastTPA using a controlled motor excitation (—).	193
7.19	Predicted SPL and partial contributions obtained in the benchmark study (in-situ TPA), and deviations for different fastTPA variants: In-situ TPA (—); and fastTPA using a roving shaker approach (—) or operational motor excitation (—).	195

7.20	Transferability validation to indicate errors in fastTPA. Narrowband representation: measured reference (—); and predicted sound pressure response using a roving shaker approach (—) or operational motor excitation (—) for system identification.	196
7.21	Predicted SPL and partial contributions obtained in the benchmark study (in-situ TPA), and deviations for interface fastTPA relation: In-situ TPA (—); and fastTPA using a roving shaker approach (—) or operational motor excitation (—).	197
7.22	Partial sound pressure contribution obtained from in-situ TPA (i.e. conventional FRF measurements (—)) and application of the interface fastTPA relation (—) using controlled roving excitations.	198
7.23	Excitation consistency for the virtual point transformation of 8 excitations (red arrows) to a 7-DoFs interface description (6 rigid DoFs + flexible χ -extension DoF) at each coupling point: (c_1) motor-side (—); and (c_2) pinion-side (—).	199
7.24	In-situ TPA (benchmark) contribution analysis (—) for the updated 7-DoFs interface connectivity and deviations for fastTPA (remote relation) using a roving shaker approach (—) or operational motor excitation (—).	201
7.25	Predicted SPL and partial contributions for a conventional VAP (1.) and deviations between different variants: Variation between conventional VAP (■) using direct (—) and reciprocal (—) forward FRFs measurements; and fastVAP using the roving shaker approach (—) or operational motor excitation (—) to predict the forward FRFs.	204
7.26	Transferability validation of the predicted sound pressure response $\mathbf{v}_{C_2,da}$ in the vehicle cabin. Narrowband representation: reference measurement (—); and fastVAP predictions (3.—) and (4.—). (Inset covers freq. range from 1 - 1.5 kHz).	205
7.27	Interface sensor array indicating the response index (see Fig. 7.28a) at each virtual point (yellow) and remote shaker excitation on the windscreen (d_3) for reciprocal measurement of the virtual point FRFs $\mathbf{Y}_{C_3,cd}$	207
7.28	Evaluation of the frequency-averaged sensor specific consistency for the 13 channels at each coupling point: (c_1) motor-side (■); (c_2) pinion-side (■), and improved overall consistency for the 9 best response DoFs selected at each virtual point.	209
7.29	Reciprocal transfer FRFs $Y_{C_3,dc}$ between the coupling interface at the subframe and the vibration response at the vehicle's windscreen. Narrowband representation for translational force excitation (top) and moment excitation (bottom): reciprocal shaker measurement (—); and prediction (—) using the controlled motor.	210
A.1	Translational and rotational driving-point mobilities of the resiliently suspended cocoon adapter using finite difference approximation. Narrowband representation for translational (top) and rotational (bottom) DoFs: experimentally obtained reference (—); numerical FE simulation (—) used during the design.	223

A.2 Mode shape of the first non-rigid mode (bending along the x-axis) of the interface adapter. The locally flexible behaviour, for example, between the response channels (c_{2x}) and (c_{4x}) at the interface, limit the frequency range of the finite difference approximation. 224

List of Tables

2.1	Commonly used frequency response functions along their relations. The mobility can be found from the accelerance/receptance: $Y_{ik} = A_{ik}/(j\omega) = j\omega R_{ik}$ [21].	15
2.2	Definition of the mechanical impedance and related frequency response functions. The impedance can be converted: $K_{ik} = j\omega Z_{ik}$ or $M_{ik} = Z_{ik}/(j\omega)$ [21].	16
5.1	Geometry, material properties and excitation/response positions for the free-free rod, where; l -length, h - height, E_0 - Young's modulus, ρ - density and ν - Poisson's ratio, and x_{ik} - DoF positions of (a), (c), (d) and (b).	114
5.2	Geometry and material properties for the exchanged plate receivers (B ₁) and (B ₂), where; l -length, w - width, h - height, E_0 - Young's modulus, ρ - density and ν - Poisson's ratio.	135

Acknowledgements

Research is far from an individual achievement, and I want to thank everyone who has contributed to this adventure. The work presented in this thesis has been carried out at the Acoustics Research Centre at the University of Salford in collaboration with Robert Bosch Automotive Steering LLC.

First, I would like to express my sincere gratitude towards Prof. Andy Moorhouse for his continuous support, commitment and patience. Andy, you have been a source of inspiration throughout the project, and I admire your passion for research, professional knowledge and positive spirit. I feel very fortunate and couldn't have asked for a better supervisor for my PhD studies. I would also like to thank Dr. Andy Elliott and Dr. Joshua Meggitt for their guidance, insightful comments and encouragement.

Special thanks go to Rosie and Josh, not only for your hospitality but also for making me feel welcomed in Salford and the countless times you played 'Helene Fischer' for me. Also in need of special thanks are my fellow post-graduates and the staff members at the Acoustics Research Centre. The past 3/4 years would certainly have been a lot less enjoyable without you all.

This project would not have been possible without the support of Robert Bosch Automotive Steering LLC. I would like to thank Michael Yankonis and the colleagues of the NVH and Testing Department for our pleasant times, collaboration and shared ideas. And most of all to Dr. Michael Sturm – it has been a joy to work with you, turning presentations into artworks, or spend the weekend with some vehicle measurements. I never thought an internship in acoustics could turn into a passion. You introduced me to the world of blocked force and set me on the path to becoming a researcher.

On a more personal note, I would like to thank my family, Danica, Robert and Sarah, and my beloved Katharina. Your endless support and encouragement led me to a PhD on the other side of the world and cheered me on throughout it. From the bottom of my heart, **thank you.**

Author Publications

This thesis presents the theoretical and experimental findings resulting from a three-year research project in cooperation with Robert Bosch Automotive Steering LLC. Other intermediate results, not per definition reflected in this thesis, have been reported in [1, 2], whereas [3] is presented in almost original form.

Journal Publications

- [3] K. Wienen, M. Sturm, A.T. Moorhouse, J.W.R. Meggitt. ‘Generalised round-trip identity - for the determination of structural dynamic properties at locations inaccessible or too distant for direct measurement’. In: *Journal of Sound and Vibration*, 511, Article 116325, 2021.
- [2] J.W.R. Meggitt, A.T. Moorhouse, K. Wienen, M. Sturm. ‘A framework for the propagation of uncertainty in Transfer Path Analysis’. In: *Journal of Sound and Vibration*, 483, Article 115425, 2020.

Conference Publication

- [1] K. Wienen, M. Sturm, A.T. Moorhouse, J.W.R. Meggitt. ‘Robust NVH engineering using experimental methods - source characterization techniques for Component Transfer Path Analysis and Virtual Acoustic Prototyping’. In: *Proceedings of Noise and Vibration Conference and Exhibition*, Grand Rapids (USA), SAE Technical Paper Series, 2019.

IP Application

- M. Sturm, K. Wienen, M. Yankonis, A.T. Moorhouse. ‘Controlled blocked force exciter (cBFE) for system identification in assembled structures’. Invention report, U.S. Non-Provisional Patent Appl. No.: 17/396,412, 2021.

Nomenclature

The defined symbols tabulated below are used recurrently throughout this thesis.

Roman Symbols

B	Transformation matrix	p	Sound pressure
<i>E</i>	Young's modulus	R	Modal reduction / IDM matrix
F	Force matrix	<i>S</i>	Auto-/cross-spectrum
f	Force	T	Generalised transmissibility matrix
H	Vibro-acoustic transfer function matrix	V	Velocity matrix
<i>h</i>	Height	v	Velocity
<i>j</i>	Imaginary unit ($j = \sqrt{-1}$)	<i>x, y, z</i>	Cartesian coordinates
<i>l</i>	Length	Y	Mobility matrix
<i>n</i>	Number of DoFs	Y_{ik}	Mobility element

Greek Symbols

α, β, γ	Rotational coordinates	ρ	Density
ε	Strain	σ	Stress
η	Loss factor	τ	Moment
μ	Residual	χ, ψ, ζ	Flexible extension coordinates
ν	Poisson's ratio	ω	Angular frequency
ψ	Angular velocity		

Accents and Other Symbols

$\hat{\square}$	Operational quantity	$\hat{\square}$	Free quantity
\angle	Phase angle	$\bar{\square}$	Blocked quantity
Δ	Separation distance	$\tilde{\square}$	Approximated quantity
$\dot{\square}$	Derivative		

Subscripts and Superscripts

\square^*	Complex conjugate	\square_B	Pertaining to receiver (B)
\square^+	Moore-Penrose pseudo inverse	\square_b	Receiver-side remote DoF
\square^H	Complex conjugate transpose	\square_C	Pertaining to assembly (C)
\square^T	Transpose	\square_c	Coupling interface DoF
\square_+	Solution to the right	\square_d	Receiver-side target DoF
\square_-	Solution to the left	\square_e	Source-side target DoF
\square_A	Pertaining to source (A)	\square_I	Pertaining to isolator (I)
\square_a	Source-side remote DoF		

Abbreviations

CAD	Computer-Aided Design	NVH	Noise, Vibration and Harshness
CR-	Component Replacement	OBV	On-Board Validation
DoF	Degree of Freedom	OPAX	Operational Path Analysis with eXogeneous inputs
ECU	Electronic Control Unit	OTPA	Operational Transfer Path Analysis
EMPC	Equivalent Multi-Point Connection	PAC	Phase Assurance Criterion
EPS	Electric Power Steering	REPS	Rack-and-pinion Electric Power Steering
FE	Finite Element	RMS	Root Mean Square
FRAC	Frequency Response Assurance Criterion	SB	Structure-Borne
FRF	Frequency Response Function	SCU	Steering Control Unit
ICC	Interface Completeness Criterion	SEMM	System Equivalent Model Mixing
IDM	Interface Displacement Mode	SNR	Signal-to-Noise Ratio
ISO	International Organisation for Standardization	SPL	Sound Pressure Level
iTPA	In-situ Transfer Path Analysis	SVD	Singular Value Decomposition
LTI	Linear and Time-Invariant	TF	Transfer Function
MCC	Measurement Consistency Criterion	TPA	Transfer Path Analysis
MEMS	Micro-Electro-Mechanical Systems	TSVD	Truncated Singular Value Decomposition
MIMO	Multiple-Input Multiple-Output	VAP	Virtual Acoustic Prototyping

Nomenclature Convention

Throughout this thesis, formulations and symbols are, for the most part, given in the frequency domain unless otherwise specified. For clarity, explicit dependence on the radian frequency ω has been omitted, except where confusion may arise. The following typological conventions have been adopted:

- ▶ Scalars are denoted by italic lower-case characters, e.g. f , v ;
- ▶ Vectors are denoted by bold lower-case characters, e.g. \mathbf{f} , \mathbf{v} ; or specified by braces $\{ \}$;
- ▶ Matrices and vector arrays are denoted by bold capital characters, e.g. \mathbf{Y} , \mathbf{F} ; or specified by brackets $[\]$;
- ▶ Capitalised subscripts denote the sub-structure (e.g. source (A), receiver (B)) or assembly (C) to which the quantity belongs, e.g. \mathbf{f}_B ... force vector applied to sub-structure (B);
- ▶ Lower-case subscripts denote a subset of DoFs at a defined location (e.g. receiver-side (b), source-side (a)) on the structure, e.g. $\mathbf{f}_{A,c}$... force vector applied to sub-structure (A) at the interface DoFs (c).
- ▶ In a sequence of two lower-case subscripts, the first one generally defines the response position whereas the second subscript refers to the excitation location, e.g. $\mathbf{Y}_{C,ba}$... transfer mobility matrix of assembly (C) (excitation and response degree of freedom do not coincide), with response at (b), excited at (a). A similar notation is used for response measurements, e.g. $\mathbf{v}_{A,ca}$... velocity vector of the free source (A) measured at (c) due to an excitation at (a). (Exception: transmissibility matrices, where both subscripts define response positions)
- ▶ Lower-case superscripts denote the excitation position, in case the DoFs cannot be specified by lower-case subscripts, e.g. $\mathbf{T}_{C,db}^{(a)}$... transmissibility matrix of the coupled assembly (C) measured between the response DoFs (d) and (b) due to an excitation at (a); $\bar{\mathbf{f}}_{A,c}^{(a)}$... blocked force of the source (A) present at the interface (c) due to an excitation mechanism at (a).
- ▶ Equations framed in a grey box typically highlight the governing expression of a derivation, method or theory. This should provide guidance through the different chapters and improve recognition of the focus topic.

Abstract

Under certain driving and road conditions, steering manoeuvres may provoke audible noise inside the vehicle compartment induced by the electric power steering (EPS) system. Regarding noise, vibration and harshness (NVH), engineers require practical tools to assess, design and troubleshoot steering noise in vehicles. For acoustic development and refinement, test-based methodologies such as Transfer Path Analysis (TPA) are used to analyse noise and vibration propagation in complex systems. In response to the evolving demands in acoustic engineering, TPA approaches have been continuously improved to provide reliable diagnostic information, simplify the procedure or accelerate development time. Although an established tool in many industries, TPA is a rather complex and time-intensive procedure. Furthermore, state-of-the-art TPA approaches also tend to suffer from a variety of practical limitations such as impracticality to include particular paths for structure-borne sound transmission (e.g. in-plane), inability to measure rotational dynamics (e.g. moment excitation), insufficient signal-to-noise ratios (SNR), or simply restricted access. These inherent challenges have led to near-routine neglect of transmission paths, potentially providing an engineer with unrealistic diagnoses to make informed design changes. This thesis addresses most of the above challenges by proposing a variety of novel experimental techniques to augment state-of-the-art TPA methods with the aim to increase reliability of in-vehicle and bench-based NVH system development while significantly reducing measurement time and effort.

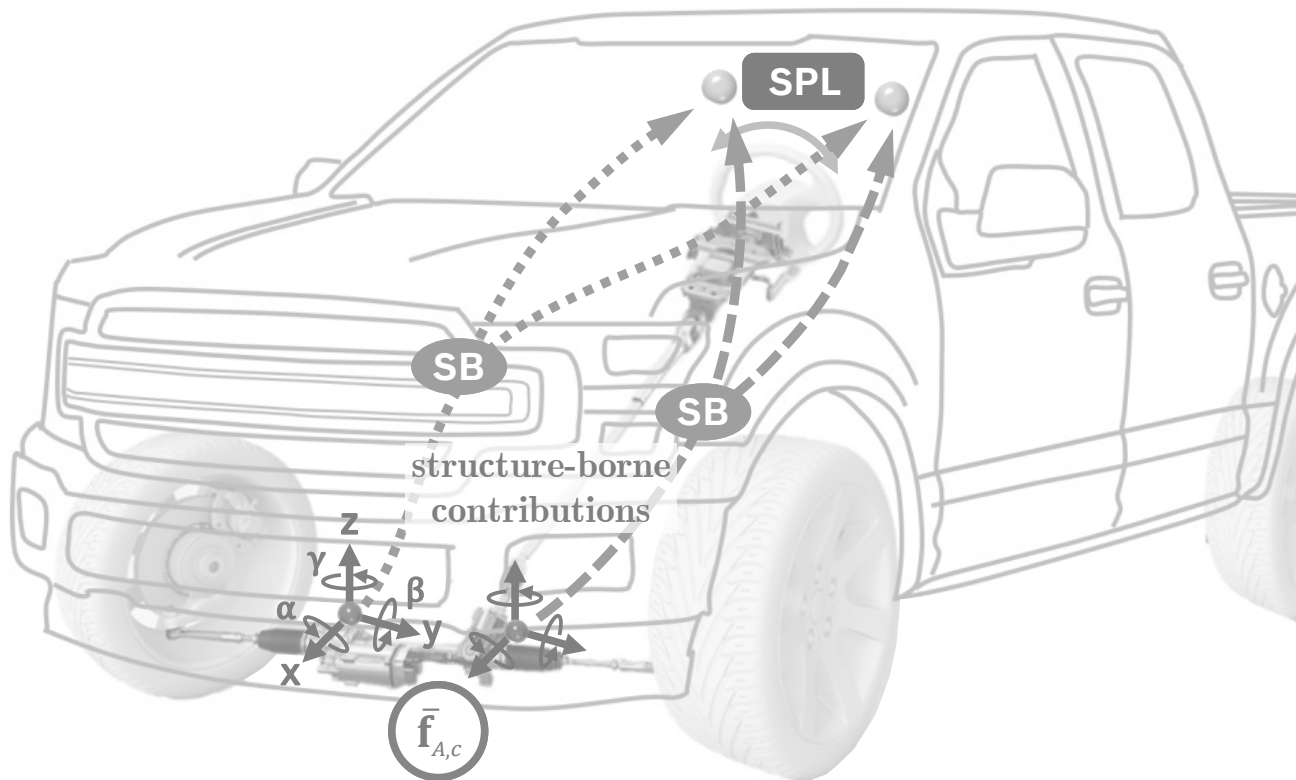
A key step, also the most time-consuming part, of any TPA is the measurement of frequency response functions (FRFs). These measurements may be difficult or impossible if the measurement locations are inaccessible or difficult to excite (e.g. in-plane directions). Therefore, a framework for indirect measurement is proposed, by invoking the round-trip identity, providing experimentalists with the ability to relocate measurements to more convenient positions on the test structure. A generalisation of this identity is proposed to reconstruct FRFs between an interface and some selected points using only remote measurement positions. Within this generalised concept, direct measurement of rotations or inaccessible points is avoided altogether to reduce complexity in the measurements commonly involved in TPA. Manipulation of the identity yields a formulation for long distance transfer FRFs, expressed by multiple shorter paths with a better SNR, to facilitate TPA in heavy-weight or extensively large structures.

Classical TPA measurements require each transmission path to be characterised by the dynamic output (e.g. vibration or sound pressure) in response to a known input load (e.g. force or moment excitation). More recently, measurements using output quantities only have been developed, but the reduced measurement time they allow comes at the expense of clarity and accuracy. This thesis proposes an alternative approach in which in-situ system identification of all physically existing transfer paths is performed simultaneously by converting any vibration source into a multiple degree of freedom (DoF) blocked force exciter. The concept is to exploit the invariance of the source's blocked force, so that the same blocked force can be assumed to act irrespective of the receiver to which the source is attached. This source excitation has to be characterised on a test bench in the so-called calibration stage prior to installing the same (calibrated) source in the target assembly. In the subsequent system identification stage, exact structural and vibro-acoustic transmission paths can then be characterised by simple operational response measurements in the installation due to the known blocked force excitation.

This two-stage system identification method with a controlled source provides a convenient alternative to conventional FRF measurements with an instrumented hammer or shaker. Especially in the context of TPA, in which such FRFs are required for inverse force identification and forward response prediction, significant time savings can be achieved. As a diagnostic tool, this process is denoted as 'fastTPA'. It is shown that concepts adopted from control theory, more specifically controllability and observability, are strongly related to fastTPA and provide practical guidelines.

The thesis concludes with an experimental case study utilising the introduced methods to analyse steering induced sound and vibration in a fully assembled vehicle. It is demonstrated that a steering system, calibrated as a controlled blocked force exciter (multi-DoF shaker), can be used to obtain high-accuracy structural and vibro-acoustic FRFs in a multi-kHz range. For a time-efficient yet precise estimation of path contributions, these FRFs are used for fastTPA and to construct a realistic Virtual Acoustic Prototype capable of predicting the operational pressure response in the vehicle compartment. When benchmarked against the latest advancements in component-based TPA approaches, fastTPA is found to be significantly faster with at least the same accuracy and reliability.

PART I. Introduction, Literature Review and Theory



1

Introduction

This introductory chapter will outline the context behind the research project presented and introduce the concept of fast system identification. Following this, the aims and objectives of this thesis will be discussed, and lastly, its structure outlined.

Chapter contents:

1.1	Background and Motivation	2
1.2	Concepts for Reliable and Fast TPA	6
1.3	Thesis Aims and Objectives	8
1.4	Thesis Outline	10

1.1 Background and Motivation

Rapidly increasing product complexity together with quickly evolving customer expectations on functionality, performance and quality attributes drive manufacturers to shorten product development cycles whilst the number of product variants increases. To minimise costs and time-to-market, there is a strong trend towards fewer physical prototypes, even to dispense with them altogether. However, in the absence of physical prototypes, practical tools are required to assess, design and troubleshoot noise and vibration behaviour which raises specific technical challenges. Ideally, these tools should consider both objective and subjective factors since acoustic targets in the development process need to meet customer expectations. Hence, noise, vibration and harshness (NVH) engineering is a challenging and often iterative process, spanning a physical and perceptual domain.

NVH development strives to minimise the overall vibration and/or noise levels or shape their characteristics to sound more pleasant by utilising sound masking or filtering techniques. While driving a vehicle, multiple sound sources are acting in parallel. One source contribution of special interest in this research project is steering noise, particularly when steering at high speeds, such as for parking manoeuvres. The operating noise of a Rack-and-Pinion Electric Power Steering (REPS) system might not be an immediate concern for vehicles with internal combustion engines but becomes more relevant once changing to hybrid or fully electric powertrains. After all, interior noise levels in these vehicles will likely drop further, leaving the driver fully exposed to the typical actuation noise of the steering system and all sorts of clunks and rattles that are related to dynamic road feedback.

REPS systems are optimised for high power density, i.e. high mechanical performance is achieved with a lightweight and compact design, which, to some extent, may contradict low-noise NVH design guidelines. Furthermore, these systems are typically custom-designed for a specific vehicle platform, with additional differentiation for various trim lines. For example, the gear ratio may be changed for sports and performance editions to improve the vehicle's handling, whereas, in other variants, the steering system is mounted resiliently (like a combustion engine supported by rubber mounts) to focus on driving comfort. Although resilient coupling elements (e.g. vibration dampers) are an effective way to reduce vibration transmission, added flexibility reduces stiffness in the lateral (sideways) direction and compromises handling. Experience has shown that these variants may create noises with different characteristics when operated in a vehicle. However, if a different noise is experienced in the vehicle cabin, this does not directly imply that source excitation (i.e. the vibration generating mechanism) has changed. As a consequence, reducing steering noise requires NVH approaches based on testing on a vehicle level.

The above example demonstrates that NVH engineering, in vehicles for example, needs to account for the actively vibrating component and the transmission of these vibrations through the assembled structure. This interaction between the operating REPS system and the connected receiver structure is often referred to as 'the transfer path problem' [4]. In other words, high noise levels in the cabin may be caused by a high dynamic load of the source, a sensitive transfer path, or a combination of both. One way to look at the link between source excitation and received response is using a source-transmission-receiver model. Consider the automotive example of a steering system mounted in a vehicle. The REPS system is connected to the front

subframe, steering shaft and wheel-suspension assemblies, which are in turn coupled to the chassis and bodywork. The vehicle assembly can be decomposed into active (source) and passive (receiver) parts to analyse the transfer path problem. The coupling interface is the common boundary between these sub-components. This concept is visualised in Fig. 1.1, where steering noise and vibration are propagated through the vehicle structure.

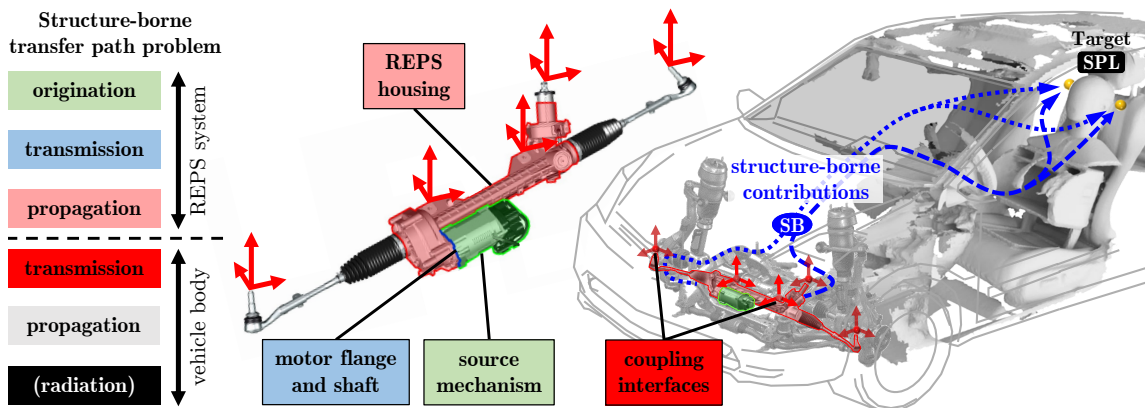


Figure 1.1: Structure-borne (SB) vibrations induced by the REPS system (source) are propagated through the passive vehicle body (receiver) to the target response at the driver's ear.

During operation, vibrations are generated inside the electric motor and transmitted via the motor shaft and its flange onto the REPS system. Usually, the entire active REPS system is considered the source, as it is often challenging to identify excitation mechanisms individually due to their complexity. Therefore, it is chosen to consider all excitation mechanisms as one collective source of vibrations. This way, the source excitation (red arrows at each source-receiver mounting point in Fig. 1.1) is separated from the vehicle's structural/acoustic transfer characteristics. Steering noise is predominantly of structure-borne (SB) nature (evidence is presented in Sec. 7.3.1), that is, vibrations are transmitted over the structural interface and radiated further downstream on the receiver-side. As such, vibrations are propagated through different transfer paths of the vehicle body and radiated from components (e.g. panels in the vehicle interior) at the passive side. Altogether, they contribute to the total sound pressure level (SPL) at the target position inside the vehicle cabin. Analysis of the source-transmission-receiver model provides the level of detail required to troubleshoot steering noise in coupled assemblies.

As far as automotive NVH engineering is concerned, Transfer Path Analysis (TPA) is considered the most suitable process to analyse noise and vibration propagation in complex built-up structures. TPA's role is to predict (and auralise) the contribution of each active component (red arrows in Fig. 1.1) to an operational response at some chosen target position. To do so, the source activity, or 'strength', must first be estimated; then, the transmission paths of each component are identified. Based on their relative contributions, an engineer can identify troublesome vibration sources/transmission paths and investigate appropriate design changes. Often a contribution ranking of the underlying source and transmission mechanisms is thought of as the basis for effective NVH design. As such, TPA has become an essential tool in product development and refinement, particularly with regards to testing and validating the vibro-acoustic performance in physical prototypes. It provides the information and level of detail necessary to make informed design changes, e.g. whether a structural modification will affect the NVH behaviour inside the vehicle cabin.

Although an established tool in many industries, TPA is a rather complex and time-intensive procedure. Over the years, various TPA methodologies have been proposed to simplify the procedure or accelerate development time (the reader is referred to [4] for a detailed review of the history and development of TPA). The main challenge in TPA studies is that they involve time-consuming system identification to characterise all contributing transfer paths, which prohibits their use on a widespread basis. Whilst collecting operational data by performing (manual) left/right steering only takes a couple of minutes, the required system identification step (i.e. the measurement of the transfer paths) in complex automotive assemblies cannot be performed in a time-efficient way. For example, performing TPA to quantify the contributions of steering induced noise from a REPS system to the overall cabin sound in a vehicle can take up to a week, depending on the level of detail and the system's complexity. State-of-the-art TPA approaches also tend to suffer from a variety of practical limitations such as the impracticality to include particular paths (e.g. in-plane), the inability to measure rotational dynamics (e.g. moment excitation), insufficient signal-to-noise ratios (SNR), or simply restricted access. These inherent challenges have led to near-routine neglect of transmission paths, potentially providing an engineer with unrealistic diagnoses to make informed design changes. Furthermore, the potential to predict the effect of design changes is limited; structural modifications applied to the passive receiver (e.g. vehicle) would

require new transfer path measurements. Therefore, TPA methods do not offer the flexibility desired to predict NVH performance during an iterative design process.

Therefore, this thesis aims to propose and test new TPA procedures which address many of the above mentioned challenges. In the following, the principal concept of a novel TPA method for fast and reliable diagnoses in complex systems is outlined. This method is referred to as ‘fastTPA’.

1.2 Concepts for Reliable and Fast TPA

Over the years, many TPA variants have been developed, differing in their implementation and interpretation. Emphasis is on test-based methods, as the development of accurate numerical models is rather limited given the high-frequency aspect and complexity of vehicle components. Popular variants include classical [5], in-situ [6], component-based [7] and operational [8] TPA. Different methods can be chosen to meet specific testing requirements, e.g. to reduce time and experimental effort, usually at the expense of the level of detail and confidence. That said, TPA can be adapted to a wide range of applications and adjusted for either quick troubleshooting or thorough analysis. Although these methods are well-established in many industries, it appears as yet few studies consider TPA in its full detail. Practical challenges encountered in the measurements (e.g. in-plane or rotations) have led to near-routine neglect of transmission paths. For example, when performing an in-situ TPA, access to the source-receiver interface is often limited, and some of the required measurements cannot be undertaken. In this case, it is possible to redefine the interface elsewhere, probably at a less meaningful but accessible location, or some transmission paths are simply not considered in the analysis. Either scenario can lead to unrealistic diagnoses, particularly if too few path are considered or important transmission paths are neglected. In this sense, it appears that errors in TPA are often associated with the failure to identify all contributing paths in a feasible way, a common challenge to most TPA variants¹. Hence, there is a need for fast and reliable methods of system identification that we can begin to perform thorough TPA so that their true capabilities may be exploited.

¹ Operational TPA avoids transfer path measurements altogether and instead identifies dominant contributions using output quantities (e.g. operational accelerations), usually at the expense of clarity and accuracy. Although faster, operational TPA does not provide the level of detail expected from a TPA study since source excitation and the transfer characteristics are not separated.

For reliable TPA, all transfer paths need to be considered through which noise and vibrations are propagated. Typically, structural transfer paths are determined one at a time using instrumented hammers or electro-dynamic shakers. If physically relevant transfer paths cannot be obtained through direct measurement, indirect approaches may be applied to relocate (hard-to-access) measurement positions to more convenient locations. A similar concept was proposed by Moorhouse et al. [9] where a relocation could be achieved through the ‘round-trip identity’. However, the original formulation does not facilitate the indirect characterisation of transfer paths. Therefore, novel approaches are required, particularly for transfer paths inaccessible or too distant for direct measurement. Such indirect approaches may be integrated as part of state-of-the-art TPA methods to provide more reliable and thorough analyses, whilst interpreting the TPA results remains unchanged. This way, all transfer paths can be considered for a correct representation of the complex system by a set of source excitations and transfer paths.

Although indirect approaches can readily be implemented in existing TPA methodologies, system identification is still time-consuming to apply. This makes it challenging to use TPA as a standard engineering tool on a daily basis. To perform transfer path measurements in a time effective way, this research project also explores a novel concept where all transfer paths are characterised simultaneously by converting a vibration source into a multi-degree of freedom (DoF) blocked force exciter. As such, a reproducible excitation is applied with a controlled vibration source to facilitate multi-input multi-output (MIMO) system identification even in complex technical structures, such as entire vehicles. Prior to installing the source/exciter in the target assembly, the active component must be calibrated on a test bench to determine the applied excitation. In the subsequent system identification stage, the same (known) excitation is reproduced in the target assembly to characterise transfer paths using simple response measurements. This way, the two-stage procedure with a controlled source provides a convenient and fast alternative to conventional transfer path measurements with an instrumented hammer or shaker. Using the controlled exciter concept in a diagnostic context will be referred to as fastTPA due to the significant time advantage. Alternatively, these transfer paths can be used to construct a Virtual Acoustic Prototype (VAP), denoted as fastVAP, to ‘listen’ to a virtual assembly without it having to exist physically.

Considering the example shown in Fig. 1.1, the REPS system may be operated as a multi-DoF exciter by controlling its electric motor. After the system identification step is completed, the REPS system can be operated under normal conditions to perform dynamic steering in the same vehicle to acquire operational data without installing additional measurement equipment. Besides the potential time saving, this novel concept is also beneficial with respect to gaining consistent sets of transfer functions and operational data.

1.3 Thesis Aims and Objectives

Within this research direction, the primary aim of this thesis is to develop techniques for quick yet reliable system identification of complex MIMO systems (i.e. characterised by frequency response functions (FRFs)) and their implementation in a fast and thorough TPA approach, providing an engineer with realistic diagnoses to make informed design changes. Practical applications focus on the structure-borne transmission of steering noise into the vehicle's interior. To provide useful guidance to address the aim of this research project, the following objectives have to be achieved:

- ▶ *Develop a general method for in-situ system identification:*

Measurement of structural dynamic properties in assembled structures is often complicated due to inaccessible excitation positions. Therefore, a test-based approach has to be developed that avoids practical challenges commonly involved in experimental testing; particularly inaccessible and long distance FRF measurements. Extended via other state-of-the-art experimental methods, the concept should allow for simultaneous characterisation of translational and rotational transfer paths in complex built-up structures. Theoretical and practicable feasibility is to be tested in experimental or analytical studies.

- ▶ *Develop and investigate strategies to operate a structure-borne source as a controlled multi-DoF exciter for system identification:*

A concept has to be developed to apply a known broad-band excitation with a controlled operational source at its coupling interface DoFs (similar to electrodynamic shakers for conventional single-excitation transfer path measurements). The applied excitation needs to be reproducible and invariant of the connected receiver structure for system identification in different assemblies. Different

operating conditions of the multi-DoF exciter need to be considered, e.g. operational or external forces applied on the source, to generate mutually independent excitation vectors spanning a wide frequency range. Special interest is in the operational excitation using electric motors but also external excitation, feasible for purely passive (i.e. not controllable) sources. The source is calibrated in an application-specific setup (calibration assembly). If required, a custom bench or measurement setup for in-situ characterisation has to be developed to account for all coupling DoFs at the interface, including forces and moments.

- ▶ *Integrate these methods into a workflow for fastTPA:*

Development of a methodology to perform inverse force identification (operational blocked force) and prediction of their contributions to the total response in a target assembly (e.g. the noise level experienced by a vehicle occupant), different from the calibration setup. This fastTPA is based on the methods for fast system identification, where the vibration source (e.g. REPS system) is controlled as a broad-band exciter. Similarly, the exciter concept may be utilised to construct a VAP. Techniques such as singular value decomposition (SVD) may be considered to reduce noise in the obtained results.

- ▶ *Validation of the obtained methodology to diagnose and predict steering induced noise and vibration:*

An experimental procedure based on bench (calibration setup) and vehicle (target assembly) measurements has to be outlined. For this purpose, a workflow from measurement preparation and instrumentation to post-processing and quality assessment has to be established. The case study needs to consider active source characterisation and forward response prediction to diagnose and predict steering noise experienced in a vehicle. To highlight potential benefits with respect to reliability and time/measurement effort, the results are to be benchmarked against other state-of-the-art TPA approaches.

The methodology and experimental approaches developed within this thesis shall be feasible for any type of source-receiver assembly, not limited to steering systems.

1.4 Thesis Outline

The thesis introduces a novel methods for system identification and tools (i.e. fastTPA and fastVAP) to analyse the propagation of structure-borne noise and vibration in complex systems. To introduce the reader to the test-based concepts, the manuscript is divided into five parts as follows:

Part I. provides an overview of the literature pertinent to the context and aims of this thesis. Following the introductory discussion, Chapter 2 introduces the relevant topics and state-of-the-art concepts of independent source characterisation, experimental description of the source-receiver interface, and Transfer Path Analysis.

Part II. introduces novel system identification methods for source-receiver assemblies to reduce the complexity commonly encountered in TPA. A framework for indirect measurement of structural dynamic properties is presented in Chapter 3, emphasising inaccessible and long distance transfer paths. Following this, the system identification methods are extended in Chapter 4 via the transmissibility concept, allowing for a faster TPA with a calibrated source installed in an arbitrary assembly.

In **Part III.**, the methods presented through Chapters 3-4 are applied for system identification in different case studies.

Part IV. demonstrates the application of the proposed fastTPA for steering noise prediction in a vehicle. Chapter 6 considers the calibration of a steering gear as a multi-path exciter, utilised in Chapter 7 for system identification and contribution analysis of steering noise at the driver's ear.

Part V. summarises the most relevant conclusions of the work and discusses areas for future research activities.

Review of Structure-Borne Sound Characterisation

In this chapter, a brief overview of acoustic characterisation concepts is given, particularly relevant to the context and aims of this thesis. The following sections consider passive and active system properties, meaningful description of the interface between connected sub-structures alongside its experimental uncertainty, as well as TPA principles. The literature review will introduce the reader to these concepts, outline their theoretical development and highlight their current state-of-art.

Chapter contents:

2.1	Passive System Properties	11
2.2	Independent Source Characterisation	16
2.3	Rotational Degrees of Freedom	22
2.4	Uncertainty in the Interface Description	33
2.5	Introduction to Transfer Path Analysis	42

2.1 Passive System Properties

The previous chapter has discussed the test-based TPA methodology used to analyse noise and vibration propagation in complex built-up structures, e.g. electric power steering systems. In TPA, the assembly is subdivided into active and passive components, the dynamic properties of which are determined separately from one another. This section considers a description of the assembly's passive properties (e.g. its response to a unit excitation). In this respect, correct and 'fast' identification of the structural dynamic properties was stressed to be one of the most fundamental tasks to be achieved within this study.

Developing accurate numerical models of the structural and/or vibro-acoustic behaviour of complex machinery is particularly challenging. Instead, their passive behaviour may be characterised experimentally, while the system's dynamics can, in theory, be modelled in different domains. In fact, the structural properties may be described in any of the five domains: physical (using mass, stiffness and damping matrices), modal (eigenvector/value and modal damping matrices), state-space, time or frequency domain [10, 11]. All formulations facilitate multi-input multi-output characterisation, however, which domain is finally chosen often depends on the targeted analysis, experimental testing or numerical modelling resources, and perhaps personal preferences. This section outlines experimental characterisation by frequency response functions, such as compliance, mobility or accelerance and its inverse counterparts.

Note that all methods presented in this thesis invoke principles and concepts based upon linear (mass, stiffness and damping properties are independent of the system's state) and time-invariant (constant system matrices) (LTI) system behaviour. As such, the system's output behaviour may be regarded as weighted linear combinations of the inputs whilst being independent upon the time at which the inputs are applied [12].

2.1.1 Mobility and Related Frequency Response Functions

The frequency dependent dynamic characteristics of a linear and time-invariant system can be described by the mobility function $\mathbf{Y}(\omega)$,

$$\mathbf{v}(\omega) = \mathbf{Y}(\omega) \mathbf{f}(\omega) \quad \mathbf{v} \in \mathbb{C}^m, \mathbf{f} \in \mathbb{C}^n \text{ and } \mathbf{Y} \in \mathbb{C}^{m \times n}. \quad (2.1)$$

In experimental studies, the mobility matrix of a structure is typically determined by employing roving instrumented hammers or shakers. Excitations are applied one at a time to each investigated DoF, whilst the structure responds freely. This implies that external forces at all remaining DoFs are constrained to zero, i.e. $f_{i \neq k} = 0$. The individual elements of the mobility matrix $\mathbf{Y}(\omega)$ are determined as the complex ratio of the rectilinear or angular velocity response $v_i(\omega)$ to a single force or moment excitation $f_k(\omega)$, given by,

$$Y_{ik}(\omega) = \left. \frac{v_i(\omega)}{f_k(\omega)} \right|_{f_{i \neq k} = 0}. \quad (2.2)$$

The individual mobility elements $Y_{ik}(\omega)$ are invariant and remain unchanged if additional DoFs are considered in the matrix [13, 14]. In that respect, the mobility may be measured in the actual assembly or even determined from the individual sub-components, which forms the basis of dynamic sub-structuring.

To describe the dynamics of a MIMO system with multiple excitation and response DoFs, the mobility elements in Eq. (2.2) may be organised in a more convenient matrix formulation $\mathbf{Y}(\omega)$. Regarding the input (force) and output (velocity) DoFs, a distinction is made between positional and coordinate-DoF. Whilst the former refers to the spatial position on the structure, the latter accounts for the orientation in a defined global coordinate system such as a Cartesian system. Typically, measurement at a single positional-DoF may account for six coordinate-DoFs¹; x , y , and z -translation, alongside their rotations α , β , and γ . Therefore, the mobility matrix may contain elements with the response measurement directly at the excitation location (identical positional and coordinate-DoF) or response measurements somewhat remote from the excitation (different positional and/or coordinate-DoFs). For collocated excitation and response DoFs, such as ($i = k$), the so-called ‘driving point mobility’ is arranged on the main diagonal of $\mathbf{Y}(\omega)$. Otherwise, non-collocated excitation and response measurements, i.e. ($i \neq k$), are referred to as ‘transfer mobility’. Considering the mobility elements, Eq. (2.1) may be rewritten more explicitly as,

$$\begin{Bmatrix} v_1 \\ v_2 \\ \vdots \\ v_m \end{Bmatrix} = \begin{bmatrix} Y_{11} & Y_{12} & \cdots & Y_{1n} \\ Y_{21} & Y_{22} & \cdots & Y_{2n} \\ \vdots & \vdots & \ddots & \vdots \\ Y_{m1} & Y_{m2} & \cdots & Y_{mn} \end{bmatrix} \begin{Bmatrix} f_1 \\ f_2 \\ \vdots \\ f_n \end{Bmatrix}. \quad (2.3)$$

Note that for convenience, the frequency dependence (ω) is omitted in Eq. (2.3). Each applied excitation (f_1, \dots, f_n) will result in a mobility vector, including m response DoFs (v_1, \dots, v_m). Each vector may be arranged as a column of the mobility matrix $\mathbf{Y}(\omega) \in \mathbb{C}^{m \times n}$, thus considering additional response DoF m expands the number of rows. In practice, the matrix may include more responses than force inputs or vice versa, resulting in a complex, non-square mobility matrix.

To obtain a complete mobility matrix for a MIMO structure, its excitation can prove problematic, particularly in practical scenarios where access may be limited (e.g. in

¹ Of these, the exact measurement of angular velocities and moment excitations is particularly challenging. Experimental techniques to account for rotations in the mobility measurement are outlined in Sec. 2.3 without requiring specific hardware.

an engine bay or for encapsulated structures). For LTI systems, the principle of reciprocity may be invoked to interchange the position of response and excitation, i.e. $Y_{ik} = Y_{ki}^T$ ('T' denotes matrix transpose), so as to simplify a transfer function measurement [15]. As such, an ideal mobility matrix has to be symmetric about the main diagonal, a property often employed in experimental testing to validate the quality of measured FRFs using correlation-type quality assurance criteria such as FRAC/PAC [16]. For transfer paths that can not be characterised by direct or reciprocal FRF measurement, e.g. response and excitation positions are both inaccessible, indirect methods may be applied to determine the full mobility matrix. The 'round-trip identity' (see Sec. 3.2) presented by Moorhouse et al. [9] allows determining driving-point FRFs from relocated (easy-to-access) remote measurements on the structure. Sec. 3.4 extends previous work into a more generalised formulation and proposes an indirect approach for transfer FRFs. It is important to note that the correct position of an excitation is essential to obtain an accurate mobility measurement. With anti-resonances being dependent upon the excitation and response position, the experimental uncertainty of these measurements is subject to the skill of the experimentalist, i.e. hammer inaccuracy. To this end, the International Organisation for Standardisation (ISO) provides guidelines for the measurement of mechanical mobility in [17–19].

Analysis of the passive properties may also include vibro-acoustic (also: structural-acoustic) FRFs,

$$H_{ik}(\omega) = \left. \frac{p_i(\omega)}{f_k(\omega)} \right|_{f_{i \neq k} = 0} \quad (2.4)$$

determined as the complex ratio of the radiated sound pressure response p_i (expressed in the unit Pa) to the single force excitation f_k (expressed in N). Structural and vibro-acoustic FRFs can straightforwardly be combined² in Eq. (2.3), as both types of responses are force-induced. Reciprocal measurement of vibro-acoustic FRFs, however, is far from trivial and requires specific hardware, e.g. acoustic excitation by a volume-velocity source and response measurements using accelerometers [20]. However, as with structural FRFs, any correctly measured reciprocal vibro-acoustic FRF can be transformed into its direct analogue, assuming LTI conditions are met and proper mathematical conversions may be applied as required.

² Note that the general notation $\mathbf{H}(\omega)$ is used to denote vibro-acoustic matrices, which collectively includes vibro-acoustic noise, H_{ik} , and structural transfer functions, Y_{ik} . Instead, $\mathbf{Y}(\omega)$ explicitly refers to mobility matrices with the same quantities throughout all rows and columns.

Note that the following discussion is based on the mobility concept, with the dependence on radian frequency ω omitted for clarity. For brevity, modifications to include vibro-acoustic FRFs are straightforward but not explicitly shown. It is stressed that any other FRF notation (e.g. receptance or accelerance) can be converted into mobility functions; definitions for the complex ratio of displacement or acceleration responses to the structural excitation and their relation are shown in Table 2.1 [21]. It is standard practice to obtain the mobility function from acceleration response measurements. Here, integration in the time domain corresponds to a multiplication by $(j\omega)^{-1}$ in the frequency domain.

Table 2.1: Commonly used frequency response functions along their relations. The mobility can be found from the accelerance/receptance: $Y_{ik} = A_{ik}/(j\omega) = j\omega R_{ik}$ [21].

Symbol	Name	Unit	Constraint	R_{ik}	Y_{ik}	A_{ik}
R_{ik}	Receptance	(m/N)	$\frac{x_i}{f_k} \Big _{f_{i \neq k}=0}$	1	$(j\omega)^{-1}$	$-\omega^{-2}$
Y_{ik}	Mobility	(ms ⁻¹ /N)	$\frac{\dot{x}_i}{f_k} \Big _{f_{i \neq k}=0}$	$j\omega$	1	$(j\omega)^{-1}$
A_{ik}	Accelerance	(ms ⁻² /N)	$\frac{\ddot{x}_i}{f_k} \Big _{f_{i \neq k}=0}$	$-\omega^2$	$j\omega$	1

2.1.2 Impedance and Inverse Frequency Response Functions

The impedance function $\mathbf{Z}(\omega)$ is the inverse counterpart of the mobility description, defined by,

$$\mathbf{f}(\omega) = \mathbf{Z}(\omega) \mathbf{v}(\omega) \quad \mathbf{f} \in \mathbb{C}^n, \mathbf{v} \in \mathbb{C}^m \text{ and } \mathbf{Z} \in \mathbb{C}^{n \times m}. \quad (2.5)$$

In practice, measurement of the impedance matrix is often impractical, if not impossible. Velocities are applied one at a time to each investigated DoF, whilst responses at all remaining DoFs are constrained to zero, $v_{i \neq k} = 0$, i.e. the structure is not allowed to respond freely [22]. The elements $Z(\omega)$ of the impedance matrix are determined as the complex ratio of the force or moment response $f_i(\omega)$ to a single rectilinear or angular velocity excitation $v_k(\omega)$, given by,

$$Z_{ik}(\omega) = \frac{f_i(\omega)}{v_k(\omega)} \Big|_{v_{i \neq k}=0}. \quad (2.6)$$

Due to practical challenges in the direct measurement of Eq. (2.6), the impedance is often obtained through the inversion³ of the mobility matrix, $\mathbf{Z}(\omega) = \mathbf{Y}(\omega)^{-1}$.

³ For a square matrix ($n = m$), a unique solution is found through the inverse mobility matrix, provided that $\mathbf{Y}(\omega)$ is full rank. For a non-square matrix, i.e. ($n \neq m$), the classic matrix inverse may be interpreted as a Moore-Penrose pseudo inverse [23], leading to a least squares solution; here, the explicit notation '+' is omitted for brevity.

Unlike the invariant mobility, the impedance elements $Z_{ik}(\omega)$ depend on the number of observed (blocked) DoFs [13]. This difference has profound implications for the in-situ blocked force approach discussed later on and indicates why the mobility formulation is often preferred, if not the only choice in the experimental setting.

Nonetheless, impedance formulations are popular within frequency-based dynamic sub-structuring methods [24], e.g. classical impedance coupling (also referred to as primal formulation), or the in-situ characterisation of resilient elements [25, 26]. Similar to the mobility expression, the impedance may be related to the dynamic stiffness or effective mass, as shown in Table 2.2.

Table 2.2: Definition of the mechanical impedance and related frequency response functions. The impedance can be converted: $K_{ik} = j\omega Z_{ik}$ or $M_{ik} = Z_{ik}/(j\omega)$ [21].

Symbol	Name	Unit	Constraint	K_{ik}	Z_{ik}	M_{ik}	
inverse	K_{ik}	Dynamic stiffness	(N/m)	$\frac{f_i}{x_k} _{x_{i \neq k}=0}$	1	$j\omega$	$-\omega^2$
	Z_{ik}	Mechanical impedance	(Ns/m)	$\frac{f_i}{\dot{x}_k} _{\dot{x}_{i \neq k}=0}$	$(j\omega)^{-1}$	1	$j\omega$
	M_{ik}	Effective mass	(Ns ² /m)	$\frac{f_i}{\ddot{x}_k} _{\ddot{x}_{i \neq k}=0}$	$-\omega^{-2}$	$(j\omega)^{-1}$	1

2.2 Independent Source Characterisation

In TPA, the source activity and the passive properties of the system are characterised separately. Although numerical models can determine the structural properties with reasonable accuracy, the active mechanisms that induce vibratory excitation often lay outside their capabilities. This section considers experimental source characterisation in its full complexity (i.e. multi-contact, multi-DoF) as an alternative to modelling the internal mechanisms. The fundamental aim is to describe the active source behaviour to allow for predictions of an operational response in some other scenario. In NVH engineering, a suitable characterisation method often needs to address additional requirements, e.g. comparing one source with another or to a set limit and quantifying changes in a design optimisation context [27].

For the characterisation of an air-borne source, sound power L_W based methods meet the above objectives through a single value (frequency dependent) quantity, which have been standardised and subsequently adopted within the industry [28, 29]. Characterisation of their structure-borne counterpart, on the other hand, is more than often a complex procedure, owed in part to the strong mechanical coupling between the source and the connected receiver structure. As such, power-based methods are proposed, where the source is mounted to a standardised receiver structure

(e.g. reception plate method [30, 31]), to adopt standard air-borne procedures for structural sources [32]. Moreover, a line of research focusses on structure-borne source characterisation methods, including: operational force [33, 34], pseudo force [35], source descriptor [36], characteristic power [27], free velocity, and blocked force, to name a few.

These characterisation methods are typically categorised as either direct or indirect. Direct methods are the most straightforward in terms of their implementation, as the target quantity is directly obtained by experiment. In contrast, indirect approaches infer the target quantity from other quantities that can be measured more conveniently or accurately (often using inverse approaches). Depending upon the method employed, the determined quantity may provide an independent source description, i.e. it is insensitive to what the source is connected to. An independent quantity is an intrinsic property of the source, and therefore unaffected by any structural modifications made to its assembly. It is only with the independent characterisation that experimental data from different test settings can be interchanged (hypothetically, they are fully correlated) in a physically representative manner. In the following, these methods will be referred to as ‘independent’ characterisation of structure-borne sources. In contrast, conventional characterisation methods (e.g. source description by contact forces) depend on the dynamics of the connected receiver, and therefore the obtained description is only valid for the source-receiver installation in which it is characterised.

This thesis concerns the development and implementation of a fastTPA methodology, emphasising that the source description must be obtained in a transferable manner. This objective motivates the employment of independent techniques for a multi-DoF characterisation of the operational source activity. There exist two fundamental (independent) quantities; the blocked force and the free velocity. Both quantities provide a detailed (multi-DoF) description of the individual translational and rotational contributions as opposed to a collapsed single (frequency-dependent) variable often used in power-based methods like characteristic power. The direct measurement of these quantities is, however, less well adopted, not because of greater complexity, but due to their experimental difficulties as outlined in Sections 2.2.1 and 2.2.3, respectively. Ignoring these practical limitations, recent work by Moorhouse et al. [37] introduced an in-situ approach to determine the blocked force using an inverse method. This most common approach for independent source characterisation, specified in ISO 20270:2019 [38], is discussed in Sec. 2.2.2. Although not explicitly

outlined, the hybrid interface method [7, 39, 40] is an alternative method that allows indirect measurement of the blocked force involving flexible receiver structures. It involves measurement of the contact force or steps in which the source needs to be disconnected from the receiver, adding uncertainty due to the required dismantling.

2.2.1 Direct Measurement of the Blocked Force

The blocked force is defined as the reaction force present at the source-receiver interface (c) of an active sub-structure (A) when the velocity (also acceleration and displacement) response at the coupling interface is constrained to zero (i.e. blocked),

$$\bar{\mathbf{f}}_{A,c} = \mathbf{f}_{C,c} |_{\mathbf{v}_{C,c}=0} \quad (2.7)$$

where the over-bar accent has been introduced to denote a blocked force, as opposed to a contact force. In the above, upper-case subscripts ‘ A ’ and ‘ C ’ represent the source sub-structure and the coupled assembly, respectively; the lower-case subscript ‘ c ’ denotes the coupling interface DoFs that separate the source and receiver sub-structures. Note that both $\mathbf{f}_{C,c}$ and $\mathbf{v}_{C,c}$ are properties of the coupled assembly, $\bar{\mathbf{f}}_{A,c}$ may be read as the blocked force at the interface (c) of the source. By blocking the interface DoFs (c), the blocked force provides an invariant source quantity, unaffected by the dynamics of a coupled receiver (B), i.e. the blocked force characterises the structural source activity as an independent property of the vibration source [41]. Direct measurement of the blocked force requires rigid termination at the interface to sufficiently constrain interface dynamics; in practice, an approximation may be obtained over a limited frequency range at the cost of a large, impractical test rig. For complex multi-point connected structures, this requires force transducers to be placed between the source and the (purpose-built) rigid foundation [42].

2.2.2 In-Situ Blocked Force Approach (ISO 20270)

It was shown by Elliott and Moorhouse et al. in [37, 43, 44] that the blocked force may be acquired ‘in-situ’ (i.e. without dismantling the source from its intended installation) through an inverse procedure whilst the source is coupled to an arbitrary receiver. The in-situ blocked force approach is quite similar to an inverse contact force synthesis and has recently been standardised in ISO 20270:2019 [38]. Prior to the experimental characterisation, the source (A) of the assembly has to be identified; that is, the location of the source-receiver (active-passive) interface (c) has to

be defined. At the chosen interface DoFs, the blocked force provides an independent description of the vibration generating mechanisms within the structural source. Typically, the interface is defined at a physical coupling connection (e.g. bolts, machine foots, flanges, etc.) clearly separating the source and receiver sub-structures, i.e. somewhat remote from any internal source mechanism. This location is often chosen for convenience and may vary depending on the desired level of complexity. Alternatively, a ‘virtual interface’ may just as well be defined internally to the source sub-component, perhaps near each internal excitation mechanism (e.g. belt pulley, bearing shells, etc.) or over an enveloping surface that encloses these mechanisms.

The blocked force is acquired through an inverse procedure using measurements performed with the source in its intended installation; thus, realistic mounting and operation conditions are retained. It has since been acknowledged that the in-situ blocked force relation is a special case of the theorem on the representation of equivalent fields of forced vibrations in a composite elastic system, proposed by Bobrovnikskii [45]. Considering in-situ measurements at the defined interface, the blocked force relation is given by,

Interface blocked force relation:

$$\bar{\mathbf{f}}_{A,c} = \mathbf{Y}_{C,cc}^{-1} \mathbf{v}_{C,ca} \quad (2.8)$$

where $\mathbf{Y}_{C,cc} \in \mathbb{C}^{n \times n}$ is the square and symmetric driving-point mobility matrix measured at the contact interface (c), and $\mathbf{v}_{C,ca} \in \mathbb{C}^n$ is the corresponding operational velocity vector at (c) (note that accelerance and acceleration may be used in place of mobility and velocity). Therefore, the characterisation of the blocked force $\bar{\mathbf{f}}_{A,c} \in \mathbb{C}^n$ requires a two-stage measurement in which source (A) and receiver (B) remain connected. In part 1, the source is turned off, and the passive assembly properties are measured, that is, the mobility matrix $\mathbf{Y}_{C,cc}$ of the assembly. In part 2, the source is operated, and the operation velocity $\mathbf{v}_{C,ca}$ is measured at the interface DoFs, collocated to the previous FRF excitations. Care should be taken during the measurement of $\mathbf{Y}_{C,cc}$, as the inverse in Eq. (2.8) of poor experimental data (e.g. inconsistency in the input data [46]) is likely to increase the chance of unacceptable errors. Such errors vary significantly depending on the case, e.g. the experimental uncertainty of roving hammer tests is highly subject to the skill of the experimentalist. Although there exist numerical techniques to minimise large uncertainties, it

is recommended that effort be spent acquiring reliable experimental data, instead of relying on such post-processing techniques [47, 48].

Often FRF and operational velocity measurements at the defined interface can prove to be problematic, particularly in practical scenarios where access may be limited. In this case, Eq. (2.8) may be rewritten to obtain the blocked forces vector, $\bar{\mathbf{f}}_{A,c}$, from receiver-side measurements at remote DoFs (b), further downstream of the defined interface (c),

Remote blocked force relation:

$$\bar{\mathbf{f}}_{A,c} = [\mathbf{Y}_{C,cb}^T]^+ \mathbf{v}_{C,ba} \quad (2.9)$$

thus providing separate blocked force relations for coupling interface and receiver-side remote DoFs. The transfer mobility $\mathbf{Y}_{C,bc} \in \mathbb{C}^{m \times n}$ relates the remote DoFs (b), at which the velocity $\mathbf{v}_{C,ba} \in \mathbb{C}^m$ is measured, to the coupling interface DoFs (c), where the blocked force is defined. Implementation of Eq. (2.9) requires the same two-stage procedure as above, however, operational responses are measured at non-collocated DoFs (b) away from the interface. If more convenient, the FRF matrix can be measured reciprocally, as $\mathbf{Y}_{C,bc} = \mathbf{Y}_{C,cb}^T$. This allows the FRF matrix to be measured without having to excite the interface, instead, excitations are relocated to accessible remote DoFs (b). To acquire a determined solution, the number of remote DoF ($n_b = m$) must be equal to the defined interface DoF ($n_c = n$), that is, ($m = n$). However, Eq. (2.9) does facilitate over-determination by including additional remote DoF (b), resulting in the inverse of a non-square FRF matrix. For ($m > n$), the Moore-Penrose pseudo-inverse [23], denoted by '+', may be used in place of the standard matrix inverse, leading to a least-squares solution of the inverse problem, likely to reduce inversion errors when implemented correctly.

In case access is unrestricted, the interface relation and its remote counterpart may be used together, i.e. the DoF set (b) may include the interface DoFs (c) as a subset. This provides an over-determined relation, where Eqs. (2.8) and (2.9) are combined by means of a partitioned matrix and vector,

General blocked force relation:

$$\bar{\mathbf{f}}_{A,c} = \begin{bmatrix} \mathbf{Y}_{C,cc} \\ \mathbf{Y}_{C,bc} \end{bmatrix}^+ \begin{bmatrix} \mathbf{v}_{C,ca} \\ \mathbf{v}_{C,ba} \end{bmatrix} \quad (2.10)$$

where the combined FRF matrix formed from $\mathbf{Y}_{C,cc}$ and $\mathbf{Y}_{C,bc}$ is $\in \mathbb{C}^{(n+m) \times n}$ and the corresponding velocity vector from $\mathbf{v}_{C,ca}$ and $\mathbf{v}_{C,ba}$ is $\in \mathbb{C}^{(n+m)}$ [21]. All three equivalent in-situ blocked force expressions presented above provide an independent source characterisation to account for practical scenarios where measurements prove problematic or may be improved by over-determination. Since its introduction and validation in [37], the in-situ blocked force approach has been widely adopted within industry, e.g. for the characterisation of automotive components [49–53], building-mounted wind turbines [54, 55] and the optimisation of compressors [53, 56–58], to name a few.

2.2.3 Direct Measurement of the Free Velocity (ISO 9611)

Unlike the direct blocked force measurement, where the interface response is constrained to zero (i.e. blocked), the free velocity requires the source to be uncoupled and freely suspended [59]. Its characterisation is specified in ISO 9611 [60], where a direct procedure is outlined to approximate the free velocity for resiliently mounted machinery. The free velocity $\hat{\mathbf{v}}_{A,ca} \in \mathbb{C}^n$ is defined as the operational response at the interface (c) of an active, freely suspended source (A),

$$\hat{\mathbf{v}}_{A,ca} = \mathbf{v}_{A,ca} |_{\mathbf{f}_{A,c}=0} \quad (2.11)$$

without external forces $\mathbf{f}_{A,c}$ being applied to the sub-structure. As such, the free velocity is an independent property of the source.

Although ISO 9611 provides a simple measurement procedure, operational tests under a freely suspended condition are often impractical, if not impossible. To approximate free suspension, the source needs to be operated when mounted on resilient mounts (isolators) separate from any rigid support. In practice, this prohibits characterisation of most sources running under load [50]. Moreover, similar to the direct measurement of blocked forces, acquiring free velocity only applies to sources that can physically be separated from an installation. Besides, potential variation in the mounting conditions between characterisation and intended installation (e.g. static pre-load, local distortion or additional stresses) may introduce considerable experimental uncertainty to the true free velocity. Although the free velocity is widely accepted within the structural dynamic community, to the extent that it has been standardised, practical challenges prevent its industrial application. Nevertheless,

studies for virtual acoustic prototyping and the prediction of structure-borne noise emission from resiliently mounted machinery can be found in [1, 61, 62].

To avoid free mounting or load-less operating conditions, the free velocity vector may be obtained via the blocked force vector (or vice versa),

$$\hat{\mathbf{v}}_{A,ca} = \mathbf{Y}_{A,cc} \bar{\mathbf{f}}_{A,c} \quad (2.12)$$

where $\mathbf{Y}_{A,cc} \in \mathbb{C}^{n \times n}$ is the free mobility matrix of the unconstrained coupling interface DoFs. Also, it was shown by Moorhouse et al. [9] that the free velocity may be obtained from in-situ operational methods conducted under representative mounting conditions, partly avoiding the need for free suspension. A similar relation is presented in Sec. 3.5 via the application of the generalised round-trip identity [63].

2.3 Rotational Degrees of Freedom

For an independent source characterisation via the in-situ blocked force or the free velocity converted into its equivalent blocked quantity, the ‘source strength’ (i.e. structural source activity) is defined at the source-receiver interfaces. In theory, there is no limitation on the number of interfaces being solved for, assuming sufficient conditioning of the inverse problem and that the assembly remains locally linear during its characterisation. The connecting interfaces (c) are typically represented by point-like contacts, assuming that the structure surrounding the interface behaves rigidly. In a Cartesian coordinate system, each point-like⁴ interface includes six coordinate-DoFs: x , y , and z -translations, along with their axial rotations, α , β , and γ . For mechanical systems, translations and rotations (coordinate-DoFs) are often associated with force f and moment (or torque) τ excitation or rectilinear v and angular ψ velocity response, respectively [64]. As such, each defined interface (positional-DoF) may be characterised by a blocked force vector, $\bar{\mathbf{f}} = \{\bar{f}_x, \bar{f}_y, \bar{f}_z, \bar{\tau}_\alpha, \bar{\tau}_\beta, \bar{\tau}_\gamma\}^T \in \mathbb{C}^6$. To account for these interface DoFs, translational and rotational FRF terms need to be considered in the in-situ blocked force relations Eqs. (2.8) - (2.10).

Therefore, a complete source description accounts for a full FRF matrix, including translational, rotational, and cross terms (e.g. rectilinear response linked to moment

⁴ Approximation of point-like contacts is valid over a particular frequency range, beyond which simplifications of the continuous connectivity are no longer acceptable. An experimental example for a flexible extension of 6-DoFs rigid coupling is given in Sec. 7.5.3.

excitation or vice versa). For a single pair of translational and rotational DoFs (e.g. f_{0_x} and τ_{0_γ} excitation; v_{0_x} and ψ_{0_γ} response), the assembly's driving-point mobility matrix at the interface (c_0) (positional-DoF (0)) is given by,

$$\mathbf{Y}_{C,00} = \begin{bmatrix} Y_{C,v_0f_0} & Y_{C,v_0\tau_0} \\ Y_{C,\psi_0f_0} & Y_{C,\psi_0\tau_0} \end{bmatrix} \quad (2.13)$$

$$\text{with } \begin{cases} Y_{C,v_0f_0} = \left. \frac{v_0}{f_0} \right|_{\tau_0=0} & \text{force mobility} \\ Y_{C,v_0\tau_0} = \left. \frac{v_0}{\tau_0} \right|_{f_0=0} & \text{cross mobility} \\ Y_{C,\psi_0f_0} = \left. \frac{\psi_0}{f_0} \right|_{\tau_0=0} & \text{cross mobility} \\ Y_{C,\psi_0\tau_0} = \left. \frac{\psi_0}{\tau_0} \right|_{f_0=0} & \text{moment mobility} \end{cases}$$

where, τ_0 and ψ_0 represent the applied moment and resultant angular velocity, respectively. Each matrix element of Eq. (2.13) is defined by the complex ratio of kinematic response to the single force or moment excitation. It is important to note that Eq. (2.13) considers a single pair of translational and rotational DoF. The full matrix at this positional-DoF is $\mathbf{Y}_{C,00} \in \mathbb{C}^{6 \times 6}$ and includes the coordinate-DoF of the complete excitation vector, $\mathbf{f} = \{f_x, f_y, f_z, \tau_\alpha, \tau_\beta, \tau_\gamma\}^T$, and the responses, $\mathbf{v} = \{v_x, v_y, v_z, \psi_\alpha, \psi_\beta, \psi_\gamma\}^T$.

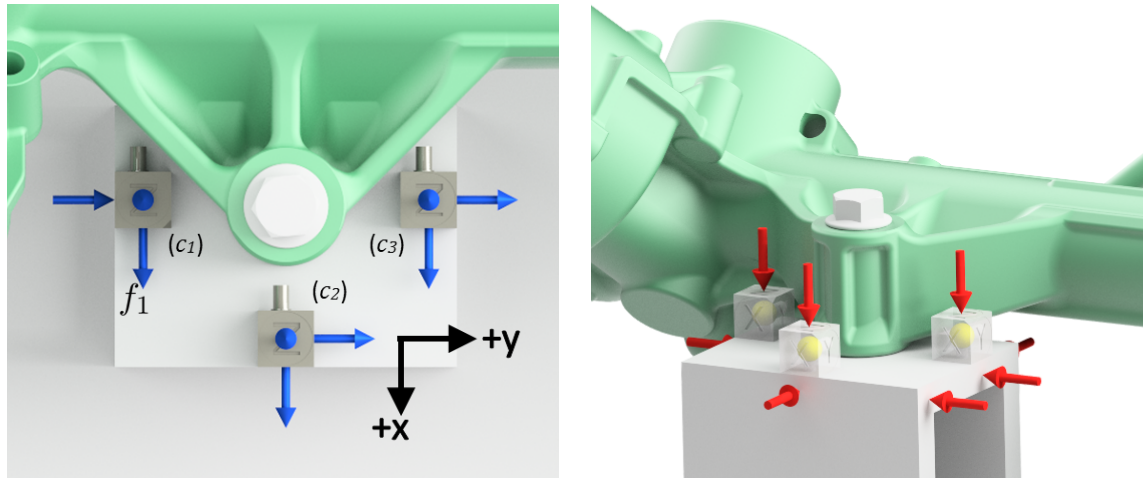
However, very few guidelines exist for the experimental description of a coupling interface. Also, the measurement of rotational FRF terms is considerably more complex than their translational counterparts [64]. That is to say, practical challenges have led to a near-routine neglect of rotational DoFs within industry. For this reason, it has become standard practice to describe an interface by three translational DoFs; x , y and z in an attempt to balance experimental effort with accuracy. In practice, one triaxial sensor at each interface and simple force excitation in the sensor's directions are sufficient to obtain a 3-DoFs (incomplete) blocked force source characterisation (compare Eq. (2.8)). According to Moorhouse and Elliott [65], however, the importance of rotational DoFs to accurately predict structure-borne transmission should not be understated. Also, in the inverse of a mobility matrix, all significant translations and rotations should be included to obtain a representative impedance matrix ($\mathbf{Y}_{C,00}^{-1} = \mathbf{Z}_{C,00}$) [66]. Unlike mobilities, the impedance function is not an invariant property of the structure and thus subject to the other impedances in the matrix [13].

To obtain a complete source characterisation, this section outlines different established techniques to account for rotational DoFs with the use of minimal additional hardware. Alternative methods using a twin shaker arrangement [67, 68], magnetostrictive exciters [69, 70], synchronised hammers [71], or structural modifications [72] are not considered.

2.3.1 Equivalent Multi-Point Connection

Perhaps the simplest approach to account for translational and rotational DoFs is to extend the common 3-DoFs point-like connections by including additional coupling points in the proximity of the same interface. The equivalent multi-point connection (EMPC) method, as its name implies, considers coupling of multiple translational FRFs to account for rotations implicitly. In practice, sensors are placed at the so-called interface indicator DoFs (positional-DoFs) in an area (locally rigid) near the interface to couple all translational and rotational directions [73].

The EMPC approach is often chosen due to its straightforward implementation and routine employment in practice, e.g. using 3 tri-axial sensors at the positional-DoFs (c_1) - (c_3) (not in line) as depicted in Fig. 2.1a [74]. As such, the interface description has redundancy; a set of 9 indicator DoFs (blue arrows) is included, yet only 6 are physically present (assuming the negligible distortion of the planes). The translational FRFs at each indicator point (yellow sphere in Fig. 2.1b) may be obtained from excitations (red arrows) applied close to the sensors or directly on the sensors' surfaces. This way, the 6-DoFs interface connection is represented by a 9×9 multi-point FRF matrix $\mathbf{Y}_{C,cc} \in \mathbb{C}^{9 \times 9}$. To retain a plausible description of the interface dynamics, it is proposed to discard the 3 smallest singular values from the multi-point FRF matrix $\mathbf{Y}_{C,cc}$ when its inversion is performed. In this simple regularisation, the least significant singular values are rejected since the dominant singular values (i.e. singular value 1 through 6 for rigid coupling) are likely to represent the independent interface modes, while lower-order values are typically composed of measurement error and noise [46]. Note that in the theoretical case, there are 6 non-zero and 3 zero singular values, corresponding to the redundant modes. We assume that this situation will be approximately reproduced in a non-ideal case (i.e. experimental scenario), hence the justification for discarding the 3 smallest singular values.



(a) Top view: Sensor responses (blue arrows) at indicator points ($c_1 - c_3$).

(b) Excitation measurements (red arrows) close to/on the sensors' surfaces.

Figure 2.1: Equivalent multi-point connection by considering 9-DoFs translational coupling at 3 indicator points ($c_1 - c_3$) in the proximity of the interface. The source-receiver setup contains: REPS - source (A); mounting fixture - receiver (B); multi-point tri-axial sensor array - coupling interface (c).

The EMPC defines the coupling points at the measurement positions, and as such, a different sensor arrangement yields a new (hence incompatible) interface description. Physically, the measurements from different assemblies can only be combined when using exactly the same EMPC sensor/excitation configuration; otherwise, the interface DoFs would not line up, resulting in considerable errors. Furthermore, the EMPC interface description is typically incompatible with other measurements due to its implicit nature. The matrix regularisation by means of a singular value truncation retains the reduced interface dynamics, in theory, 6 rigid displacement modes. However, the interface DoFs cannot be identified in the corresponding FRF matrix, as the various rows and columns (here: $\mathbf{Y}_{C,cc} \in \mathbb{C}^{9 \times 9}$) are not assigned to explicit coupling DoFs.

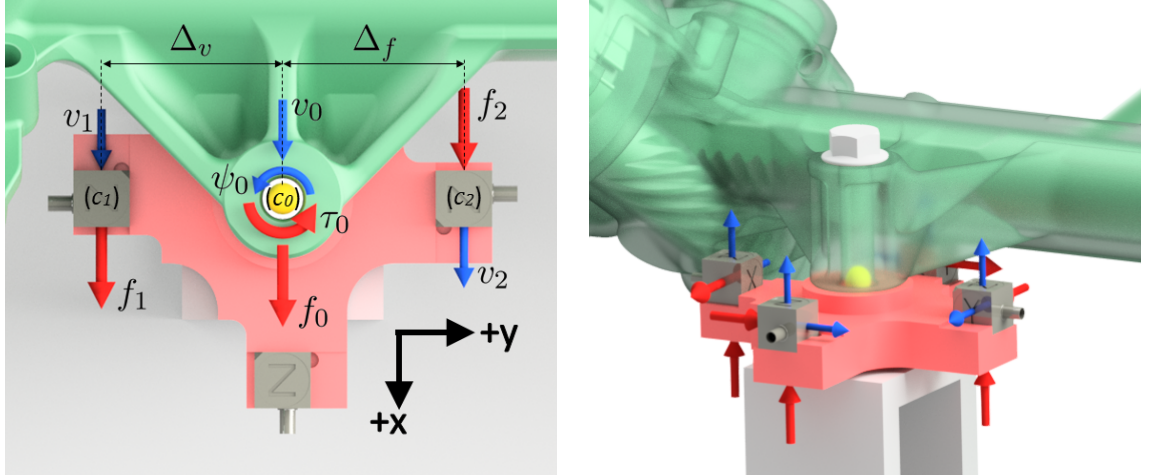
Concluding, the EMPC method allows for quick multi-DoF coupling that can easily be adapted to replace a standard 3-DoFs single-point description. The incorporation of multi-point connections within in-situ approaches has proven to enhance coupling results; some notable examples include response predictions in the same assembly [2, 75] or different virtual environments [56, 57]. However, most diagnostic and predictive tasks, as of TPA, require an explicit calculation of the rotational components, particularly within the field of contribution analysis [6].

2.3.2 Finite Difference Approximation

Rotational DoFs can be approximated from translations measured at closely spaced points at known distances from each other. The finite difference approach (also referred to as central difference [76]) requires translational excitation and responses, separated by a finite distance, to allow for both moment excitation and angular velocities to be approximated without directly measuring or applying either. Without requiring any modifications to be made to the structure under investigation, the finite difference approach offers a convenient way to include rotational DoFs in the source description, while using only standard measurement equipment.

The finite difference approximation for a positional-DoF (c_0) is illustrated in Fig. 2.2a. In this example, the translational x -coordinate-DoF and its axial rotation γ , together with their related cross mobilities (compare Eq. (2.13)), are of particular interest. Note that coordinate subscripts are omitted for brevity and instead replaced by the corresponding indicator index ($c_0 - c_2$). Here, the indicator positions (c_1, c_2) are already aligned in the global Cartesian coordinate system (x, y, z) with a mathematically positive orientation. Moment excitation τ_0 is generated by the pair of applied external forces, f_1 and f_2 , at two positional-DoFs centred about c_0 , thus effectively using the structure's separation distance Δ_f as a lever [77]. Similarly, the angular velocity ψ_0 can be obtained from a spaced accelerometer pair separated by a finite distance $2\Delta_v$.

Compared to a driving-point measurement with direct force excitation at (c_0), off-centre measurements at either (c_1) or (c_2) will result in a superposed response, including translational force and angular moment contributions. However, in the spaced setup, force and moment excitation may be separated, allowing to determine the individual mobility terms of Eq. (2.13). Following the typical sign convention, the force f_1 (see Fig. 2.2a) causes a positive moment at (c_0), whereas f_2 generates an equal but opposite moment excitation. The force excitation may be extracted by the averaged sum of both excitations, as the opposite moment terms cancel at c_0 . The averaged difference of f_1 and f_2 , in contrast, cancels the contribution of the aligned forces, resulting in an expression for the moment excitation only [66]. Similar considerations apply to the spaced response measurements to separate translational and angular velocities.



(a) Top view: Response (blue arrows) and excitation (red arrows) positions facilitating 2-DoF finite difference approximation.

(b) Cross-like element instrumented with 4 bi-axial sensors to obtain full 6-DoF kinematics at the REPS mount.

Figure 2.2: Finite difference configuration for the approximation of the interface dynamics at the REPS mount (c_0) from response and excitation measurements at the indicator DoFs (c_1) and (c_2). The source-receiver setup contains: REPS - source (A); mounting fixture - receiver (B); cross-like element - coupling interfaces (c).

As shown by Sattinger⁵ [76], and later by Elliott et al. [77], translational, rotational and cross terms in Eq. (2.13) may be approximated from the translational mobilities (i.e. driving-point and transfer FRFs) measured at (c_1) and (c_2) according to,

$$\tilde{Y}_{C,v_0f_0} \approx \frac{Y_{C,v_1f_1} + Y_{C,v_2f_1} + Y_{C,v_1f_2} + Y_{C,v_2f_2}}{4} \quad (2.14)$$

$$\tilde{Y}_{C,\psi_0f_0} \approx \frac{-Y_{C,v_1f_1} + Y_{C,v_2f_1} - Y_{C,v_1f_2} + Y_{C,v_2f_2}}{4 \Delta_v} \quad (2.15)$$

$$\tilde{Y}_{C,v_0\tau_0} \approx \frac{-Y_{C,v_1f_1} - Y_{C,v_2f_1} + Y_{C,v_1f_2} + Y_{C,v_2f_2}}{4 \Delta_f} \quad (2.16)$$

$$\tilde{Y}_{C,\psi_0\tau_0} \approx \frac{Y_{C,v_1f_1} - Y_{C,v_2f_1} - Y_{C,v_1f_2} + Y_{C,v_2f_2}}{4 \Delta_v \Delta_f} \quad (2.17)$$

where, \tilde{Y} indicates the finite difference approximation. In the experimental setting, just two excitation and response measurements are required to simultaneously determine the force and moment driving-point mobility, together with their related cross terms. The above formulations in Eqs. (2.14) - (2.17) are theoretically correct

⁵ In [76], Sattinger also addressed the ‘forward difference’ and ‘backward difference’ to facilitate rotational approximation from alternative non-centred measurements. For brevity, only the ‘central difference’ approach, here referred to as the finite difference approach, is considered, potentially having the widest practical application.

and may be re-written in a more convenient matrix form,

$$\begin{bmatrix} \tilde{\mathbf{Y}}_{C,v_0f_0} & \tilde{\mathbf{Y}}_{C,v_0\tau_0} \\ \tilde{\mathbf{Y}}_{C,\psi_0f_0} & \tilde{\mathbf{Y}}_{C,\psi_0\tau_0} \end{bmatrix} = \begin{bmatrix} \frac{1}{2} & \frac{1}{2} \\ -\frac{1}{2\Delta_v} & \frac{1}{2\Delta_v} \end{bmatrix} \begin{bmatrix} Y_{C,v_1f_1} & Y_{C,v_2f_1} \\ Y_{C,v_1f_2} & Y_{C,v_2f_2} \end{bmatrix} \begin{bmatrix} \frac{1}{2} & -\frac{1}{2\Delta_f} \\ \frac{1}{2} & \frac{1}{2\Delta_f} \end{bmatrix} \quad (2.18)$$

or more compactly as,

$$\tilde{\mathbf{Y}}_{C,00} = \mathbf{B}_v \mathbf{Y}_C \mathbf{B}_f^T \quad (2.19)$$

$$\text{with } \begin{cases} \mathbf{B}_v = \mathbf{B}_f & \text{for } \Delta_v = \Delta_f \\ \mathbf{Y}_{C,00} = \tilde{\mathbf{Y}}_{C,00} + \mu \end{cases}$$

where \mathbf{B}_v and \mathbf{B}_f are the transformation matrices for the rectilinear/angular velocity (row based operation) and force/moment (column based operation) approximation, respectively. However, with respect to the practical implication of finite difference approximation, the obtained (transformed) mobility matrix $\tilde{\mathbf{Y}}_{C,00}$ is not strictly identical to the theoretical solution. One example for errors may be a non-linear behaviour, present when over-exciting a structure with an impact hammer, in which local deformation dissipates a part of the impact energy. For this reason, the error term μ is added in Eq. (2.19). An explanation of its meaning is provided in the following. Note that the approximation in Eq. (2.19) is not limited to driving-point measurements. Instead, transfer mobilities may be considered with spaced responses and/or excitations at non-collocated DoFs. For instance, to obtain translational and angular responses, the transfer FRFs may be pre-multiplied by \mathbf{B}_v , whilst post-multiplication by \mathbf{B}_f yields a one-sided transformation of translational force and moment excitations. For the convenient case where $\Delta_v = \Delta_f$ (e.g. direct force excitation on the sensors' surfaces), the transformation matrices \mathbf{B}_v and \mathbf{B}_f are, in fact, identical.

Conceptually, the formulated approximation in Eq. (2.19) applies to the trivial case considering two coordinate-DoF at a single positional-DoF. However, the experimental setup can be extended to larger problems. An example for a full 6-DoF characterisation is illustrated in Fig. 2.2b, where a steering system is coupled to a representative receiver structure via cross-like elements. An explicit notation of the transformation matrices can be found in the experimental case study in Sec. 6.2.

For simplicity, a detailed validation of the finite difference approach is provided by Elliott et al. [77] alongside a numerical error analysis; neither will be presented here.

This error analysis for an analytical beam indicated that approximation errors are directly proportional to the separation distances (Δ_v, Δ_f) and frequency whilst being inversely proportional to the mobility magnitude and bending stiffness [44]. That said, the error associated with the finite difference technique defines a lower/upper frequency bound for a robust approximation at a given separation distance:

- ▶ At lower frequencies, the measured translational FRFs (centred about the point of interest) become too similar⁶. Thus the calculated difference from a pair of spaced mobilities (close to identical) introduces noise. A larger sensor/excitation spacing may resolve and/or shift low-frequency noise below the frequency range of interest.
- ▶ At high frequencies, the limit is defined by the breakdown of the local rigid behaviour, as the bending wavelength becomes comparable to the total sensor/excitation spacing (i.e. $2\Delta_v$ or $2\Delta_f$) [77]. Largely spaced excitations load the interface in a flexible manner, therefore, responses contain rigid and flexible contributions. Smaller separation distances reduce the effect of flexible interface motion and extend the upper-frequency limit, however, the transformation becomes more sensitive to experimental errors (e.g. misalignment or absolute errors on the position).

In practice, a working frequency range is defined by the conflicting high and low frequency requirements of the separation distance. The residual term μ in Eq. (2.19) indicates such uncertainties associated with the finite difference approximation. Compared to other techniques (see Sec. 2.3.3), the finite difference approach clearly provides a more robust but less flexible transformation method for the explicit calculation of translational and rotational contributions.

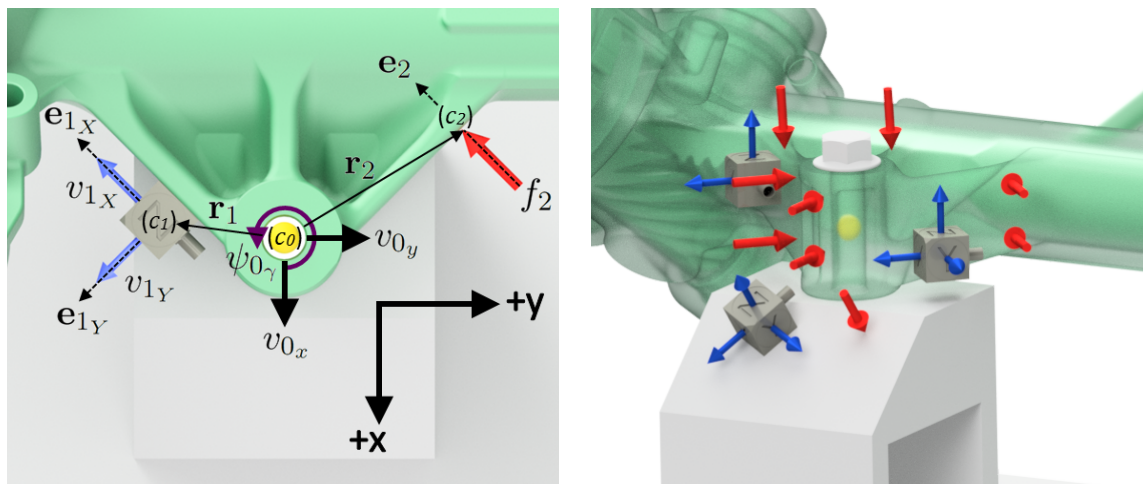
2.3.3 Virtual Point Transformation

The virtual point transformation may be considered a generalisation of the finite difference approximation, whereby the responses and excitations can be positioned rather arbitrarily at chosen indicator DoFs. The virtual point approach, proposed by van der Seijs et al. [78], relies on the kinematic relations between a set of indicator DoFs at the interface and a defined ‘virtual coupling point’ at which the translational

⁶ Especially at low frequencies, where the bending wavelength is very large compared to the accelerometer spacing, the measured mobilities at both sensor positions are close to identical. Comparing such mobilities in the finite difference operation results in a noisy, unstable mobility approximation [66].

and rotational DoFs are determined. Clearly, the virtual coupling point may be defined near a physical interface or at any representative location where the interface truly is (e.g. at the inaccessible centre of a steering system mount, see Fig. 2.3). With a user-chosen virtual point, this approach requires exact knowledge of each sensor/excitation position and orientation with respect to the associated virtual point [21].

The virtual point transformation defines a set of interface displacement modes (IDMs) per coupling interface (i.e. virtual point DoFs) and projects the surrounding indicator DoFs onto this subspace [79]. Fig. 2.3 shows the indicator response (blue arrows) and excitation (red arrows) measurements mapped onto 6 coordinate-DoFs in the virtual point (yellow sphere), also referred to as rigid interface modes. The somewhat arbitrary FRF matrix between these indicator DoFs is denoted by $\mathbf{Y}_{C,mn}$. The theoretical concept to obtain the IDMs is shown in Fig. 2.3a, where the kinematic relations are described for two indicator DoFs, (c_1) and (c_2) , in the proximity of the virtual point (c_0) . Note that the following derivation uses a notation, which may differ from the original publication's convention [78].



(a) Top view: Relations between response and excitation measurements at different indicator DoFs and the virtual point.

(b) Instrumentation with 3 tri-axial sensors and 9 excitations grouped around the virtual point to obtain full 6-DoF kinematics.

Figure 2.3: Virtual point transformation to map user-chosen response (blue arrows) and excitation (red arrows) measurements onto the virtual point DoFs (c_0) . The source-receiver setup contains: REPS - source (A); mounting fixture - receiver (B); virtual point (c_0) with the coupling interface centred in the REPS mount.

Starting with the response transformation, the sensor IDM matrix $\mathbf{R}_v \in \mathbb{R}^{m \times 6}$ maps the local response vector $\mathbf{v}_m \in \mathbb{C}^m$ measured at multiple interface indicator DoFs

(c_1, \dots, c_m) onto the generalised motion $\tilde{\mathbf{v}}_0$ in a virtual point, including a residual term $\boldsymbol{\mu}$. The following relation is obtained,

$$\mathbf{v}_m = \mathbf{R}_v \tilde{\mathbf{v}}_0 + \boldsymbol{\mu} \quad \text{with} \quad \tilde{\mathbf{v}}_0 = \{\tilde{v}_{0_x}, \tilde{v}_{0_y}, \tilde{v}_{0_z}, \tilde{\psi}_{0_\alpha}, \tilde{\psi}_{0_\beta}, \tilde{\psi}_{0_\gamma}\}^T \in \mathbb{C}^6 \quad (2.20)$$

where \mathbf{R}_v contains the orientation and relative position of the sensor responses defined in the virtual point coordinates (equivalent to the previously defined separation distance Δ_v). A complete derivation of the virtual point equations is presented by van der Seijs et al. [10] alongside detailed information on how to construct \mathbf{R}_v .

Note that the IDM matrix \mathbf{R}_v needs to be full rank for an independent characterisation of all 6-DoFs per virtual point. In theory, a pair of tri-axial sensors may measure 6 response DoFs; the transformation from two indicator positions (positional-DoFs) will result in a linear dependence. The two sensors are unable to describe the rotational motion around the axis spanned between them, regardless of their position and orientation. Instrumentation in practice, therefore, requires a third sensor (over-determined), such that the three sensors span a surface in proximity to the virtual point. Whenever the interface reduction is over-determined, i.e. the number of measured DoFs (standard practice: 9 indicator responses) exceeds the set of virtual point DoFs (6-DoFs assuming a locally rigid interface), the residual $\boldsymbol{\mu}$ may become non-zero. This typically indicates a ‘flexible’ behaviour of the interface as the indicator responses are not in the subspace of the rigid modes defined in the virtual point. A consistency criterion to identify flexibilities in the transformation process is outlined in Sec. 2.4.2.

Similarly, for a typical configuration with 9-12 excitations (c_1, \dots, c_n) per virtual point (see red arrows in Fig. 2.3b), the indicator vector $\mathbf{f}_n \in \mathbb{C}^n$ can be transformed to a set of virtual point forces and moments $\tilde{\mathbf{f}}_0$, defined by,

$$\tilde{\mathbf{f}}_0 = \mathbf{R}_f^T \mathbf{f}_n \quad \text{with} \quad \tilde{\mathbf{f}}_0 = \{\tilde{f}_{0_x}, \tilde{f}_{0_y}, \tilde{f}_{0_z}, \tilde{\tau}_{0_\alpha}, \tilde{\tau}_{0_\beta}, \tilde{\tau}_{0_\gamma}\}^T \in \mathbb{C}^6 \quad (2.21)$$

where the force IDM matrix $\mathbf{R}_f \in \mathbb{R}^{n \times 6}$ contains the information about the direction and the relative distance of each indicator excitation with respect to (c_0) . Note that Eq. (2.21) requires no residual term $\boldsymbol{\mu}$, as the virtual loads⁷ are, in fact, a direct result of the applied indicator forces [78].

⁷ Unlike velocities, forces at the indicator positions cannot be obtained from known virtual loads in a unique transformation ($\tilde{\mathbf{f}}_0 \rightarrow \mathbf{f}_n$). To exemplify this, different force combinations (indicator DoFs) applied to a cantilever beam can generate the same moment at its fixed end (virtual point). The other way around, the calculation of virtual loads from applied forces at known positions and orientations is straightforward and obtained without a residual term.

Finally, the indicator FRFs $\mathbf{Y}_{C,mn}$ can be transformed into a virtual driving-point matrix $\tilde{\mathbf{Y}}_{C,00}$ using an inverse formulation of Eqs. (2.20) and (2.21). Note that both IDM matrices, \mathbf{R}_v and \mathbf{R}_f , facilitate over-determination, i.e. if the number of indicator DoFs can exceed the virtual point DoFs, resulting in the inversion of a non-square matrix. Thus, the inverse is obtained applying the Moore-Penrose pseudo inverse,

$$\tilde{\mathbf{v}}_0 = \underbrace{[\mathbf{R}_v^T \mathbf{R}_v]^{-1} \mathbf{R}_v^T}_{\mathbf{B}_v} \mathbf{v}_m \quad \text{with} \quad \mathbf{B}_v \in \mathbb{R}^{6 \times m} \quad (2.22)$$

$$\mathbf{f}_n = \mathbf{R}_f \underbrace{[\mathbf{R}_f^T \mathbf{R}_f]^{-1}}_{\mathbf{B}_f^T} \tilde{\mathbf{f}}_0 \quad \text{with} \quad \mathbf{B}_f^T \in \mathbb{R}^{n \times 6} \quad (2.23)$$

where $[\mathbf{R}_v^T \mathbf{R}_v]^{-1} \mathbf{R}_v^T$ represents the pseudo-inverse of \mathbf{R}_v and $\tilde{\mathbf{v}}_0$ is the least-squares solution, i.e. minimising the squared error term expressed as the Euclidean norm $\|\mathbf{v}_m - \mathbf{R}_v \tilde{\mathbf{v}}_0\|_2$. The transformation matrices \mathbf{B}_v (row operation) and \mathbf{B}_f (column operation) denote the sensor and excitation transformation matrices, respectively, as constructed from the IDMs. They are equivalent to the finite difference approximation in Eq. (2.19), however, the indicator measurements are not restricted to spaced DoFs centred about the point of interest. This is because the virtual point transformation matrices contain information about the relative DoF coordinates (position and orientation) with respect to the chosen virtual point (thus vector information), whereas finite-difference approximation assumes spaced measurements at a given distance. As such, the virtual point can be redefined in a post-processing step (by amending the IDM matrices) to establish a physically compatible interface position, which is a considerable advantage in dynamic sub-structuring. Note that the formulations above may easily be extended to include a weighting matrix to assign each indicator DoF a certain importance in the transformation process, see [80].

The two transformations in Eqs. (2.22) and (2.23) allow determining a 6×6 virtual point FRF matrix $\tilde{\mathbf{Y}}_{C,00}$ from the measured $m \times n$ indicator matrix $\mathbf{Y}_{C,mn}$,

$$\mathbf{v}_m = \mathbf{Y}_{C,mn} \mathbf{f}_n \quad (2.24)$$

$$\tilde{\mathbf{v}}_0 = \mathbf{B}_v \mathbf{Y}_{C,mn} \mathbf{B}_f^T \tilde{\mathbf{f}}_0 \quad \text{with} \quad \tilde{\mathbf{Y}}_{C,00} = \mathbf{B}_v \mathbf{Y}_{C,mn} \mathbf{B}_f^T. \quad (2.25)$$

It is stressed that not all interface connections can be properly described by simple point-like contacts considering rigid interface modes. This is of particular interest for assemblies comprising continuous or larger connecting surfaces. In such a case, the IDM matrices \mathbf{R}_v and \mathbf{R}_f may be augmented to consider flexible behaviour if

desired [81]. Although not derived here, Sec. 7.5.3 outlines the flexible extension of the 6-DoF interface description.

This section emphasises the characterisation of rotational FRFs, however, all transformation principles may also be applied to operational measurements (e.g. direct blocked force or free velocity characterisations). In the following derivations, and throughout the remainder of this thesis, the explicit notation of the transformation matrices will be dropped, unless otherwise specified. Instead, the interface description (by its FRF matrix) is assumed to account for 6 coordinate-DoFs. For brevity, vectors that collectively include forces and moments will be referred to as ‘load vectors’ (e.g. the term ‘blocked forces’ is used herein interchangeably with the term ‘blocked loads’).

2.4 Uncertainty in the Interface Description

Assuming each source-receiver contact behaves rigidly, the measurement of a complete FRF matrix requires excitations in 6 coordinate DoFs; x, y and z translations, alongside their corresponding rotations. Experimentally, this type of measurement is often restricted by the impracticality of applying a controlled excitation in a particular direction (e.g. in-plane or moment). These practical challenges have led to a near-routine neglect of in-plane and rotational interface DoFs, potentially resulting in an unrealistic blocked force description of the source. More than often, a subset of interface DoFs is of particular importance to characterise the vibratory excitation and its propagation; thus, assumptions can be made to simplify the measurement procedure. With this in mind, the ability to assess the experimental error of a given setup and, therefore, understand the uncertainties involved is essential.

In recent work, guidelines for instrumentation to reduce uncertainty are given in [82, 83], and [84] provides a framework for evaluating uncertainties in the blocked force. This section outlines three measurement quality indicators to assess experimental uncertainties; on-board/transferability validation, transformation consistency, and the Interface Completeness Criterion, to obtain and apply an experimental blocked force vector with confidence. Together, likely sources of error can be identified, and measures of their severity provided. Although we will consider the concepts of validation, consistency and completeness primarily from a blocked force perspective, it is stressed that many of these challenges apply equally in the context of dynamic sub-structuring (coupling and decoupling).

Other quality indicators, e.g. the classic coherence function, reciprocity checks or analysis of the SNR, are considered basic requirements and are not explicitly outlined. The Measurement Consistency Criterion (MCC) proposed by Meggitt et al. [46] indicates inconsistencies in the blocked force characterisation, introduced by the two-stage procedure; passive FRF properties and operational measurement. Any change in the passive properties between the two measurement stages (e.g. stiffening may occur during operational loading) will lead to an imperfect cancellation and resonant-artefacts in the blocked force vector. However, implementation of the MCC is often impractical due to freely suspended measurements involved in its calculation and thus not explicitly outlined as it requires future research efforts. Note that the MCC is not related to the transformation consistency presented in Sec. 2.4.2.

2.4.1 On-Board and Transferability Validation

The perhaps most straightforward approach to assess the uncertainty associated with the experimentally determined blocked force is to use them in the prediction of some known quantity. One example, commonly referred to as ‘on-board validation’ (OBV), employs the in-situ blocked forces to predict additional velocity responses at the validation DoFs (d) within the same source-receiver installation (C). The OBV is an essential part of ISO 20270:2019 [38] to estimate uncertainties in the in-situ blocked force measurement procedure. In Eq. (2.10), the blocked force vector is determined via a set of operational responses at the coupling interface (c) and/or remote indicator DoFs (b). Subsequently, the validation responses $\mathbf{v}_{C,da}$ are predicted via the transfer FRF matrix $\mathbf{Y}_{C,dc}$ measured in the same assembly.

On-board validation:

$$\mathbf{v}_{C,da} = \mathbf{Y}_{C,dc} \bar{\mathbf{f}}_{A,c} \quad \text{with} \quad \tilde{\mathbf{v}}_{C,da} \stackrel{\text{def}}{=} \mathbf{v}_{C,da} \quad (2.26)$$

These predicted responses, $\mathbf{v}_{C,da}$, then are compared to the actual measurements of the operational response at (d) to assess errors included in the blocked force vector, even for complex technical applications. These reference velocities $\tilde{\mathbf{v}}_{C,da}$ are recorded during the blocked force measurements, thus allowing for a realistic prediction to be made under identical operational conditions. It is important to note that the selected validation DoFs (d) are not used in the in-situ blocked force characterisation, i.e. $d \notin \{c, b\}$, whilst being as linearly independent as possible from those indicator DoFs. That said, the validation sensors are located downstream of

interface (*c*) somewhat remote, yet not too far distant, to still establish a reliable phase relationship between the blocked force excitation and the resulting response (*d*). As such, the OBV is often used as an indicator of whether sufficient remote DoFs (*b*) (i.e. degree of over-determination) have been accounted for in the inverse blocked force characterisation.

Due to its invariant property, the blocked forces can be transferred between assemblies for a prediction procedure similar in concept to that of on-board validation. The transfer into a secondary assembly tests the independent nature of the blocked force, which has implications for the completeness of the interface description. A more thorough discussion on the concept of interface completeness is presented in Sec. 2.4.3. The ‘transferability validation’ procedure considers the blocked force vector from one assembly, denoted by the subscript (C_1), to predict operational validation responses in a different source-receiver installation (C_2).

Transferability validation procedure:

Blocked force calculation in assembly (C_1),

$$\{\bar{\mathbf{f}}_{A,c}\}_{(C_1)} = \left[\begin{array}{c} \mathbf{Y}_{C_1,cc} \\ \mathbf{Y}_{C_1,bc} \end{array} \right]^+ \left\{ \begin{array}{c} \mathbf{v}_{C_1,ca} \\ \mathbf{v}_{C_1,ba} \end{array} \right\} \quad (2.27)$$

and prediction of the validation response in assembly (C_2),

$$\mathbf{v}_{C_2,da} = \mathbf{Y}_{C_2,dc} \{\bar{\mathbf{f}}_{A,c}\}_{(C_1)} \quad \text{with} \quad \tilde{\mathbf{v}}_{C_2,da} \stackrel{\dagger}{=} \mathbf{v}_{C_2,da} \quad (2.28)$$

The transferability validation requires the vibration source (*A*) to be removed from the original assembly (C_1) and transferred to another (C_2), where the forward transfer FRFs $\mathbf{Y}_{C_2,dc}$ and the reference velocities $\tilde{\mathbf{v}}_{C_2,da}$ are measured. As such, the validation responses at (*d*) are linearly independent from the blocked force measurements at (*c*) and/or (*b*). However, the comparison between prediction and reference requires repeated active (operational) tests in different assemblies, where a lack of repeatability may introduce additional uncertainty to this validation procedure.

To avoid such errors, the ‘operational’ source excitation may be replaced by an ‘external force’ to simulate the active behaviour of the source component. In practice, the validation procedures in Eqs. (2.26) and (2.28) consider artificial excitation applied to the source sub-structure via an instrumented hammer or shaker whilst the source is turned off. Often, validation of the true operational response (e.g. of electric motors, pumps, etc.) consists of multiple sharp tonal components, which may

be hard to compare visually. Instead, broadband excitation is free from such tones and favoured over operational validation, since errors associated with FRF matrix inversion can only be detected at sufficiently excited frequency ranges. Although the external source excitation arguably provides a simpler validation procedure, the unrealistic blocked force vector (i.e. changed interface contribution) may not reflect the uncertainty of the operated source.

2.4.2 Transformation Consistency of Indicator DoFs

The transformation approaches outlined in Sec. 2.3 require multiple response and excitation measurements to approximate translational and rotational point-like coupling. Unless rotations are accounted for implicitly, the exact position and orientation of each indicator DoF are essential to obtain representative results at the defined interface point. As such, the classic coherence function may provide meaningful insights into the measurement quality of single FRFs, however, successful implementation relies heavily upon dynamically plausible data sets. To this end, the measurement consistency at each interface evaluates the geometry of the sensor and excitation points used in the transformation matrix, particularly useful for high channel counts. In theory, the sensor/excitation consistency indicates if the interface behaves rigidly (represented by 6-DoFs), but often serves a less sophisticated purpose and identifies ‘non-consistent’ responses/excitations in the transformation. Due to the different nature of the indicator measurements, the consistency of the sensor responses and the force excitations are evaluated separately. It is important to note that consistency relates to the geometry and the dynamics shared between the indicator DoFs and the defined virtual interface point. However, it does not describe the degree to which the coupling interface has been correctly represented, e.g. whether enough DoFs have been included (this concept of completeness is outlined in Sec. 2.4.3).

Overall and Specific Sensor Consistency

The sensor consistency function, originally proposed in [73] as an indicator for locally rigid behaviour, evaluates the consistency of the response channels in the proximity of the interface. The measured indicator responses implicitly contain rigid but also flexible motion (i.e. 6+ DoFs) of the interface, whilst after the transformation, the interface behaviour is typically represented by 6 rigid DoFs. For the sensor consistency, the translational and rotational dynamics at the virtual interface may,

again, be expanded onto the indicator sensors and compared to the original measured responses.

The consistency of the indicator sensors is evaluated from a single artificial excitation $\mathbf{f}_{C,a_i} = \{0, \dots, 0, f_{C,a_i}, 0, \dots, 0\}^T$ on the assembly's source sub-structure. The source-side excitation (a_i) is applied somewhat remote from the interface to ensure rather global responses \mathbf{v}_{C,ca_i} at the indicator DoFs with a reasonable signal contribution in all directions. Pre-multiplication with the transformation matrix \mathbf{B}_v (row based operation) maps the translational indicator responses onto the virtual interface, typically defined by 6 rigid interface displacement modes. For flexible phenomena, often due to measurement errors, the residual $\boldsymbol{\mu}$ will become non-zero (Eqs. (2.19) and (2.20)). In an expansion step, the virtual responses (rigid 6-DoFs) are pre-multiplied by \mathbf{B}_v^+ to approximate the indicator responses $\tilde{\mathbf{v}}_{C,ca_i}$, applying modal filtering as the residual flexible behaviour is mathematically discarded. The original indicator vector \mathbf{v}_{C,ca_i} and the filtered velocity response $\tilde{\mathbf{v}}_{C,ca_i}$ are defined as [10],

$$\mathbf{v}_{C,ca_i} \triangleq \{v_{C,c_1a_i}, \dots, v_{C,c_ia_i}, \dots, v_{C,c_{n_c}a_i}\}^T = \mathbf{Y}_{C,ca} \mathbf{f}_{C,a_i} \quad (2.29)$$

$$\tilde{\mathbf{v}}_{C,ca_i} \triangleq \{\tilde{v}_{C,c_1a_i}, \dots, \tilde{v}_{C,c_ia_i}, \dots, \tilde{v}_{C,c_{n_c}a_i}\}^T = \mathbf{B}_v^+ \mathbf{B}_v \mathbf{Y}_{C,ca} \mathbf{f}_{C,a_i} \quad (2.30)$$

The modal filtering performed by the reduction and expansion step effectively removes any flexible behaviour by reconstructing the indicator responses from 6 virtual DoFs, i.e. $\tilde{\mathbf{v}}_{C,ca_i} = \mathbf{v}_{C,ca_i} - \boldsymbol{\mu}$.

The response vectors, as defined in Eqs. (2.29) and (2.30), consider a single excitation DoF (a_i). In theory, a single excitation may be sufficient to characterise the sensor consistency, however, multiple forces each applied in a different direction and position (a_1, a_2, \dots, a_{n_a}) may generate mutually independent excitations to excite all independent vibration modes at the interface (c). In this case, the vectorised responses, $\mathbf{v}_{C,ca} = \{\mathbf{v}_{C,ca_1}, \mathbf{v}_{C,ca_2}, \dots, \mathbf{v}_{C,ca_{n_a}}\}^T$ and $\tilde{\mathbf{v}}_{C,ca} = \{\tilde{\mathbf{v}}_{C,ca_1}, \tilde{\mathbf{v}}_{C,ca_2}, \dots, \tilde{\mathbf{v}}_{C,ca_{n_a}}\}^T$ may be used in place of \mathbf{v}_{C,ca_i} and $\tilde{\mathbf{v}}_{C,ca_i}$, respectively. To quickly determine if the complete data set is dynamically plausible the norm of the two velocity vectors $\mathbf{v}_{C,ca}$ and $\tilde{\mathbf{v}}_{C,ca}$ can be evaluated,

$$\rho_{\mathbf{v}_{C,ca}}(\omega) = \frac{\|\tilde{\mathbf{v}}_{C,ca}(\omega)\|}{\|\mathbf{v}_{C,ca}(\omega)\|} \quad (2.31)$$

where the overall sensor consistency $\rho_{\mathbf{v}_{C,ca}}$ is bounded between 0 (no consistency) and 1 (full consistency). High consistency, indicated by $\rho_{\mathbf{v}_{C,ca}}(\omega) = 1$, suggests that all

indicator sensors are correctly calibrated, positioned, and orientated; otherwise, an incorrect geometrical transformation of at least one channel would reduce the overall consistency. A value $\rho_{\mathbf{v}_{C,ca}}(\omega) < 1$ suggests some form of inconsistency. A consistency drop may be expected at higher frequencies, as it indicates flexible interface modes due to the breakdown of locally rigid behaviour [78]. Consequently, an accurate interface description would require an extension of 6-DoFs point-like contacts to the flexible regime [81].

It is important to note that the overall sensor consistency, although able to indicate inconsistency, is unable to determine its principal cause (e.g. whether it's due to an incorrectly connected measurement channel or simply experimental error). Instead, the sensor specific consistency uses an expansion of the spectral coherence function,

$$\text{coh}(x, y) \triangleq \frac{(x + y)(x^* + y^*)}{2(xx^* + yy^*)} \quad \text{with} \quad \text{coh} = \begin{cases} 1 & \text{for } x = y \\ 1/2 & \text{for } x \perp y \\ 0 & \text{for } x = -y \end{cases} \quad (2.32)$$

to evaluate differences between two complex frequency-domain spectra, $x, y \in \mathbb{C}$. Eq. (2.32) returns a scalar value bounded between 1 and 0, allowing for an objective comparison of phase and amplitude differences in Eqs. (2.29) and (2.30). For a selected response channel $c_i \in (c_1, \dots, c_{n_c})$, the specific sensor consistency is given by,

$$\rho_{v_{C,c_i a_i}}(\omega) = \text{coh}(\tilde{v}_{C,c_i a_i}(\omega), v_{C,c_i a_i}(\omega)) \quad v_{C,c_i a_i} \in \mathbf{v}_{C,ca}. \quad (2.33)$$

The sensor specific expression allows evaluating the consistency of each individual response channel in the context of the full transformation [10]. As such, off-positioned and problematic sensors can be identified and either corrected or rejected for the transformation process to improve measurement consistency.

Overall and Specific Excitation Consistency

Similarly, the consistency can be defined for the indicator excitations, emphasising the experimental accuracy associated with shaker or repeated instrumented hammer testing.

The excitation consistency evaluates the measured indicator FRF vector $\mathbf{y}_{C,a_i c}$ with its back-projected (filtered) equivalent $\tilde{\mathbf{y}}_{C,a_i c}$. The transfer FRFs are directly obtained from the indicator excitations \mathbf{f}_{C,c_i} at $c_i \in (c_1, \dots, c_{n_c})$ and a remote response measurement on either sub-structure, here a source-side DoF (a_i). Post-multiplication with the transformation matrix \mathbf{B}_f (column based operation) projects the original indicator forces in $\mathbf{y}_{C,a_i c}$ onto 6 virtual loads at the interface. The filtered expression $\tilde{\mathbf{y}}_{C,a_i c}$ may be obtained by post-multiplication of \mathbf{B}_f^+ , i.e. the indicator forces after projection on the rigid virtual DoFs,

$$\mathbf{y}_{C,a_i c} \triangleq \{y_{C,a_i c_1}, \dots, y_{C,a_i c_i}, \dots, y_{C,a_i c_{n_c}}\} \in \mathbf{Y}_{C,ac} \quad (2.34)$$

$$\tilde{\mathbf{y}}_{C,a_i c} \triangleq \{\tilde{y}_{C,a_i c_1}, \dots, \tilde{y}_{C,a_i c_i}, \dots, \tilde{y}_{C,a_i c_{n_c}}\} \in \mathbf{Y}_{C,ac} \mathbf{B}_f \mathbf{B}_f^+ \quad (2.35)$$

The forward and subsequent backward transformation in Eq. (2.35) separates a set of filtered indicator excitations associated with a rigid load case. The flexible behaviour, often due to interface loading by the applied forces, ends up in the residual μ and is filtered out, i.e. $\mathbf{y}_{C,a_i c} = \tilde{\mathbf{y}}_{C,a_i c} + \mu$.

Eqs. (2.34) and (2.35) consider a single source-side DoF (a_i). This response location has little dynamical significance and is simply required to observe the filtering effect. Instead, multiple mutually independent responses $a_i \in (a_1, \dots, a_{n_a})$ may be used for a more robust observation of all indicator DoFs. In this case, the vectorised mobilities, $\mathbf{y}_{C,ac} = \{\mathbf{y}_{C,a_1 c}, \mathbf{y}_{C,a_2 c}, \dots, \mathbf{y}_{C,a_{n_a} c}\}$ and $\tilde{\mathbf{y}}_{C,ac} = \{\tilde{\mathbf{y}}_{C,a_1 c}, \tilde{\mathbf{y}}_{C,a_2 c}, \dots, \tilde{\mathbf{y}}_{C,a_{n_a} c}\}$ may be used in place of $\mathbf{y}_{C,a_i c}$ and $\tilde{\mathbf{y}}_{C,a_i c}$, respectively.

To get a quick indication of the excitation consistency, the norm of the filtered and original FRF terms can be compared,

$$\rho_{\mathbf{f}_{C,c}}(\omega) = \frac{\|\tilde{\mathbf{y}}_{C,ac}(\omega)\|}{\|\mathbf{y}_{C,ac}(\omega)\|} \quad (2.36)$$

which yields the overall excitation consistency $\rho_{\mathbf{f}_{C,c}}$ bounded between 0 and 1. Each individual indicator DoF can be evaluated using the coherence formulation in Eq. (2.32) to identify problematic and non-consistent excitations. The excitation specific consistency is given by,

$$\rho_{f_{C,c_i}}(\omega) = \text{coh}(\tilde{y}_{C,a_i c_i}(\omega), y_{C,a_i c_i}(\omega)) \quad y_{C,a_i c_i} \in \mathbf{Y}_{C,ca} \quad (2.37)$$

where y_{C,ac_i} and \tilde{y}_{C,ac_i} are the directly measured and projected FRFs in Eqs. (2.34) and (2.35), respectively.

A poor overall consistency (see. Eq. (2.36)) over the entire frequency range may reflect one or more troublesome excitations in practice. Instead, a sudden drop at higher frequencies indicates that the indicator excitations cannot be represented by 3 forces and 3 moments due to the breakdown of locally rigid behaviour. For instance, some indicator excitations have been positioned too far away from the defined interface, causing flexible loading. More often, errors associated with $\rho_{\mathbf{f}_{C,c}} < 1$ are position and orientation errors. In such cases, Eq. (2.37) may be used to relocate problematic excitations, correct entries in the transformation matrix or reject specific indicator DoFs. Implementation of the consistency analysis will be demonstrated throughout Chapters 6 and 7, whilst Sec. 7.7 considers the sensor consistency as a means of a ‘post-processing fix’ to improve the FRF results of a single-sided virtual point transformation.

2.4.3 ICC – Interface Completeness Criterion

Pertaining finally to the challenge of identifying erroneous source data from incomplete descriptions of the coupling interface, an interesting solution to the interface completeness problem is provided by Meggitt et al. in [46, 85]. Derived from in-situ blocked force theory [37] and relationships for coupled structures [9], a coherence-style criterion is proposed to assess the completeness of a given interface description adopted in a source characterisation (i.e. the number of DoFs used). Based on the notation of the modal assurance criterion [16], this so-called Interface Completeness Criterion (ICC) is defined as,

Interface Completeness Criterion:

$$\text{ICC}_{b_1a} = \frac{\left| \mathbf{Y}_{C,b_1a}^{(c)} \left(\mathbf{Y}_{C,b_1a}^{(c_i)} \right)^H \right|^2}{\mathbf{Y}_{C,b_1a}^{(c)} \left(\mathbf{Y}_{C,b_1a}^{(c)} \right)^H \mathbf{Y}_{C,b_1a}^{(c_i)} \left(\mathbf{Y}_{C,b_1a}^{(c_i)} \right)^H} \quad (2.38)$$

with $\mathbf{Y}_{C,b_1a}^{(c_i)} = \mathbf{Y}_{C,b_1c_i} \mathbf{Y}_{C,c_i c_i}^{-1} \mathbf{Y}_{C,c_i a}$ reconstructed through DoFs (c_i).

The coherence-style ICC_{ba} estimates the degree of model uncertainty presented in a given incomplete interface description through the mathematical blocking of a transfer function measured between a set of source-side DoF, (a), and a single receiver-side

DoF, (b_1). In the above, the measured vector $\mathbf{Y}_{C,b_1a}^{(c)}$ contains the dynamics of the actually coupled structures, that is, the complete set of interface DoFs (c). The equivalent vector $\mathbf{Y}_{C,b_1a}^{(c_i)}$ is predicted by considering only the known interface DoFs (c_i), i.e. neglecting inaccessible/unknown DoFs (in-planes, rotations, etc.), which are not accounted for in the interface description. The frequency-dependent criterion is thus bounded between zero (no interface coupling is considered) and one (all coupling DoFs are accounted for, that is, $\mathbf{Y}_{C,b_1a}^{(c)} = \mathbf{Y}_{C,b_1a}^{(c_i)}$).

In case multiple remote DoFs (b) are of interest, the FRF terms in Eq. (2.38) can be vectorised, e.g. $\mathbf{Y}_{C,ba}^{(c_i)} = [\mathbf{Y}_{C,b_1a}^{(c_i)}, \mathbf{Y}_{C,b_2a}^{(c_i)}, \dots, \mathbf{Y}_{C,b_{n_b}a}^{(c_i)}]$, to obtain an overall \mathbf{ICC}_{ba} [46]. Still, the source-side DoFs (a) considered in the ICC are unlikely to coincide with the true excitation DoF of the source (θ). In order to excite all significant modes of the coupling interface DoFs, it is recommended to excite the assembly at multiple, not coinciding directions to obtain a multidirectional artificial excitation representative for the intended operation and source mechanisms.

In the context of source characterisation, the ICC enables us to validate imposed assumptions, such as the neglect of rotational or in-plane coupling DoFs, in the attempt to reduce the measurement effort of the in-situ blocked force. Also, in the analysis of coupled structures with larger connection surfaces (i.e. continuous interfaces), it is standard practice to approximate interface coupling by a number of point-like contacts (based on points per wavelength arguments) [75]. In both cases, this criterion may be used to check whether sufficient coupling DoFs have been included in the source characterisation setup yielding an indicator for the completeness of the experimental data intrinsic to the source. A practical application of the ICC will be presented later in Part IV to indicate incompleteness due to physically absent DoFs and experimental error. Further applications of the ICC can be found in [1, 75, 86].

It is interesting to note that the mobility product $[\mathbf{Y}_{C,b_1c_i} \mathbf{Y}_{C,c_i c_i}^{-1} \mathbf{Y}_{C,c_i a}]$ in Eq. (2.38), which corresponds to the transfer FRF $\mathbf{Y}_{C,b_1a}^{(c_i)}$, can be seen to form a ‘round-trip identity’ [9]. This identity will be discussed next in Sec. 3.1, focusing on indirect system identification rather than completeness.

2.5 Introduction to Transfer Path Analysis

Transfer Path Analysis is a general term used to describe a series of experimental diagnostic and predictive methods to analyse the propagation of noise and vibration in complex built-up structures, as outlined in the introductory discussion in Chapter 1. It has become an essential engineering tool in developing, refining, and troubleshooting sources in their intended installation [33]. The principal aim of TPA is to provide the engineer with guidelines for product changes in a design optimisation context, e.g. by identifying the most significant contribution paths of sound and vibration. Over the years, many TPA variants have been proposed, differing in their implementation to reduce time and experimental effort, usually at the expense of the level of detail and confidence. A comprehensive review of their history and development can be found in the general framework for TPA [4].

Common to all variants is that an assembly is subdivided into active and passive components, the dynamic properties of which are determined separately from one another. TPA aims to identify the individual contributions of an active source to the total response at some specified target position, e.g. vibro-acoustic contributions from the steering gear to the target sound pressure probes in the vehicle cabin. Therefore, reliable TPA measurements must 1) correctly describe the excitation induced by its active source and 2) determine the structural and/or vibro-acoustic transfer paths through which they contribute (i.e. the assembly's passive properties). This separation of active and passive components can help resolve if a noise issue originates from extensive 'source strength', the structure's sensitivity to propagate and radiate the induced vibrational energy, or a combination of both. The principles on how to characterise the active and passive properties have been introduced throughout this chapter.

Regarding the transmission, a distinction is made between airborne and structure-borne contributions from an active source. Airborne sound relates to the sound pressure directly emitted by the source structure. On the other hand, structure-borne contribution considers vibrations transmitted over the structural interfaces onto the connected receiver; the latter propagates the induced vibrations and/or radiates sound. Although TPA may account for both contribution types, this thesis concerns the structure-borne transfer problem. The most popular structure-borne TPA variants are often categorised in three different groups; classical TPA, component TPA,

and transmissibility-based TPA. In the following sections, the source-receiver model is introduced, followed by a brief discussion on the main TPA groups.

2.5.1 Source - Interface - Receiver Model

This section presents a brief description of the coupled subsystems alongside the notation of the defined DoFs. The general concept of structure-borne transfer path analysis adopts the source-receiver model shown in Fig. 2.4. In this specific example (and of principal interest in this thesis), the source is characterised by blocked loads as part of component-based TPA.

In the assembly (C), an active sub-component (A), containing some sort of internal source mechanism (θ) (e.g. electric motors, meshing gears, etc.), is connected to the passive receiver (B) (e.g. mounting bracket, body panel, etc.). When operated, the source exerts dynamic forces and moments, through the coupling interface (c) (active-passive), onto the receiver; the latter simply propagates the induced vibration and/or radiates sound. Assembly (C) also contains remote locations on either side of the coupling interface, i.e. a set of source-side DoF (a), receiver-side DoF (b), and some target DoF (d) on the receiver. The DoFs (a), for instance, may describe the position of artificial excitation on the source (the TPA concept applies equally to passive structures however they are excited), whilst operational responses at (b) are typically used to infer the unknown interface loads. The target DoFs (d) may contain structural and/or sound pressure responses and are often used for validation or evaluation purposes (e.g. subjective and objective ratings at the driver's ear).

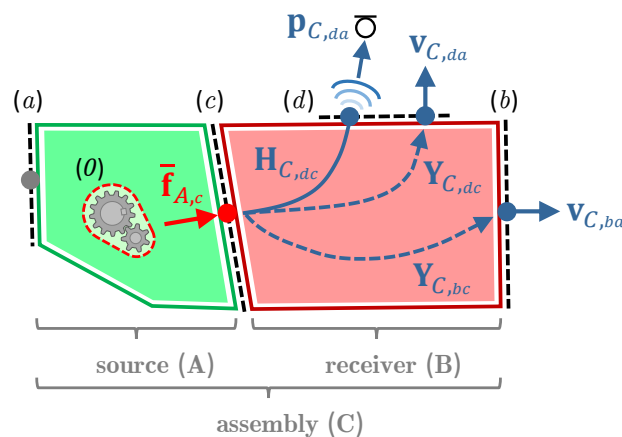


Figure 2.4: Source-receiver model used in component-based TPA to identify dominant source contributions to a particular response (d).

In this example, the source sub-structure is characterised independently using blocked loads $\bar{\mathbf{f}}_{A,c}$. Irrespective of its complexity, the source description must provide an accurate estimate of the excitation induced by its active components. The matrices $\mathbf{Y}_{C,dc}$ and $\mathbf{H}_{C,dc}$ characterise the assembly's passive properties (i.e. its response at (d) to a unit excitation at (c)) to predict the contribution of each interface load to the total operational response at (d). Note that other TPA variants may use a modified source-receiver model (e.g. contact forces instead of blocked loads or a dual interface to account for resilient coupling (compare Fig.3.2)) other than the one shown in Fig. 2.4.

2.5.2 TPA Categories and Workflow

This section provides a brief overview of the different TPA methodologies without theoretical derivation. Variants include classical- [5], in-situ- [6], operational- [8], component-replacement TPA [87], among others, most of which can be categorised into three groups shown in Fig. 2.5. Originally presented in [4], the TPA workflow may be defined by the following steps: 1) operational tests with an active source; 2) determination of the assembly's passive properties, i.e. structural and/or vibro-acoustic FRFs; 3) characterisation of the interface loads; 4) prediction of partial contributions. Depending upon the method employed, some steps may be performed in an arbitrary order or are omitted entirely.

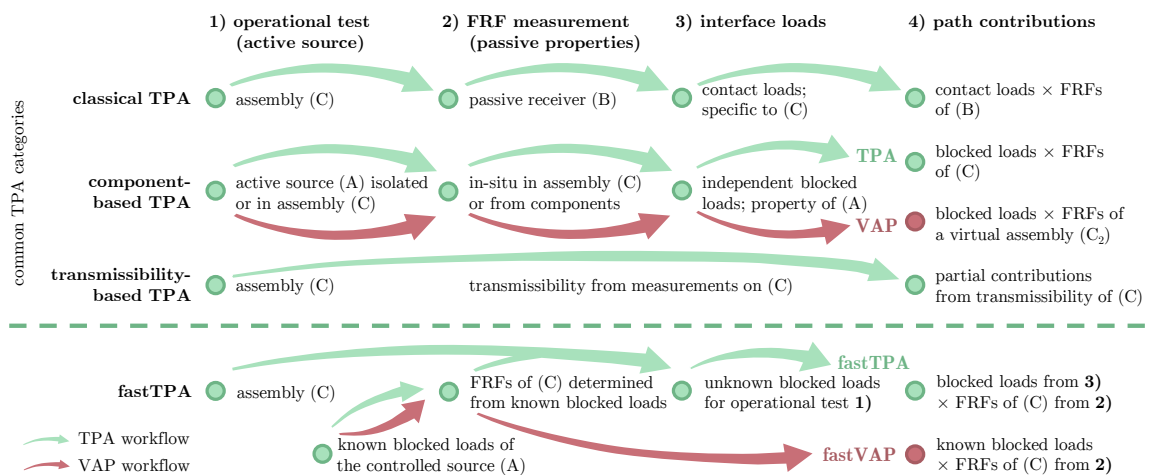


Figure 2.5: Stepwise workflow for the three TPA categories and the proposed concepts of fastTPA and fastVAP used as diagnostic and predictive tools, respectively [4].

Note that in TPA, the forward FRFs for the contribution analysis **4**) are directly measured on the same assembly. It is then used as a diagnostic tool (green arrow) to identify the dominant contributions to an operational response. In the context of component-based TPA, the forward FRFs can describe some new assembly (that not necessarily exists physically) and is predicted using, for example, dynamic substructuring (i.e. measurements of each individual sub-component are mathematically coupled to make up the assembly). The analysis is then used as a predictive tool (red arrows), referred to as virtual acoustic prototyping (VAP), providing a response prediction in a modified or ‘virtual’ assembly. How to contextualise the proposed fastTPA (and fastVAP) within Fig. 2.5 is discussed in Sec. 2.5.3.

Classical Transfer Path Analysis

Classic TPA performs operational tests on the assembly (C) to obtain a set of contact forces at the source-receiver interface (c). These forces represent the active source, that is, they fully determine the responses on the connected receiver (B). However, the contact forces obtained are dependent upon the dynamics of the receiver structure, meaning they are only valid for the source-receiver assembly in which they are acquired. Therefore, the effect of structural modification cannot be investigated, as it would require new operational tests for each design change. To calculate the system responses at the target DoFs (d), the contact forces $\mathbf{f}_{B,c}$ are applied to the interface of the separated sub-component (B), given by,

$$\mathbf{v}_{C,da} = \mathbf{Y}_{B,dc} \mathbf{f}_{B,c}. \quad (2.39)$$

Classical TPA is rather time-consuming and often impractical to apply. The assembly needs to be dismantled for FRF measurements on the uncoupled receiver, e.g. $\mathbf{Y}_{B,dc}$, and later refitted for operational tests. The decoupling can induce experimental uncertainty on the TPA model due to the varying coupling conditions leading to unrealistic predictions.

The perhaps most prominent classic TPA approach is the *matrix-inverse method* [34, 47, 48, 88]. For large-scale and heavyweight systems (e.g. ship machinery or civil testing), *direct contact force measurements* [5] are often preferred with transducers mounted directly between the active and passive components. Alternatively, the transducers can be replaced by resilient elements to determine the interface forces using their dynamic *mount stiffness* [89–91].

Component-based Transfer Path Analysis

Unlike classical TPA, which is typically used for diagnostic tests, component-based TPA methods also serve as a predictive tool. The active source is characterised independently using blocked loads; the description at the interface (c) does not depend on what the source (A) is connected to (i.e. they are transferable) [37]. This means that component-based TPA methods can predict the noise and vibration in complex built-up structures that might not exist physically, referred to as virtual acoustic prototyping [92]. Once $\bar{\mathbf{f}}_{A,c}$ is characterised, the contribution to a target response is determined using assembly transfer functions, e.g. $\mathbf{Y}_{C,dc}$, measured between the coupling interface and the chosen DoFs,

$$\mathbf{v}_{C,da} = \mathbf{Y}_{C,dc} \bar{\mathbf{f}}_{A,c}. \quad (2.40)$$

In a more general case, the effect of structural modification can be predicted using dynamic sub-structuring to construct $\mathbf{Y}_{C,dc}$ from its sub-components, therefore, these methods are referred to as component-based TPA [93]. If the blocked loads are determined using the in-situ approach (compare Eqs. (2.8) - (2.10)) developed in [37], dismantling the assembly can be avoided, and measurements obtained under realistic mounting conditions. Termed originally ‘In-situ source path contribution analysis’ by Elliott et al. [6], the *in-situ TPA* (also: blocked force TPA) has gained popularity within the structural dynamic community due to the reduced experimental effort with no impact on reliability. Alternatively, the blocked loads can be characterised using the methods discussed in Sec. 2.2, namely: *hybrid interface approach* [7, 40], *direct measurement* [39], or the *free velocity* converted into blocked loads [1, 60]. Note that component-based TPA can also be defined by a set of non-unique pseudo-forces applied on the outer surface at some source-side DoFs (a). In fact, the blocked force may be considered a special case of the *pseudo-force method*, where pseudo-forces are applied directly to the interface [35]. It is often difficult to compare the pseudo-forces of different sources due to their dependence upon measurement position, and additional measurements are required to obtain meaningful path contributions.

Transmissibility-based Transfer Path Analysis

The previous TPA categories have in common that interface loads describe the active source, whilst FRFs characterise the transmission paths through which they contribute. If the mere purpose of TPA is to identify dominant contribution paths,

transmissibility-based analysis between sensors can replace the FRF measurements. Transmissibility-based TPA avoids explicitly determining interface loads; instead, the partial contributions can be obtained from transmissibilities between sensors positioned along the transmission path. Transmissibility is defined as the complex ratio of operational velocities (also forces or mobilities) at different positional-DoFs, e.g. near the coupling interface (c) and some target DoFs (d),

$$\mathbf{v}_{C,da} = \mathbf{T}_{C,dc} \mathbf{v}_{C,ca}. \quad (2.41)$$

Although the transmissibility is subject to the sensor positions, it offers clear identification of the frequency regions of amplification and attenuation between those DoFs. *Operational TPA* [8, 94–96] has received much attention, as the transmissibility only requires operational tests of the source, reducing time and effort. Accelerometers need to be positioned at the path references (i.e. source-receiver interface) and the target DoFs to include all possible transmission paths for a realistic prognosis. Whilst $\mathbf{T}_{C,dc}$ allows characterising the partial contributions corresponding to the interface DoFs, interface loads are not explicitly calculated. This makes it unclear if a dominant contribution is caused by an excessive load (active) or a sensitive path (passive). To determine interface loads, *operational path analysis with eXogeneous inputs* (OPAX) [97, 98] combines operational and classical TPA principles. As such, operational measurements are used to estimate the mount stiffness parameters for a detailed contribution analysis.

Other TPA Extensions

In response to evolving demands, methods have been under continuous development, some of which cannot be clearly categorised due to their specific purpose. Others may be considered an extension of the TPA methods discussed in Fig. 2.5 for a more detailed analysis beyond the conventional transfer path problem. For instance, the *component replacement-TPA* (CR-TPA) proposed by Meggitt et al. [87] begins with an assembled structure and considers the replacement of an individual component, e.g. a substitute isolator. Component-based TPA methods typically limit such structural modifications to receiver components. Any source-side changes (i.e. upstream the interface) are prohibited, as they would alter the operational characteristics (i.e. blocked force) and thus invalidate any response measurements made thereafter. In contrast, CR-TAP attempts to update an existing assembly using a transmissibility-based structural modification (so-called transmodification

matrices) to simulate a sub-component replacement within the defined source. To this end, CR-TPA is considered an extension of the in-situ TPA, one that enables upstream and downstream (from the interface) structural modifications.

Another example is the *internal TPA* (also referred to as blocked force transmissibility TPA) proposed by Zabel et al. [99, 100] to analyse the contribution of a vibration generating mechanism to the blocked loads at the defined source-receiver interface. An operational transmissibility relation is characterised between responses at the source-receiver (secondary) interface (c), and some internal DoFs (primary interface) positioned upstream. As such, blocked loads determined at (c) can be related to these internal DoFs via the transmissibility. Like the CR-TPA, this internal contribution analysis extends the in-situ TPA procedure by identifying dominant contributions of the source mechanisms (θ).

2.5.3 History and Classification of FastTPA

This section categorises the fastTPA in the context of the TPA framework. Although not related to the proposed method, a ‘fast TPA’ approach was mentioned before by van der Auweraer in [101] (for differentiation, the novel proposed method is denoted ‘fastTPA’, omitting the space character).

In this earlier form, the fast TPA aimed to quickly assess dominant sources or subsystems, i.e. to roughly locate a vibration source in an assembled structure rather than a detailed analysis of each load and path. The fast TPA procedure was developed to complement typical operational troubleshooting measurements (i.e. responses at the subsystems and the target DoFs) without additional instrumentation. On the assembled system, additional FRFs are measured between some source-side DoFs (a) (often associated with the connecting interface of the different subsystems) and the response locations. Using the matrix-inverse approach, so-called ‘add-on forces’ are characterised at the excitation points (a), which are used to predict each sub-component’s contribution to the target (add-on forces \times propagating FRFs) [102, 103]. The somewhat arbitrary add-on forces are similar to the pseudo-force definition and have no significant physical meaning. Clearly, these forces depend on the position and orientation of the FRF measurements and upon the number of source-side DoFs (i.e. columns of the assembly FRF matrix). In a simple analysis, dominant subsystems can be identified by comparing the associated add-on forces and their partial contributions to an operational response. In fact, fast

TPA is similar to the in-situ TPA procedure, however, the assembly FRFs are not strictly defined in different coordinate-DoFs at the coupling interface in an attempt to simplify the measurement.

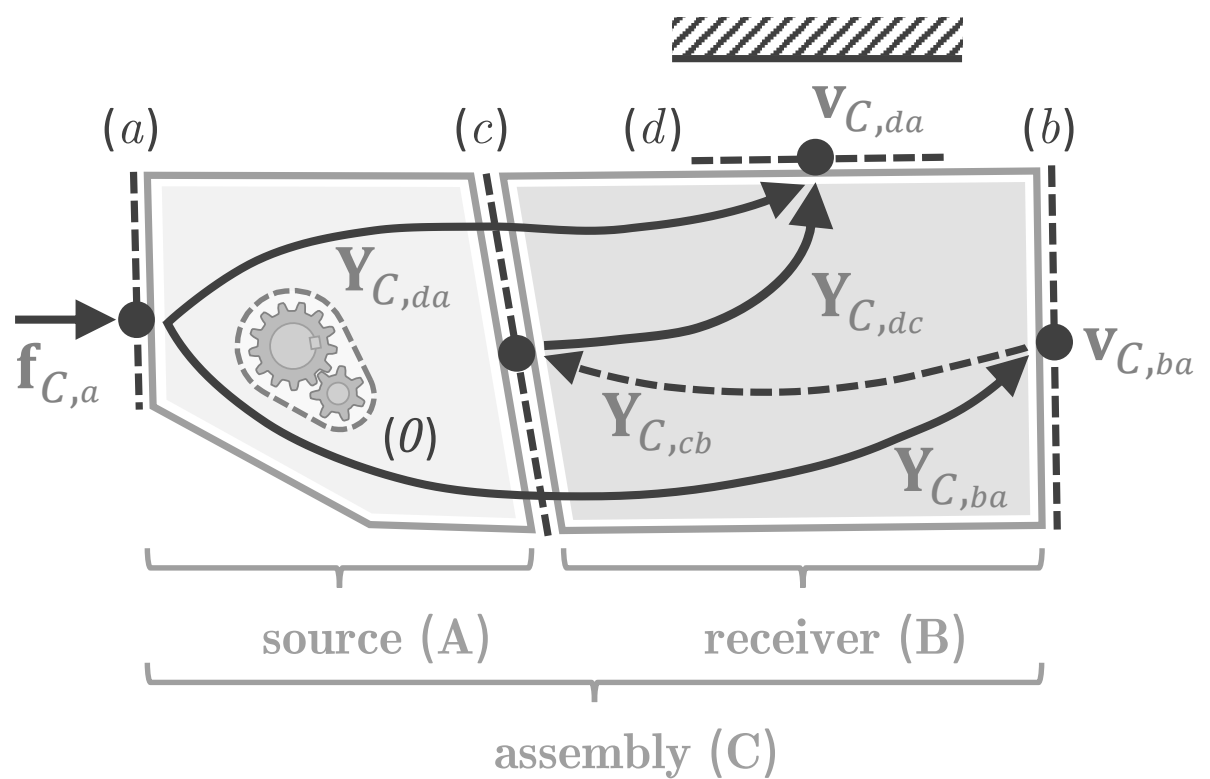
In this thesis, a novel fastTPA procedure is proposed, which follows similar objectives, that is, quick system diagnostic with minimal additional hardware. Additionally, incorporating the independent blocked force relation offers the ability to determine interface loads and their individual contribution paths. The fastTPA procedure combines the principles of component-based TPA and operational system identification in two steps:

1. In a calibration measurement, a controllable source is installed in a calibration setup, e.g. test rig, a fixture, or any other type of experiential setup. The blocked loads are characterised at the coupling interface, independently of the connected receiver, when the source is operated under controlled and sufficiently reproducible conditions. Therefore, the first step employs independent source characterisation, similar to the source description in component-based TPA.
2. In the subsequent system identification, the controlled source is installed in a target assembly. When operated under the same controlled conditions, the source is essentially used as a calibrated (multi-DoF) vibration exciter. The source induces vibrations equivalent to its intrinsic blocked loads into the target receiver via all existing coupling DoFs. With simple operational measurements, structural and/or vibro-acoustic FRFs can be determined between the coupling interfaces (known blocked force excitation **1.**) and the chosen response DoFs (based on transmissibility principles). In other words, FRFs are obtained by relating the known blocked forces from the calibration step to the corresponding response measurements in the system identification stage.

The FRFs (**2.**) can be combined with the known blocked force (**1.**) to construct a virtual acoustic prototype, referred to as fastVAP, or incorporated in a component-based in-situ TPA. The latter uses the FRFs (**2.**) to replace conventional measurements with instrumented hammers or shakers in the target assembly. Using a controlled source in the context of TPA is denoted as ‘fastTPA’ due to the significant time advantage.

To this end, the fastTPA approach is conceptually similar to other component-based TPA approaches but relies on the transfer of blocked loads between assemblies. Therefore, previous chapters focused on the independent and complete characterisation of the source. In the following, the derivation of the fastTPA is presented in Chapter 4, based on the transmissibility concept and the round-trip identity. The latter refers to an indirect measurement procedure which is outlined in Chapter 3.

PART II. Theoretical Concept of System Identification



3

Framework for Round-Trip Identity

Independent source characterisation and system identification rely on the complete determination of the FRF matrix, including in-plane, rotational and cross terms. In practical applications, test structures may not allow FRFs to be measured directly due to the impracticality of applying a controlled excitation in a particular direction (e.g. in-plane), the inability to measure rotational dynamics (e.g. moment excitation), insufficient SNR between excitation and response DoFs, or simply due to restricted access.

The following chapter presents a framework for indirect measurement of structural dynamic properties of coupled structures and their separated sub-components. A generalisation of the round-trip identity is introduced for the indirect characterisation of driving-point and transfer FRFs, forming the basis for fastTPA.

Chapter contents:

3.1	Introduction to Indirect FRF Determination Using Ideal Excitations	53
3.2	Single Interface Round-Trip Identity	54
3.3	Dual Interface Round-Trip Identity	56
3.4	Generalised Round-Trip Identity	58
3.5	Sub-Structure Round-Trip Identity	68
3.6	Controllability and Observability of the Round-Trip Relations	72
3.7	Summary and Concluding Remarks	76

3.1 Introduction to Indirect FRF Determination Using Ideal Excitations

Whilst the in-situ blocked force relation has gained popularity within the structural dynamic community, a complete characterisation (i.e. translations and rotations at multiple contacts) is undeniably inconvenient to implement as it requires operational and complex FRF measurements of the coupled assembly. Typically, driving-point and transfer FRFs of a structure are determined by employing roving instrumented hammers or shakers. With either kind of FRF measurement, its excitation can prove problematic, particularly in practical scenarios where access is limited. However, the correct position of an excitation is essential to obtain accurate FRF measurements. This is particularly so when considering diagnostic methods such as TPA or the related discipline of noise and vibration predictions in virtual assemblies [1, 50]. In these applications, it is well known that small errors, for example, due to inaccurate excitation positions, can lead to large uncertainties in the identified forces and corresponding response predictions [46]. This sensitivity highlights the challenges commonly encountered when characterising structural dynamic systems.

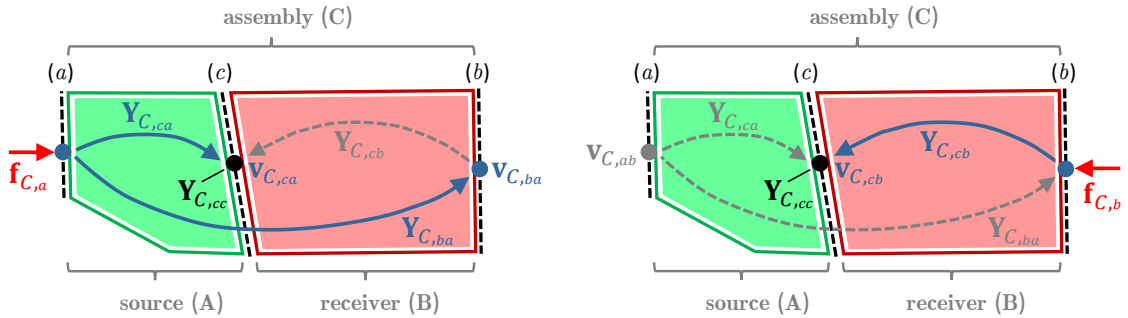
Unlike excitations, general response measurements are not considered problematic. Piezoelectric accelerometers, relatively compact in size, or miniaturised MEMS (micro electro-mechanical system) sensors can easily be placed even on complex geometries or if access is restricted [52]. In some cases, the principle of reciprocity may be invoked to interchange the position of response and excitation so as to simplify a transfer function measurement [20]. Often, reciprocal FRF measurements are not possible because both the response position and at least a subset of the coupling interface DoF are inaccessible for excitation. Hence, there is a need for indirect methods with the ability to relocate excitations to more convenient locations remote from inaccessible interfaces.

In response to this, Moorhouse et al. [9] proposed a relation for coupled structures, which was later termed the ‘round-trip identity’. Since then, the round-trip concept has been under continuous development and employed in various applications, e.g. the ICC presented in Sec. 2.4.3. Given the above discussion, the remainder of this chapter presents a framework for the round-trip identity. Concepts for indirect characterisation of structural properties are presented based on ideal excitations (i.e. impact or shaker testing), including a novel generalised round-trip relation for inaccessible FRFs and noise reduction of long distance transfer paths.

3.2 Single Interface Round-Trip Identity

In a laboratory environment, test rigs may be specifically designed to facilitate unrestricted interface access for driving-point FRF measurements, so that problems due to insufficient excitation positioning can be avoided. This, however, is generally not the case for most functional components when mounted in-situ (e.g. in an engine bay or other types of encapsulated structures). It was shown by Moorhouse et al. [9] that relocation of such inaccessible interface excitations could be achieved through the round-trip identity (note that the term ‘round-trip identity’ was introduced in [65] but not used in the original publication [9]).

The round-trip identity establishes an indirect relationship between the driving-point FRFs $\mathbf{Y}_{C,cc}$ at a coupling interface (c), and the transfer functions surrounding it (see also [104]). This identity allows the reconstruction of driving-point FRFs at an interface between connected sub-structures from relocated (easy-to-access) remote measurements on the source and receiver sub-structures. The two-step measurement is depicted in Fig. 3.1 to determine the transfer paths forming a ‘round-trip journey’ to the target interface DoFs (c).



(a) Step 1: Excitation of source-side DoFs (a) to determine the round-trip paths to interface (c) and remote location (b).

(b) Step 2: Measurement of the remaining receiver-side FRFs from the remote DoF (b) to interface (c).

Figure 3.1: Transfer paths forming a ‘round-trip’ relationship for the indirect identification of driving-point FRFs, $\mathbf{Y}_{C,cc} = \mathbf{Y}_{C,ca} \mathbf{Y}_{C,ba}^{-1} \mathbf{Y}_{C,cb}^T$ (see Eq. (3.1)), at the coupling interface (c) using excitations with a known input force at source-side locations (a) and receiver-side remote points (b).

The round-trip identity aims to obtain the coupled driving-point FRF $\mathbf{Y}_{C,cc}$ from alternative FRF measurements at (a) and (b) without having to excite the interface. The overview in Fig. 3.1 can be used as a practical guide to identify the two measurement steps required to obtain the three transfer FRF terms of the round-trip. In the

first step (Fig. 3.1a), excitation by a known input force is applied at source-side DoFs (a) to determine the transfer FRFs $\mathbf{Y}_{C,ca}$ and $\mathbf{Y}_{C,ba}$. Therefore, structural responses are recorded at the interface (c) and arbitrary remote positions (b). In step 2, as illustrated in Fig. 3.1b, excitations are applied at (b) to determine the transfer FRFs $\mathbf{Y}_{C,cb}$ between the receiver-side DoFs (b) and interface (c). As such, locations at (a) and (b) are reference DoFs that can be selected to facilitate excitation, e.g. using an instrumented hammer or shaker. Also, excitation of moments or in-plane forces at the interface is avoided, which is often impractical, if not impossible. However, the measured responses at (c) may include translational and rotational coordinate-DoFs, to calculate the corresponding driving-point FRFs. This typically requires a specific accelerometer configuration at (c) to facilitate finite difference approximation or alternative techniques (compare Sec. 2.3) [66, 76]. Otherwise, incomplete interface instrumentation is sufficient to obtain the correct driving-point FRFs for a subset of coordinate-DoFs. Certain coupling DoFs (e.g. rotational DoFs) may be neglected completely in the accelerometer setup at (c) without changing the result of the targeted driving-point FRFs [63].

A detailed description and complete derivation of the single interface round-trip identity is given in [63]; here, only the essential equations are recalled in which the interface driving-point FRF is expressed in terms of other transfer FRFs.

Single interface round-trip identity:

$$\mathbf{Y}_{C,cc} = \mathbf{Y}_{C,ca} \mathbf{Y}_{C,ba}^{-1} \mathbf{Y}_{C,cb}^T \quad (3.1)$$

or by reciprocity,

$$\mathbf{Y}_{C,cc} = \mathbf{Y}_{C,cb}^T = \mathbf{Y}_{C,cb} \mathbf{Y}_{C,ab}^{-1} \mathbf{Y}_{C,ca}^T \quad (3.2)$$

Note that the reciprocal formulation in Eq. (3.2) uses a changed notation for the inverse transfer FRF $\mathbf{Y}_{C,ba}^{-1}$. For LTI-systems, the input-output relation between DoFs at (a) and (b) remains unchanged if their force and response roles are interchanged, i.e. principle of reciprocity: $\mathbf{Y}_{C,ab} = \mathbf{Y}_{C,ba}^T$.

The product $\mathbf{Y}_{C,ca} \mathbf{Y}_{C,ba}^{-1}$ and the reciprocal relation $\mathbf{Y}_{C,cb} \mathbf{Y}_{C,ab}^{-1}$ on the right-hand side of Eqs. (3.1) and (3.2) form generalised transmissibilities of the coupled assembly (C) [9]. This transmissibility characterises the complex FRF ‘ratio’ for responses measured at the interface (c) and the remote location (b) or (a), for system excitation at (a) or (b), respectively. In theory, similar transmissibilities can be determined

from operational measurements as elaborated in Sec. (4.1). In the following, the single interface round-trip identity is extended to facilitate indirect system identification for a modified source-isolator-receiver model with a dual interface.

3.3 Dual Interface Round-Trip Identity

Whilst the original round-trip formulation considers a conventional single interface source-receiver assembly, a subsequent derivation by Meggitt et al. [25, 105] introduces a dual interface counterpart, accounting for isolator coupling. In this modified scenario, the dual interface round-trip identity allows for indirect characterisation of the coupled transfer FRFs \mathbf{Y}_{C,c_2c_1} between two interfaces.

Throughout many engineering disciplines, vibration isolators between the source and the receiver sub-structure are common design elements to provide vibration decoupling, e.g. silent bushings at steering gear mounts. To effectively minimise the propagation of structure-borne vibration through the interface, the dynamic properties are often determined at both connections to the resilient element to predict its performance in the assembly. To account for the dual interface nature, the source-receiver model in Fig. 3.2 includes a resilient element (I) between the two sub-structures. In the following, the coupling DoFs at the source-isolator and the isolator-receiver interface are referred to as (c_1) and (c_2) , respectively.

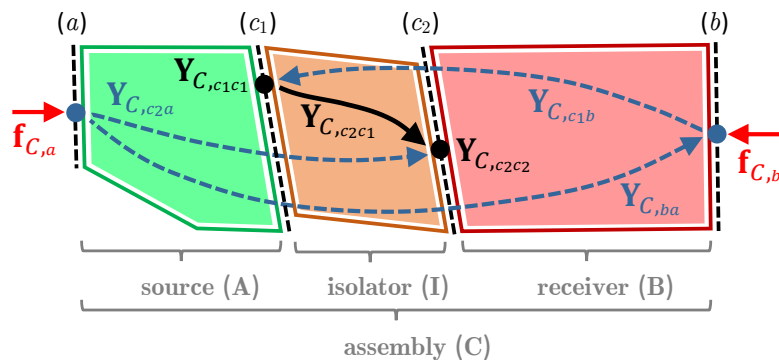


Figure 3.2: Transfer paths of the dual interface round-trip identity for the indirect measurement of transfer FRFs, $\mathbf{Y}_{C,c_2c_1} = \mathbf{Y}_{C,c_2a} \mathbf{Y}_{C,ba}^{-1} \mathbf{Y}_{C,c_1b}^T$ (see Eq. (3.3)), between interfaces (c_1) and (c_2) of a source-isolator-receiver system.

This dual interface round-trip allows for indirect measurement of the transfer FRF between the two defined interfaces, e.g. to characterise the coupling element (I) in terms of its transfer impedance ($\mathbf{Z}_{I,c_2c_1} = \mathbf{Y}_{C,c_2c_1}^{-1}$) whilst installed under representative mounting and load conditions [25]. It was shown by Moorhouse et al. [63] that

the dual interface round-trip also applies to rigidly coupled structures, e.g. larger multi-point or continuous contact interfaces between sub-structures. A potential application is to divide the interface DoFs into two subsets (c_1 and c_2) whilst instrumentation is required only at one interface at a time. Therefore, system FRFs are first measured with interface instrumentation at (c_1), which is later moved to (c_2) to reduce the number of required sensors to a lower channel count. The dual interface round-trip identity may be employed to merge the separate measurements to a complete interface FRF matrix, including cross terms (i.e. \mathbf{Y}_{C,c_2c_1}).

A complete characterisation of the interface dynamics for the source-isolator-receiver model illustrated in Fig. 3.2 considers both driving-point and transfer FRFs. Using indirect methods, the single interface round-trip identity may be applied twice to determine the driving-point FRFs, \mathbf{Y}_{C,c_1c_1} and \mathbf{Y}_{C,c_2c_2} . However, the original round-trip identity does not account for the dual interface nature [21, 105]. To indirectly determine the transfer FRFs between interfaces, i.e. \mathbf{Y}_{C,c_2c_1} or \mathbf{Y}_{C,c_1c_2} , Meggitt [21] defined the dual round-trip identity for resiliently coupled sub-structures.

Dual interface round-trip identity:

$$\mathbf{Y}_{C,c_2c_1} = \mathbf{Y}_{C,c_2a} \mathbf{Y}_{C,ba}^{-1} \mathbf{Y}_{C,c_1b}^T \quad (3.3)$$

or by reciprocity,

$$\mathbf{Y}_{C,c_1c_2} = \mathbf{Y}_{C,c_2c_1}^T = \mathbf{Y}_{C,c_1b} \mathbf{Y}_{C,ab}^{-1} \mathbf{Y}_{C,c_2a}^T \quad (3.4)$$

The identity is expressed in terms of three FRF matrices without the need for artificial excitation at either the source-isolator (c_1) or the isolator-receiver (c_2) interface. The round-trip journey is formed from coupling interface (c_1) to remote DoF at (b), (b) to (a), and (a) to the second coupling interface (c_2). The procedure in Eq. (3.3) requires a two-step measurement campaign with excitations applied at the source-side DoFs (a) and passive remote points (b). The resultant structural responses are measured at the isolator-receiver interface (c_2) and DoFs at (b) and (c_1), respectively. Note that the reversed reciprocal relation in Eq. (3.4) uses response measurement at (a) instead of (b). The additional coupling DoFs of the dual interface system ($n_c = n_{c_1} + n_{c_2}$) need to be considered in the number of remote points so as to avoid under-determination [105].

It is interesting to note that for collocated interface DoFs (c_1) and (c_2), such that ($c = c_1 = c_2$), the dual interface approach is reduced to driving-point FRFs. Hence the dual formulation in Eqs. (3.3) and (3.4) is effectively the same as the standard round-trip identity for a single interface as in Eqs. (3.1) and (3.2). Together, the round-trip identity and its dual interface extension provide an in-situ characterisation of resilient coupling elements using only remote excitations, that is, avoiding excitation at either interface.

The round-trip and its dual interface extension have found application in experimental structural dynamics, for example due to their ability to determine in-plane driving-point FRFs. However, this indirect characterisation has been restricted to DoFs at the coupling interface. In the following section, the round-trip concept is generalised so as to combine both mentioned round-trip variants with an extension for inaccessible transfer FRFs to arbitrary remote DoFs.

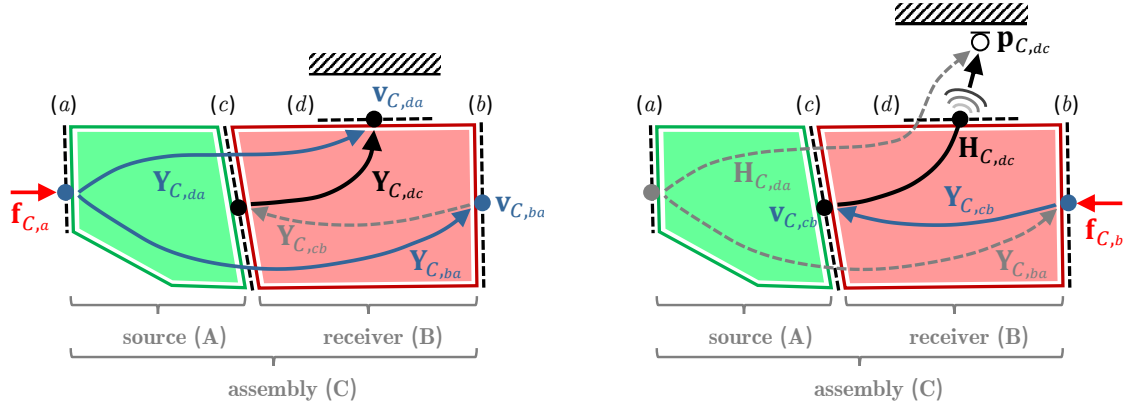
3.4 Generalised Round-Trip Identity

In this section, the round-trip concept is generalised to include transfer FRFs between a coupling interface (c) and arbitrary remote points (d). Within this novel generalised concept, direct excitation of rotational DoFs or inaccessible points on either side of the transfer path is avoided altogether and instead replaced by a number of rectilinear forces, which by choice of the experimentalist can be applied at accessible positions. As for the earlier methods in Sections 3.2 and 3.3, the DoFs (d) introduced by the generalised round-trip identity may be defined at the source-receiver interface itself to recall the single or dual interface round-trip formulation for coupling points.

The generalised round-trip concept is based on the source-receiver model shown in Fig. 3.3. Assembly (C) contains remote locations on either side of the coupling interface, i.e. a set of accessible source-side DoFs (a), accessible receiver-side DoFs (b), and some target DoFs (d) on the receiver. The target DoFs (d), that may contain structural (see Fig. 3.3a) and/or sound pressure (see Fig. 3.3b) responses, are considered encapsulated (illustrated by the hatched area), and are by definition inaccessible¹ for direct excitation. This source-receiver (active-passive) model is adopted from the TPA methodology, however, the round-trip concept applies

¹ In Fig. 3.3b, reciprocal measurement of the vibro-acoustic counterpart requires excitation by a volume velocity source, which is also considered inaccessible.

equally to purely passive structures. The generalised round-trip formulation derived in the following section addresses the combined problem of providing an indirect relationship for structural $\mathbf{Y}_{C,dc}$ and vibro-acoustic $\mathbf{H}_{C,dc}$ transfer paths. For brevity, modifications to include vibro-acoustic FRFs are straightforward but not explicitly shown in the derivation.



(a) Step 1: Source-side excitation (a) to determine FRF terms to the receiver-side location (b) and the inaccessible target DoFs (d).

(b) Step 2: Measurement of the receiver-side transfer function $\mathbf{Y}_{C,cb}$. For generality, the accelerometer at target (d) is replaced by a sound pressure probe.

Figure 3.3: Measurement steps to obtain the path segments forming the generalised round-trip identity for the indirect characterisation of structural, $\mathbf{Y}_{C,dc} = \mathbf{Y}_{C,da} \mathbf{Y}_{C,ba}^{-1} \mathbf{Y}_{C,cb}^T$ (see Eq. (3.19)), and vibro-acoustic, $\mathbf{H}_{C,dc} = \mathbf{H}_{C,da} \mathbf{Y}_{C,ba}^{-1} \mathbf{Y}_{C,cb}^T$, transfer functions.

The following derivation is essentially the same as that in [63] but includes additional points remote from the interface at (d). First, consider the dynamic assembly (C) as illustrated in Fig. 3.3a. For a harmonic input force applied to a single source-side DoF (a), the resultant velocities at the receiver locations (b) and the target DoFs (d) are given by,

$$\mathbf{v}_{C,ba_i} = \mathbf{Y}_{C,ba} \mathbf{f}_{C,a_i} \quad \text{for } n_b \text{ receiver DoFs \& one excitation } (a_i) \quad (3.5)$$

$$\mathbf{v}_{C,da_i} = \mathbf{Y}_{C,da} \mathbf{f}_{C,a_i} \quad \text{for } n_d \text{ target DoFs \& one excitation } (a_i) \quad (3.6)$$

$$\text{with } \begin{cases} \mathbf{f}_{C,a_i} = \{0, \dots, 0, f_{C,a_i}, 0, \dots, 0\}^T \\ \mathbf{v}_{C,ba_i} = \{v_{C,b_1 a_i}, v_{C,b_2 a_i}, \dots, v_{C,b_{n_b} a_i}\}^T \\ \mathbf{v}_{C,da_i} = \{v_{C,d_1 a_i}, v_{C,d_2 a_i}, \dots, v_{C,d_{n_d} a_i}\}^T \end{cases}$$

where \mathbf{v}_{C,ba_i} is the complex velocity response vector of the coupled assembly, denoted by the upper-case subscript ‘C’. The lower-case subscripts ‘a’ and ‘b’ indicate the

excitation and response DoFs, respectively, including all n_b remote measurement positions (b) on the passive-side. A similar notation applies for the target response \mathbf{v}_{C,da_i} at the remote locations (d). The external excitation f_{C,a_i} is arranged in the force vector \mathbf{f}_{C,a_i} and the subscript ' a_i ' indicates the specific source-side excitation DoF.

Applying further excitations (a_1, a_2, \dots, a_{n_a}) at other locations in (a) and arranging the columns into matrices yields the matrix equation,

$$\mathbf{V}_{C,ba} = \mathbf{Y}_{C,ba} \mathbf{F}_{C,a} \quad \text{for } n_b \text{ receiver DoFs \& } n_a \text{ source excitations} \quad (3.7)$$

$$\mathbf{V}_{C,da} = \mathbf{Y}_{C,da} \mathbf{F}_{C,a} \quad \text{for } n_d \text{ target DoFs \& } n_a \text{ source excitations} \quad (3.8)$$

$$\text{with } \begin{cases} \mathbf{F}_{C,a} = [\mathbf{f}_{C,a_1}, \mathbf{f}_{C,a_2}, \dots, \mathbf{f}_{C,a_{n_a}}] \\ \mathbf{V}_{C,ba} = [\mathbf{v}_{C,ba_1}, \mathbf{v}_{C,ba_2}, \dots, \mathbf{v}_{C,ba_{n_a}}] \\ \mathbf{V}_{C,da} = [\mathbf{v}_{C,da_1}, \mathbf{v}_{C,da_2}, \dots, \mathbf{v}_{C,da_{n_a}}]. \end{cases}$$

Here, the complex excitation matrix $\mathbf{F}_{C,a}$ contains the force vectors at each source DoF (a_i), resulting in the response matrices $\mathbf{V}_{C,ba}$ and $\mathbf{V}_{C,da}$, respectively. Equating relations (3.7) and (3.8), whilst eliminating $\mathbf{F}_{C,a}$, allows the following relation to be established,

$$\mathbf{V}_{C,da} = \underbrace{\mathbf{Y}_{C,da} \mathbf{Y}_{C,ba}^{-1}}_{\mathbf{T}_{C,db}^{(a)}} \mathbf{V}_{C,ba}. \quad (3.9)$$

Assuming the inverse to exist, which implies $n_a = n_b$, the product of the two mobility terms on the right-hand side of Eq. (3.9) formulates a generalised transmissibility term $\mathbf{T}_{C,db}^{(a)}$ [106]. As an essential requirement the columns of $\mathbf{V}_{C,ba}$ have to be sufficiently independent from one another, else the resultant response matrix will be rank deficient and therefore non-invertible. In practice, additional excitation and/or response DoFs may be included so as to over-determine the inverse problem, resulting in the inversion of a non-square matrix. In such a case, the Moore-Penrose pseudo inverse [23] is used to determine the least-squares solution, here the explicit notation '+' is omitted for brevity.

The next stage in the derivation is to apply a force at the interface location (c), rather than at (a). It is now well known [37] that the velocity field in the receiver generated by \mathbf{f}_{C,a_i} is exactly reproduced by applying the blocked force $\bar{\mathbf{f}}_{A,c}$ to the interface (c) instead [63]. The blocked force is the reaction force measured at an

infinitely rigid, and therefore blocked, interface (c), under the action of \mathbf{f}_{C,a_i} . Using the in-situ relation in Eq. (2.9), this equivalent blocked force excitation (compare Eqs. (3.5) and (3.6)) leads to,

$$\mathbf{v}_{C,ba} = \mathbf{Y}_{C,bc} \bar{\mathbf{f}}_{A,c} \quad \text{for } n_b \text{ receiver DoFs \& one excitation } (a_i) \quad (3.10)$$

$$\mathbf{v}_{C,da} = \mathbf{Y}_{C,dc} \bar{\mathbf{f}}_{A,c} \quad \text{for } n_d \text{ target DoFs \& one excitation } (a_i) \quad (3.11)$$

$$\text{with } \bar{\mathbf{f}}_{A,c}^{(a_i)} = \{\bar{f}_{A,c_1 a_i}, \bar{f}_{A,c_2 a_i}, \dots, \bar{f}_{A,c_{n_c} a_i}\}^T$$

Each applied force, denoted by the superscript ‘ (a_i) ’, will result in a blocked force vector $\bar{\mathbf{f}}_{A,c}^{(a_i)} \in \mathbb{C}^{n_c}$ at interface (c); its rows correspond to specific coupling DoFs (c_1, c_2, \dots, c_{n_c}). Repeating the concept of Eqs. (3.7) and (3.8), multiple external excitations (a_1, a_2, \dots, a_{n_a}) will result in sets of blocked force vectors, which may be arranged in columns of a blocked force matrix, $\bar{\mathbf{F}}_{A,c}$. The blocked force relation in Eqs. (3.10) and (3.11) can be extended by the matrix terms to,

$$\mathbf{V}_{C,ba} = \mathbf{Y}_{C,bc} \bar{\mathbf{F}}_{A,c} \quad \text{for } n_b \text{ receiver DoFs \& } n_a \text{ source excitations} \quad (3.12)$$

$$\mathbf{V}_{C,da} = \mathbf{Y}_{C,dc} \bar{\mathbf{F}}_{A,c} \quad \text{for } n_d \text{ target DoFs \& } n_a \text{ source excitations} \quad (3.13)$$

$$\text{with } \bar{\mathbf{F}}_{A,c} = [\bar{\mathbf{f}}_{A,c}^{(a_1)}, \bar{\mathbf{f}}_{A,c}^{(a_2)}, \dots, \bar{\mathbf{f}}_{A,c}^{(a_{n_a})}].$$

The size of the complex blocked force matrix $\bar{\mathbf{F}}_{A,c}$ has become $n_c \times n_a$, including the full set of coupling DoFs n_c and source excitations n_a . Substitution of Eqs. (3.12) and (3.13) into (3.9) yields the relation between the blocked force matrices,

$$\mathbf{Y}_{C,dc} \bar{\mathbf{F}}_{A,c} = \mathbf{Y}_{C,da} \mathbf{Y}_{C,ba}^{-1} \mathbf{Y}_{C,bc} \bar{\mathbf{F}}_{A,c}. \quad (3.14)$$

Both sides of Eq. (3.14) can be post-multiplied by the inverse of $\bar{\mathbf{F}}_{A,c}$ yielding a generalised expression for the round-trip identity.

Generalised round-trip identity:

$$\mathbf{Y}_{C,dc} = \mathbf{Y}_{C,da} \mathbf{Y}_{C,ba}^{-1} \mathbf{Y}_{C,bc} \quad (3.15)$$

The transfer function $\mathbf{Y}_{C,dc}$ is given by three alternative FRF matrices. Hence, generalised round-trip identity allows to reconstruct transfer FRFs using remote DoFs at (a) and (b).

Note that by moving points (d) to coincide with (c), i.e. identical DoFs (c) = (d), the original form of the round-trip identity as given in [63] (compare Eqs. (3.1) and (3.2)) is obtained, limited to driving-point mobilities $\mathbf{Y}_{C,cc}$ at the coupling interface. The target DoFs (d) may also be interpreted as a second, virtual interface (c_2), hence the proposed generalised expression combines both special cases of the single [9] and dual interface [25] round-trip scenario. Furthermore, this allows for a determination of passive properties for the complete assembly downstream the source, written in the more convenient matrix form as,

$$\begin{bmatrix} \mathbf{Y}_{C,cc} & \mathbf{Y}_{C,cd} \\ \mathbf{Y}_{C,dc} & \mathbf{Y}_{C,dd} \end{bmatrix} = \begin{bmatrix} \mathbf{Y}_{C,cb} & 0 \\ 0 & \mathbf{Y}_{C,ad} \end{bmatrix} \begin{bmatrix} \mathbf{Y}_{C,ab} & 0 \\ 0 & \mathbf{Y}_{C,ba} \end{bmatrix}^{-1} \begin{bmatrix} \mathbf{Y}_{C,ca}^T & \mathbf{Y}_{C,da} \\ \mathbf{Y}_{C,bc} & \mathbf{Y}_{C,db}^T \end{bmatrix}. \quad (3.16)$$

Eq. (3.15) is the main result of this section. The same identity may be obtained through equating the remote blocked force relation, as shown in Sec. 3.4.1. Following some simple rearrangements, the generalised round-trip identity features different applications as outlined in the next sections, first, in Sec. 3.4.2 to indirect determination of transfer FRFs and secondly (Sec. 3.4.3) to ‘long distance’ FRFs.

3.4.1 Alternative Derivation of the Generalised Round-Trip Identity

In the following, an alternative derivation of the generalised round-trip identity (introduced in Sec. 3.4) is given, based on the independent blocked force relation.

The expanded expressions in Eqs. (3.12) and (3.13) can be directly obtained from the remote blocked force relation in Eq. (2.9). Equating both whilst eliminating the blocked force matrix $\bar{\mathbf{F}}_{A,c}$ allows the following equality to be established,

$$\mathbf{Y}_{C,bc}^{-1} \mathbf{V}_{C,ba} = \mathbf{Y}_{C,dc}^{-1} \mathbf{V}_{C,da} \quad (3.17)$$

where $\mathbf{V}_{C,ba}$ and $\mathbf{V}_{C,da}$ are simultaneously measured velocity responses at DoFs (b) and (d). The independent responses (columns of the matrices) of the in-situ blocked force relation are typically obtained from active source measurements under varying operational conditions. Instead, the assembly’s velocity responses can be determined using artificial excitation while the source is turned off, whether through instrumented hammers or shakers. Source-side excitation may be applied at different locations (a_i) to obtain the matrix columns of $\mathbf{V}_{C,ba}$ and $\mathbf{V}_{C,da}$. The resultant velocities can then be normalised to the applied input force (i.e. velocity responses

to a unit force excitation). In this case, the velocity expressions in Eq. (3.17) are effectively mobility matrices (e.g. $\mathbf{V}_{C,ba} \rightarrow \mathbf{Y}_{C,ba}$) of the coupled assembly (C), measured between (a) and DoFs at (b) and (d). For artificial excitations, Eq. (3.17) can be rewritten as,

$$\mathbf{Y}_{C,bc}^{-1} \mathbf{Y}_{C,ba} = \mathbf{Y}_{C,dc}^{-1} \mathbf{Y}_{C,da}. \quad (3.18)$$

As such, the derivation presented in Sec. 3.4 is based on the reconstruction of an equivalent velocity field, whilst this alternative uses the equality of the independent blocked force vector (inherent to the source sub-structure). Both, Eqs. (3.14) and (3.18) yield the same generalised relation of the round-trip identity in Eq. (3.15).

3.4.2 Application I: Obtaining Inaccessible Transfer FRFs from Indirect Measurements

This section will focus on applying the generalised round-trip relation to enable indirect transfer function measurements of the assembly matrix, $\mathbf{Y}_{C,dc}$, between DoFs at the source-receiver interface and any remote location downstream of it (i.e. on the receiver structure). To provide an entirely remote characterisation method for inaccessible transfer FRFs (the generalised round-trip is valid whether or not access is restricted), all excitations need to be relocated to accessible measurement positions. ‘Accessible’ implies that there is sufficient space to apply a known excitation. It is assumed that excitation measurements at the DoFs (c) and (d) are restricted, yet both DoF locations are accessible for instrumentation (e.g. vibration sensors). In Eq. (3.15) the principle of reciprocity may be used to relocate the interface excitations (c) to the chosen measurement positions at (b), $\mathbf{Y}_{C,bc} = \mathbf{Y}_{C,cb}^T$ [20]. A practical formulation of the generalised round-trip is then given by,

Generalised round-trip identity for inaccessible FRFs:

$$\mathbf{Y}_{C,dc} = \mathbf{Y}_{C,da} \mathbf{Y}_{C,ba}^{-1} \mathbf{Y}_{C,cb}^T \quad (3.19)$$

or by reciprocity,

$$\mathbf{Y}_{C,cd} = \mathbf{Y}_{C,dc}^T = \mathbf{Y}_{C,cb} \mathbf{Y}_{C,ab}^{-1} \mathbf{Y}_{C,da}^T. \quad (3.20)$$

Using the terminology of the ‘round-trip journey’ as introduced by Moorhouse [65], the mobility elements on the right-hand side of Eq. (3.19) frame $\mathbf{Y}_{C,dc}$ in a closed loop (see Fig. 3.3). This overview can be used as a practical guide to identify the two measurement steps required to obtain all three round-trip terms.

In the first step, the coupled structure is excited at the source-side DoF (a) while the receiver response is simultaneously measured at (b) and (d) to obtain $\mathbf{Y}_{C,ba}$ and $\mathbf{Y}_{C,da}$, respectively. The second step requires a force excitation on the passive side (b), while the resulting response is measured at the interface (c) to obtain the term $\mathbf{Y}_{C,cb}$. Note that the reciprocal relation in Eq. (3.20) reverses the path of $\mathbf{Y}_{C,ba}$, hence the measurements originate on the passive sub-structure (B). This converts the DoFs at (b) to excitation-only points, whereas the positions at (a) are used for excitation and response measurement, alike. In practice, the target DoFs (d) may function solely as response points (e.g. acceleration or sound pressure) without requiring any excitation. Even rotational DoFs at either (c) or (d) may simply be included by specific sensor array setups at the interface and/or the target location. Along with the corresponding mathematical operation (e.g. finite difference approximation [77] or virtual point transformation [78]) translational responses from standard measurement accelerometers may be transformed to account for rotations in $\mathbf{Y}_{C,da}$ and/or $\mathbf{Y}_{C,cb}^T$. As a result, this procedure enables the indirect identification of structure-borne and/or vibro-acoustic transfer functions based on applied forces without special measurement equipment, such as moment exciters or volume velocity sources.

The experimental implementation of the generalised round-trip identity is presented in Chapter 5, whereby excitations at the interface and the target DoFs (hard-to-access) are relocated to more convenient remote points. In practice, the round-trip relation requires collocated excitation and response measurements at either (b) (Eq. (3.19)) or (a) (Eq. (3.20)). For collocated measurements, excitations can be applied directly on the sensor housing in the orientation of the measurement axes or somewhere on the structure close to the sensor position. Locations (a) and (b) are reference DoFs that can be selected (e.g. at corners of the geometry) so as to facilitate such an excitation. Alternatively, the remote sensor array on one side (either (b) or (a)) needs to be temporarily removed for subsequent response and excitation measurements.

3.4.3 Application II: Improving Long Distance Transfer FRFs by Sectioned Measurements

Instead of solely focusing on inaccessible driving-point and transfer FRFs the generalised round-trip concept may be applied to the identification of long distance transfer FRFs. In this section, the generalised round-trip relation is applied to establish a relation between the ‘long’ transfer term $\mathbf{Y}_{C,ba}$ measured across assembly (C) and shorter, yet equivalent, linking transfer FRFs.

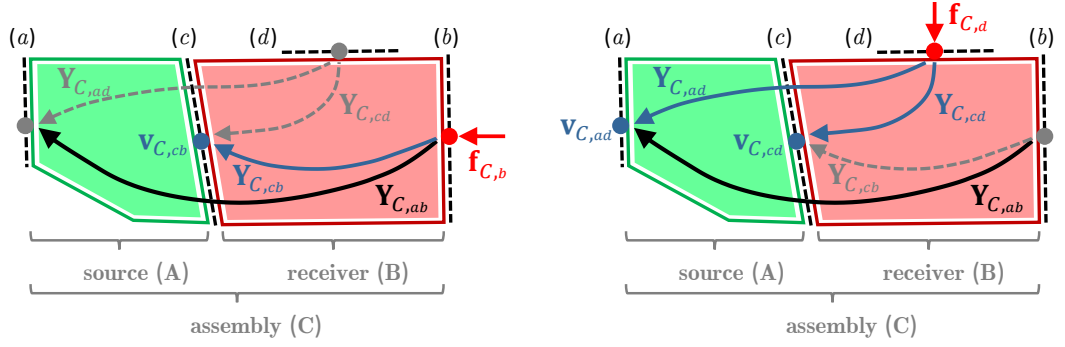
Concerning steering induced noise, experimentalists often face problems when measuring FRFs in large vehicles such as sport-utility vehicles, light-duty or even commercial trucks. Experimental errors and noise in FRF measurements due to insufficient excitation are an important reason (possibly the main reason) for unrealistic prognoses in TPA. Also, for testing of civil, marine or other heavyweight structures, the excitation energy provided by a shaker or even a sledge impact hammer² might be insufficient to achieve an acceptable signal-to-noise ratio on the response measurement. For such heavy and large structures, or other applications in which the response points are spaced too far apart from the non-located excitation (e.g. rails or pipelines), the round-trip journey in Eq. (3.15) can be re-arranged to combine shorter transfer functions to determine the long distance transfer path.

Generalised round-trip identity to reconstruct long distance FRFs:

$$\mathbf{Y}_{C,ab} = \mathbf{Y}_{C,ba}^T = \mathbf{Y}_{C,ad} \mathbf{Y}_{C,cd}^{-1} \mathbf{Y}_{C,cb} \quad (3.21)$$

In this scenario, the targeted transfer function $\mathbf{Y}_{C,ab}$ shown in Fig. 3.4 spans across the entire assembly, whereas the indirect measurement is divided into three shorter path segments, each benefiting from an improved SNR on the individual response measurements. This reciprocal measurement technique requires response measurements at (a) and (c) while external force excitations are applied in two steps at (b) and (d), with (d) now being located at accessible measurement points. An effective way to improve the SNR of the long transfer function $\mathbf{Y}_{C,ab}$ is by defining additional receiver-side excitation locations (d) halfway along the targeted path, besides using high sensitivity measurement instrumentation.

² If instrumented sledgehammers or larger shakers are used to provide more energy, the risk to cause local deformation (i.e. non-LTI system) and/or the loss of spatial discretisation due to (enormous) hammer tips or larger shaker connectors can be avoided using the proposed generalised round-trip approach.



(a) Step 1: Receiver excitations at (b) to determine $\mathbf{Y}_{C,cb}$ (like actual reciprocal measurement of $\mathbf{Y}_{C,ab}$).

(b) Step 2: Excitation at arbitrary remote positions (d) to characterise $\mathbf{Y}_{C,ad}$ and $\mathbf{Y}_{C,cd}$.

Figure 3.4: Re-arranged transfer path segments of the generalised round-trip identity to improve measurement quality of long distance transfer FRFs, $\mathbf{Y}_{C,ab} = \mathbf{Y}_{C,ad} \mathbf{Y}_{C,cd}^{-1} \mathbf{Y}_{C,cb}$ (see Eq. (3.21)), due to poor SNR or a high noise environment.

In the case that access is available to the interface DoFs (c), a similar long distance formulation can be obtained by collocating the DoFs (c) and (d),

$$\mathbf{Y}_{C,ab} = \mathbf{Y}_{C,ba}^T = \mathbf{Y}_{C,ac} \mathbf{Y}_{C,cc}^{-1} \mathbf{Y}_{C,cb}. \quad (3.22)$$

To extend this concept, the round-trip equation can be applied recursively by nesting round-trip transfer FRFs within the identity in Eq. (3.21). Conceptually, the passive sub-component (B) of the source-receiver model may be sectioned by a virtual coupling interface (e). Introducing an additional set of accessible remote DoFs (f) a recurring interface/remote DoFs layout (i.e. (c) – (d); (e) – (f)) is obtained, as depicted in Fig. 3.5.

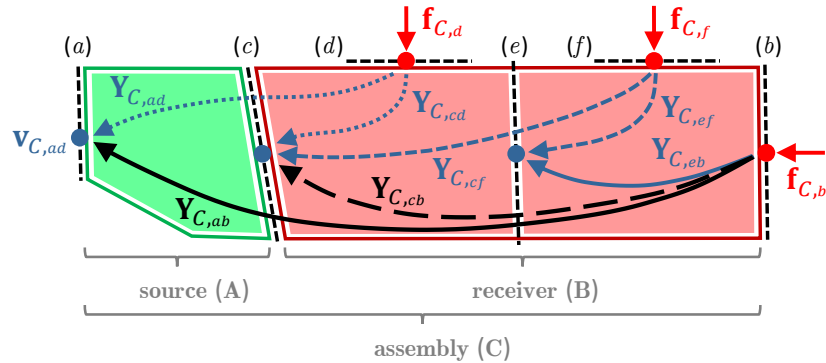


Figure 3.5: Path segments of the long distance FRF, $\mathbf{Y}_{C,ab} = \mathbf{Y}_{C,ad} \mathbf{Y}_{C,cd}^{-1} \mathbf{Y}_{C,cf} \mathbf{Y}_{C,ef}^{-1} \mathbf{Y}_{C,eb}$ (see Eq. (3.24)), using a nested generalised round-trip identity with 3 receiver-side excitation locations. The source-receiver model contains: target source DoFs (a); coupling interface (c); virtual coupling interface (e); and remote DoFs (d), (f), and (b) accessible for direct excitation.

Within the receiver sub-component (B), the separation of the coupling interface (c) and the remote DoFs (b) by the virtual interface (e) bears a resemblance to the DoF configuration of the initial assembly (compare Fig. 3.4). Recalling the composed transfer FRF concept in Eq. (3.21), the receiver-side term $\mathbf{Y}_{C,cb}$ can be expressed by three shorter path segments,

$$\mathbf{Y}_{C,cb} = \mathbf{Y}_{C,cf} \mathbf{Y}_{C,ef}^{-1} \mathbf{Y}_{C,eb} \quad (3.23)$$

which requires direct force excitation at (f) and (b). The above relation may be nested, for instance, by substituting the receiver-side term $\mathbf{Y}_{C,cb}$ into the round-trip Eq. (3.21), thus including additional FRF terms in the long distance relation,

$$\mathbf{Y}_{C,ab} = \mathbf{Y}_{C,ba}^T = \mathbf{Y}_{C,ad} \mathbf{Y}_{C,cd}^{-1} \mathbf{Y}_{C,cf} \mathbf{Y}_{C,ef}^{-1} \mathbf{Y}_{C,eb}. \quad (3.24)$$

The indirectly determined long distance transfer function $\mathbf{Y}_{C,ab}$ requires remote excitation at all 3 accessible DoF locations (d), (f), and (b). In the case that the interface DoF (c) and (e) are accessible (compare Eq. (4.22)), the collocations (c) = (d) and (e) = (f) lead to the relation,

$$\mathbf{Y}_{C,ab} = \mathbf{Y}_{C,ba}^T = \mathbf{Y}_{C,ac} \mathbf{Y}_{C,cc}^{-1} \mathbf{Y}_{C,ce} \mathbf{Y}_{C,ee}^{-1} \mathbf{Y}_{C,eb}. \quad (3.25)$$

Note that the collocated case requires the same instrumentation with accelerometers placed at (a), (c), and (e), like in the previous expression (see Eq. (3.24)), but now the external forces at (d) and (f) are relocated to the coupling interface (c) and the virtual interface (e), respectively.

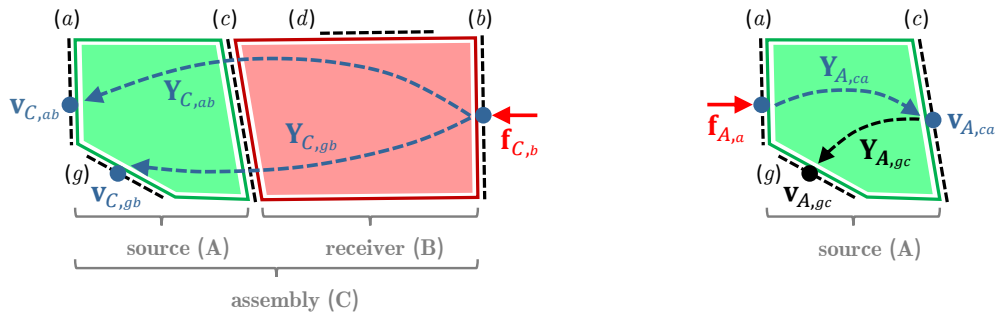
This nested extension, implemented via virtual interfaces, may prove beneficial for complex structures with extensively long path segments, as shorter FRFs typically establish a reliable phase relationship between the excitation measurement and the resulting response. This is partly due to a change in the nature of the wave propagation over long distances (e.g. standing wave to a travelling wave type), which causes the nested calculation to result in a long transfer function with a more reliable phase [21]. Positioned rather arbitrarily, multiple virtual interfaces may be considered to divide the receiver sub-component (B) in even smaller sections, thus improving the SNR and the phase relationship of the individual FRF measurements. However, the transfer segments are obtained from separate experiments, therefore, inconsistency encountered in the different experimental data may introduce errors in the predicted transfer FRFs [46].

3.5 Sub-Structure Round-Trip Identity

Next, the generalised concept is applied for the indirect characterisation of sub-structure FRFs (as opposed to assembly FRFs) following a similar approach to that of Moorhouse et al. [9].

The common problem in structural dynamics to characterise the properties of coupled structures can be projected onto the sub-components. For example, converting the free velocity into a blocked force or dynamic sub-structuring relies on a complete interface description for each sub-component, including in-plane and rotational DoFs. Therefore, indirect subsystem identification based on the round-trip identity may be used to characterise driving-point FRFs at the coupling interface, e.g. $\mathbf{Y}_{A,cc}$ or $\mathbf{Y}_{B,cc}$. Like in Sec. 3.4, the sub-structure identity presented in [9] can be generalised to include transfer FRFs between a coupling interface and arbitrary remote points.

A two-step procedure shown in Fig. 3.6 is used to determine the sub-structure properties combining measurements on the coupled assembly (C) and the uncoupled source (A). This approach assumes that the sub-structure can be reliably decoupled and suspended to obtain free-source FRFs. The structure-borne source (A) includes additional target DoFs (g) for the characterisation of the sub-component FRFs $\mathbf{Y}_{A,gc}$ between the interface (c) and (g).



(a) Step 1: Assembly measurement with excitation at (b) to determine $\mathbf{Y}_{C,ab}$ and $\mathbf{Y}_{C,gb}$.

(b) Step 2: Measurement of the resiliently suspended source (A) to determine the free mobility between DoFs at (a) and (c).

Figure 3.6: Transfer paths forming the sub-structure round-trip identity for indirect identification of $\mathbf{Y}_{A,gc} = \mathbf{Y}_{C,gb} \mathbf{Y}_{C,ab}^{-1} \mathbf{Y}_{A,ca}^T$ (see Eq. (3.32)). The two-step procedure is partly conducted on the coupled assembly (C) and the decoupled source (A).

First, consider the assembly (C) shown in Fig. 3.6a. The assembly is excited by a single force f_{C,b_i} at an arbitrary DoF (b_i) on the receiver-side. The resulting

velocity responses at source-side DoFs (a) and (g) can be expressed in terms of a contact force $\mathbf{f}_{C,c}$ acting on the interface (c) and the corresponding transfer FRFs of sub-structure (A),

$$\mathbf{v}_{C,ab_i} = \mathbf{Y}_{A,ac} \mathbf{f}_{C,c} \quad \text{for } n_a \text{ source DoFs \& one excitation } (b_i) \quad (3.26)$$

$$\mathbf{v}_{C,gb_i} = \mathbf{Y}_{A,gc} \mathbf{f}_{C,c} \quad \text{for } n_g \text{ target DoFs \& one excitation } (b_i) \quad (3.27)$$

$$\text{with } \begin{cases} \mathbf{f}_{C,c}^{(b_i)} = \{f_{C,c_1b_i}, f_{C,c_2b_i}, \dots, f_{C,c_{n_c}b_i}\}^T \\ \mathbf{v}_{C,ab_i} = \{v_{C,a_1b_i}, v_{C,a_2b_i}, \dots, v_{C,a_{n_a}b_i}\}^T \\ \mathbf{v}_{C,gb_i} = \{v_{C,g_1b_i}, v_{C,g_2b_i}, \dots, v_{C,g_{n_g}b_i}\}^T. \end{cases}$$

Applying further excitations at other locations in (b) and arranging the force and velocity vectors into matrices yields the matrix equation,

$$\mathbf{V}_{C,ab} = \mathbf{Y}_{A,ac} \mathbf{F}_{C,c} \quad \text{for } n_a \text{ source DoFs \& } n_b \text{ receiver excitations} \quad (3.28)$$

$$\mathbf{V}_{C,gb} = \mathbf{Y}_{A,gc} \mathbf{F}_{C,c} \quad \text{for } n_g \text{ target DoFs \& } n_b \text{ receiver excitations.} \quad (3.29)$$

Assuming the inverse of the sub-structure FRF matrices exist, Eqs. (3.28) and (3.29) can be pre-multiplied by $\mathbf{Y}_{A,ac}^{-1}$ and $\mathbf{Y}_{A,gc}^{-1}$, respectively. Equating both matrix expressions yields the following relation,

$$\mathbf{Y}_{A,gc}^{-1} \mathbf{V}_{C,gb} = \mathbf{F}_{C,c} = \mathbf{Y}_{A,ac}^{-1} \mathbf{V}_{C,ab} \quad (3.30)$$

whilst eliminating the interface force matrix $\mathbf{F}_{C,c}$. Since the artificial excitations applied at (b) are arbitrary, they can be considered unit forces. In this case, the velocity matrices are effectively mobility matrices of the coupled structure (C), e.g. $\mathbf{V}_{C,gb} \rightarrow \mathbf{Y}_{C,gb}$. A practical round-trip expression for the separated source (A) can be rewritten as,

Sub-structure round-trip identity for source (A):

$$\mathbf{Y}_{A,cg} = \mathbf{Y}_{A,ca} \mathbf{Y}_{C,ab}^{-T} \mathbf{Y}_{C,gb}^T \quad (3.31)$$

or by reciprocity,

$$\mathbf{Y}_{A,gc} = \mathbf{Y}_{A,cg}^T = \mathbf{Y}_{C,gb} \mathbf{Y}_{C,ab}^{-1} \mathbf{Y}_{A,ca}^T. \quad (3.32)$$

For the source (A), the sub-structure round-trip identity is obtained in two steps: 1) artificial force excitation at receiver-side DoFs (b) on the assembly (C) to determine

$\mathbf{Y}_{C,ab}^{-T}$ and $\mathbf{Y}_{C,gb}^T$ and 2) after separating, the resiliently suspended source (A) is excited at (a) to measure $\mathbf{Y}_{A,ca}$. For collocated response DoFs at (c) and (g), such that (c) = (g), the original form of the sub-structure round trip identity as given in [9] is obtained,

$$\mathbf{Y}_{A,cc} = \mathbf{Y}_{A,ca} \mathbf{Y}_{C,ab}^{-T} \mathbf{Y}_{C,cb}^T. \quad (3.33)$$

This sub-structure round-trip identity may be used for frequency based sub-structuring [65] or to transform the free velocity into a blocked force. In [9] Moorhouse et al. proposed an extension of the free velocity by incorporating Eq. (3.33) to determine the free velocity from operational measurements conducted in-situ, and therefore under representative mounting condition. In the free velocity - blocked force relation (compare Eq. (2.12)), the so-called free mobility $\mathbf{Y}_{A,cc}$ is substituted by the round-trip identity in Eq. (3.33). This leads to an equivalent free velocity characterisation,

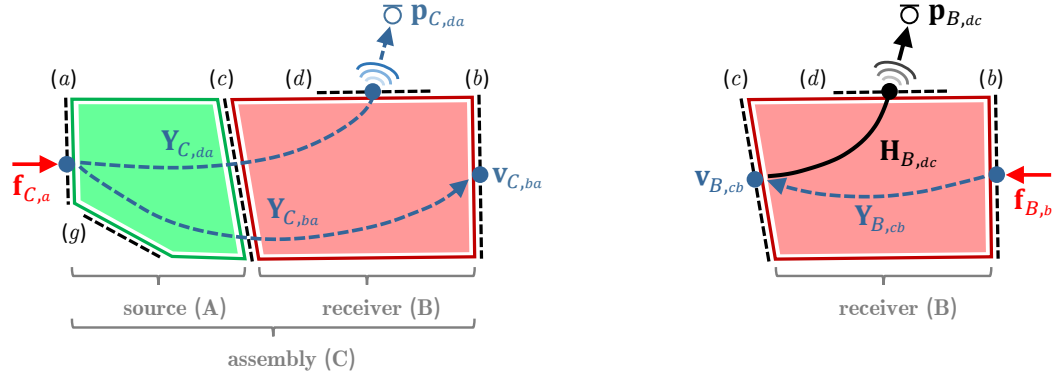
$$\hat{\mathbf{v}}_{A,ca} = \mathbf{Y}_{A,cc} \bar{\mathbf{f}}_{A,c} \quad \text{free velocity - blocked force relation} \quad (3.34)$$

$$\hat{\mathbf{v}}_{A,ca} = \mathbf{Y}_{A,ca} \mathbf{Y}_{C,ab}^{-T} \mathbf{v}_{C,ba} \quad (3.35)$$

$$\text{with} \quad \bar{\mathbf{f}}_{A,c} = \mathbf{Y}_{C,bc}^{-1} \mathbf{v}_{C,ba}$$

where operational tests $\mathbf{v}_{C,ba}$ are performed in the coupled state. In practice, the free velocity can be obtained from operational measurement with the source normally installed (e.g. any test bench), together with FRFs of the coupled structure and the source. This enables free velocity measurements of many machines and components running under load, as opposed to the restrictions by ISO 9611 [60]. Note that FRF matrices in Eq. (3.35) are obtained from measurements on different structures in separate experiments, therefore, inconsistency encountered in the different experimental data may introduce errors (e.g. resonant artefacts) in the free velocities [46, 107]. A detailed discussion of the concept in Eq. (3.35) is presented in [9].

The novel sub-structure relations in Eqs. (3.31) and (3.32) can also be formulated for the passive side. By simply reversing the sub-structures, a similar derivation is obtained for the receiver (B). Fig. 3.7 shows a systematic overview of the two separate measurement steps, now obtained from the assembly (C) and the decoupled receiver sub-structure (B). In this example, the target response DoFs are defined at a receiver-side location (d) represented by a microphone.



(a) Step 1: Assembly measurement with excitation at (a) to determine FRFs to the receiver-side DoFs (b) and (d).

(b) Step 2: Measurement of the resiliently suspended receiver (B) to determine the free transfer FRFs between (b) and (c).

Figure 3.7: Transfer paths forming the sub-structure round-trip identity for indirect identification of $\mathbf{Y}_{B,dc} = \mathbf{Y}_{C,da} \mathbf{Y}_{C,ba}^{-1} \mathbf{Y}_{B,cb}^T$ (see Eq. (3.40)). For generality, the target sound pressure probe (d) may be replaced by an accelerometer.

The responses are recorded at receiver-side DoFs (b) and (d) due to a force excitation at a source-side DoF (a_i). Mathematically, the structural responses of the assembly (C) are expressed in terms of the interface forces $\mathbf{f}_{C,c}$ and the transfer mobilities of sub-structure (B) via the relation,

$$\mathbf{v}_{C,ba_i} = \mathbf{Y}_{B,bc} \mathbf{f}_{C,c} \quad \text{for } n_b \text{ remote DoFs \& one excitation } (a_i) \quad (3.36)$$

$$\mathbf{v}_{C,da_i} = \mathbf{Y}_{B,dc} \mathbf{f}_{C,c} \quad \text{for } n_d \text{ target DoFs \& one excitation } (a_i) \quad (3.37)$$

$$\text{with } \begin{cases} \mathbf{f}_{C,c}^{(a_i)} = \{f_{C,c_1 a_i}, f_{C,c_2 a_i}, \dots, f_{C,c_{n_c} a_i}\}^T \\ \mathbf{v}_{C,ba_i} = \{v_{C,b_1 a_i}, v_{C,b_2 a_i}, \dots, v_{C,b_{n_b} a_i}\}^T \\ \mathbf{v}_{C,da_i} = \{v_{C,d_1 a_i}, v_{C,d_2 a_i}, \dots, v_{C,d_{n_d} a_i}\}^T. \end{cases}$$

The above expressions are equivalent to Eqs. (3.26) and (3.27) of the source sub-component procedure. Following the same steps (compare Eqs. (3.28) and (3.29)) with multiple force excitations at (a), the interface contact force matrix $\mathbf{F}_{C,c}$ may be eliminated to establish the following relation,

$$\mathbf{Y}_{B,bc}^{-1} \mathbf{V}_{C,ba} = \mathbf{F}_{C,c} = \mathbf{Y}_{B,dc}^{-1} \mathbf{V}_{C,da}. \quad (3.38)$$

Normalised to the input force (i.e. unit force excitation) allows rewriting the velocity expressions $\mathbf{V}_{C,ba}$ and $\mathbf{V}_{C,da}$ as mobility matrices. Thus, we arrive at an equivalent sub-structure round-trip identity for the receiver,

Sub-structure round-trip identity for receiver (B):

$$\mathbf{Y}_{B,cd} = \mathbf{Y}_{B,cb} \mathbf{Y}_{C,ba}^{-T} \mathbf{Y}_{C,da}^T \quad (3.39)$$

or by reciprocity,

$$\mathbf{Y}_{B,dc} = \mathbf{Y}_{B,cd}^T = \mathbf{Y}_{C,da} \mathbf{Y}_{C,ba}^{-1} \mathbf{Y}_{B,cb}^T. \quad (3.40)$$

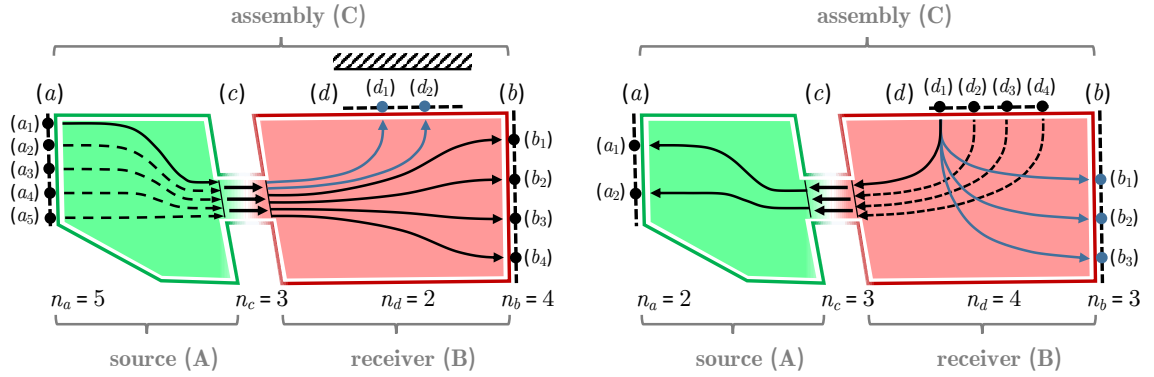
A practical application for indirect receiver identification can be seen in classical TPA (see Sec. 2.5.2), particularly matrix-inverse methods, where receiver FRFs are used to reconstruct the interface loads or identify partial path contributions. These FRFs are typically measured on the passive subsystem (B), which requires the source component (A) to be dismantled. Nevertheless, the required FRFs may be partially inaccessible due to surrounding machinery, e.g. in an engine compartment. Consequently, the round-trip identity in Eqs. (3.39) and (3.40) can be employed to relocate excitations to other (easy-to-access) remote DoFs (*a*) and (*b*). As such, vibro-acoustic sub-component FRFs can be determined without excitation at the interface or the need for a volume velocity source, e.g. vehicle FRFs from the motor mounts to the driver's ears.

3.6 Controllability and Observability of the Round-Trip Relations

In practice, multi-contact assemblies often include translational and rotational coupling at interface (*c*). The question then arises as to how many remote DoFs at (*a*), (*b*) and (*d*) (for long distance applications) are required to sufficiently perform the round-trip identity for the MIMO case. The following explanation considers the generalised round-trip identity, however, it equally applies to the single and dual interface round-trip relation.

A requirement is defined by control theory [108], more specifically by the concepts of observability and controllability. Considering $\mathbf{Y}_{C,ba}$ of the inaccessible round-trip scenario (see Eq. (3.19)), the mutually independent force inputs at (*a*) are channelled through n_c DoFs at interface (*c*) and transmitted to DoFs (*b*) and (*d*) on the passive-side (see Fig. 3.8a). For $\mathbf{Y}_{C,ba}$ to be full rank and therefore invertible, the n_a source-side excitations (a_1, a_2, \dots, a_{n_a}) must each be applied in a different direction and position to ensure that all independent vibration modes at the interface (*c*) are

excited. Controllability requires $n_a \geq n_c$ to obtain a sufficient contribution through all coupling DoFs (n_c) from external excitations (n_a).



(a) Propagation model for inaccessible transfer functions $\mathbf{Y}_{C,dc}$.

(b) Propagation model for long distance transfer functions $\mathbf{Y}_{C,ab}$.

Figure 3.8: Concept of controllability and observability effectively limiting the independent modes of vibration transmitted across the interface (bottleneck effect).

The notion of controllability can be understood by considering the contact forces present at interface (c) when excitations $\mathbf{F}_{C,a}$ are applied. Eq. (3.7) can be rewritten for the separated receiver sub-component (B) using the receiver mobility matrix $\mathbf{Y}_{B,bc}$ and the contact force matrix $\mathbf{F}_{B,c}$ applied at (c) [10],

$$\mathbf{V}_{C,ba} = \mathbf{Y}_{B,bc} \mathbf{F}_{B,c} \quad \text{with} \quad \mathbf{F}_{B,c} = (\mathbf{Y}_{A,cc} + \mathbf{Y}_{B,cc})^{-1} \mathbf{Y}_{A,ca} \mathbf{F}_{A,a}. \quad (3.41)$$

Note that the above subsystem expression considers excitations applied on the source sub-component, $\mathbf{F}_{A,a}$, hence the subscript of the excitation matrix $\mathbf{F}_{C,a}$ is replaced by 'A'. On the passive-side, the transmitted vibrations from independent external excitations (n_a in $\mathbf{F}_{A,a}$) are effectively limited by the number of interface/ contact forces (n_c in $\mathbf{F}_{B,c}$). The interface reduces the independent response cases observed at (b) and, therefore, the effective rank of the mobility matrix $\mathbf{Y}_{C,ba}$ to a maximum of n_c . This constraint imposed by the coupling interface is regarded as a bottleneck effect [10]. The effect of the source excitation is observed on the receiving side by n_b remote DoFs at (b). Whilst this may place further restrictions on the rank of $\mathbf{Y}_{C,ba}$, the observability condition requires $n_b \geq n_c$ to capture the entire set of interface dynamics of $\mathbf{F}_{B,c}$.

Assuming the external excitations at the source-side DoFs (a) are mutually independent, it is best practice to define $n_a \geq n_b$. Theoretically, the rank n_r of the over-determined matrix $\mathbf{Y}_{C,ba}$ is limited by the number of linear independent responses n_b

(rows of $\mathbf{Y}_{C,ba}$). Linear dependencies, resulting in a rank deficient matrix ($n_r < n_b$), indicate either that the assembly is identified to contain $n_c = n_r = \text{rank}(\mathbf{Y}_{C,ba})$ DoFs with the bottleneck effect actively restricting the number of independent excitations passing through the interface (c), or the inability of the source-side excitation n_a to excite all interface DoFs n_c (insufficient controllability). To determine which of these possibilities is the case in a given situation, the effective rank can be analysed using a singular value decomposition (SVD). Additional source-side excitations can be applied using an instrumented hammer to see if the number of significant singular values increases, which indicates insufficient controllability. Hence, additional excitations n_a (columns of $\mathbf{Y}_{C,ba}$) are required to establish sufficient controllability of $\mathbf{Y}_{C,ba}$ [10]. Similar considerations apply for a test of full observability. Additional remote sensors at (b) can be added, which will, in theory, improve the observability of the interface. If the number of significant singular values in $\mathbf{Y}_{C,ba}$ increases during the process, it is a good indicator that additional remote sensors are required for full observability.

Consequently, full controllability and observability requires the round-trip identity in Eq. (3.19) to meet the condition $n_a \geq n_b \geq n_c$, whereas the reversed reciprocal relation in Eq. (3.20) must satisfy $n_b \geq n_a \geq n_c$. Both versions consider additional DoF at either (a) and/or (b), in other words, n_a may differ from n_b . For the non-square mobility matrix $\mathbf{Y}_{C,ba}$, the standard matrix inverse is then replaced by the Moore-Penrose pseudo inverse [23]. These conditions are independent of the number n_d of target DoFs (d), which are defined as points requiring controlled interface dynamics $n_a \geq n_c$ (or by reciprocity: $n_b \geq n_c$) but are not essential for the observation of the interface dynamics. It is highlighted that despite the reference to and the restrictions by the number of coupling DoFs (n_c), no explicit information is required about the interface DoFs. The bottleneck constraint, imposed by the coupling condition, is independent of the sensor instrumentation at (c). Certain coupling DoFs (e.g. rotational DoF) may be neglected completely in the accelerometer setup at (c) without changing the result of the predicted inaccessible transfer FRFs [63].

Similar considerations of controllability and observability are adopted for the concept of long distance transfer FRFs (see Eq. (3.21)), shown in Fig. 3.8a. Considering the inverse matrix $\mathbf{Y}_{C,cd}$, mutually independent excitations at (d) are observed at the interface DoFs (c). The same interface response $\mathbf{V}_{C,cd}$ can be expressed by a set of

interface contact loads $\mathbf{F}_{A,c}$ applied to the source sub-component (A),

$$\mathbf{V}_{C,cd} = \mathbf{Y}_{A,cc} \mathbf{F}_{A,c} \quad \text{with} \quad \mathbf{F}_{A,c} = (\mathbf{Y}_{B,cc} + \mathbf{Y}_{A,cc})^{-1} \mathbf{Y}_{B,cd} \mathbf{F}_{B,d}. \quad (3.42)$$

Note that in the subsystem relation above, the force $\mathbf{F}_{C,d}$ is applied to the separated receiver structure (B), thus denoted by $\mathbf{F}_{B,d}$. The external excitations (n_d in $\mathbf{F}_{B,d}$) requires $n_d \geq n_c$ to fully control the interface dynamics (n_c in $\mathbf{F}_{A,c}$), else $\mathbf{Y}_{C,cd}$ will be rank deficient and non-invertible. Limiting the number of independent vibration modes, the responses are observed at the interface itself, restricting the possibility to improve observability. At the same time, the instrumentation must include all coupling DoFs through which physical coupling occurs, which may include in-plane and rotational DoFs. For the collocated case (see Eq.(4.22)), the transfer FRFs $\mathbf{Y}_{C,cd}$ reduces to a square symmetric matrix $\mathbf{Y}_{C,cc}$, thus requiring response and excitation measurements at all coupling DoFs. For completeness, similar considerations apply to virtual interfaces of the nested extension, for instance $\mathbf{Y}_{C,ef}$ and $\mathbf{Y}_{C,ee}$ in Eqs. (3.24) and (3.25), respectively, as every interface may be associated with a virtual bottleneck effect. In contrast, the nature of external forces at (b) together with response measurement at (a) do not control or observe the interface dynamics and thus may be correctly placed at the targeted locations of the long distance transfer function.

Lastly, the concept of control theory also applies to the sub-structure round-trip identity. To fully control and observe the interface dynamics during the assembly measurements, the sub-structure round-trip identity in Eqs. (3.31) and (3.32) requires $n_b \geq n_a \geq n_c$. In contrast, the reversed case for the receiver sub-structure in Eqs. (3.39) and (3.40) must satisfy $n_a \geq n_b \geq n_c$. Here, external excitations applied at a remote location pass through the interface (bottleneck) and are observed by the remote sensor array on the other side of the interface. After dismantling the assembly, measurements are performed on the corresponding sub-structure at the former source-receiver interface, i.e. $\mathbf{Y}_{A,ca}$ and $\mathbf{Y}_{B,cd}$. It is interesting to note that no explicit information of the interface is required, i.e. the sub-structure round-trip identity provides correct FRF results for an incomplete interface description. The sensor array at (c) simply defines which transfer mobilities are computed, hence, only the interface DoFs of interest (e.g. translations) need to be instrumented.

3.7 Summary and Concluding Remarks

This chapter has been concerned with the indirect characterisation of structural and/or vibro-acoustic frequency response functions, using ideal excitations from instrumented hammers or shakers. The presented framework reviewed the concept of round-trip identity typically categorised according to their interface characteristics: single interface- [63], dual- [25], and sub-structure [9] relation. A fourth generalised round-trip expression for coupled systems has been introduced in Sec.3.4 to include transfer FRFs between a coupling interface and arbitrary remote points (d). Applications include identifying FRFs whose excitation and response positions are inaccessible for direct measurement and improving the measurement quality of long distance transfer functions. Therefore, the presented round-trip methods can readily be implemented to avoid these practical challenges commonly encountered in TPA measurements for a more reliable and thorough analysis.

Practical guidelines have been provided based on control theory for MIMO systems and notions of controllability and observability for transmitted vibrations restricted by the interface's bottleneck effect (active-passive). For collocated locations of (c) and (d), such that (c) = (d), the generalised round-trip formulates a driving-point matrix relation, which is in exact agreement with the single interface round-trip identity [9]. The target DoF (d) may also be interpreted as a second virtual interface. Hence the proposed 'generalised expression' combines both special cases of the single and dual interface round-trip scenario [105] and, furthermore, allows for a determination of passive properties for the complete assembly downstream the source.

It is noted that the round-trip formulation, alongside the proposed generalisation, are based on the assumptions of linearity, time-invariance and that the interface can be described by a finite number of terms (i.e. in matrix form) [63]. Unlike alternative methods, the generalised round-trip applies to any complex built-up structure and, since no assumptions have been introduced, hypothetically reconstructs exact FRFs from experimental tests. In the search for an alternative approach, System Equivalent Model Mixing (SEMM) adopts the concept of frequency based sub-structuring to create a hybrid model for describing inaccessible and/or long distance transfer FRFs [109–111]. SEMM couples the dynamics of a measurement-based overlay model to the DoF-structure of an equivalent, yet not identical, parent model (e.g. full numerical models, analytical methods or detailed experimental DoF-models from a

demonstrator study) [112]. Although SEMM can determine the structural dynamic properties at DoFs other than the ones measured, the hybrid model requires some digital twin of the assembled structures while assuming shared boundary DoFs between the models. While the aims of SEMM may be similar to those of the round-trip approach, they are fundamentally different concepts in that the former requires a model to reconstruct FRFs, whereas the latter achieves this solely from experimental data. It is therefore argued that the experimental round-trip approach offers significant advantages in terms of convenience, representativeness as well as consistency and/or compatibility of the involved system model.

4

Operational System Identification and Concept of FastTPA

The previous framework considered the indirect determination of structural dynamic properties using external excitations. In the following chapter, this concept is further extended for operational system identification by incorporating experimental techniques, including; the generalised transmissibility concept, the blocked force relation and a controlled excitation from an embedded vibration generating source mechanism. These methods will be used in conjunction with control theory principles to propose a fastTPA procedure in which any sufficiently controllable structure-borne sound source can be turned into a calibrated MIMO blocked force exciter. When operated in an assembly, this calibrated exciter can then be used to simultaneously measure all transfer paths between the exciters coupling DoFs and arbitrary target DoFs, including translational and rotational contributions. Due to the significant time-saving during the system identification step while exploiting the invariance of the blocked force (obtained in a calibration step), the proposed method is referred to as ‘fastTPA’.

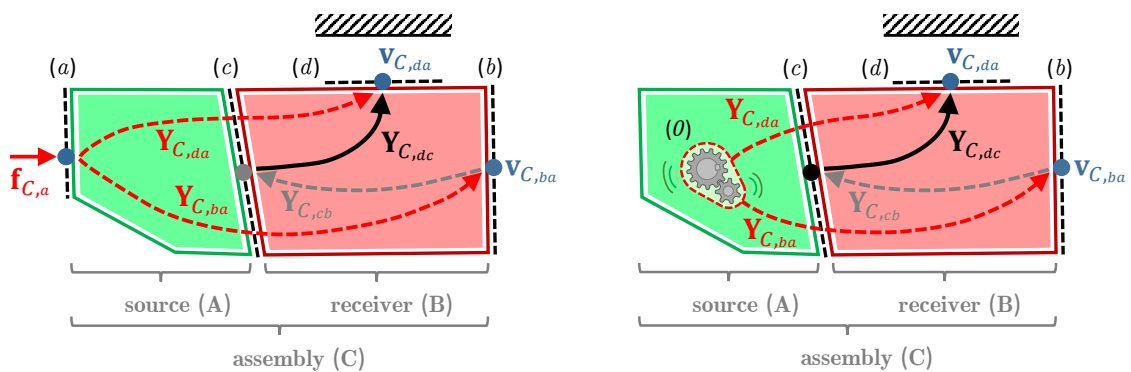
Chapter contents:

4.1	Introduction to the Transmissibility Concept	79
4.2	Round-Trip System Identification Using Operational Transmissibilities	86
4.3	Two-Stage MIMO System Identification Using a Controlled Blocked Force Exciter	93
4.4	Summary and Concluding Remarks	110

4.1 Introduction to the Transmissibility Concept

The previously discussed indirect system identification methods have in common that three alternative FRFs are determined using ideal excitations applied to remote DoFs on the source and receiver sub-structure. Consequently, the framework presented in Chapter 3 requires a known force input applied with an instrumented hammer or shaker. Whilst the generalised round-trip identity presents an alternative to conventional FRF measurements involved in TPA, further simplifications may be achieved by utilising the transmissibility concept with the objective to substitute the externally applied excitation by the source's embedded source mechanisms.

For example, the generalised round-trip relation in Eq. (3.15) requires source-side excitation at some DoF (a), depicted in Fig. 4.1a. A transmissibility term $\mathbf{T}_{C,db}^{(a)} = \mathbf{Y}_{C,da} \mathbf{Y}_{C,ba}^+$ is formed by the product of the first two FRF terms on the right-hand side of the round-trip formulations, as highlighted in Eq. (3.9). Therefore, the FRF paths (highlighted in red in Fig. 4.1a) can be replaced by generalised transmissibility terms, which can be obtained from source-side excitations using a set of unknown operational, internal or external forces. Consequently, an embedded vibration generating mechanism (θ) is considered in the source-receiver model¹ shown in Fig. 4.1b, as opposed to the purely passive source structures in Chapter 3.



(a) Generalised round-trip identity (step 1) requiring ideal source-side excitation with a known force at (a).

(b) Simplified system identification using unknown forces generated via the internal source mechanism (θ) of sub-structure (A).

Figure 4.1: Transfer paths forming the generalised round-trip identity via ideal excitations or operational forces generated by an embedded source. The generalised transmissibility term may replace the highlighted paths requiring ideal remote excitation.

¹ Strictly speaking, Fig. 4.1a shows the transfer path $\mathbf{Y}_{C,ba}$ and $\mathbf{Y}_{C,da}$, whilst Fig. 4.1b visualises $\mathbf{Y}_{C,b\theta}$ and $\mathbf{Y}_{C,d\theta}$, respectively (although the same subscripts are used in the drawing). The targeted round-trip FRF, $\mathbf{Y}_{C,dc}$, however, will remain the same independent of whether external excitations are applied at (a) or operational excitations are acting at internal DoFs (θ).

Replacing the transfer FRFs measurements with the generalised transmissibility terms offers a number of potential advantages.

- ▶ If access to source-side remote points (a) is restricted, excitation from unknown operational forces or naturally occurring sources can simplify the experimental procedure. In this case, a part of the data is obtained under operational conditions, requiring less time and experimental effort than conventional FRF testing.
- ▶ Implementation of the generalised round-trip identity relies on a sufficient phase relationship, typically indicated by good coherence between excitation and response signals. If the nearest accessible FRF excitation position (a) is located too distant from the remote points, an implementation may prove difficult due to uncorrelated phase relations between the excitation and the responses at (d) and (b). Hence, there is a need for alternative excitation concepts.
- ▶ Experimental uncertainty associated with conventional FRF testing is reduced, e.g. the need for repeatable coherent excitation or errors associated with excitation inaccuracy. In theory, the transmissibility can be obtained from external forces applied by a non-instrumented hammer to avoid an insufficient SNR or excitation of a narrow frequency range.

This chapter considers the case where ideal excitations are replaced by unknown internal or external excitations, generalised as ‘operational force’ to provide source-side excitations. The following sections will focus on the transmissibility concept and its incorporation within the generalised round-trip identity.

4.1.1 Transmissibility Concept for Single-DoF Systems

The classic transmissibility concept for a single-degree of freedom systems (e.g. conventional mass-spring model) is defined as the ratio between a response DoF and a second reference response [106, 113]. Mathematically, this ratio may be calculated from a set of two FRFs, Y_{ik} and Y_{lk} , with a shared force input. Let us assume a force is applied at a positional-DoF k ; according to the standard notation, the

transmissibility element $T_{il}^{(k)}$ is defined as,

$$T_{il}^{(k)} = \frac{Y_{ik}}{Y_{lk}} = \frac{v_i}{v_l} = \frac{N_{ik}}{N_{lk}} \quad (4.1)$$

$$H_{ik} = \sum_{r=1}^{n_m} \left(\frac{\phi_{ir} L_{kr}}{s - \lambda_r} + \frac{\phi_{ir}^* L_{kr}^*}{s - \lambda_r^*} \right) \triangleq \frac{N_{ik}}{D} \quad (4.2)$$

relating the i -th to the l -th response DoF. In Eq. (4.1), both FRFs share a common excitation f_k that cancels in the fraction; thus, no assumption about this force's nature is required. Therefore, the transmissibility expression may be reduced to a relation of system responses v_i and v_l (also acceleration or displacement responses), assuming that the unknown force is sufficiently contributing to both concerned responses. More insight into the transmissibility characteristics can be gained from the pole-zero representation of the transfer functions H_{ik} , specified in Eq. (4.2) [114, 115]. Note that n_m denotes the number of modes; whereas the modal parameters λ , ϕ and L are, respectively, the pole, mode shape and modal participation factor of mode r . For simplicity, we consider a numerator N_{ik} and a common denominator D term, i.e. $H_{ik} = N_{ik}/D$ and $H_{lk} = N_{lk}/D$. As such, the expanded numerator polynomial N_{ik} represents zeros of the specific transfer function, while the denominator term D contains the system poles defined by polynomial roots. Thus, the common denominator polynomial describes common system properties (e.g. natural frequencies), whilst the expanded numerator polynomial is specific to the location of the DoFs and thus to each transfer function. Note that in a pole-zero representation, the common-denominator polynomial D disappears by taking the transmissibility ratio of two FRFs. The nominator ratio N_{ik}/N_{lk} implies properties of the classic transmissibility concept:

- ▶ Peaks in the transmissibility function do not coincide with the system's resonance frequencies (i.e. peaks in the magnitude of the transfer FRFs) [115]. At a system's resonance frequency, the transmissibility actually represents the ratio between the modal amplitudes between the two DoFs [8].
- ▶ For a single force excitation, the transmissibility only depends on the location of the force, but not on the amplitude of the force signal nor its nature [116].
- ▶ Defined for a single-DoF system as the ratio of velocities (also mobilities or forces [117, 118]), the transmissibility provides a clear identification of amplification and attenuation regions.

The classical transmissibility formulation in Eq. (4.1) describes the trivial case for single-DoF systems, however, practical applications are often associated with more complex multi-DoF systems. Instead, Ribeiro et al. [106] proposed a generalisation of the transmissibility concept extended for complex multi-DoF structures. In what follows, the generalised transmissibility for the source-receiver model presented in Fig. 4.1b will be introduced. The mobility relation (transmissibility) of the generalised round-trip identity is then replaced by equivalent velocity terms for operational system identification.

4.1.2 Generalised Transmissibility for Multi-DoF Systems

In this section, the generalised transmissibility concept is outlined, alongside its properties for multi-DoF systems.

First, consider the dynamic assembly (C) as illustrated in Fig. 4.1b. For an unknown excitation, e.g. from an internal source mechanism (θ), the applied load vector $\dot{\mathbf{f}}_{C,a}$ may contain translational force and rotational moment excitations. For brevity, the unknown operational excitation is denoted by the subscript ‘ a ’, instead of ‘ θ ’. It is assumed that for all these excitation DoFs, a complete set of FRFs is provided from measurements or analytical and numerical computation. For a single operational force vector, the resulting velocities at the remote locations (b) and (d) are given by,

$$\dot{\mathbf{v}}_{C,ba} = \mathbf{Y}_{C,ba} \dot{\mathbf{f}}_{C,a} \quad \text{for } n_b \text{ receiver DoFs \& operational excitation} \quad (4.3)$$

$$\dot{\mathbf{v}}_{C,da} = \mathbf{Y}_{C,da} \dot{\mathbf{f}}_{C,a} \quad \text{for } n_d \text{ target DoFs \& operational excitation} \quad (4.4)$$

$$\text{with } \dot{\mathbf{f}}_{C,a}^{(\theta_i)} = \{ \dot{f}_{C,a_1\theta_i}, \dot{f}_{C,a_2\theta_i}, \dots, \dot{f}_{C,a_{n_a}\theta_i} \}^T$$

where ‘ $\dot{}$ ’ indicates an operational quantity. Next, both sides of Eq. (4.3) can be pre-multiplied by the inverse of the mobility matrix $\mathbf{Y}_{C,ba}$. Subsequent substitution into Eq. (4.4), whilst eliminating $\dot{\mathbf{f}}_{C,a}$, allows the following relation to be established,

$$\dot{\mathbf{v}}_{C,da} = \mathbf{Y}_{C,da} \mathbf{Y}_{C,ba}^+ \dot{\mathbf{v}}_{C,ba}. \quad (4.5)$$

Eq. (4.5) relates the operational system response at remote DoFs (b) to the target DoFs (d) due to the active source with internal forces acting at (a). The relation formed by the term $\mathbf{Y}_{C,da} \mathbf{Y}_{C,ba}^+$ may be considered a generalised transmissibility

matrix $\mathbf{T}_{C,db}^{(a)}$ [106]. Eq. (4.5) can be rewritten as,

$$\hat{\mathbf{v}}_{C,da} = \mathbf{T}_{C,db}^{(a)} \hat{\mathbf{v}}_{C,ba} \quad \text{with} \quad \mathbf{T}_{C,db}^{(a)} = \mathbf{Y}_{C,da} \mathbf{Y}_{C,ba}^+. \quad (4.6)$$

In other words, the transmissibility matrix relates the velocity response between two positional sets of DoFs on the passive receiver, i.e. $\hat{\mathbf{v}}_{C,ba} \rightarrow \hat{\mathbf{v}}_{C,da}$ [119, 120]. Thus, the size of the obtained transmissibility matrix becomes $n_d \times n_b$, obfuscating the number n_a of shared source-side excitations (columns of the FRF matrices) in the original transfer FRF terms. These excitations, denoted by the superscript '(a)', are implicitly included in the transmissibility formulation. A more detailed insight into the transmissibility relation can be obtained by re-writing Eqs. (4.3) and (4.4) in terms of the subsystem FRFs as,

$$\begin{bmatrix} \hat{\mathbf{v}}_{C,ba} \\ \hat{\mathbf{v}}_{C,da} \end{bmatrix} = \underbrace{\begin{bmatrix} \mathbf{Y}_{B,bc} \\ \mathbf{Y}_{B,dc} \end{bmatrix} [\mathbf{Y}_{A,cc} + \mathbf{Y}_{B,cc}]^{-1} \mathbf{Y}_{A,ca}}_{\begin{bmatrix} \mathbf{Y}_{C,ba} \\ \mathbf{Y}_{C,da} \end{bmatrix}} \hat{\mathbf{f}}_{A,a} \quad (4.7)$$

where the equations are considered in a partitioned matrix form. The transfer functions $\mathbf{Y}_{C,ba}$ and $\mathbf{Y}_{C,da}$ are expressed in terms of the individual subsystems, i.e. using sub-component FRF matrices of the source (A) and receiver (B). Therefore, the operational excitation of the assembly $\hat{\mathbf{f}}_{C,a}$ (compare Eqs. (4.3) and (4.4)) is now applied to the source sub-component (A), hence denoted by $\hat{\mathbf{f}}_{A,a}$. A derivation of the above expansion is presented in [10], based on the conditions of force equilibrium and compatibility at the interface.

The velocity responses in Eq. (4.7) may be expressed in terms of free velocity $\hat{\mathbf{v}}_{A,ca}$ or, alternatively, a contact force $\hat{\mathbf{f}}_{B,c}$ applied to the receiver sub-component. Hence, the following substitutions can be made on the right-hand side of Eq. (4.7),

$$\begin{bmatrix} \hat{\mathbf{v}}_{C,ba} \\ \hat{\mathbf{v}}_{C,da} \end{bmatrix} = \begin{bmatrix} \mathbf{Y}_{B,bc} \\ \mathbf{Y}_{B,dc} \end{bmatrix} [\mathbf{Y}_{A,cc} + \mathbf{Y}_{B,cc}]^{-1} \hat{\mathbf{v}}_{A,ca} \quad (4.8)$$

$$= \begin{bmatrix} \mathbf{Y}_{B,bc} \\ \mathbf{Y}_{B,dc} \end{bmatrix} \hat{\mathbf{f}}_{B,c} \quad (4.9)$$

$$\text{with} \begin{cases} \hat{\mathbf{v}}_{A,ca} = \mathbf{Y}_{A,ca} \hat{\mathbf{f}}_{A,a} \\ \hat{\mathbf{f}}_{B,c} = [\mathbf{Y}_{A,cc} + \mathbf{Y}_{B,cc}]^{-1} \mathbf{Y}_{A,ca} \hat{\mathbf{f}}_{A,a} \end{cases}$$

The expansion in Eq. (4.7) concerns the propagation of vibrations from an operational excitation at (*a*) onto the remote DoFs (*b*) and (*d*) on the passive side. As demonstrated in Eqs. (4.7) - (4.9), the operational excitation $\hat{\mathbf{f}}_{A,a}$ (or $\hat{\mathbf{f}}_{C,a}$ considering the notation for the coupled assembly) can be represented by a free velocity vector $\hat{\mathbf{v}}_{A,ca}$, or an operational interface force $\hat{\mathbf{f}}_{B,c}$. The three equivalent formulations are interchangeable and contain the same information about the operational condition of the source; hence they produce the same structural response on the receiver-side.

It is interesting to note that the three subsystem expansions are identical up to the propagating FRF terms $[\mathbf{Y}_{B,bc} | \mathbf{Y}_{B,dc}]^T$, which describe the propagation in (B) [10, 37]. In the context of the transmissibility ‘ratio’ between the velocities $\hat{\mathbf{v}}_{C,da}$ and $\hat{\mathbf{v}}_{C,ba}$, identical terms in Eqs. (4.7) - (4.9) cancel. For example, it can be seen in Eq. (4.9) that the interface force vector $\hat{\mathbf{f}}_{B,c}$ is identical for the operational responses at (*b*) and (*d*); the only difference is in the sub-component mobilities $\mathbf{Y}_{B,bc}$ and $\mathbf{Y}_{B,dc}$, respectively. Therefore, the transmissibility in Eq. (4.6), which is formulated in terms of assembly FRFs, can be expressed by mobilities of the receiver-side only. Provided that $\mathbf{Y}_{B,bc}$ can be inverted, an equivalent transmissibility relation is defined using sub-structure FRFs, while the transmissibility matrix $\mathbf{T}_{B,db}^{(c)}$ becomes a specific property of the receiver only,

$$\hat{\mathbf{v}}_{C,da} = \mathbf{T}_{B,db}^{(c)} \hat{\mathbf{v}}_{C,ba} \quad \text{with} \quad \mathbf{T}_{B,db}^{(c)} = \mathbf{Y}_{B,dc} \mathbf{Y}_{B,bc}^+ \quad (4.10)$$

A fourth expression for the subsystem expansion can be defined, replacing the free velocity $\hat{\mathbf{v}}_{A,ca}$ in Eq. (4.8) with a blocked force vector $\bar{\mathbf{f}}_{A,c}$. Recalling the free velocity - blocked force relation in Eq. (2.12), the following substitution can be made,

$$\begin{bmatrix} \hat{\mathbf{v}}_{C,ba} \\ \hat{\mathbf{v}}_{C,da} \end{bmatrix} = \underbrace{\begin{bmatrix} \mathbf{Y}_{B,bc} \\ \mathbf{Y}_{B,dc} \end{bmatrix} [\mathbf{Y}_{A,cc} + \mathbf{Y}_{B,cc}]^{-1} \mathbf{Y}_{A,cc}}_{\begin{bmatrix} \mathbf{Y}_{C,bc} \\ \mathbf{Y}_{C,dc} \end{bmatrix}} \bar{\mathbf{f}}_{A,c} \quad (4.11)$$

$$\text{with } \hat{\mathbf{v}}_{A,ca} = \mathbf{Y}_{A,cc} \bar{\mathbf{f}}_{A,c}$$

redefining the structural responses for a blocked force vector $\bar{\mathbf{f}}_{A,c}$ applied to assembly (C) at its interface (*c*). In other words, the operational source excitation is represented by a blocked force vector, whilst the assembly FRFs $\mathbf{Y}_{C,bc}$ and $\mathbf{Y}_{C,dc}$

characterise the transmission of vibrations to (b) and (d) , respectively. This implies that the generalised transmissibilities $\mathbf{T}_{C,db}^{(a)}$ and $\mathbf{T}_{B,db}^{(c)}$ (Eqs. (4.6) and (4.10)) can also be expressed by a different set of coupled FRFs, $[\mathbf{Y}_{C,bc} | \mathbf{Y}_{C,dc}]^T$, omitting the internal transmission through the source sub-structure. Assuming the inverse of the transfer FRF matrix $\mathbf{Y}_{C,bc}$ exists, the following transmissibility relation can be obtained,

$$\hat{\mathbf{v}}_{C,da} = \mathbf{T}_{C,db}^{(c)} \hat{\mathbf{v}}_{C,ba} \quad \text{with} \quad \mathbf{T}_{C,db}^{(c)} = \mathbf{Y}_{C,dc} \mathbf{Y}_{C,bc}^+ \quad (4.12)$$

between the remote DoFs (b) and (d) , due to an applied blocked force vector at the interface. Comparing Eqs. (4.10) and (4.12), the same transmissibility will be obtained whether or not the source sub-component (A) is attached to the receiver (B) [121]. In other words, the transmissibilities for the coupled assembly and the receiver are identical ($\mathbf{T}_{C,db}^{(c)} = \mathbf{T}_{B,db}^{(c)}$). This invariance allows measuring the same transmissibility in a new assembly (C_2), where a different or modified source is connected to the receiver (B). This concept is exploited in component-replacement TPA [87], where transmissibility-based structural modifications are investigated, e.g. replacing isolators upstream of the source-receiver interface.

Given the discussion above, the generalised transmissibility is invariant to the position and nature of the applied force. The question then arises as to how many excitations (i.e. independent operational conditions) at (a) are required to obtain a transmissibility matrix that is generally valid to describe the problem ($\hat{\mathbf{v}}_{C,ba} \rightarrow \hat{\mathbf{v}}_{C,da}$) under different excitations from the source (e.g. forces that are not included in the transmissibility calculation) [10].

According to the expansion in Eq. (4.7), the transmission of structure-borne vibrations from n_a independent excitations to all remote receiver DoFs n_b and target DoFs n_d is constrained by the coupling interface. In this case, the parameters n_a and n_b , respectively, control and observe the dynamics at the interface. More specifically, controllability depends upon the number of independent source excitations n_a , whilst observability is specific to the receiver defined by the remote DoFs n_b . The coupling interface acts as a bottleneck for all vibrations passing through the physical n_c coupling DoFs. This limits the effective rank of the transmissibility matrix, e.g. $\mathbf{T}_{C,db}^{(a)}$, to a maximum of n_c . In fact, to gain full controllability of the interface, all independent excitation modes of the interface must be sufficiently excited from the chosen set of source-side excitation DoFs, i.e. $n_a \geq n_c$. If the interface dynamics are also fully observed on the passive side, i.e. $n_b \geq n_c$, the transmissibility matrix

provides a reliable description of all transmitted vibrations ($\hat{\mathbf{v}}_{C,ba} \rightarrow \hat{\mathbf{v}}_{C,da}$), even for source excitations that were not considered in the measurements of $\mathbf{T}_{C,db}^{(a)}$. Therefore, the generalised transmissibility can relate the responses at (b) to the targets (d) for any source excitation.

This indicates that, under the assumption that all transfer paths are considered, excitation could either be applied directly on sub-structure (B) or through an intermediate coupled structure (A). In practice, any excitation (e.g. $\hat{\mathbf{f}}_{C,a}$, $\hat{\mathbf{f}}_{B,c}$ or $\bar{\mathbf{f}}_{A,c}$) upstream of the interface that provides full controllability at (c) will result in Eqs. (4.6), (4.10) and (4.12) converging to the same generalised transmissibility matrix, simply \mathbf{T}_{db} [122].

Invariance of the generalised transmissibility matrix:

$$\hat{\mathbf{v}}_{C,da} = \mathbf{T}_{db} \hat{\mathbf{v}}_{C,ba} \quad (4.13)$$

$$\text{with } \mathbf{T}_{db} = \mathbf{Y}_{C,da} \mathbf{Y}_{C,ba}^+ = \mathbf{Y}_{C,dc} \mathbf{Y}_{C,bc}^+ = \mathbf{Y}_{B,dc} \mathbf{Y}_{B,bc}^+$$

The invariance of the generalised transmissibility matrix enables us to obtain the FRF relation of the generalised round-trip identity (compare Eq. (3.15)) from measured operational velocities, as proposed in the next section [106].

4.2 Round-Trip System Identification Using Operational Transmissibilities

In the expressions provided in Eq. (4.13), the transmissibility matrix is defined in terms of mobilities. Whilst these mobilities are readily measurable quantities, requiring a known input force and measured velocity response (or more practically an acceleration response), we are interested in a practical alternative. To avoid FRF measurements, it is possible to define the transmissibility in terms of output only quantities. In this section, the transmissibility in the generalised round-trip identity (see Eq. (3.15)) is replaced by a term based on measurement of the operational velocity only.

The following derivation is essentially the same as that in Sec. 4.1.2 but includes additional unknown source-side excitations. The nature of the source-side excitation is quite general. In theory, a distinction could be made between externally applied

forces at different positional-DoFs (a_i) (e.g. using a non-instrumented hammer) and operational excitations by controllable active components (o_i) (e.g. embedded vibration generating mechanisms). For simplicity, any unknown source-side excitation is denoted by a DoF ' (a_i) '. Let us consider the case where a number of unknown external and/or internal forces are applied to (a). The mutually independent force vectors $\hat{\mathbf{f}}_{C,a}^{(a_i)}$ may be arranged as columns of a force matrix $\hat{\mathbf{F}}_{C,a}$. Similarly, the corresponding velocity response vectors at (b) and (d) due to each excitation can be arranged in velocity matrices. Applying further excitations, Eqs. (4.3) and (4.4) may be rewritten as,

$$\hat{\mathbf{V}}_{C,ba} = \mathbf{Y}_{C,ba} \hat{\mathbf{F}}_{C,a} \quad \text{for } n_b \text{ receiver DoFs \& } n_a \text{ op. excitation} \quad (4.14)$$

$$\hat{\mathbf{V}}_{C,da} = \mathbf{Y}_{C,da} \hat{\mathbf{F}}_{C,a} \quad \text{for } n_d \text{ target DoF \& } n_a \text{ op. excitation} \quad (4.15)$$

$$\text{with } \begin{cases} \hat{\mathbf{F}}_{C,a} = [\hat{\mathbf{f}}_{C,a}^{(a_1)}, \hat{\mathbf{f}}_{C,a}^{(a_2)}, \dots, \hat{\mathbf{f}}_{C,a}^{(a_{n_a})}] \\ \hat{\mathbf{V}}_{C,ba} = [\hat{\mathbf{v}}_{C,ba_1}, \hat{\mathbf{v}}_{C,ba_2}, \dots, \hat{\mathbf{v}}_{C,ba_{n_a}}] \\ \hat{\mathbf{V}}_{C,da} = [\hat{\mathbf{v}}_{C,da_1}, \hat{\mathbf{v}}_{C,da_2}, \dots, \hat{\mathbf{v}}_{C,da_{n_a}}]. \end{cases}$$

Following similar steps to that of Eq. (4.5), a transmissibility relation can be acquired accounting for the unknown force and operational velocity matrices. Pre-multiplication by the inverse velocity matrix yields a generalised transmissibility relation in terms of operational velocity matrices alone.

Generalised transmissibility in terms of operational velocities:

$$\hat{\mathbf{V}}_{C,da} = \mathbf{T}_{C,db}^{(a)} \hat{\mathbf{V}}_{C,ba} \quad \text{and} \quad \mathbf{T}_{C,db}^{(a)} = \hat{\mathbf{V}}_{C,da} \hat{\mathbf{V}}_{C,ba}^+ \quad (4.16)$$

Eq. (4.16) provides an equivalent expression to the FRF-based transmissibilities listed in Eq. (4.13). However, successful implementation requires a reliable phase relationship between the DoFs of each velocity vector (i.e. between the elements in $\hat{\mathbf{v}}_{C,ba_i}$ and $\hat{\mathbf{v}}_{C,da_i}$) that make up $\hat{\mathbf{V}}_{C,ba}$ and $\hat{\mathbf{V}}_{C,da}$, respectively. Therefore, the time averaged auto-spectra of the measured responses is not sufficient to determine a transmissibility matrix unless an appropriate phase is applied beforehand, e.g. using the cross-spectrum phase to a reference sensor [47]. In structural and vibro-acoustic applications, a phase relation for each operational response vector can be established from the cross-spectrum S_{k_i} between the individual channels \hat{x}_i and a

phase reference \hat{x}_k ,

$$\begin{aligned} \hat{x}_i &= \sqrt{S_{ii}} e^{j\angle S_{ki}} \quad |_{i \in [1, \dots, n_i]} \text{ and } i \neq k && \text{for } n_i \text{ remote DoFs} \\ \hat{x}_k &= \sqrt{S_{kk}} && \text{for chosen reference DoF } k \end{aligned} \quad (4.17)$$

$$\text{velocity response vector } \hat{\mathbf{v}}_{C,ba} \left\{ \begin{array}{l} \left[\begin{array}{c} \hat{v}_{C,b_1a} \\ \hat{v}_{C,b_2a} \\ \vdots \\ \hat{v}_{C,b_{n_b}a} \end{array} \right] = \left[\begin{array}{c} \sqrt{S_{b_1b_1}} \\ \sqrt{S_{b_2b_2}} \\ \vdots \\ \sqrt{S_{b_{n_b}b_{n_b}}} \end{array} \right] \odot \left[\begin{array}{c} e^{j0} \\ e^{j\angle S_{b_1b_2}} \\ \vdots \\ e^{j\angle S_{b_1b_{n_b}}} \end{array} \right] \end{array} \right.$$

where \odot denotes the element-wise (Hadamard) vector product, and \hat{x} may represent any operational response (e.g. velocity but also acceleration, sound pressure, etc.). In other words, each vector element is calculated from its auto-spectrum S_{ii} (square root) and its phase with respect to the chosen reference signal k [21, 123]. The reference channel k could be one of the sensors at (c), (b) or an additional sensor close to the vibration generating mechanism, i.e. on the source-side close to (θ). In the given example for $\hat{\mathbf{v}}_{C,ba}$, a phase relationship is established for the operational remote responses (b) to the reference DoF (b_1). In theory, any correlated signal may be used to establish a phase reference, for example, the input current signal in the case vibrations are induced by a shaker or an AC-electric motor.

Note that Eq. (4.17) provides meaningful data only if the response signals \hat{x}_i correlate with the chosen reference \hat{x}_k . If the reference signal is uncorrelated, which may be the case for multiple uncorrelated inputs at (a), assigning a phase proves to be difficult due to arbitrary phase shifts in the cross-spectrum ($\angle S_{ki}$). An alternative to the vector form (where a single reference sensor is used) has been proposed by Elliott et al. [6], where a cross-spectral matrix is defined for a set of reference sensors close to the source-side excitation DoFs. An SVD of this cross-spectral matrix yields some principal components of the source, also referred to as ‘virtual sources’, as a reference for the velocity spectra [124, 125].

For steady state source behaviour, constant phase relationships can be assumed, thus Eq. (4.17) would typically be obtained from the time-averaged auto- and cross-spectra of each velocity vector [114]. To account for dynamic source variations (e.g. run-up of an electric motor), the time domain response signals may be sectioned into sequential time-blocks compatible with the windowing function’s sample length, accounting for an appropriate overlap. Instead of time averaged responses, Eq. (4.17)

may consider sequential spectra for each Fourier transformed time-block, i.e. the dynamic source behaviour is contained in multiple vectors $\hat{\mathbf{v}}_{C,ba}$ to make up $\hat{\mathbf{V}}_{C,ba}$ [58, 126]. The sequential spectra² retain the time structure of the dynamic operational condition and thus provides, in essence, a frequency domain representation of slightly independent response cases. Therefore, the matrices $\hat{\mathbf{V}}_{C,ba}$ and $\hat{\mathbf{V}}_{C,da}$ may contain slightly independent velocity vectors from the sliced time-blocks to improve controllability.

After all, the transmissibility matrix can be estimated by means of Eq. (4.16) or, more conveniently, using the concept of the H_1 -estimator for the cross- and auto-spectra of the operational responses [130, 131]. Consider the generalised transmissibility expression in Eq. (4.16). Post-multiplication of $\hat{\mathbf{V}}_{C,da} = \mathbf{T}_{C,db}^{(a)} \hat{\mathbf{V}}_{C,ba}$ with the complex conjugate transpose velocity matrix $\hat{\mathbf{V}}_{C,ba}^H$ yields a H_1 -like expression of the transmissibility matrix $\mathbf{T}_{C,db}^{(a)}$,

$$\mathbf{T}_{C,db}^{(a)} = \hat{\mathbf{V}}_{C,da} \hat{\mathbf{V}}_{C,ba}^H [\hat{\mathbf{V}}_{C,ba} \hat{\mathbf{V}}_{C,ba}^H]^{-1} \quad (4.18)$$

$$\mathbf{T}_{C,db}^{(a)} = \mathbf{S}_{db} \mathbf{S}_{bb}^{-1}. \quad (4.19)$$

Eq. (4.19) can be seen as a least-squares estimate, similar to the H_1 -estimator, which is a commonly used principle in experimental FRF testing of MIMO systems [132]. Unlike the FRF estimation, which uses an input force, the transmissibility is obtained from the auto-spectra ($\mathbf{S}_{bb} = \hat{\mathbf{V}}_{C,ba} \hat{\mathbf{V}}_{C,ba}^H$) of remote responses (b) and the cross-spectral matrix ($\mathbf{S}_{db} = \hat{\mathbf{V}}_{C,da} \hat{\mathbf{V}}_{C,ba}^H$) between the target and remote responses. Likewise, the transmissibility matrix can be estimated using the principle of the H_2 , H_v or H_s -estimator to balance the error between inputs and outputs [133–135]. It is noted that inputs and outputs of the transmissibility are both operational responses; thus, the SNRs are expected to be similar (provided that the same sensor type is used).

In what follows, the concept of generalised transmissibility is applied to the round-trip relation, as presented in Eq. (3.19). The indirect relation is defined as,

$$\mathbf{Y}_{C,dc} = \mathbf{Y}_{C,da} \mathbf{Y}_{C,ba}^+ \mathbf{Y}_{C,cb}^T. \quad (4.20)$$

² A similar procedure may be applied for VAP auralisation of continuous or transient sounds [1, 127]. Sequential blocked force vectors can be calculated for each velocity vector to retain the time structure. An inverse Fourier transform using the overlap-add method provides a time domain source characterisation or realistic synthesis of a VAP prediction. Alternatively, results can be calculated in the time domain, for example, by convolution with impulse response functions or specifically formulated time domain methods (e.g. the blocked force reconstruction using an adaptive algorithm proposed by Sturm et al. [128, 129]).

The right-hand side of Eq. (4.20) contains the transfer FRF product $\mathbf{Y}_{C,da} \mathbf{Y}_{C,ba}^+$, which has the same form as the generalised transmissibility matrix $\mathbf{T}_{C,db}^{(a)}$ in Eq. (4.13). The matrix $\mathbf{T}_{C,db}^{(a)}$ relates the receiver-side velocities at the target DoFs (d) and remote DoFs (b) due to some known excitation at (a). In other words, the transmissibility term replaces all FRFs requiring source-side excitation. This term can, in theory, be determined from operational velocities resulting from some unknown excitations at (a) using the transmissibility formulation in Eq. (4.16). Substitution of Eq. (4.16) into Eq. (4.20) yields,

Transmissibility-based generalised round-trip relation:

$$\mathbf{Y}_{C,dc} = \mathbf{T}_{C,db}^{(a)} \mathbf{Y}_{C,bc} = \hat{\mathbf{V}}_{C,da} \hat{\mathbf{V}}_{C,ba}^+ \mathbf{Y}_{C,cb}^T. \quad (4.21)$$

Having removed the need for direct source excitation with a known force, Eq. (4.21) utilises the generalised transmissibility concept to provide an alternative approach for the indirect identification of structural dynamic properties. Hence, the original generalised round-trip system identification in Eq. (4.20) is reduced to a single FRF measurement of the receiver-side term $\mathbf{Y}_{C,cb}^T$ and an operational transmissibility term. As such, this approach is particularly useful for inaccessible or encapsulated sources, where source-side FRF measurements are impractical, if not impossible. However, the transmissibility matrix in Eq. (4.21) requires the inversion of an operational velocity matrix. For $\hat{\mathbf{V}}_{C,ba}$ to be full rank, the interface dynamics need to be fully controllable (sufficient mutually independent excitations through enough variation in the operational conditions) and observable (property of the receiver-side DoFs (b)).

It is important to note that the product $\hat{\mathbf{V}}_{C,ba}^+ \mathbf{Y}_{C,bc}$ in Eq. (4.21) may be rewritten as an inverse blocked force matrix $\bar{\mathbf{F}}_{A,c}^+$ present at the coupling interface (c). This independent property of the transmissibility based generalised round-trip relation is used in the so-called ‘fastTPA’ approach, as discussed in the following section.

Considering the different implementations of the generalised round-trip identity, similar substitutions can be made for long distance transfer FRFs³. First, the long distance relation of the generalised round-trip identity in Eq. (3.21) may be rewritten

³ With the methods introduced through this thesis being focused on system identification, for completeness, the transmissibility concept is introduced to the long distance relation outlined in Sec. 3.4.3. However, the following derivation is considered an aside, not directly linked to the main objectives of this thesis.

using the reciprocal relations $\mathbf{Y}_{C,cd}^+ = \mathbf{Y}_{C,dc}^{+T}$ and $\mathbf{Y}_{C,cb} = \mathbf{Y}_{C,bc}^T$,

$$\mathbf{Y}_{C,ab} = \mathbf{Y}_{C,ad} \mathbf{Y}_{C,dc}^{+T} \mathbf{Y}_{C,bc}^T. \quad (4.22)$$

The transposed FRF product $\mathbf{Y}_{C,dc}^{-T} \mathbf{Y}_{C,bc}^T$ may be expressed as $[\mathbf{Y}_{C,bc} \mathbf{Y}_{C,dc}^+]^T$. Substitution into Eq. (4.22) yields,

$$\mathbf{Y}_{C,ab} = \mathbf{Y}_{C,ad} [\mathbf{Y}_{C,bc} \mathbf{Y}_{C,dc}^+]^T. \quad (4.23)$$

The FRF relation in the bracketed term formulates a generalised transmissibility $\mathbf{T}_{C,bd}^{(c)}$. Unlike previous transmissibility matrices, the roles of the DoFs (b) and (d) are interchanged,

$$\mathbf{T}_{C,bd}^{(c)} = \mathbf{Y}_{C,bc} \mathbf{Y}_{C,dc}^+. \quad (4.24)$$

The matrix $\mathbf{T}_{C,bd}^{(c)}$ relates the velocity response at the remote receiver locations (b) and the additional DoFs (d) (halfway along the targeted path) due to some applied excitations at the coupling interface (c). For $\mathbf{Y}_{C,dc}$ to be invertible, the interface dynamics need to be fully observed at the DoFs (d), whilst (b) defines the target DoFs of the long distance FRF $\mathbf{Y}_{C,ab}$. Using the invariance of the transmissibility matrix in Eq. (4.13), the forces applied at the interface (c) can be relocated to other upstream DoFs (a) on the source, i.e. $\mathbf{T}_{C,bd}^{(c)} = \mathbf{T}_{C,bd}^{(a)}$. This term may, in theory, be determined from operational velocities from some unknown source-side excitation, for example, by the internal mechanism (θ). Replacing Eq. (4.24) by the velocity-based transmissibility formulation in Eq. (4.16) and substitution into Eq. (4.23) yields,

Transmissibility based long distance relation:

$$\mathbf{Y}_{C,ab} = \mathbf{Y}_{C,ad} [\mathbf{T}_{C,bd}^{(a)}]^T = \mathbf{Y}_{C,ad} [\dot{\mathbf{V}}_{C,ba} \dot{\mathbf{V}}_{C,da}^+]^T \quad (4.25)$$

or for collocated DoFs (d) = (c),

$$\mathbf{Y}_{C,ab} = \mathbf{Y}_{C,ac} [\mathbf{T}_{C,bc}^{(a)}]^T = \mathbf{Y}_{C,ac} [\dot{\mathbf{V}}_{C,ba} \dot{\mathbf{V}}_{C,ca}^+]^T. \quad (4.26)$$

Eq. (4.25) provides an alternative approach to characterise long distance transfer FRFs, whilst instrumentation or force excitation at the interface DoFs (c) is avoided. Hence, the previous indirect measurement is reduced to a single FRF, $\mathbf{Y}_{C,ad}$, to overcome the issues of accessibility, plus an operational transmissibility. However,

Eq. (4.25) conflicts with the principal concept presented in Sec. 3.4.3, where additional excitations (i.e. at accessible DoFs (d)) are applied further downstream on the receiver to benefit from shorter paths with an improved SNR. Utilising the transmissibility concept in Eqs. (4.25) and (4.26), all excitations lie on the source sub-component (A), while the ‘longer’ paths in $\mathbf{Y}_{C,ad}$ are again prone to insufficient SNR.

Note that the source-side DoFs (a) of the FRF term $\mathbf{Y}_{C,ad}$ (or $\mathbf{Y}_{C,ac}$ for the collocated relation) are independent of the excitations in $\mathbf{T}_{C,bd}^{(a)}$ (or $\mathbf{T}_{C,bc}^{(a)}$, respectively). In fact, the FRF $\mathbf{Y}_{C,ad}$ defines the target DoFs (a) of the long distance transfer function $\mathbf{Y}_{C,ab}$, whilst the same or other (arbitrary) unknown excitations (a) may be used for full controllability of the transmissibility. The nature and location of the latter source-side excitation are quite arbitrary. As such, an external excitation, for example, with a non-instrumented hammer, can be used to determine the transmissibility matrix. In theory, the unknown forces can be located in the vicinity of the interface or generated by an internal source mechanism (θ).

A potential application, however, could be system identification in structures that are generally difficult to excite with traditional impact hammer or shaker excitation techniques but feature high-strength internal vibration generating mechanisms. Challenges in conventional FRF measurements may result from: The trade-off between high-intensity impact and LTI assumptions (i.e. deformation of the impact area), limitations of the excitation frequency range (e.g. softer hammer tips to avoid the former issue), or availability of shakers in larger sizes. In this case, the internal excitation may be sufficiently strong to overcome SNR issues. A potential example is the analysis of vibration propagation through industrial forging or hydraulic presses [136], where the rigid foundation transmits vibrations into the building. Whilst $\mathbf{Y}_{C,ac}$ can be determined with an instrumented hammer or shaker, the operational impact excitation of the forging process may be used to determine the transmissibility term $\mathbf{T}_{C,bc}^{(a)}$ with the remote DoFs (b) located somewhere (far distant) on the rigid foundation. In this application, the DoFs (d) observe the interface dynamics on the receiver-side while (b) defines the target response of the long distance FRFs.

Although an operational transmissibility matrix would provide far greater flexibility in any long distance FRF measurement, its experimental validation is considered beyond the scope of this thesis.

4.3 Two-Stage MIMO System Identification Using a Controlled Blocked Force Exciter

The transmissibility-based round-trip relation in Eq. (4.21) can readily be applied to determine driving-point and transfer FRFs and thus reduce complexity in the measurements commonly involved in TPA. However, the relation still requires measurement of $\mathbf{Y}_{C,cb}^T$, which may be inconvenient, if not impossible, to measure in complex assemblies. Therefore, we are interested in substituting the conventional measurement of $\mathbf{Y}_{C,cb}^T$ in the target assembly with an equivalent measurement obtained in a different (easy-to-access) setup, i.e. remote from the intended installation. In this section, the invariance of the blocked force is exploited to split up the measurements involved in the transmissibility-based system identification and perform tests on two different assemblies. As such, conventional FRFs can be obtained in a purpose-built ‘calibration setup’, prior to operational measurements with the source in its intended installation (target assembly). This two-stage procedure may then be used to characterise inaccessible FRFs or, more generally, the transfer functions required for inverse force synthesis and forward prediction as of TPA.

First, the transmissibility-based round-trip identity in Eq. (4.21) may be rewritten using the reciprocal relation $\mathbf{Y}_{C,cb}^T = \mathbf{Y}_{C,bc}$,

$$\mathbf{Y}_{C,dc} = \hat{\mathbf{V}}_{C,da} \hat{\mathbf{V}}_{C,ba}^+ \mathbf{Y}_{C,bc}. \quad (4.27)$$

Rearranging the terms in Eq. (4.27) yields,

$$\hat{\mathbf{V}}_{C,da}^+ \mathbf{Y}_{C,dc} = \hat{\mathbf{V}}_{C,ba}^+ \mathbf{Y}_{C,bc} \quad (4.28)$$

$$\text{with } \begin{cases} \bar{\mathbf{F}}_{A,c}^+ = \hat{\mathbf{V}}_{C,da}^+ \mathbf{Y}_{C,dc} & \text{for } n_d \text{ target DoFs} \\ \bar{\mathbf{F}}_{A,c}^+ = \hat{\mathbf{V}}_{C,ba}^+ \mathbf{Y}_{C,bc} & \text{for } n_b \text{ remote DoFs.} \end{cases}$$

Considering the right-hand side of Eq. (4.28), the matrix product, $\hat{\mathbf{V}}_{C,ba}^+ \mathbf{Y}_{C,bc}$, may be rewritten as $[\mathbf{Y}_{C,bc}^+ \hat{\mathbf{V}}_{C,ba}]^+$. The term within the bracket can be seen to take the same form as the in-situ blocked force relation in Eq. (2.9), evaluated for multiple velocity vectors in $\hat{\mathbf{V}}_{C,ba}$. Similar considerations apply to the left-hand side of Eq. (4.28), where a blocked force relation can be formulated for remote DoFs (d), as opposed to (b). Therefore, both sides in Eq. (4.28) may be expressed by an inverse blocked force matrix $\bar{\mathbf{F}}_{A,c}^+$ present at the source-receiver coupling interface (c). As

noted in Sec. 2.2, the blocked force matrix is, by definition, a source property independent of the connected receiver. As such, $\bar{\mathbf{F}}_{A,c}$ may be obtained from different assemblies assuming a controllable excitation mechanism at (a), that is, the same operating conditions can be reproduced in a different installation. In other words, Eq. (4.28) may be extended to place the remote DoFs (b) and (d) on two different assemblies, denoted by (C_1) and (C_2),

$$\hat{\mathbf{V}}_{C_2,da}^+ \mathbf{Y}_{C_2,dc} = \hat{\mathbf{V}}_{C_1,ba}^+ \mathbf{Y}_{C_1,bc} \quad (4.29)$$

or vice versa for interchanged assemblies (C_1) and (C_2),

$$\hat{\mathbf{V}}_{C_1,da}^+ \mathbf{Y}_{C_1,dc} = \hat{\mathbf{V}}_{C_2,ba}^+ \mathbf{Y}_{C_2,bc}. \quad (4.30)$$

The different assemblies are constructed by connecting a source (A) to different receiver structures (B_1) and (B_2). If the operational excitation can not be reproduced, any variation between (C_1) and (C_2) will alter the corresponding blocked force matrix ($\bar{\mathbf{F}}_{A,c}^+$ on the left- or right-hand side) and invalidate Eqs. (4.29) or (4.30) and any predictions made thereafter. The extent to which real sources can produce repeatable excitation after being removed and reinstalled is a question which will need to be investigated further in Chapters 5 and 7.

Clearly, a known blocked force matrix obtained from any assembly (e.g. measurements of $\hat{\mathbf{V}}_{C_1,ba}^+ \mathbf{Y}_{C_1,bc}$ in (C_1)) can be used to identify FRFs in a different installation (e.g. target assembly (C_2)). Some simple rearrangement of Eq. (4.29) yields,

$$\mathbf{Y}_{C_2,dc} = \hat{\mathbf{V}}_{C_2,da} \underbrace{\hat{\mathbf{V}}_{C_1,ba}^+ \mathbf{Y}_{C_1,bc}}_{\bar{\mathbf{F}}_{A,c}^+} \quad (4.31)$$

which is, in fact, an extension of the transmissibility-based generalised round-trip relation derived in Eq. (4.21), whilst accounting for different assemblies. Hence, the aim to provide an expression of $\mathbf{Y}_{C_2,dc}$ without conventional FRF measurements in the target assembly (C_2) is achieved. As such, the FRF term $\mathbf{Y}_{C_1,bc}$ may be determined in a different assembly, remote from the intended installation. The operational velocity term $\hat{\mathbf{V}}_{C_2,da} \hat{\mathbf{V}}_{C_1,ba}^+$ forms a transmissibility⁴ between the DoFs at (d) and (b) located on different assemblies due to reproduced operational excitations at (a). When access to the contact interface (c) is unrestricted, the blocked

⁴ Strictly speaking, the term $\mathbf{T}_{C_1,2,db} = \hat{\mathbf{V}}_{C_2,da} \hat{\mathbf{V}}_{C_1,ba}^+$ is derived based on transmissibilities, however, the velocity relation is not a transmissibility in a traditional sense. Conventional transmissibilities usually relate like-quantities between DoFs of the same assembly. Here, the transmissibility relates velocities between different DoFs of two different assemblies, i.e. from the target assembly (C_2) to the responses used in the calibration setup (C_1).

force matrix $\bar{\mathbf{F}}_{A,c}^+$ can be obtained by collocating the DoFs $(b) = (c)$, as defined in Eq. (2.10). In this more general case, where driving-point and transfer FRFs may be used together in a partitioned matrix, Eq. (4.31) can be expressed in the form,

MIMO system identification using blocked force excitation:

$$\mathbf{Y}_{C_2,dc} = \dot{\mathbf{V}}_{C_2,da} \underbrace{\begin{bmatrix} \dot{\mathbf{V}}_{C_1,ca} \\ \dot{\mathbf{V}}_{C_1,ba} \end{bmatrix}^+}_{\bar{\mathbf{F}}_{A,c}^+} \begin{bmatrix} \mathbf{Y}_{C_1,cc} \\ \mathbf{Y}_{C_1,cb}^T \end{bmatrix}. \quad (4.32)$$

where the partitioned matrix formed from coupled mobilities $\mathbf{Y}_{C_1,cc}$ and $\mathbf{Y}_{C_1,cb}^T$ of the first assembly (C_1) is pre-multiplied by the pseudo-inverse of the partitioned matrix of the velocity responses $\dot{\mathbf{V}}_{C_1,ca}$ and $\dot{\mathbf{V}}_{C_1,ba}$. Conceptually, Eq. (4.32) performs a downstream transmissibility-based modification⁵ of structure (C_1). The measured FRF terms $\mathbf{Y}_{C_1,cc}$ and/or $\mathbf{Y}_{C_1,cb}^T$ on the right-hand side are modified by a transmissibility relating two different assemblies to estimate structural properties of (C_2). A similar concept is adopted in CR-TPA [87], where the term ‘transmodification matrix’ is chosen to characterise a component replacement, usually applied to facilitate upstream assembly modifications in TPA.

To formulate a passive relation, i.e. for difficult-to-control sources, the operational responses may be generated using external excitations in place of an operational activity. If the controlled excitations are applied using an instrumented hammer or shaker, Eq. (4.32) may be rewritten in terms of FRFs (i.e. its response to a unit excitation).

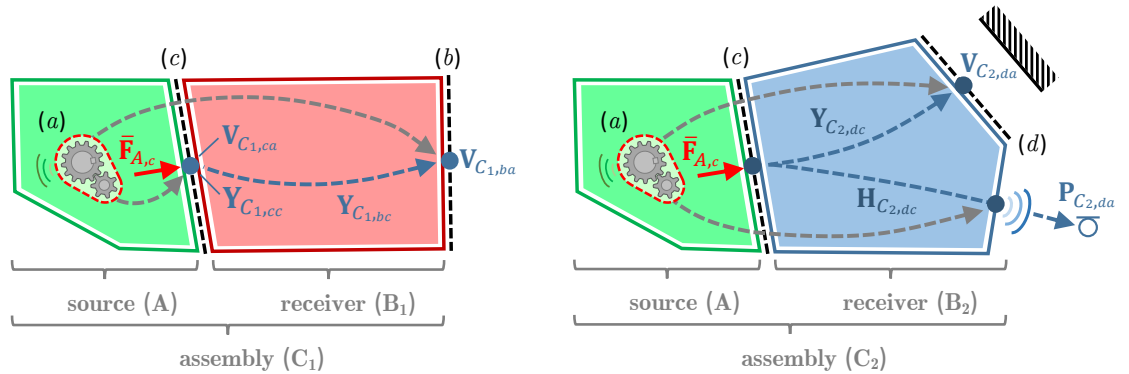
$$\mathbf{Y}_{C_2,dc} = \mathbf{Y}_{C_2,da} \underbrace{\begin{bmatrix} \mathbf{Y}_{C_1,ca} \\ \mathbf{Y}_{C_1,ba} \end{bmatrix}^+}_{\bar{\mathbf{F}}_{A,c}^+} \begin{bmatrix} \mathbf{Y}_{C_1,cc} \\ \mathbf{Y}_{C_1,cb}^T \end{bmatrix} \quad (4.33)$$

Strictly speaking, $\bar{\mathbf{F}}_{A,c}^+$ in Eq. (4.33) is not a blocked force matrix in the traditional sense, as it is a unitless matrix applied as a structural filter to the dynamics of assembly (C_2). In this context, $\bar{\mathbf{F}}_{A,c}$ might be considered a blocked force matrix per unit force input.

⁵ In contrast to frequency-based dynamic sub-structuring, Eq. (4.32) does not attempt to build an assembly out of individual components. Instead, it takes an assembled structure (C_1) and considers the transmissibility-based replacement of the receiver component.

In essence, Eqs. (4.32) and (4.33) convert any physical structure which can be operated sufficiently controllably and reproducibly into a multi-DoF ‘blocked force vibration exciter’. In principle, any source structure may generate such a controlled excitation. The underlying vibration generating mechanism can either be embedded directly in the structure (e.g. mechanical components like gears or electric motors) or an external mechanism (which may be installed permanently or in a roving instrumentation manner). From a practical perspective, the same source can be operated in any assembly to determine structural and/or vibro-acoustic FRFs. Compared to the original expression in Eq. (4.21), the above relation facilitates system identification in the same (i.e. $(C_2) = (C_1)$) or multiple different assemblies, e.g. (C_2) , (C_3) , etc. For brevity, the following discussion considers Eq. (4.32), whilst modifications to include the passive expression in Eq. (4.33) are straightforward but not explicitly shown.

Using the terminology of a calibration and system identification setup, the matrix terms on the right-hand side of Eq. (4.32) can be obtained in two stages (see Fig. 4.2). This overview can be used as a practical guide to identifying the two measurement stages required to obtain all three matrix terms.



(a) Stage 1: Calibration of the source (A) as a controlled blocked force exciter, $\bar{F}_{A,c}$, in assembly (C_1) .

(b) Stage 2: System identification of assembly (C_2) from a known excitation $\bar{F}_{A,c}$ and operational measurements at (d).

Figure 4.2: Two-stage procedure of Eq. (4.32) to characterise the source component (A) as a controlled blocked force exciter and subsequent MIMO system identification of $Y_{C_2,dc}$ and/or $H_{C_2,dc}$ in a different assembly (C_2) .

In the first stage shown in Fig. 4.2a, the source component is installed in assembly (C_1) and calibrated as a controlled blocked force exciter. For the in-situ measurement of $\bar{F}_{A,c}^+$ the source is turned off, and the FRFs $Y_{C_1,cb}$ and/or $Y_{C_1,cc}$ are obtained

from conventional impact hammer or shaker excitations at (b) and/or (c) , respectively. The correct position of interface DoFs (c) is essential, as these locations will define the ‘excitation’ DoFs of the controlled blocked force exciter for $\mathbf{Y}_{C_2,dc}$. The source is then operated under a sequence of controlled conditions (or a set of external excitations for Eq. (4.33)) to measure the operational velocity responses at the chosen DoFs. In theory, the matrix $\overline{\mathbf{F}}_{A,c}^+$ can also be obtained through alternative approaches outlined in Sec. 2.2, measured on special test rigs (e.g. perfectly rigid receiver to measure blocked forces directly or resiliently mounted to measure free velocity).

The second stage is performed with the source (A) installed in the target assembly (C_2), as shown in Fig. 4.2b. The source is operated under the same (controlled) conditions used during the calibration measurement (stage 1) and utilised as a multi-DoF blocked force exciter. FRFs between the interface and some target DoFs can be determined from simple response measurements, e.g. using microphones and accelerometers at the target locations (d) . This identification requires no conventional FRF measurement in assembly (C_2), and thus the target DoFs (d) may be placed at locations inaccessible for excitation (illustrated by the hatched area).

It is interesting to note that for the remote expression in Eq. (4.31) (or second row of the partitioned formulation in Eq. (4.32)), an incomplete interface description may be sufficient in stage 1, without impairing the results. In other words, the result $\mathbf{Y}_{C_2,dc}$ is correct even if a single coupling DoF (c) (or any incomplete subset of (c)) is considered in the post-multiplied FRF terms $\mathbf{Y}_{C_1,cb}^T$. This property of the generalised round-trip relation has been noted before in Sec. 3.6. However, if certain forces or loads are neglected, the computed FRFs in $\mathbf{Y}_{C_2,dc} \in \mathbb{C}^{n_d \times n_c}$ will also not include the missing interface DoFs (c) .

At first sight, it is not obvious that this invariance from the interface description is a feature of the transmissibility term $\mathbf{T}_{C_1,2,db}$ and not a property of the matrix product that makes up $\overline{\mathbf{F}}_{A,c}^+$. This is made clearer by considering the nature of the reproduced force excitation $\hat{\mathbf{F}}_{C,a}$. The velocity responses of the transmissibility term, for example, $\hat{\mathbf{V}}_{C_1,ba}$ and $\hat{\mathbf{V}}_{C_2,da}$, measured during the different stages, can be

written in terms of their excitation and the subsystem mobilities,

$$\hat{\mathbf{V}}_{C_1,ba} = \mathbf{Y}_{C_1,bc} \mathbf{Y}_{A,cc}^{-1} \mathbf{Y}_{A,ca} \hat{\mathbf{F}}_{A,a} \quad (4.34)$$

$$\hat{\mathbf{V}}_{C_2,da} = \mathbf{Y}_{C_2,dc} \mathbf{Y}_{A,cc}^{-1} \mathbf{Y}_{A,ca} \hat{\mathbf{F}}_{A,a} \quad (4.35)$$

$$\text{with } \bar{\mathbf{F}}_{A,c} = \mathbf{Y}_{A,cc}^{-1} \mathbf{Y}_{A,ca} \hat{\mathbf{F}}_{A,a}.$$

Note that the subscript ‘ C ’ of the applied excitation changes to $\hat{\mathbf{F}}_{A,a}$ when expanded in terms of its subsystem mobilities. For full controllability over the vibrations that occur at the interface (from the chosen forces $\hat{\mathbf{F}}_{A,a}$), the velocity responses $\hat{\mathbf{V}}_{C_1,ba}$ and $\hat{\mathbf{V}}_{C_2,da}$ downstream of the source-receiver interface include contributions from all physical coupling DoFs (c). It is clear from the above that the source-side FRF terms are in exact agreement⁶ (same controlled source (A) is used), and cancellation will occur in a transmissibility expression. The applied excitation $\hat{\mathbf{F}}_{A,a}$ on sub-structure (A) (i.e. due to reproduced operational conditions) can thus be represented by an appropriate blocked force $\bar{\mathbf{F}}_{A,c}$ applied at the interface to the connected receiver. Due to the controllability, the blocked force matrix considers all physical coupling DoFs, that is, applying a multi-DoF blocked force excitation. Hence, the controlled vibration generating mechanism is termed ‘in-situ blocked force exciter’. In other words, the reproduced blocked force excitation is implicitly ‘contained within’ the velocity terms that make up the transmissibility matrix, thus independent of the interface description in $\mathbf{Y}_{C_1,cb}^T$. This FRF term simply relates the remote positions (b) to the coupling interface DoFs, without imposing constraints such as interface completeness. As such, the requirement of completeness (imagine the blocked force would physically be applied at the interface) is replaced by the controllability of the interface. Further details on the controllability and observability of the two-stage procedure are presented in Sec. 4.3.3. Note that similar considerations apply to the collocated expression (i.e. $(b) = (c)$ in the upper row of the partitioned formulation in Eq. (4.32)), however, full observability of $\hat{\mathbf{V}}_{C_1,cc}$ always requires complete interface instrumentation.

In the MIMO case discussed above, Eq. (4.32) exploits the invariance of the blocked force to identify FRFs based on reproduced multi-DoF source excitations. The fundamental principle can be broken down into a more trivial case for a single

⁶ Note that any change in the source properties between the calibration (whilst measuring $\hat{\mathbf{V}}_{C_1,bc}$) and system identification (whilst measuring $\hat{\mathbf{V}}_{C_2,dc}$) stage, e.g. due to an applied torque or stiffening effect when under operation, may introduce an inconsistency in Eq. (4.32). As such, the blocked force matrix in Eqs. (4.34) and (4.35) will differ and lead to errors in the acquired FRFs.

coordinate-DoF. Imagine the source is connected to a receiver at a single contact, and the blocked force excitation is applied in one interface DoF k . The structural dynamic properties are determined as the complex ratio of the coupled velocity response $v_{C,i}$ to the blocked force excitation $\bar{f}_{A,k}$. Compared to the general mobility relation in Eq. (2.2), the blocked force expression is limited to coupled structures, whilst mobilities are also defined for the separated sub-structures. Both cases require all remaining forces to be constrained to zero, while the physically unconstrained structure responds freely.

General mobility relation:

$$Y_{ik}(\omega) = \left. \frac{v_i(\omega)}{f_k(\omega)} \right|_{f_{i \neq k} = 0} \quad (4.36)$$

Blocked force mobility relation for source-receiver assemblies (C):

$$Y_{C,ik}(\omega) = \left. \frac{v_{C,i}(\omega)}{\bar{f}_{A,k}(\omega)} \right|_{f_{i \neq k} = 0} \quad (4.37)$$

Although not explicitly specified, the mobility concept in Eq. (4.37) may be extended to other response types, e.g. acceleration, displacement or pressure response.

With the proposed two-stage procedure, MIMO system identification is performed simultaneously, including in-plane and rotational DoFs. Hence, it may be used to complement the task of conventional FRF testing in component-based TPA, just like the generalised round-trip identity, or to formulate a novel TPA approach. In the latter case, the two-stage procedure may be incorporated within the in-situ TPA approach to allow, in theory, for faster and potentially more reliable diagnostic tests in the target assembly (C_2). In other words, the FRFs to perform in-situ TPA can all be obtained simultaneously using a controlled multi-DoF exciter. Assuming full controllability and observability, Eq. (4.32) allows to include all physical interface DoFs (and their corresponding transfer paths) in the analysis, even those usually impractical to measure with impact hammers or shakers.

Using the FRFs obtained with the two-stage exciter concept in the context of TPA is denoted as ‘fastTPA’ due to the significant time advantage. Based on the in-situ TPA methodology, fastTPA relies on the same two-part workflow; 1) inverse source characterisation (in the form of a blocked force) and 2) forward response prediction. As such, Eq. (4.32) may be used to obtain FRFs for in-situ blocked force characterisation (inverse force identification) in the target assembly (C_2) and to determine

each blocked force's contribution (forward prediction) to the total operational response at the target location (d). In the following, the measurement steps (i.e. the workflow including 1) and 2)) of the novel fastTPA are outlined.

4.3.1 FastTPA – Inverse Force Identification

As discussed in the introductory Chapter 1, practical challenges associated with the FRF measurements in component-based TPA (e.g. in-situ TPA) have led to a near-routine neglect of coupling DoFs in the interface description. More than often, some measurements cannot be undertaken; for example, if access to the measurement DoFs is restricted, a moment excitation needs to be applied, or special measurement equipment is required, to name but a few. Unless advanced techniques, e.g. the generalised round-trip identity, are used to identify all remaining FRFs that cannot be measured directly, engineers are not given the chance to analyse vibration problems in their full complexity. However, these measurements to fully describe each point-like contact by 6-DoFs are time-consuming to apply.

FastTPA avoids the challenges described above by instead using a controlled multi-DoF exciter to obtain all FRFs in a time-efficient manner for a reliable analysis. In the following, we are interested in characterising the operational excitation of the source (in the form of a blocked force $\{\bar{\mathbf{f}}_{A,c}\}_{(C_2)}$) in the target assembly using exciter FRFs from Eq. (4.32). This is considered the first part of the fastTPA workflow. Note that the subscript '(C₂)' indicates the assembly in which the operational blocked force vector is characterised, since the previous section introduced measurements on different coupled structures.

Let us first review the measurements required in a conventional in-situ TPA (which forms the basis of fastTPA). In in-situ TPA, the blocked force characterisation requires measurement of both, $\mathbf{Y}_{C_2,dc}$ and $\mathbf{v}_{C_2,da}$ in the same (target) assembly (C₂),

$$\{\bar{\mathbf{f}}_{A,c}\}_{(C_2)} = \mathbf{Y}_{C_2,dc}^+ \mathbf{v}_{C_2,da} \quad (4.38)$$

this is referred to as inverse force identification [6, 37]. Compared to Eq. (2.9), the in-situ blocked force relation above considers some receiver-side target DoFs (d) instead of the notation (b). The matrix $\mathbf{Y}_{C_2,dc}$ relates the DoFs (d) at which the velocity is measured to the coupling interface (c), where the blocked force vector is defined. Conceptually, the inversion of the mobility matrix has the effect of rigidly

constraining all DoFs other than that of the applied excitation. If a notable incomplete interface description is used in $\mathbf{Y}_{C_2,dc}$, the coupling DoFs will not be sufficiently constrained when the inversion is performed. Therefore, all important interface DoFs must be included in the measurements to obtain a correct blocked force vector. As mentioned before, problematic measurements of $\mathbf{Y}_{C_2,dc}$ may be avoided through methods like the round-trip identity or the multi-DoF exciter concept, as shown in the following.

In fastTPA, the blocked force characterisation is also based on Eq. (4.38), however, the mobility matrix $\mathbf{Y}_{C_2,dc}$ is obtained in a time-efficient way using the controlled source as a multi-DoF exciter. Therefore, the two-stage FRF measurement relation in Eq. (4.32) (only the second row for brevity) is substituted into Eq. (4.38). This yields a transmissibility-based blocked force relation,

$$\{\bar{\mathbf{f}}_{A,e}\}_{(C_2)} = [\dot{\mathbf{V}}_{C_2,da} \dot{\mathbf{V}}_{C_1,ba}^+ \mathbf{Y}_{C_1,cb}^T]^+ \mathbf{v}_{C_2,da}. \quad (4.39)$$

Eq. (4.39) provides an in-situ characterisation of the source (A) and may readily be used in place of Eq. (4.38) if convenient. This alternative approach avoids the often problematic measurement of $\mathbf{Y}_{C_2,dc}$ by incorporating more easy-to-acquire data from a (purpose-built) calibration assembly (C_1). The blocked force vector is still obtained in-situ, and therefore under representative loading and mounting conditions, whilst the source (A) is connected to different receiver structures (calibration and system identification stage) during the process. The advantages herein are of practical nature: for instance, all conventional FRF measurements are conducted in a calibration assembly (C_1) remote from the target installation. As such, test rigs may be specifically designed to facilitate unrestricted interface access to determine $\mathbf{Y}_{C_1,cb}^T$ or even $\mathbf{Y}_{C_1,bc}$, so that problems due to insufficient excitation or response positioning can be avoided. In addition, tailored fixtures can be used to include rotations⁷ in the blocked force vector. For example, Fig. 6.2 in Chapter 6 shows such a calibration setup (C_1), where adapters are connected at the source-receiver interfaces to simplify response and excitation measurements for finite difference approximation. The velocity matrix $\dot{\mathbf{V}}_{C_1,ba}$ is also measured in the calibration assembly (C_1), whilst the source is operated under different controlled conditions.

⁷ Unlike the two-stage procedure to identify individual FRFs, the completeness of the interface description in fastTPA is essential if the blocked force is to be characterised correctly. To compute $\bar{\mathbf{f}}_{A,c}$ including forces and moments, the corresponding translational and rotational DoFs must be considered in $\mathbf{Y}_{C_1,cb}^T$.

Once the calibration is performed (i.e. measurement of $\dot{\mathbf{V}}_{C_1,ba}$ and $\mathbf{Y}_{C_1,cb}^T$), the controlled source is installed and operated in its intended installation (C_2). The blocked force vector $\bar{\mathbf{f}}_{A,c}$ is obtained from velocity measurements of $\dot{\mathbf{V}}_{C_2,da}$ and $\mathbf{v}_{C_2,dc}$. These measurements are easy to set up; thus, the process can be repeated multiple times with the source (i.e. blocked force exciter) installed in the same, a modified or a different assembly. Note that these response measurements at (d) are independent of one another. The velocity vector $\mathbf{v}_{C_2,da}$ describes the source activity to obtain the blocked force for a specific manoeuvre (i.e. subject to the NVH task at hand), whilst $\dot{\mathbf{V}}_{C_2,da}$ is measured when the source is operated under the same controlled conditions used in the previous calibration setup. In other words, $\dot{\mathbf{V}}_{C_2,da}$ contains the responses in the target assembly for the known (reproduced) blocked force excitation with the multi-DoF exciter.

The term within the bracket in Eq. (4.39) can be simplified to avoid the need for a double matrix inversion, thus the above formulation may be rewritten in a more convenient form.

FastTPA inverse blocked force identification:

$$\{\bar{\mathbf{f}}_{A,c}\}_{(C_2)} = [\mathbf{Y}_{C_1,bc}^+ \dot{\mathbf{V}}_{C_1,ba} \dot{\mathbf{V}}_{C_2,da}^+] \mathbf{v}_{C_2,da} \quad (4.40)$$

or using external excitations,

$$\{\bar{\mathbf{f}}_{A,c}\}_{(C_2)} = [\mathbf{Y}_{C_1,bc}^+ \mathbf{Y}_{C_1,ba} \mathbf{Y}_{C_2,da}^+] \mathbf{v}_{C_2,da} \quad (4.41)$$

Eqs. (4.40) and (4.41) provide formulations to obtain the operational blocked force of the device in complex built-up structures. In essence, the transmissibility-based concept uses the controlled vibration generating mechanism to identify the structural FRFs $\mathbf{Y}_{C_2,dc}$ for the inverse procedure and later troubleshoots the operational behaviour ($\mathbf{v}_{C_2,da}$) of this source. Note that the mobility formulation in Eq. (4.41) considers external excitations (compare Eq. (4.33)) to control the multi-DoF exciter, which define an in-situ blocked force procedure for passive or difficult-to-control sources. The reciprocal relation $\mathbf{Y}_{C_1,bc} = \mathbf{Y}_{C_1,cb}^T$ may be used to simplify the measurements further.

Considering the inverse step, it becomes clear why the proposed fastTPA is not categorised as a transmissibility-based TPA method, as shown in the overview in Fig. 2.5 presented in Sec. 2.5.2. Compared to operational transfer path analysis (OTPA), both approaches use an operational transmissibility with the motivation

to accelerate the diagnostic test. Despite the similarities between fastTPA and OTPA, there are several fundamental differences. The OTPA concept is based on a response-response relationship, whilst a high response level at the path input does not imply a force is entering the system at that location (i.e. the ‘co-existence’ of a target and reference response does not imply causality) [97, 114, 137]. In contrast, fastTPA uses a load-response relationship, which means the effect of a particular interface load on the total response can be analysed. To this end, the fastTPA measurements in the target assembly may seem similar to OTPA, however, interface loads are obtained using measurements from the calibration stage.

In fastTPA, Eqs. (4.40) or (4.41) are used first to characterise the active components in-situ; this is referred to as the inverse step. Having characterised the blocked force vector, $\bar{\mathbf{f}}_{A,c}$ is then used to predict an operational response or the partial path contributions based on the acquired blocked force. This is referred to as the forward step and is typically used as an on-board validation procedure, as specified by ISO 20270:2019 [38]. The forward prediction and the concept of controllability and observability for the transmissibility-based fastTPA will be discussed in the following sections.

4.3.2 FastTPA – Forward Prediction, Validation and FastVAP

Having estimated the blocked force in an inverse step (Eqs. (4.40) or (4.41)), the forward prediction of an operational response can be made. This is considered the second part of the fastTPA workflow. The forward step applies not only to a TPA response prediction, but also to the on-board validation procedure as standardised by ISO 20270:2019 [38] (see Sec. 2.4.1). In either case, the predicted total response at (d') is given by,

$$\begin{bmatrix} \mathbf{P}_{C_2,d'a} \\ \mathbf{v}_{C_2,d'a} \end{bmatrix} = \begin{bmatrix} \mathbf{H}_{C_2,d'c} \\ \mathbf{Y}_{C_2,d'c} \end{bmatrix} \{\bar{\mathbf{f}}_{A,c}\}_{(C_2)} \quad (4.42)$$

where the blocked force vector $\{\bar{\mathbf{f}}_{A,c}\}_{(C_2)}$ originates from Eqs. (4.40) or (4.41). Note that the target DoF is denoted by the subscript ‘ d' ’. The distinction by an apostrophe is made to indicate that (d') is not part of the remote DoFs (d) used in the inverse force identification. In a diagnostic context, Eq. (4.42) is typically broken down as a sum of partial contributions to predict the contribution of each element in $\bar{\mathbf{f}}_{A,c}$ to the total operational response. For example, the total sound pressure

response $\mathbf{p}_{C_2,d'a}$ at some target DoF (d') can be expressed by,

$$\mathbf{p}_{C_2,d'a} = \sum_{i=1}^{n_c} p_{C_2,d'c_i} = \sum_{i=1}^{n_c} H_{C_2,d'c_i} \bar{f}_{A,c_i} \quad \text{for } n_c \text{ coupling DoFs} \quad (4.43)$$

where $p_{C_2,d'c_i}$ is the relative contribution of excitation force \bar{f}_{A,c_i} . The above facilitates contribution ranking to identify potential issues and troubleshoot dominant excitations and transmission paths.

In fastTPA, the forward FRFs $\mathbf{H}_{C_2,d'c}$ (or $\mathbf{Y}_{C_2,d'c}$ if we consider structural responses) used in Eq. (4.42) are replaced by the two-stage expression in Eq. (4.32) to avoid conventional FRF measurements in (C_2). The forward prediction in Eq. (4.42) can be rewritten as,

FastTPA forward response prediction:

$$\begin{bmatrix} \mathbf{p}_{C_2,d'a} \\ \mathbf{v}_{C_2,d'a} \end{bmatrix} = \begin{bmatrix} \dot{\mathbf{P}}_{C_2,d'a} \\ \dot{\mathbf{V}}_{C_2,d'a} \end{bmatrix} \dot{\mathbf{V}}_{C_1,ba}^+ \mathbf{Y}_{C_1,bc} \{\bar{\mathbf{f}}_{A,c}\}_{(C_2)}. \quad (4.44)$$

In practice, partial responses are obtained by selecting the corresponding coupling DoFs (c) in the FRF term and calculate Eq. (4.44) for \mathbf{Y}_{C_1,bc_i} . The so obtained partial responses may be used to analyse the contribution of each blocked force DoFs to the total vibration or sound pressure response. It is worth noting that the above velocity and FRF matrices are readily available from the force identification in Eq. (4.40), and require no additional experimental work. It is, however, necessary to include a corresponding target DoFs (d') during the system identification measurements in (C_2). As such, the responses $\dot{\mathbf{P}}_{C_2,d'a}$ and/or $\dot{\mathbf{V}}_{C_2,d'a}$ are recorded simultaneously to $\dot{\mathbf{V}}_{C_2,da}$ during the controlled operation of the calibrated blocked force exciter.

However, the forward prediction step in fastTPA, as given by Eq. (4.44), may not be used as an on-board validation procedure as described in the following. Expanding the blocked force vector with the inverse force identification in Eq. (4.40) yields,

$$\begin{bmatrix} \mathbf{p}_{C_2,d'a} \\ \mathbf{v}_{C_2,d'a} \end{bmatrix} = \begin{bmatrix} \dot{\mathbf{P}}_{C_2,d'a} \\ \dot{\mathbf{V}}_{C_2,d'a} \end{bmatrix} \dot{\mathbf{V}}_{C_1,ba}^+ \mathbf{Y}_{C_1,bc} \left[\mathbf{Y}_{C_1,bc}^+ \dot{\mathbf{V}}_{C_1,ba} \dot{\mathbf{V}}_{C_2,da}^+ \right] \mathbf{v}_{C_2,da}. \quad (4.45)$$

It is clear from the above that the terms $\mathbf{Y}_{C_1,bc}$ and $\dot{\mathbf{V}}_{C_1,ba}$ will cancel in the forward prediction. This cancellation can be interpreted as removing the effect of the assembly (C_1) in which the source was calibrated, i.e. the blocked force characterisation

at the interface DoFs. In case a perfect cancellation occurs, Eq. (4.44) reduces to a transmissibility term $\mathbf{T}_{C_2, d' d}^{(a)}$,

$$\begin{bmatrix} \mathbf{p}_{C_2, d' a} \\ \mathbf{v}_{C_2, d' a} \end{bmatrix} = \underbrace{\begin{bmatrix} \dot{\mathbf{P}}_{C_2, d' a} \\ \dot{\mathbf{V}}_{C_2, d' a} \end{bmatrix}}_{\mathbf{T}_{C_2, d' d}^{(a)}} \dot{\mathbf{V}}_{C_2, da}^+ \mathbf{v}_{C_2, da} + \boldsymbol{\mu} \quad (4.46)$$

between the target DoFs (d') and (d) due to an unknown excitation (a). The forward prediction above can therefore be interpreted as a transmissibility measurement in the same assembly (C_2). The information about the coupling DoFs (c) to compute the partial responses is added from the calibration measurements in (C_1). Note that any inversion error and measurement inconsistency in the matrix terms will lead to an improper cancellation of $\mathbf{Y}_{C_1, bc} \mathbf{Y}_{C_1, bc}^+$ and $\dot{\mathbf{V}}_{C_1, ba}^+ \dot{\mathbf{V}}_{C_1, ba}$ and may introduce some numerical uncertainty $\boldsymbol{\mu}$ to the transmissibility relation. However, the effect of an incomplete interface description in the FRF term $\mathbf{Y}_{C_1, bc}$ or unwanted variation in the reproduced excitation are not considered in the total response. Thus the convenient on-board validation procedure, as standardised in ISO 20270:2019 [38], is not suitable to assess potential errors in fastTPA.

Instead, a transferability validation approach can be adopted, where the inverse force identification and forward propagation step are separated, as outlined in Sec. 2.4.1. Here, the forward prediction uses a blocked force vector obtained from a different assembly. In essence, the transferability validation can be considered a virtual prototyping methodology. A blocked force vector from the calibration setup (C_1) is virtually recombined with the forward FRFs of assembly (C_2) to construct a VAP. With a controlled source exciter, a set of forward FRFs can be obtained from operational measurements, even for complex MIMO systems. Like fastTPA, using a controlled source in the context of VAP is denoted as ‘fastVAP’. This allows to ‘virtually’ interchange the receiver (B_1, B_2, \dots) connected to the source (A) and predict their operational response.

Validation / fastVAP procedure:

$$\begin{bmatrix} \mathbf{p}_{C_2, d' a} \\ \mathbf{v}_{C_2, d' a} \end{bmatrix} = \begin{bmatrix} \dot{\mathbf{P}}_{C_2, d' a} \\ \dot{\mathbf{V}}_{C_2, d' a} \end{bmatrix} \dot{\mathbf{V}}_{C_1, ba}^+ \mathbf{Y}_{C_1, bc} \{\bar{\mathbf{f}}_{A, c}\}_{(C_1)} \quad (4.47)$$

with $\{\bar{\mathbf{f}}_{A, c}\}_{(C_1)} = \mathbf{Y}_{C_1, bc}^+ \mathbf{v}_{C_1, ba}$ characterised in (C_1)

As noted above, the blocked force vector $\bar{\mathbf{f}}_{A,c}$ is obtained in assembly (C_1) using conventional FRF measurements to avoid matrix cancellation. Used as a validation tool, the predicted responses in Eq. (4.47) are then compared to a reference measurement made in (C_2). This transferability validation considers the velocity matrices characterised during the two stages, and thus variations in the reproduced excitation (i.e. between $\hat{\mathbf{V}}_{C_1,ba}$ and $\hat{\mathbf{V}}_{C_2,d'a}$) are accounted for. Note that the inverse velocity matrix is often ill-conditioned and contributes most to the level of uncertainty⁸ in fastTPA and/or fastVAP. However, the blocked force vector in Eq. (4.47) is obtained from conventional in-situ blocked force measurements (ISO 20270:2019), avoiding the in-situ characterisation as part of fastTPA. With the two-stage FRF procedure being neglected, the uncertainty associated with the inverse force identification is clearly not representative. Hence, Eq. (4.47) may indicate errors in the two-stage procedure of characterising FRFs rather than providing a complete validation of the fastTPA approach.

Practical application of Eq. (4.47) for validation purposes or in the context of fastVAP are presented in Sections 7.5.1 and 7.6, respectively. In addition, Chapter 7 presents a benchmark study for a detailed validation and compares the fastTPA procedure to a more conventional in-situ TPA measurement.

4.3.3 Controllability and Observability in FastTPA

The bottleneck effect and the concept of controllability and observability are strongly related to fastTPA and provide practical guidelines for the transmissibility measurement involved. As stated before, the fastTPA inverse step and forward prediction consider a set of n_a independent controlled source-side excitations, whilst the interface can be regarded as a bottleneck. Hence, the interface may limit the number of independent excitations transmitted to the passive side. Further downstream, the effect of the source excitation is observed by some remote DoFs, which are often over-determined so that a linear dependency exists in the responses relative to the interface DoFs (as the source excitations are channelled through (c)).

⁸ The uncertainty contribution from each term in fastTPA/fastVAP can be analysed using a linear covariance-based approach, as outlined in [84, 138–140]. The FRF and operational response uncertainty can be propagated through the inverse procedure onto the blocked force to identify the significant error terms. However, further discussion on this topic is considered outside the scope of this thesis. Here, regularisation techniques to minimise noise-induced errors in the inverse of an ill-conditioned matrix complicate the propagation of uncertainty and require further research [2].

The derivation of the fastTPA is based on transmissibilities and their invariance to the location of the applied excitation. The inverse force (Eq. (4.40)) is acquired via the transmissibility $\hat{\mathbf{V}}_{C_1,ba} \hat{\mathbf{V}}_{C_2,da}^+$, whilst the forward prediction (Eq. (4.44)) considers the term $\hat{\mathbf{V}}_{C_2,da} \hat{\mathbf{V}}_{C_1,ba}^+$. Note that the roles of $\hat{\mathbf{V}}_{C_2,da}$ and $\hat{\mathbf{V}}_{C_1,ba}$ are interchanged in the two steps. The invariance of the transmissibility terms is subject to controllability and observability of the inverse matrices, which function as an ‘input’.

In the following, the rank of $\hat{\mathbf{V}}_{C_2,da}$ (for the inverse step) and $\hat{\mathbf{V}}_{C_1,ba}$ (for the forward prediction) is investigated as an indicator for controllability and observability. Continuing the discussion in Sec. 3.6, four common scenarios for controllability and observability are depicted in Fig. 4.3. The examples in this overview are essentially the same as in [10]. In what follows, n_a , n_c and n_b/n_d are considered the number of independent source-side excitations, interface modes, and the number of receiver-side remote DoFs, respectively. For simplicity, DoFs (b) and (d) are positioned at the same receiver-side locations.

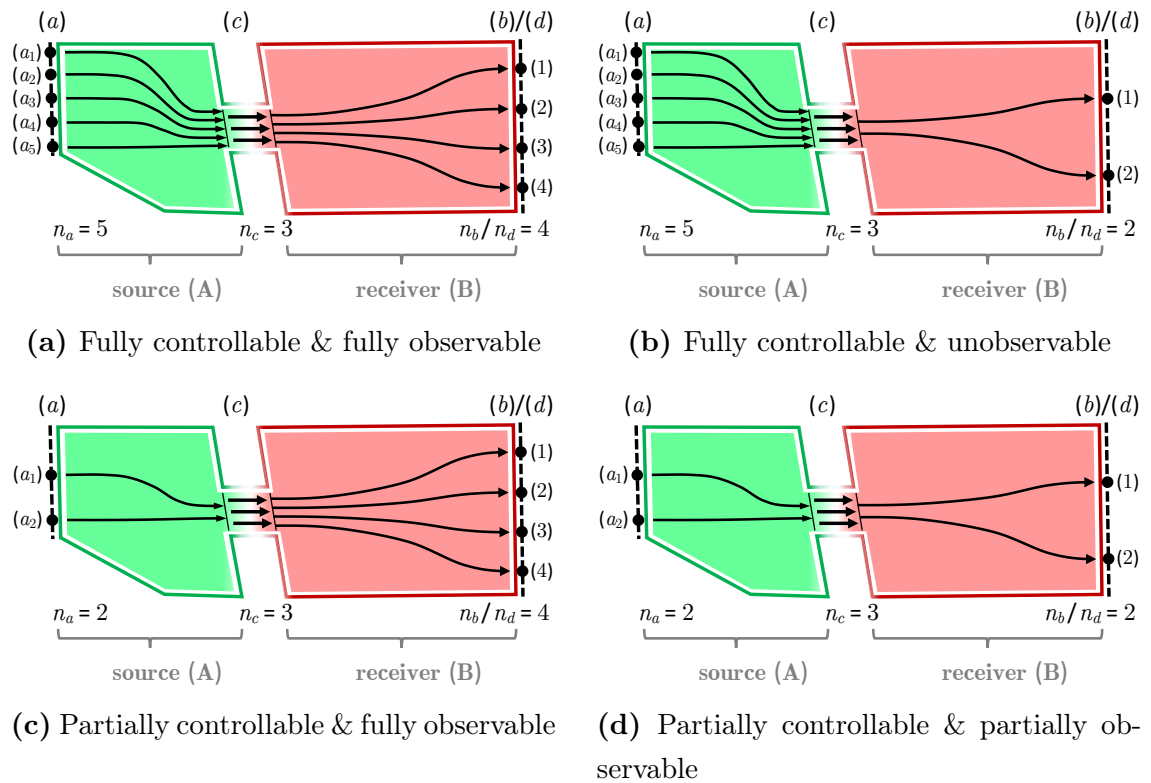


Figure 4.3: Different scenarios of controllability and observability encountered in the inverse force and forward prediction step of fastTPA. Vibrations from the controlled source (A) are channelled through the interface (bottleneck) and transmitted onto the receiver-side [10].

Note that controllability relates to the independent columns (n_a source excitation), whilst observability is a property of the rows (n_b or n_d remote DoFs) in the velocity matrices $\hat{\mathbf{V}}_{C_1,ba} \in \mathbb{C}^{n_b \times n_a}$ and $\hat{\mathbf{V}}_{C_2,da} \in \mathbb{C}^{n_d \times n_a}$, respectively. In contrast, the number of independent vibration modes at (c) is a property of the coupled structures, here fully described by $n_c = 3$ DoFs.

- (a) *Fully controllable & fully observable*: The interface (c) is fully excited from (a), with the bottleneck effect actively restricting the number of independent excitations passing through the interface. The independent response cases are fully observed on the receiving side by an over-determined set of remote DoFs (b)/(d). Therefore, the rank of $\hat{\mathbf{V}}_{C_1,ba}$ and $\hat{\mathbf{V}}_{C_2,da}$ is n_c , noticeably by a large jump in singular values due to the bottleneck effect. The fastTPA transmissibility matrices are invariant and become a property of the receiver only. In other words, the transmissibility term generally relates the responses on the passive side, even for arbitrary source excitations (a) that were not considered in the original transmissibility measurements.
- (b) *Fully controllable & unobservable*: The interface (c) is fully excited and the number of independent vibration modes is effectively restricted by the bottleneck effect. However, the n_c independent vibrations can not be observed on the passive side, thus the rank of $\hat{\mathbf{V}}_{C_1,ba}$ is n_b ($\hat{\mathbf{V}}_{C_2,da}$ is n_d) without a large jump in singular values. The transmissibility matrices are not invariant, thus additional remote sensors should be added to improve observability.
- (c) *Partially controllable & fully observable*: The independent excitations can be observed on the receiver-side, however, not all interface DoFs are excited. The excitations at (a) are unable to provide a sufficient contribution through all interface DoFs, hence the rank of $\hat{\mathbf{V}}_{C_1,ba}$ and $\hat{\mathbf{V}}_{C_2,da}$ is n_a (the bottleneck effect is not active). The transmissibility matrix correctly relates receiver responses for the excitations used at (a), yet unable to describe an arbitrary source-side force (not included in the original measurement). If additional excitations (e.g. manually with an impact hammer) are applied at (a), an increase in the number of significant singular values is a good indicator for partial controllability.
- (d) *Partially controllable & partially observable*: Not all interface modes are excited, hence the interface is not acting as a bottleneck. Although the two excitations can be observed on the passive side, the number of remote DoFs is insufficient to observe the full ($n_c = 3$) interface dynamics.

Ideally, scenario **(a)** provides an invariant transmissibility relation for the inverse and forward step in fastTPA. In other words, the ‘blocked force exciter’ implicitly accounts for all physical interface DoFs and provides a robust estimation of the assembly FRFs used in the calculation. As discussed in Sec. 3.6, it is good practice to consider $n_a \geq n_{b/d} \geq n_c$, however, to generate mutually independent operational excitations is not straightforward. In practice, full controllability may be achieved by operating the active source (A) under varying conditions to apply different load cases on the receiver (e.g. operating an electric motor under different speeds and loads). Such an approach is beneficial for completely enclosed and inaccessible sources. When access is unrestricted, external forces may be applied anywhere on the source (different positional-DoFs) to generate mutually independent excitations. Besides, in [131] it is suggested that external excitation, e.g. by an instrumented hammer, whilst the source is turned off, leads to better conditioning of the transmissibility matrix compared to a sequence of operational excitations. As for full observability, too few remote sensors $(b)/(d)$ (or too distant) may lead to neglecting essential transmission paths, i.e. some operational excitations are not observable from these points [141]. In contrast, too many remote DoFs $(b)/(d)$ (or too close to one another) can result in an ill-conditioned velocity matrix, prone to numerical inversion errors.

If the system is fully controllable and observable, the transmissibility matrices of the fastTPA approach can be determined from the dominant singular values of the velocity measurements. Typically, the rank of $\hat{\mathbf{V}}_{C_1,ba}$ and $\hat{\mathbf{V}}_{C_2,da}$ is limited by the number of interface DoFs n_c (bottleneck effect). This implies, that for $n_b > n_c$ (full observability) the operational matrices are rank deficient, although sufficient excitations are considered $n_a > n_c$ (controllability). Therefore, it is common practice to perform a truncated singular value decomposition (TSVD) of $\hat{\mathbf{V}}_{C_1,ba}$ and $\hat{\mathbf{V}}_{C_2,da}$. The lower order singular values may be rejected when the inverse is performed, since they are likely composed of measurement noise, to identify the independent system modes that are transferred across the interface [10, 137, 142].

Throughout the remainder of this thesis, unless otherwise stated, the inverse problem inherent to the transmissibility-based fastTPA is solved using a TSVD regularisation. For the rigidly coupled case, 6 significant singular values are considered at each point-like coupling interface accounting for 6 coordinate-DoFs (x , y and z translations, alongside their corresponding rotations). Other, in a sense, more complex regularisation techniques are not considered, as the system identification tries to determine a complete set of FRFs, including less dominant paths represented by low singular values, which may otherwise be subject to rejection.

4.4 Summary and Concluding Remarks

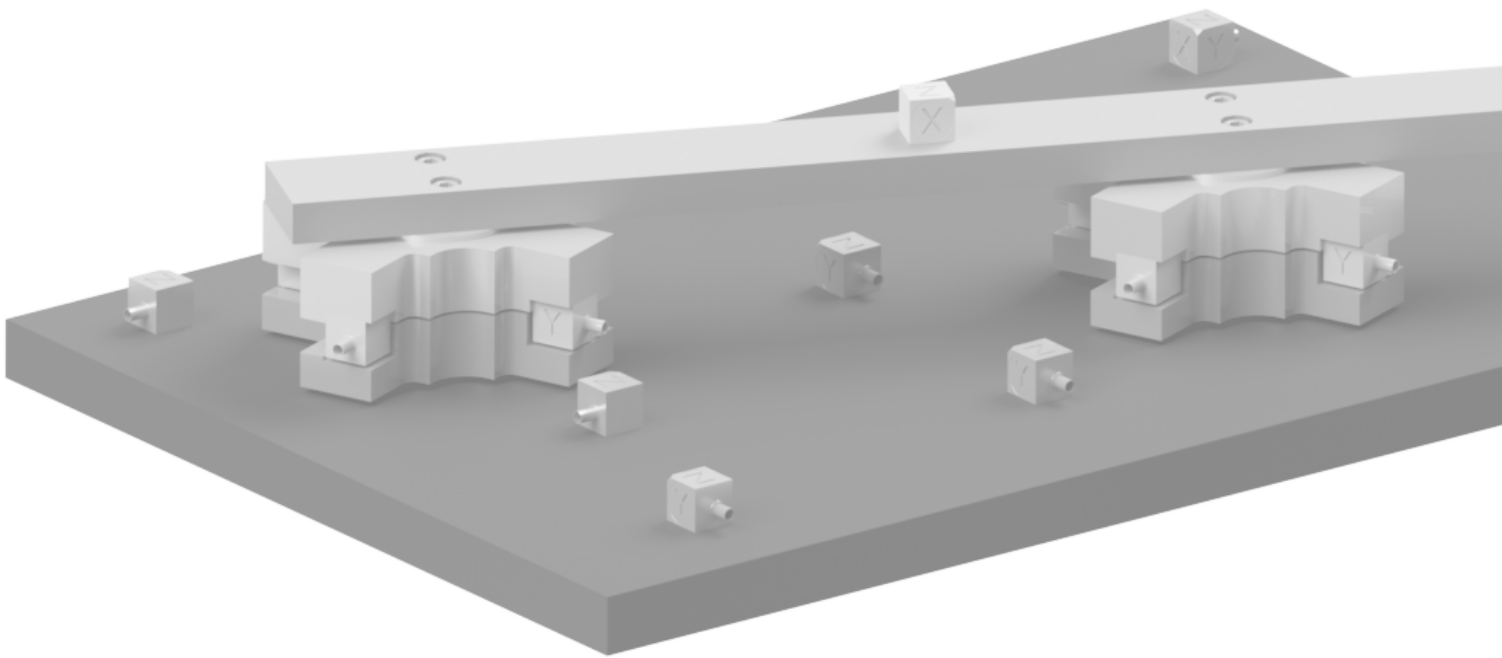
In this chapter, an alternative expression of the generalised round-trip identity has been derived complementing component-based TPA measurements, i.e. to account for a complete set of transmission paths. The concept of generalised transmissibility has been presented to simplify the implementation of the round-trip mobility relation. It has been shown that transmissibility is strongly related to the concepts of controllability and observability, whilst the same transmissibility matrix can be obtained independent of the location (on the source) where the excitation is applied. This invariance has been used to replace FRF measurements in the generalised round-trip relation by an unknown operational excitation of the active source. Concepts to obtain such an operational transmissibility matrix with a reliable phase relationship have been presented, e.g. using an H_1 -like expression or an assigned cross-spectrum phase. Hence, the generalised round-trip for inaccessible and long distance FRFs can be determined using operational velocities and is thus easier to implement.

To avoid any conventional FRF measurement in the target assembly, the already simplified round-trip relation has been split up into a two-stage measurement procedure. In a calibration stage, the blocked force output of the active source is characterised, e.g. on some specifically designed test bench. The subsequent system identification stage exploits the invariance of the blocked forces, where structural and vibro-acoustic FRFs are determined from operational response measurements only. In essence, a controlled source (e.g. the electric motor of an EPS system) operated under the same conditions is utilised as a calibrated multi-DoF blocked force exciter. Similar to the mobility concept, the FRFs of the assembly are measured as the complex ratio of a velocity response to the blocked force excitation. The two-stage measurement concept may be viewed as an extension to component-based TPA approaches, one that avoids conventional FRF measurements in the target assembly.

The blocked force exciter (two-stage procedure) not only allows us to determine a subset or even the full FRF matrix for one of the established component-based TPA methods, but also to formulate a novel fastTPA approach. The proposed method facilitates in-situ inverse force identification using blocked forces and forward prediction of total or partial responses. The experimental implementation of this relation

has been discussed alongside some potential practical benefits of the remote calibration measurement. The forward prediction step applies not only to the fastTPA response prediction, but also to a validation procedure. A transferability validation concept has been presented, which, in fact, is a virtual acoustic prototyping procedure, referred to as fastVAP. The fastTPA approach, and its VAP counterpart, facilitate reliable diagnostic tests within a very short time and minimal instrumentation effort in the target assembly. With clear advantages over conventional methods, the indirect system identification and the fastTPA approach are further investigated in the following chapters, particularly regarding their experimental validation.

PART III. Concept Testing and Simulations



5

System Identification and Validation

In this chapter, the concepts in Part II, used in the derivation of fastTPA, are validated, namely, the generalised round-trip identity, the invariance of the transmissibility, and the controlled blocked force exciter. The indirect system identification of inaccessible and long-distance FRFs is demonstrated for coupled assemblies or their sub-components. The tests are performed on different structures to investigate a single contact case, a complex MIMO system, and a long-distance scenario.

Chapter contents:

5.1	Generalised Round-Trip Identity for a Single Contact Assembly	113
5.2	Indirect System Identification for MIMO Systems	123
5.3	Steering Setup – Characterisation of Long Distance Transfer Functions	139
5.4	Summary and Concluding Remarks	144

5.1 Generalised Round-Trip Identity for a Single Contact Assembly

The previous chapters introduced the generalised round-trip identity for indirect FRF characterisation, whilst its implementation will vary depending on the context of the application. The round-trip for inaccessible FRFs is used in the development and derivation of fastTPA. In this sense, it appears essential to validate the underlying system identification concept, before considering its application to complex MIMO systems. Following its theoretical development in Sec. 3.4, the generalised

round-trip identity is validated first analytically and then experimentally, using a single contact assembly.

In this initial study, the indirect round-trip approach is applied to characterise inaccessible driving-point and transfer FRFs of a single contact (single-DoF) assembly. The coupled structure consists of two free rods joined end-to-end at point (c), as shown (not to scale) in Fig. 5.1. A prismatic rod was chosen because a closed-form analytical solution exists for the coupled system and, furthermore, it allows for the in-situ approach to be demonstrated on a non-resilient and strongly coupled assembly. The left-hand side of interface (c) is considered the source (A), and the right-hand side the receiver sub-structure (B). The DoFs (a) on the source, (b) and (d) on the receiver and (c) at the interface are defined on the axis along the centre of the rod, whilst only the +x direction (in-plane) is considered. This particular case for internal in-plane FRFs is a prime example for indirect system identification since only the two free ends (DoFs (a) and (b)) are accessible for excitation and response measurements. Other in-plane DoFs (at the interface (c) and target point (d)) are located at inaccessible positions inside the structure and cannot be directly measured or excited. Hence, driving-point and transfer FRFs need to be determined indirectly.

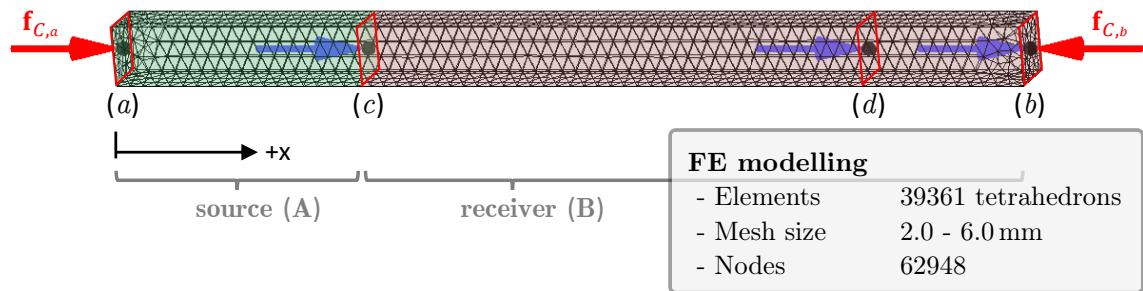


Figure 5.1: Coupled rods joined end-to-end at (c), discretised using 3D quadratic tetrahedron elements. In this single contact case, the accessible DoFs (a) and (b) at the free end, as well as the internal target location (d) and the interface (c) are defined in the x-direction.

The geometry and material properties of the aluminium rod are given in Table 5.1. Also given are the excitation and response positions used in the study.

Table 5.1: Geometry, material properties and excitation/response positions for the free-free rod, where; l -length, h - height, E_0 - Young's modulus, ρ - density and ν - Poisson's ratio, and x_{ik} - DoF positions of (a), (c), (d) and (b).

Material	l (m)	h (m)	E_0 (N/m ²)	ρ (kg/m ³)	ν (-)	x_{ik} (m)
Aluminium	1.83	0.025	69×10^9	2670	0.32	{0, 0.50, 1.50, 1.83}

To compare the indirect results for $Y_{C,cc}$ and $Y_{C,dc}$ usually requires a direct reference measurement. However, in a real measurement, the excitation at the coupling interface (c) or the target location (d) is impractical, if not impossible. In such a case, in-plane excitation is often applied off-centre via some rigid block glued to the outer surface of the rod, effectively causing a force and moment excitation at the internal in-plane DoF (centre axis). Instead, reference data may be obtained through an analytical or numerical finite element (FE) simulation. Such an FE model can easily be generated due to the simplicity of the rod's geometry (without small features or curved surfaces) and does not require a detailed mesh [143]. Both computational approaches are used in Sec. 5.1.2 to validate experimental round-trip results for the driving-point and transfer mobility.

Before the experimental implementation, an analytical model of the coupled rods is presented to test the generalised round-trip relation [9]. Later, the findings are combined with experimental and numerical data to validate the practical application for a single-DoF case.

5.1.1 Free-Free Rod Model – Analytical Verification

The following case study provides an initial verification of the theoretical developments in Sec. 3.4.2, based on an analytical model of two rigidly coupled rods. The individual path segments for the generalised round-trip identity in Eq. (3.19) and the special case for driving-points in Eq. (3.1) are obtained from a full-length rod model. The analytical expressions for the mobility terms are combined to reconstruct the internal transfer and driving-point mobilities, $Y_{C,dc}$ and $Y_{C,cc}$, respectively, which are then compared to the exact analytical solution. By modelling the structural FRFs of the assembly, the generalisation of the round-trip concept is tested analytically, free from noise and measurement errors.

For simple geometries, such as a free-free rod, longitudinal vibration modes can be calculated from the one-dimensional wave equation [144]. Partial differential equations typically describe the dynamic behaviour depend on time and spatial coordinates [145, 146]. This expression solved for free boundary conditions may be transformed into the frequency domain to obtain a mobility formulation. Considering longitudinal vibrations, the in-plane mobility of a free-free rod excited at an

arbitrary point (x_k) is given by [9, 147] as,

$$Y_{ik} = \frac{v_i}{f_k} = \begin{cases} \frac{-j \cos kx_i \cos k(l-x_k)}{\rho A c_L \sin kl}, & \text{for } x_i \leq x_k \\ \frac{-j \cos k(l-x_i) \cos kx_k}{\rho A c_L \sin kl}, & \text{for } x_i \geq x_k \end{cases} \quad (5.1)$$

$$\text{with } \begin{cases} c_L = \frac{\omega}{k} & \text{longitudinal wave speed} \\ k = \sqrt{\frac{\rho}{E}} \omega & \text{longitudinal wavenumber} \end{cases}$$

where (x_i) denotes the response position. The mobility is determined in terms of the imaginary unit $j = \sqrt{-1}$, the longitudinal wave number k , the wave speed c_L in the rod, and the cross-sectional area A together with the rod's length l . Note that mobility expressions in Eqs. (5.1) and (5.2) depend on the excitation position on the rod with respect to the response DoF, i.e. one must distinguish whether $x_i \leq x_k$ or $x_i \geq x_k$.

It can be confirmed that the expressions in Eqs. (5.1) and (5.2) satisfy the boundary conditions of a free-free rod. The axial stress σ must be equal to zero at both free ends ($x_i = 0, x_i = l$),

$$\sigma(x_i, t) = E \varepsilon(x_i, t) = E \frac{\partial u(x_i, t)}{\partial x_i} = 0 \quad (5.3)$$

with Hooke's law stating direct proportionality between the stress σ to the axial strain ε expressed by the gradient of the longitudinal displacement u [59, 148]. At the unconstrained free ends, the natural boundary condition is given by,

$$\left. \frac{\partial u(x_i, t)}{\partial x_i} \right|_{x_i=0} = 0, \quad \left. \frac{\partial u(x_i, t)}{\partial x_i} \right|_{x_i=l} = 0. \quad (5.4)$$

Note that the conditions are given as partial differentials with respect to the spatial coordinate. For the mobility relations above, it is generally more convenient to express the imposed boundary condition in the frequency domain as a velocity constraint,

$$v(x_i) = \frac{\partial u(x_i, t)}{\partial t} = j\omega u(x_i) \quad (5.5)$$

through the first time derivative of displacement u . In the frequency domain, an equivalent boundary condition for the free ends can be defined,

$$j\omega \left. \frac{\partial v(x_i)}{\partial x_i} \right|_{x_i=0} = 0, \quad j\omega \left. \frac{\partial v(x_i)}{\partial x_i} \right|_{x_i=l} = 0. \quad (5.6)$$

For completeness, the analytic rod model satisfies the boundary conditions in Eq. (5.6) at its free ends, in conjunction with the continuity of motion and the equilibrium condition at the excitation point. The following kinematic continuity and equilibrium conditions between neighbouring elements are enforced,

$$v(x_i)_- \Big|_{x_i \rightarrow x_k} = v(x_i)_+ \Big|_{x_i \rightarrow x_k} \quad (5.7)$$

$$\left(\frac{\partial v(x_i)_-}{\partial x_i} - \frac{\partial v(x_i)_+}{\partial x_i} \right) \Big|_{x_i \rightarrow x_k} = \frac{j\omega}{AE} f_k \quad (5.8)$$

where v_- and v_+ denote the solutions to the left and right, respectively, of the excitation point x_k [144]. The equilibrium condition for $x_i \rightarrow x_k$ considers the axial stresses (compare Eq. (5.3)) by differentiating Eqs. (5.1) and (5.2) and substituting $x_i = x_k$. Subtracting the left and right solutions gives the expected discontinuity due to the applied excitation f_k .

To verify the concept of the generalised round-trip identity in Eq. (3.19), the excitation ($x_k = (a), (b)$) and response ($x_i = (d), (b), (c)$) positions of the three transfer path segments are substituted into Eqs. (5.1) and (5.2) to obtain an analytic expression of each mobility term. For the prismatic rod in Fig. 5.1 the following transfer mobility terms between the four positional-DoFs are obtained,

$$Y_{C,da} = \frac{-j}{\rho Ac_L} \frac{\cos k(l-d) \cos ka}{\sin kl} \quad \text{with } x_k = a \text{ and } x_i = d \quad (5.9)$$

$$Y_{C,ba} = \frac{-j}{\rho Ac_L} \frac{\cos k(l-b) \cos ka}{\sin kl} \quad \text{with } x_k = a \text{ and } x_i = b \quad (5.10)$$

$$Y_{C,cb}^T = \frac{-j}{\rho Ac_L} \frac{\cos k(l-b) \cos kc}{\sin kl} \quad \text{with } x_k = b \text{ and } x_i = c. \quad (5.11)$$

Combining the three path segments in Eqs. (5.9) - (5.11) to the generalised round-trip according to Eq. (3.19) yields the transfer mobility,

$$Y_{C,dc} = Y_{C,da} Y_{C,ba}^{-1} Y_{C,cb}^T = \frac{-j}{\rho Ac_L} \frac{\cos kc \cos k(l-b)}{\sin kl} \quad (5.12)$$

between the virtual coupling interface (c) and an arbitrary target location (d) on the receiver-side (B) of the rod. The same mobility relation can be obtained from the appropriate substitution of ($x_k = (c)$) and ($x_i = (d)$) in Eq. (5.2). This confirms the generalisation of the round-trip concept for this case with exact modelled data. It is clear from the above that a cancellation occurs between the denominator and the numerator of the coupled mobility terms. An inconsistency between the three, for example, due to them being obtained from separate tests or changing conditions, will lead to an imperfect cancellation and artefacts in the reconstructed mobility $Y_{C,dc}$.

Note that by moving points (d) to coincide with (c), i.e. identical DoFs ($c = (d)$), the single interface form of the round-trip identity as given in Eq. (3.1) is obtained. Hence, the analytical mobility term $Y_{C,da}$ is replaced by $Y_{C,ca}$ to determine the driving-point mobility at the interface of the two rigidly coupled rods,

$$Y_{C,ca} = \frac{-j}{\rho A c_L} \frac{\cos k(l-c) \cos ka}{\sin kl} \quad \text{with } x_k = a \text{ and } x_i = c \quad (5.13)$$

$$Y_{C,cc} = Y_{C,ca} Y_{C,ba}^{-1} Y_{C,cb}^T = \frac{-j}{\rho A c_L} \frac{\cos kc \cos k(l-c)}{\sin kl}. \quad (5.14)$$

Evaluating the exact result from Eqs. (5.1) or (5.2) for collocated excitation and response DoFs, i.e. $x_i = x_k = (c)$, is again in agreement with the single interface round-trip result in Eq. (5.14) [9].

It has been shown that the analytical expression of the in-plane transfer and driving-point mobility for two virtually coupled rods can be obtained indirectly via the generalised round-trip identity. In what follows, the practical implementation of the indirect in-situ system identification concept is demonstrated.

5.1.2 Force Excited Rod – Experimental Validation

The experimental validation presented in this section demonstrates a practical application of generalised round-trip identity using a relatively simple but realistic single-DoF structure. Instead of using two coupled sub-structures, the rod, shown (not to scale) in Fig. 5.2, is virtually separated into two sides, a source (A) and a receiver (B). For the measurement campaign, the aluminium rod is resiliently suspended to achieve free boundary conditions.

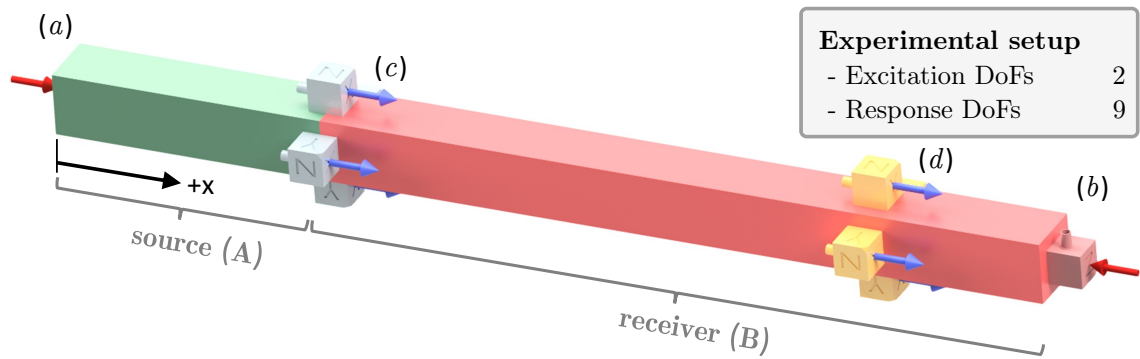


Figure 5.2: Experimental setup of two virtually coupled rods for indirect identification of the structural properties using the generalised round-trip identity. Four surface-mounted accelerometers characterise the inaccessible coupling interface (c) and target DoF (d).

In this experimental setting, only the in-plane DoFs at (a) and (b) are accessible for direct excitation at the free ends. Hence, this single-DoF system does not facilitate over-determination by considering additional DoFs. At the inaccessible DoFs (c) and (d), 4 spaced accelerometers are placed on the different sides of the rod to approximate an in-plane measurement in the centre. From a practical point of view, this sensor configuration accounts for the surface mounted position with a lever to the rod's centre (similar to the finite difference approximation in Sec. 2.3.2) and is likely more robust than a single sensor. Averaging the spaced mobilities in x-directions effectively removes superimposed rotational contributions (bending of the rod) from the idealised translational measurement, for example, due to an off-centre excitation at (a) or (b). An additional remote sensor is positioned at (b), directly aligned in the in-plane direction at the free end. The round-trip measurement procedure (1.-3.), including the validation process (*), may be outlined as follows:

1. The assembly FRFs $\mathbf{Y}_{C,da} \in \mathbb{C}^{4 \times 1}$ and $\mathbf{Y}_{C,ba} \in \mathbb{C}^{1 \times 1}$ are measured simultaneously using a shaker excitation (red arrow) at the source-side DoF (a).
 2. To avoid misalignment and inconsistency, the transfer FRFs $\mathbf{Y}_{C,cb} \in \mathbb{C}^{4 \times 1}$ on the passive side are determined by direct excitation (red arrow) on the sensor housing at (b), whilst the responses (blue arrows) are measured at (c).
 3. The rows of the spaced 4×1 mobilities ($\mathbf{Y}_{C,da}$ and $\mathbf{Y}_{C,cb}$) are averaged to approximate the transfer mobility in the central point. Using the generalised round-trip formulation in Eq. (3.19), the inaccessible FRFs $\mathbf{Y}_{C,cc} \in \mathbb{C}^{1 \times 1}$ and $\mathbf{Y}_{C,dc} \in \mathbb{C}^{1 \times 1}$ are predicted from indirect measurements.
- * To provide a validation method, reference FRFs are obtained from the analytical model in Sec. 5.1.1 and a numerical simulation.

In this example, the analytical and numerical results of $Y_{C,cc}$ and $Y_{C,dc}$ are of particular interest for the validation * of experimental data since the direct measurement is simply not feasible. As such, the inaccessible driving-point and transfer FRFs are modelled analytically using Eqs. (5.1) and (5.2) for a free-free rod of equal length. Redundant information for the validation may be obtained from a numerical simulation using a truncated modal summation. A finite element (FE) model of the rod is illustrated in Fig. 5.1, using a mesh with tetrahedral elements¹. To account for the effect of structural damping in both analytical and numerical approaches, a complex elastic Young's modulus is considered,

$$E = E_0(1 + j\eta) \quad (5.15)$$

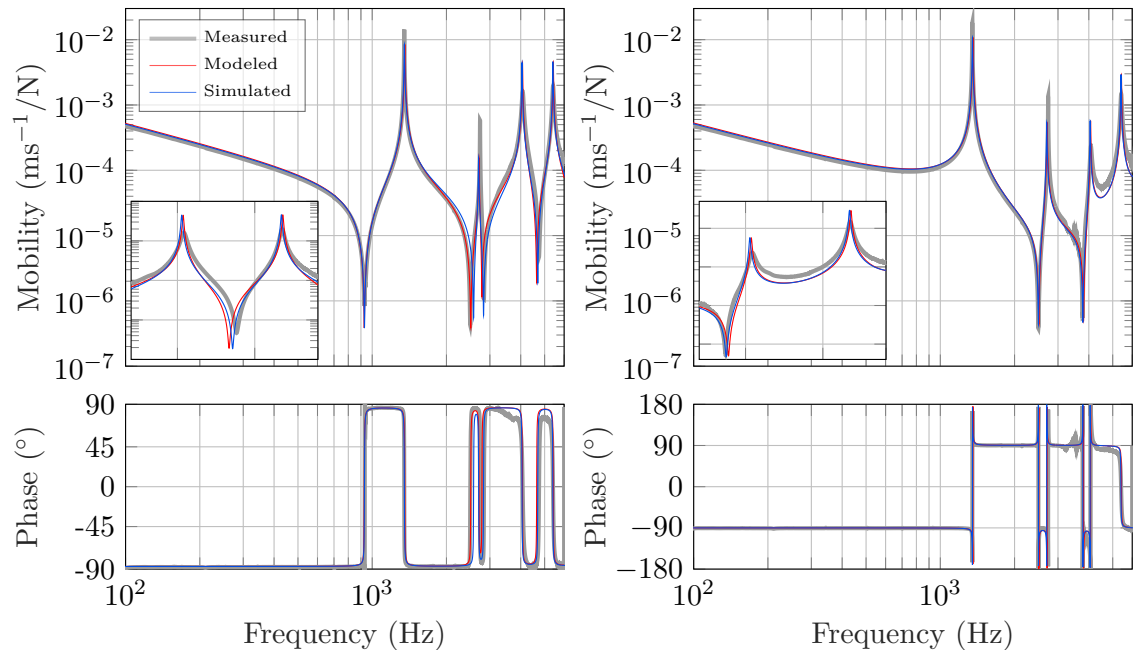
with an assigned structural loss factor η of 0.4%, which also affects the associated wave number k [149]. However, achieving matching results and idealised free boundary conditions can often be challenging when comparing the computed and experimental scenario. Differences between the analytical/numerical results and the experiments are avoided, in part, by adjusting the material parameters given in Table 5.1 in an updating procedure (using a gradient-based optimisation; *fmincon()* in MATLAB). The chosen updating parameters are the global material properties: density ρ , Young's modulus E_0 and loss factor η .

Experimental data in this section and throughout the thesis are captured at 12 kHz using a multi-channel HEAD Acoustics data acquisition system (HEADlab) while all further post-processing is performed in MATLAB. For conventional FRF measurements, acceleration responses are measured using tri-axial and single-axis accelerometers (PCB 356A14 and 352A24), whilst a miniaturised shaker (LMS Q-MSH) is used to apply broadband (white noise) force excitation. Assuming the input excitation is comparatively free from noise, all FRFs are calculated using the H_1 -estimator at a frequency resolution of 0.732 Hz and a corresponding FFT length of 16384 samples. Lastly, each FRF is determined from the linear average of a 90 s recording.

Shown in Fig. 5.3a is the experimentally determined in-plane driving-point mobility $Y_{C,cc}$ using the indirect generalised round-trip approach in Eq. (3.19) (—), compared to the directly computed results of the analytic model (—) and the FE simulation (—). It can be seen that both the calculations are in near-perfect agreement with

¹ The structural mesh built from tetrahedron elements may appear to be bad practice for FE modelling of prismatic geometries. However, this element type, supported by the MATLAB mesh generator, yields sufficient results, whilst the focus of this case study is not on creating a highly accurate numerical model.

the indirectly measured driving-point mobility. This may in itself be considered a validation of the single interface form of the round trip identity as given in [9].



(a) In-plane driving-point mobility: $Y_{C,cc}$ (b) In-plane transfer mobility: $Y_{C,dc}$
(Inset covers freq. range from 3.5 - 6 kHz) (Inset covers freq. range from 3.5 - 6 kHz)

Figure 5.3: Validation of the generalised round-trip identity for the interface driving-point mobility and the transfer FRF from (c) to the target DoF (d) of the single contact assembly. Narrowband representation of amplitude (top) and phase spectra (bottom): experimental round-trip data (—); analytically modelled (—); and FE simulation (—).

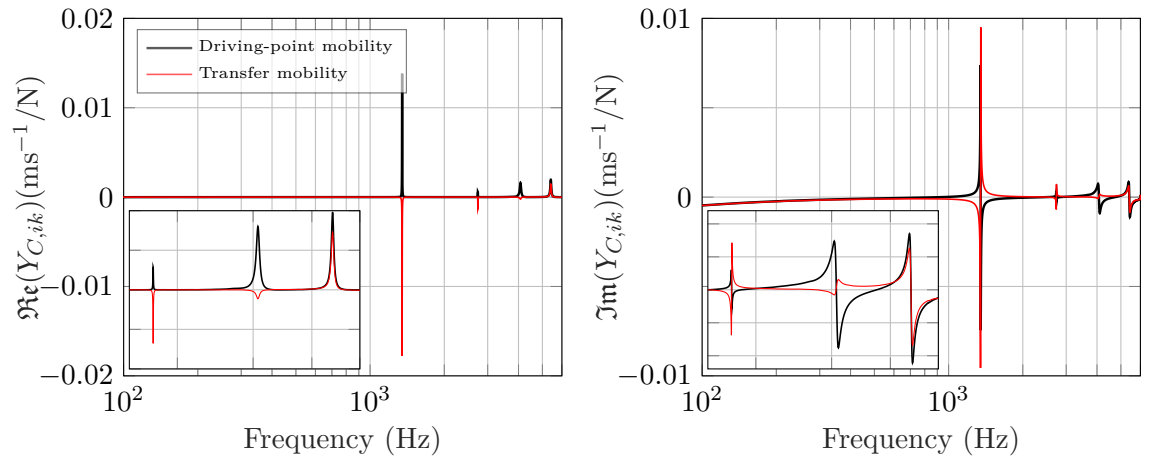
The proposed extension for receiver-side target DoFs (d) is demonstrated in Fig. 5.3b with a similar, remarkably good agreement. As shown more clearly in the insets of Fig. 5.3, shifts in the resonant frequencies are on the scale of numerical error or result from inaccurate determined geometrical or material properties. Especially geometrical variations evoke anti-resonance shifts due to their dependence on the response and excitation position [145, 150]. Furthermore, it can be seen that the analytical and numerical predictions tend to underestimate the free rod resonances at frequencies below 3 kHz. This is likely a result of some minor frequency dependence in the material properties, e.g. of the loss factor η , which are not accounted for in the simplified models. High frequency noise at the 3.8 kHz anti-resonance encountered in the round-trip measurement in Fig. 5.3b is caused by an insufficient SNR on the measurement of $Y_{C,ba}$, due to the relatively long transmission path. However, undesired measurement noise may be reduced by over-determination (shown in the following multi-DoF case study), that is, additional excitation/responses are

considered at (a) and (b). The agreement of the analytical mobility terms with the direct FE simulation not only confirms the potential of the model presented in the previous section, but also validates the experimental application of the generalised round-tip identity for single-DoF systems, albeit on a simple assembly.

When examining the reconstructed round-trip FRFs, it is useful to check if the driving-point and transfer measurements are dynamically plausible. Note that by moving points (d) to coincide with (c), i.e. identical DoF ($c = d$), the single interface form of the round-trip identity is obtained. Such driving-point measurements are referred to as ‘collocated’ vibration problem and associated with a minimum phase system. Typically, as shown in Fig. 5.3a, the amplitude of a driving-point mobility is a sequence of alternating anti-resonances and resonances with a phase confined between $\pm 90^\circ$ [144, 151]. On the other hand, transfer mobilities are measured between ‘non-collocated’ excitation and response positions. As shown in the inset of Fig. 5.3b, natural frequencies do not necessarily alternate with anti-resonances, and the phase is not bounded. To summarise, the variation from collocated DoFs ($c = d$) to non-collocated ($c \neq d$) interface and target positions changes the minimum-phase system, which can be seen in the real- and imaginary part of the mobilities. The complex mobility matrix (compare Eq. (2.3)) may be written more explicitly as,

$$\mathbf{Y}_{ik}(\omega) = \Re\{\mathbf{Y}_{ik}(\omega)\} + j \cdot \Im\{\mathbf{Y}_{ik}(\omega)\} = \mathbf{G}(\omega) + j \cdot \mathbf{B}(\omega) \quad (5.16)$$

where the conductance $\mathbf{G}(\omega)$ and the susceptance $\mathbf{B}(\omega)$ matrices represent the real and imaginary part, respectively [13, 42]. The separated real part is a square matrix with diagonal symmetry that is either positive definite or positive semi-definite. This condition results from passivity, since the vibrational power applied at the driving-point can only flow into the structure, thus always positive, resulting in a displacement in the same direction [59]. As a requirement, the real part of the driving-point mobilities (\mathbf{G}), i.e. the diagonal elements in the conductance matrix $\mathbf{G}(\omega)$, must be greater than or equal to zero. On the other hand, the off-diagonal transfer mobility elements (\mathbf{B}) are not bound to be positive real, as shown in the experimental data in Fig. 5.4a. A negative real part indicates an energy transfer back to the exciter, which occurs in the illustrated transfer mobility function $Y_{C,dc}$. The imaginary part $\mathbf{B}(\omega)$ in Fig. 5.4b relates to the reactive character of the structure, which may either be mass or stiffness-like, indicated by a negative or positive imaginary part, respectively [59, 149, 152].

(a) Real part of $Y_{C,cc}$ and $Y_{C,dc}$

(Inset covers real part from 2.5-6 kHz)

(b) Imaginary part of $Y_{C,cc}$ and $Y_{C,dc}$

(Inset covers imaginary part from 2.5-6 kHz)

Figure 5.4: Representation of the real \Re and imaginary \Im part of the experimentally determined driving-point mobility $Y_{C,cc}$ (—) and the transfer mobility $Y_{C,dc}$ (—) using the generalised round-trip identity.

It has been shown that passive properties of two virtually coupled rods can be obtained experimentally via the generalised round-trip identity, without the need to apply direct excitation at the interface or the target DoF. The specific characteristics of the real and imaginary part of the complex mobility term can be used to examine the reconstructed FRFs and as an indicator for measurement errors. In the following, the generalised round-trip concept is experimentally validated for a more complex MIMO system (multi-contact, multi-DoF).

5.2 Indirect System Identification for MIMO Systems

In this section, the experimental validation considers a case with more than one degree of freedom at the interface. The indirect system identification of the assembly, the receiver, or the source installed in a different assembly will be demonstrated as part of three experimental multi-contact, multi-DoF examples. In the first example, the indirect approach outlined in Sec. 3.4.2 is adopted to characterise translational and rotational FRF terms inaccessible for direct force excitation. With previous works having focused on the theory and validation of the single interface round-trip identity [9, 153] (limited to driving-point FRFs), this section will consider the generalised implementation for transfer functions with non-collocated excitation and response measurements. The second part considers the sub-structure

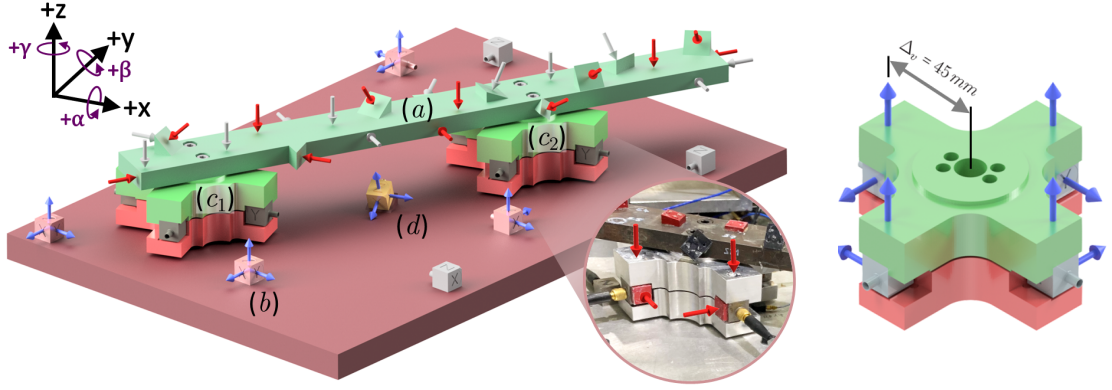
form of the round-trip, as proposed in Sec. 3.5, and the invariant property of the transmissibility matrix. The third part then uses the source sub-component as a multi-contact, multi-path vibration exciter for system identification in a different installation. These FRF measurements with an exciter form the basis of fastTPA, however, the inverse force identification and forward prediction steps for the analysis are not demonstrated (see case studies in Chapter 7). Note that indirect characterisation of long distance transfer functions is presented in Sec. 5.3 in a separate study for a sufficient path length.

In these experimental studies, a miniaturised shaker was used to apply broadband (white noise) force excitation for FRF measurements. Alternatively, all FRFs may be obtained experimentally using impact excitations, however, the experimental uncertainty of roving hammer tests is highly subject to the skill of the experimentalist. In addition, the application of mini-shakers is preferred in this study since the force output can easily be controlled as required for the experiments described in Sec. 5.3.

5.2.1 Beam-Plate Assembly – Generalised Round-Trip Identity for Inaccessible Assembly FRFs

This experimental study focuses on the ability of the generalised round-trip concept to determine inaccessible transfer functions of a complex multi-DoF structure. A steel beam rigidly coupled to an aluminium plate (see Fig. 5.5a) was chosen so as to introduce sharp, minimally damped resonances, representing what may be encountered in a challenging practical scenario. The cross-like coupling elements (see Fig. 5.5b), denoted by (c_1) and (c_2) , have been designed to facilitate the characterisation of 6 DoFs by using 2 bi-axial sensor pairs (separation distance $\Delta_v = 45 \text{ mm}$). From the acceleration measurements indicated by blue arrows, translational and angular responses are approximated in the central point of each cross using the finite difference approach [77].

The inaccessible transfer FRFs $\mathbf{Y}_{C,d}$ are determined from all 12 DoFs of the cross-like coupling elements (c_1) and (c_2) to the target tri-axial accelerometer (d) , highlighted in yellow. Note that a wedge, as part of the receiver structure, rotates the direction of the target sensor to capture the structural response with a superposed contribution from all significant coupling DoFs (c) . Per definition, the sensor (d) , located below the beam, and both coupling interfaces are inaccessible for direct force excitation, prohibiting the direct measurement of the transfer functions.



(a) Multi-connection beam-plate assembly for experimental validation of inaccessible FRFs between the cross-like coupling elements (c_1, c_2) and target positions (d), covered by the beam. (b) Cross-like interface with 4 bi-axial accelerometers.

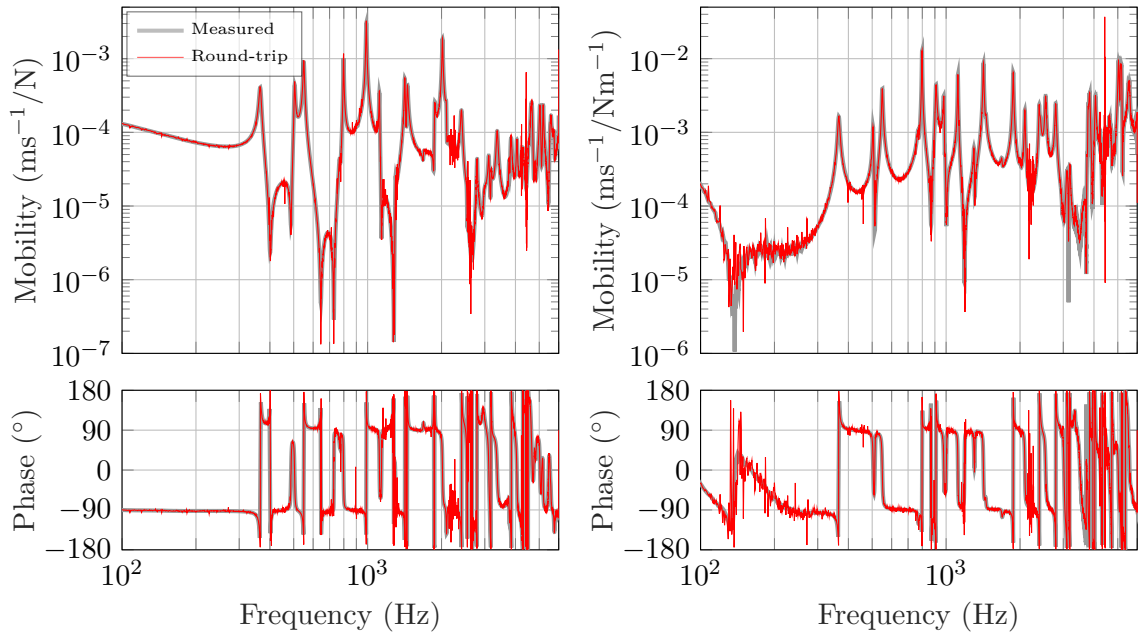
Figure 5.5: Test structure for indirect determination of \mathbf{Y}_{C,dc_1} and \mathbf{Y}_{C,dc_2} . Arrows indicate the excitation (red) and response (blue) measurements utilised in the FRF reconstruction using the generalised round-trip concept, whilst excitations depicted in the close-up inset are required for the reference measurements. The source-receiver setup contains: beam - source (A); plate - receiver (B); cross-like elements with the coupling interfaces (c_1, c_2) being positioned exactly in its center plane; inaccessible target DoFs (d).

The round-trip is calculated from 12 artificial source-side excitations (beam - (a)), depicted by red arrows, applied in different directions distributed over the entire beam. This generates mutually independent excitations to satisfy the controllability requirement for a determined system (i.e. $n_a = n_c = 12$), as described in Sec. 3.6. The responses are observed downstream of the cross-like elements on the passive side (plate - (b)) by 4 tri-axial accelerometers. Later, 12 additional excitations (a) and 3 remote response sensors (b), indicated in grey (see Fig. 5.5a), are used for an over-determination of the round-trip equation. The round-trip measurement procedure (1. - 3.), including the validation process (*), may be outlined as follows:

1. The assembly matrices $\mathbf{Y}_{C,da} \in \mathbb{C}^{3 \times 12}$ and $\mathbf{Y}_{C,ba} \in \mathbb{C}^{12 \times 12}$ are measured simultaneously using a roving shaker approach (see Fig. 5.5a), with 12 excitations (red arrows) at different source-side locations (a) on the beam.
2. The matrix $\mathbf{Y}_{C,cb} \in \mathbb{C}^{12 \times 12}$ on the passive side is determined by direct force excitation on the accelerometers' faces at (b) and response measurements at the interface, indicated by blue arrows in Fig. 5.5b.
3. Using the generalised round-trip formulation in Eq. (3.19), the inaccessible transfer FRFs $\mathbf{Y}_{C,dc} \in \mathbb{C}^{3 \times 12}$ are predicted from indirect measurements.

* To provide a validation method, reference FRFs are directly obtained from measurements on the cross-like elements. The tailored design allows for conventional FRF measurements, depicted by red arrows in the inset of Fig. 5.5a.

Shown in Fig. 5.6 are the predicted transfer FRFs using the indirect generalised round-trip approach in Eq. (3.19) (—), compared to the conventional validation measurement (—). The selected transfer functions ($\mathbf{Y}_{C,dc} \in \mathbb{C}^{3 \times 12}$) displayed here describe the out-of-plane force (see Fig. 5.6a) and in-plane moment (see Fig. 5.6b) excitation at (c_1), whereas the target response is measured in the rotated out-of-plane direction (d). Over a multi-kHz range (100 Hz - 6 kHz), the reconstructed mobilities are in good agreement with the reference measurement, although influenced by undesired measurement noise, most notably in Fig. 5.6b. This can be understood from the experimental setup (see Fig. 5.5a): most excitations are pointing in the z -direction, making it difficult to excite the in-plane coupling DoFs sufficiently and explains the higher deviations for the moment excitation.



(a) Out-of-plane force: $Y_{C,dc} - (d)/(c_{1z})$

(b) In-plane moment: $Y_{C,dc} - (d)/(c_{1\gamma})$

Figure 5.6: Validation of inaccessible transfer functions $\mathbf{Y}_{C,dc}$ using a determined system of equations ($n_a = n_b = n_c = 12$). Narrowband representation of amplitude (top) and phase spectra (bottom): reference measurement (—); compared to the indirect generalised round-trip identity (—).

Matrix inversions are known to amplify the effect of noise, and so the assembly matrix $\mathbf{Y}_{C,ba}$ is sensitive to experimental error. In this particular example, the

highly resonant assembly tends to cause poor conditioning, therefore, $\mathbf{Y}_{C,ba}$ is ill-conditioned and susceptible to inversion errors. At lower frequencies, the bending wavelength is large compared to the spacing of the remote DoFs (b) on the receiver. The similar responses measured at (b) result in some mutual dependence between columns of the corresponding FRF matrix. Inverse methods, such as the generalised round-trip approach considered in this work, are often susceptible to noise-induced errors and uncertainty arising from the experimental test and ill-conditioning. Although there exist numerical techniques to minimise this effect (e.g. regularisation), it is recommended to spend some effort on acquiring reliable experimental data instead of relying on such post-processing techniques. Nevertheless, even the most carefully executed experiments will be subject to some degree of uncertainty. For a more detailed discussion, previous works have focused on this issue, particularly reducing experimental uncertainty through over-determination or regularisation methods [47, 48].

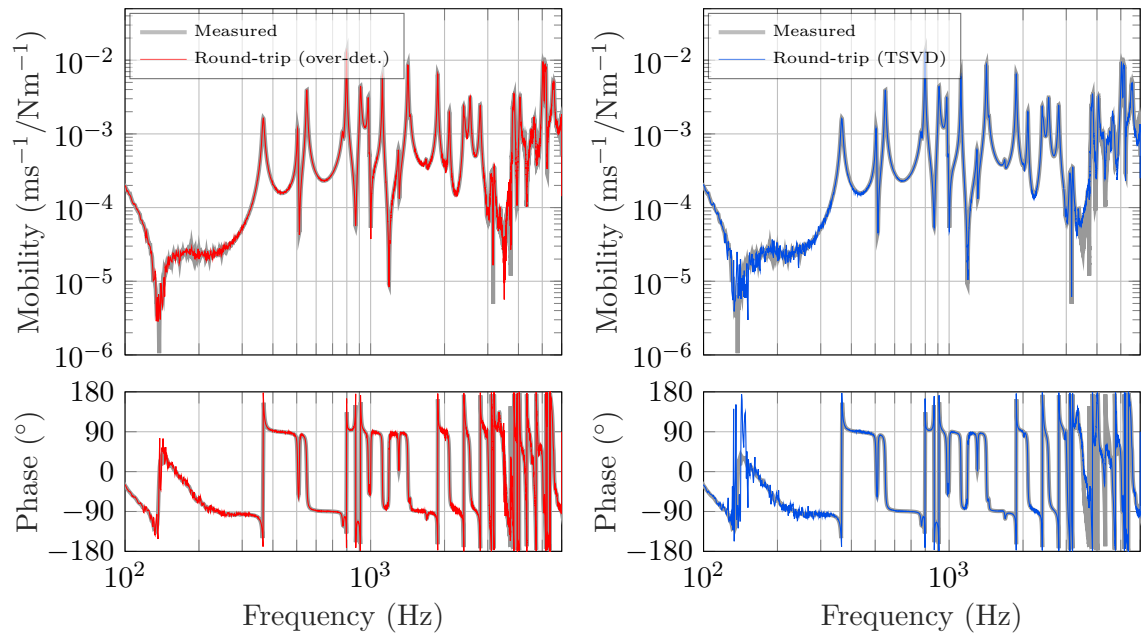
The above concepts of over-determination and regularisation may be adapted straightforwardly to reduce noise in the round-trip result. Eq. (3.19) does facilitate over-determination by including additional remote DoFs at (a) and (b), respectively. As indicated in Fig. 5.5a, 12 additional beam excitations and 3 tri-axial response sensors (depicted in grey) are considered in the amended mobility terms ($\mathbf{Y}_{C,da} \in \mathbb{C}^{3 \times 24}$; and $\mathbf{Y}_{C,cb} \in \mathbb{C}^{12 \times 21}$). This results in the inversion of a non-square, over-determined FRF matrix, $\mathbf{Y}_{C,ba} \in \mathbb{C}^{21 \times 24}$. Hence, the standard matrix inverse is replaced by a Moore-Penrose pseudo-inverse [23], leading to a least-squares solution of the problem, likely to reduce inversion errors when implemented correctly. This over-determined mobility reconstruction is shown in Fig. 5.7a for the in-plane moment mobility. Over-determination of the inverse problem by a set of remote DoFs ($n_a \geq n_b \geq n_c = 12$) provides a robust prediction by exceeding the basic requirement for controllability and observability (see Sec. 3.6).

Alternatively, Fig. 5.7b shows the improvement of the moment mobility by a truncated singular value decomposition of the initial determined system ($n_a = n_b = n_c = 12$) [154]. In this simple regularisation, the two least significant singular values of $\mathbf{Y}_{C,ba}^{-1} \in \mathbb{C}^{12 \times 12}$ are rejected since lower order singular values are likely composed of measurement error and noise. In this case, rejection of 2 singular values can be interpreted as reducing the interface description at each point-like (positional-DoF) contact to 5 coordinate-DoFs. It is assumed that there is redundancy in the multi-contact interface description; hence not all 12 coupling DoFs are required to

represent the physical coupling dynamics. The truncated matrix inverse may be determined through the SVD factorisation of $\mathbf{Y}_{C,ba}$, given by,

$$\mathbf{Y}_{C,ba}^{-1} = \mathbf{V}(\mathbf{W}\mathbf{\Sigma})^{-1}\mathbf{U}^T \quad \text{with} \quad \mathbf{W} = \begin{bmatrix} 1 & 0 & 0 & 0 & 0 \\ 0 & \ddots & 0 & 0 & 0 \\ 0 & 0 & 1 & 0 & 0 \\ \hline 0 & 0 & 0 & 0 & 0 \\ 0 & 0 & 0 & 0 & 0 \end{bmatrix} \in \mathbb{R}^{12 \times 12} \quad (5.17)$$

where the columns of \mathbf{U} and \mathbf{V} are the left and right singular vectors, respectively. The diagonal matrix $\mathbf{\Sigma} = \text{diag}(\sigma_1, \sigma_2, \dots, \sigma_{12})$ contains the singular values σ_i of $\mathbf{Y}_{C,ba}$ in descending order. The weighting matrix \mathbf{W} effectively removes the two least contributing singular values (σ_{11} and σ_{12}) [47]. The truncated round-trip is obtained by substituting the regularised inverse formulation of Eq. (5.17) into Eq. (3.19).



(a) Over-determined system: $Y_{C,dc} - (d)/(c_{1\gamma})$ (b) Truncated system: $Y_{C,dc} - (d)/(c_{1\gamma})$

Figure 5.7: Validation of the inaccessible FRF $\mathbf{Y}_{C,dc}$ for an over-determined solution ($n_a \geq n_b \geq n_c = 12$) of the generalised round-trip identity and results for the determined system (as in Fig. 5.6b) subject to singular value rejection. Narrowband representation of amplitude (top) and phase spectra (bottom): reference measurement (—); over-determined generalised round-trip identity (—); and round-trip result using TSVD (—).

Without requiring additional instrumentation or experimental effort (compared to over-determination), the truncation shown in Fig. 5.7b significantly improves the result of the determined setup, although minor deviations occur between 3.3-5 kHz.

This implies that the truncated singular values contain information about the structural dynamics, which are explicitly required to reconstruct the transfer mobility at high frequencies. Note that the results presented are, in a sense, based on a trivial rejection of 2 singular values, however, more sophisticated (also frequency-dependent [155]) approaches may be adopted but are considered beyond the scope of this thesis.

Considering the moment mobility in Fig. 5.7, both approaches significantly reduce noise to a level sufficient for most practical applications. The remaining noise between 100 - 300 Hz is likely caused by a finite difference error and perhaps unreliable shaker measurements at low frequencies. The measured translational FRFs of the sensor pairs, which resolve the rotational DoF, are too similar², and thus the calculated difference of the spaced mobilities introduces noise [66]. Hence, this error is not the fault of the generalised round-trip procedure and may be resolved by a larger sensor spacing at the cross-like elements. Note that the reference measurement (—) contains a similar error due to the finite difference approximation of the forces applied at (c) (see close-up inset in Fig. 5.5).

For clarification, the accuracy of the indirect approach is independent of the number of computed transfer FRFs. With a particular interest in the translational terms (x, y, z -coordinate-DoFs) of $\mathbf{Y}_{C,dc}$, incomplete interface instrumentation at (c_1) and (c_2) with single tri-axial accelerometers simplifies the experimental setup without impairing the accuracy of the result. As stressed in Sec. 3.6, the conditions of controllability and observability capture the interface dynamics, whereas the DoFs (c) in $\mathbf{Y}_{C,cb}$ simply define which transfer mobilities are computed. In other words, the results in Fig. 5.7 can be obtained by considering any incomplete subset of interface DoFs, or only the γ -rotation at (c_1). However, the number of physical important coupling DoFs at the rigid interface remains unchanged.

5.2.2 Plate Receiver – Sub-Structure Round-Trip Identity for Receiver FRFs

The case studies presented so far have considered the generalised round-trip identity to reconstruct assembly FRFs. This study concerns the sub-structure form of the round-trip identity for receiver FRFs, i.e. $\mathbf{Y}_{B,dc}$, to reduce complexity in the

² Especially at low frequencies, where the bending wavelength is very large compared to the accelerometer spacing, the measured mobilities at both sensor positions are, in fact, identical. Comparing such mobilities in the finite difference operation results in a noisy, unstable mobility approximation [66].

measurements commonly involved in classical TPA. Measurements on the receiver sub-structure are then used to demonstrate the invariance of the transmissibility matrix, as outlined in Sec. 4.1.2.

The sub-structure round-trip identity in Eq. (3.40) combines FRFs of the coupled assembly (C) and the separated receiver (B). The assembly measurements are essentially the same as in the previous case study (see step 1. in Sec. 5.2.1), hence $\mathbf{Y}_{C,ba}$ and $\mathbf{Y}_{C,da}$ are used to calculate a determined and over-determined round-trip solution. For the subsequent receiver measurements shown in Fig. 5.8, the source (A), that is the beam structure and the upper half of the cross-like elements, is removed from the assembly. The receiver FRFs $\mathbf{Y}_{B,cb}$ are determined from forces (red arrows) directly applied on the accelerometers at (b) and response measurements at the coupling interfaces (c_1, c_2) (blue arrows). Using 12 source-side DoFs (a) (see Fig. 5.5a) and the same number of remote DoFs (b) provides a determined system ($n_a = n_b = n_c = 12$). Like in the previous study, 12 additional beam excitations and 3 tri-axial response sensors, indicated in grey (see Fig. 5.8), are considered to over-determine ($n_a \geq n_b \geq n_c = 12$) the relation, i.e. $\mathbf{Y}_{C,ba} \in \mathbb{C}^{21 \times 24}$, $\mathbf{Y}_{C,da} \in \mathbb{C}^{3 \times 24}$ and $\mathbf{Y}_{B,cb} \in \mathbb{C}^{12 \times 21}$.

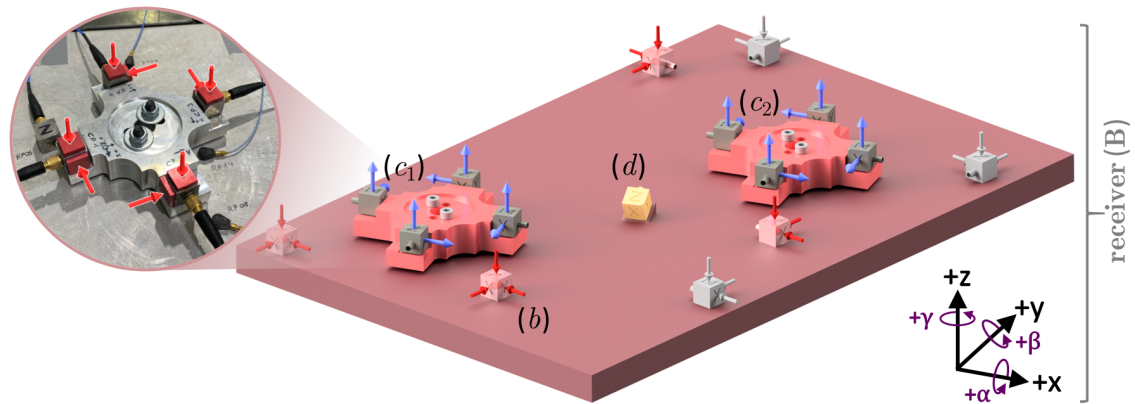
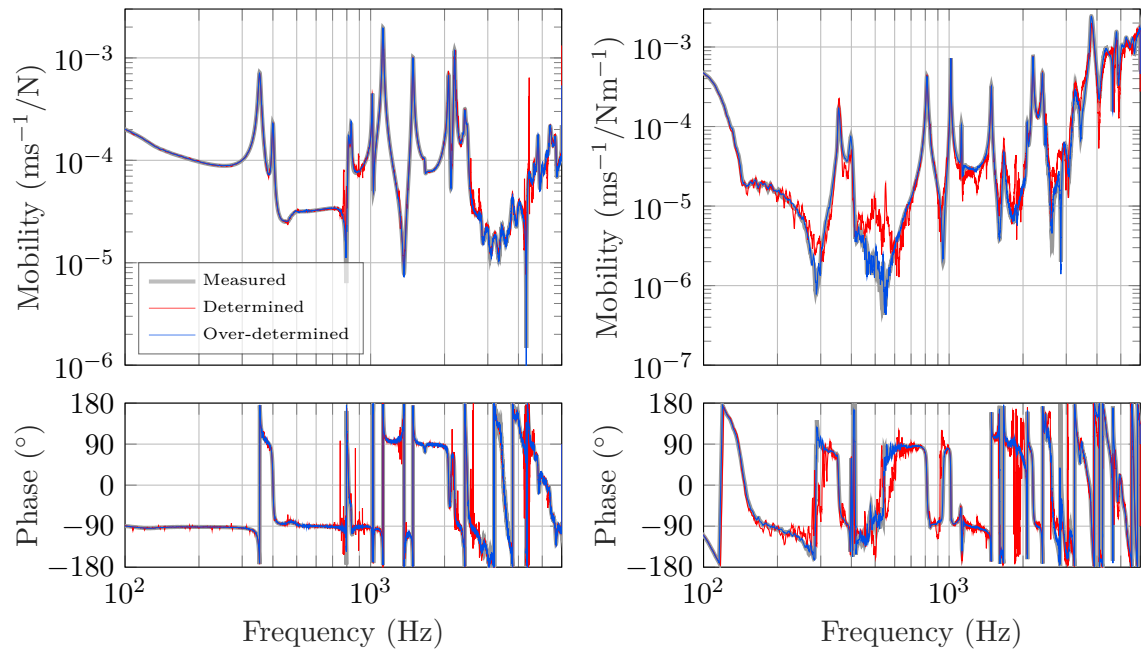


Figure 5.8: Receiver (B) for indirect measurement of $\mathbf{Y}_{B,dc}$ using the sub-structure round-trip identity. Arrows indicate the excitation (red) and response (blue) measurements utilised in the FRF reconstruction, whilst excitations depicted in the close-up inset are required for the reference measurement.

The reference FRFs $\mathbf{Y}_{B,dc} \in \mathbb{C}^{3 \times 12}$ are directly obtained from measurements on the cross-like elements to validate the sub-structure round-trip identity. The forces applied for the conventional FRF measurement are shown in the close-up inset of Fig. 5.8. Note that finite difference approximation is used to transform 8 excitations (red arrows) at each cross-like element into 3 translational and 3 rotational mobility entries in $\mathbf{Y}_{B,dc}$.

Shown in Fig. 5.9 are the reconstructed round-trip FRFs (Eq. (3.40)) of the receiver plate for the determined (—) and over-determined (—) case, compared to the validation measurement (—). The selected transfer functions ($\mathbf{Y}_{B,dc} \in \mathbb{C}^{3 \times 12}$) are the same as in Sec. 5.2.1 and describe the out-of-plane force (see Fig. 5.9a) and in-plane moment (see Fig. 5.9b) excitation at (c_1). While the result presented for the determined case in Fig. 5.9a shows good agreement to the validation reference, there are clearly many errors for its rotational counterpart.



(a) Out-of-plane force: $Y_{B,dc} - (d)/(c_{1z})$

(b) In-plane moment: $Y_{B,dc} - (d)/(c_{1\gamma})$

Figure 5.9: Validation of the receiver FRF $\mathbf{Y}_{B,dc}$ for a determined ($n_a = n_b = n_c = 12$) and over-determined ($n_a > n_b > n_c$) solution of the sub-structure round-trip identity. Narrowband representation of amplitude (top) and phase spectra (bottom): reference measurement (—); compared to the determined (—); and over-determined (—) sub-structure round-trip result.

As shown in Fig. 5.9b, the round-trip mobility fails to determine $\mathbf{Y}_{B,dc}$ accurately, most noticeable at anti-resonances. That said, this error of the indirect approach may result from; experimental error in the measurement of mobilities, or perhaps insufficient controllability and/or observability of the rotational DoFs. It is certainly not guaranteed that the $n_a = 12$ source-side excitations at (a) are mutually independent and provide full controllability over all interface DoFs. For example, the dynamic behaviour of the source (A) is similar to a clamped-clamped beam, thus the source itself may function as a ‘structural filter’. From excitations at (a), it is

difficult to create a moment contribution about the z -axis at (c) , making it considerably more challenging to achieve full controllability over the γ -coupling DoFs. Therefore, the determined case is able to provide an accurate result for the z -DoF, but large deviations occur for the corresponding rotation. This can be avoided, in part, by considering additional remote DoFs at (a) and (b) , i.e. $n_a > n_b > n_c$. For the over-determined case, the reconstructed receiver FRFs (—) are in near-exact agreement (differences on the level of numerical error) with the reference measurement. Over-determination can be seen here to remedy many of the noisy deviations observed in the determined mobilities, most notably in Fig. 5.9b at approximately 150 - 800 Hz.

The indirect characterisation of receiver FRFs may prove useful in classical TPA, where the interface and the target DoFs are inaccessible for excitation. Besides validation of the sub-structure form of the round-trip, the reference measurements performed in this study also provide the receiver transmissibility $\mathbf{T}_{B,db}^{(c)}$. Recalling the invariant properties of the transmissibility, it can be shown that the three transmissibility expressions in Eq. (4.13) are, in fact, interchangeable. It is important to reiterate that this invariance is assumed to derive the controlled blocked force exciter concept, essential for fastTPA. These transmissibilities are obtained from measurements in (C) and (B), thus combining the case studies provides all required experimental data. In both studies, the location of the response measurements at (b) and (d) remains unchanged; in theory, invariant transmissibilities should provide the same result.

The transmissibilities shown in Fig. 5.10a are defined as follows. In the coupled assembly (C), the term $\mathbf{T}_{C,db}^{(a)} = \mathbf{Y}_{C,da} \mathbf{Y}_{C,ba}^+$ (—) is determined using 24 source-side excitations at (a) , and the second matrix $\mathbf{T}_{C,db}^{(c)} = \mathbf{Y}_{C,dc} \mathbf{Y}_{C,bc}^+$ (—) is based on the excitation of all 12 coupling DoFs. The source-side excitation is indicated in Fig. 5.5a by red arrows on the beam, whilst the applied interface forces for $\mathbf{T}_{C,db}^{(c)}$ are shown in the close-up inset. Note that $\mathbf{T}_{C,db}^{(a)}$ is determined using a TSVD, retaining 12 significant singular values in $\mathbf{Y}_{C,ba}^+$. The transmissibility measurements $\mathbf{T}_{B,db}^{(c)} = \mathbf{Y}_{B,dc} \mathbf{Y}_{B,bc}^+$ (—) on the separated receiver (B) are shown in the close-up inset of Fig. 5.8, where 16 forces (red arrows) are applied at the cross-like elements to approximate excitation of 12 interface DoFs (finite difference).

As expected, the three transmissibilities shown in Fig. 5.10a are in close agreement; this demonstrates its invariant nature and indicates full controllability and observability of the measurements. In a multi-kHz range, the two assembly measurements

$\mathbf{T}_{C,db}^{(a)}$ and $\mathbf{T}_{C,db}^{(c)}$ converge with the receiver transmissibility. The transmissibilities generally capture the vibrations transmitted onto the receiver and become, in fact, a property of the receiver structure only. Consequently, the same result is obtained whether or not the source (A) is connected to the receiver (B), i.e. $\mathbf{T}_{C,db}^{(c)} = \mathbf{T}_{B,db}^{(c)}$. If a source (A) is connected, the transmissibility is also independent of the location where the excitation is applied, i.e. $\mathbf{T}_{C,db}^{(a)} = \mathbf{T}_{C,db}^{(c)}$. As such, forces can be considered directly at the interface (c) or somewhere on the source (a), making the transmissibility irrespective of the nature of the excitation mechanism, assuming controllability and observability requirements are met. Clearly, the different transmissibility expressions in Eq. (4.13) can be interchanged, as used in the derivation of fastTPA.

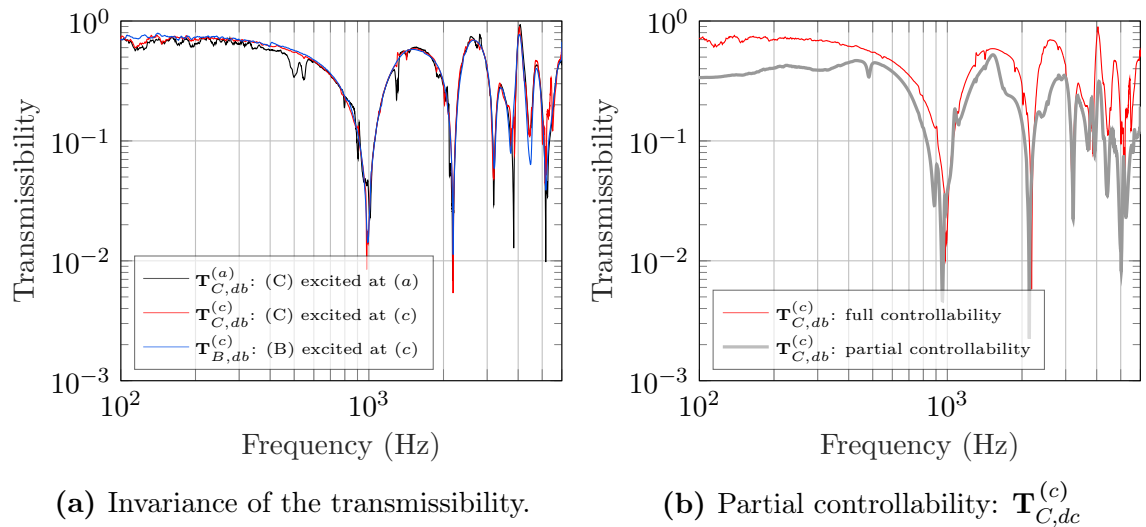


Figure 5.10: Transmissibilities for the receiver (—) and the assembly (C), with excitations applied on the source (—) or at the interface (—), assuming full controllability/observability. An incomplete subset of interface excitations, e.g. discarding rotations in $\mathbf{T}_{C,dc}^{(c)}$ (—), leads to a not invariant matrix.

Note that Fig. 5.10a describes one selected element of the 3×21 transmissibility matrices; shown are the transmissibilities for out-of-plane DoFs (+z measurement direction in Fig. 5.8) at (b) and (d). Other matrix elements (not shown for brevity) are also in close agreement, however, transmissibilities between in-plane DoFs become dominated by noise at frequencies below 800 Hz, likely due to nearly identical in-plane responses measured on the plate-receiver at (b) and (d).

However, the invariance demonstrated in Fig. (5.10a) is highly subject to the controllability and observability of the interface. Calculating the transmissibility³ $\mathbf{T}_{C,db}^{(c)} = \mathbf{Y}_{C,dc} \mathbf{Y}_{C,bc}^+$ for a subset of excitations applied at (*c*) leaves the interface partially controllable. For example, rotations can be discarded mathematically by removing the associated columns in the FRF matrices, i.e. $\mathbf{Y}_{C,bc} \in \mathbb{C}^{21 \times 12} \rightarrow \mathbb{C}^{21 \times 6}$. Omitting rotational excitations, the size of the transmissibility matrix remains $n_b \times n_d$, obfuscating the interface excitations associated with the original FRFs. Fig. 5.10b demonstrates the example of partial controllability (—) considered here, compared against the invariant measurement (—) from Fig. 5.10a. As expected, the two transmissibilities are seen to differ considerably. The transmissibility $\mathbf{T}_{C,db}^{(c)}$ is no longer invariant and becomes a property of the assembly. Clearly, the amended transmissibility relates responses between (*b*) and (*d*) only for the translational (*x, y, z*) contributions transmitted over the interface. This highlights the deviations one might expect by considering too few excitations in the generalised round-trip identity, which would completely neglect certain contribution paths.

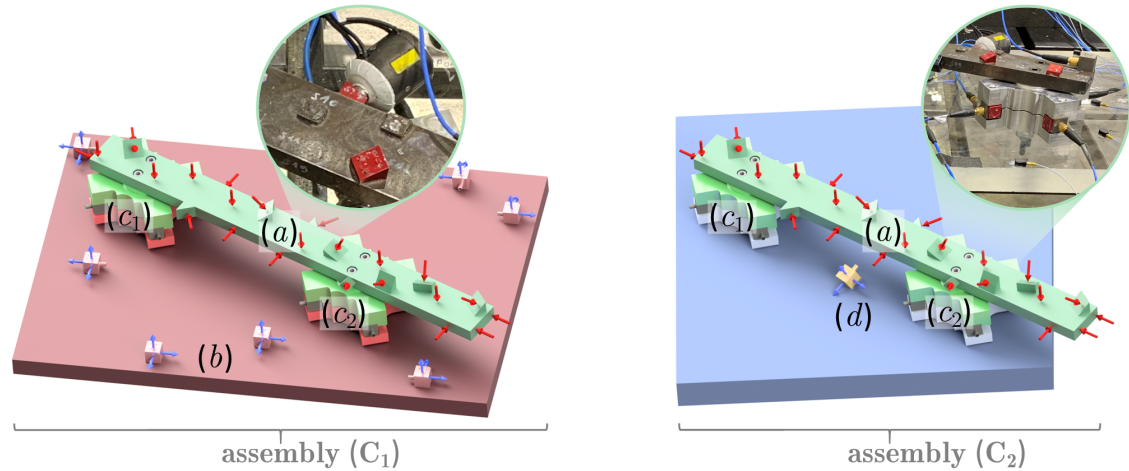
5.2.3 Beam-Plate Assemblies – Controlled Blocked Force Exciter Concept

Having dismantled the original beam-plate assembly (C_1) used in the previous examples, the source (A) can be connected to a different plate receiver (B_2) and used as a calibrated blocked force exciter. This part of the study concerns the characterisation of transfer FRFs $\mathbf{Y}_{C_2,dc}$ in a different assembly (C_2), obtained from a controlled and reproduced source excitation. Two particular cases of the controlled blocked force exciter concept are validated; the mobility (normalised unit force excitation) and phase referenced velocity expression in Eqs. (4.33) and (4.32), respectively. This characterisation forms the basis of the proposed fastTPA approach, where it is used to determine the FRFs for inverse force identification and forward response prediction.

Following the two-stage procedure described in Sec. 4.3, the blocked force vibration exciter requires first a calibration of the controlled excitation, prior to its installation in the target assembly. The calibration is performed in the previously outlined

³ The chosen example uses excitations directly applied at (*c*), hence, controllability of the interface is straightforward. Alternatively, the same considerations apply to $\mathbf{T}_{B,db}^{(c)}$ and $\mathbf{T}_{C,db}^{(a)}$. In the latter case, however, excitations are applied further upstream at (*a*), making controllability of the individual interface DoFs less obvious.

assembly (C_1), where a beam (source - (A)) is connected to an aluminium plate (receiver - (B_1)). The source is then connected to a plastic plate (B_2) for system identification in a different (target) assembly (C_2). Shown in Fig. 5.11 are the experimental setups for the calibration and system identification stage, similar to the schematic representation of the concept in Fig. 4.2.



(a) Stage 1: Calibration of the source (A) as a controlled blocked force exciter in assembly (C_1).

(b) Stage 2: System identification of assembly (C_2) from a reproduced excitation and operational responses at (d).

Figure 5.11: Test structures (C_1) and (C_2) for the two-stage system identification using the source (A) as a blocked force exciter. Controlled roving excitation (red arrows) are applied with a shaker, as shown in the close-up inserts. The source-receiver setups contain: beam - source (A); aluminium plate - receiver (B_1); plastic plate - receiver (B_2).

The geometry and material properties of the aluminium and plastic (acrylic glass) receiver plate are given in Table 5.2. The source calibration⁴ is performed in a highly resonant assembly (C_1), whilst the receiver (B_2) introduces considerable damping to the assembly in the identification stage.

Table 5.2: Geometry and material properties for the exchanged plate receivers (B_1) and (B_2), where; l -length, w -width, h -height, E_0 -Young's modulus, ρ -density and ν -Poisson's ratio.

Material	Receiver	l (m)	w (m)	h (m)	E_0 (N/m ²)	ρ (kg/m ³)	ν (-)
Aluminium	(B_1)	0.450	0.300	0.019	69×10^9	2670	0.32
Acrylic	(B_2)	0.350	0.350	0.030	4.5×10^9	1180	0.37

⁴ The selection of calibration and target assembly is arbitrary. Theoretically, the method can be applied irrespective of the receiver structure, as long as vibrations can be measured sufficiently (e.g. as per definitions provided in ISO 20270:2019).

In this example, only the over-determined solution is considered. For the controlled operation of the passive source structure, roving excitation (red arrows) is applied at 24 different DoFs (a), as outlined in the previous round-trip studies. The excitations are applied using an electro-dynamic shaker (see inset of Fig. 5.11b). For the calibration in assembly (C_1), the responses (blue arrows) are observed downstream of the cross-like elements by 21 remote DoFs (b). In the target assembly (C_2), the inaccessible transfer FRFs $\mathbf{Y}_{C_2,dc}$ are determined between all 12 coupling DoFs (c_1, c_2) and the target accelerometer (d), depicted in yellow. The simplistic setup in Fig. 5.11b highlights perhaps the main advantages of the controlled exciter concept: its minimal instrumentation effort in (C_2) without any restrictions on the measurement position due to limited access. The measurement procedure on the two different assemblies may be outlined as follows:

1. The source is calibrated in assembly (C_1). The transfer FRFs $\mathbf{Y}_{C_1,cb} \in \mathbb{C}^{12 \times 21}$ (or $\mathbf{Y}_{C_1,bc} \in \mathbb{C}^{21 \times 12}$ if convenient) are measured using a roving shaker approach. The control mechanism uses 24 roving excitations on (A) to determine $\mathbf{Y}_{C_1,ba} \in \mathbb{C}^{21 \times 24}$ and $\dot{\mathbf{V}}_{C_1,ba} \in \mathbb{C}^{21 \times 24}$. (These measurements are the same as those used in Sec. 5.2.1.)
 2. In the system identification step, the source is connected to the plastic receiver structure (B_2) (including the lower cross-fixtures). The excitation on (A) is repeated to measure $\mathbf{Y}_{C_2,da} \in \mathbb{C}^{3 \times 24}$ and $\dot{\mathbf{V}}_{C_2,da} \in \mathbb{C}^{3 \times 24}$ in the target assembly.
 3. Using the blocked force exciter concept in Eqs. (4.33) and (4.32), the transfer FRFs $\mathbf{Y}_{C_2,dc} \in \mathbb{C}^{3 \times 12}$ are estimated.
- * For the validation of the blocked force exciter approach, forces are applied to the coupling interface (c) of the new assembly (C_2) to measure the reference transfer mobilities $\mathbf{Y}_{C_2,dc}$.

Following this, $\mathbf{Y}_{C_2,da}$ may be calculated in **3.** based on the mobility (Eq. (4.33)) or velocity (Eq. (4.32)) expression of the two-stage procedure. The two variants differ in the calculation of their transmissibility matrix, $\mathbf{T}_{C_1,2,db}^{(a)}$. For example, Eq. (4.33) uses a mobility-based transmissibility matrix, that is the velocity responses are normalised to the input force of the shaker (unit force excitation). The variant in Eq. (4.32) uses a velocity transmissibility, $\dot{\mathbf{V}}_{C_2,da} \dot{\mathbf{V}}_{C_1,ba}^+$, containing phase referenced velocity responses from (C_1) and (C_2) (not normalised to the force amplitude). The phase was applied using the cross-spectrum approach in Eq. (4.17). The current input of the shaker was chosen as the phase reference for the cross-spectra. Both

transmissibility terms are built using the 12 largest singular values of $\mathbf{Y}_{C_1,ba}$ and $\hat{\mathbf{V}}_{C_1,ba}$, when the matrix inverse is performed.

Shown in Fig. 5.12 are the transmissibilities, determined via the product of mobilities $\mathbf{Y}_{C_2,da} \mathbf{Y}_{C_1,ba}^+$ (—), and the velocities $\hat{\mathbf{V}}_{C_2,da} \hat{\mathbf{V}}_{C_1,ba}^+$ (—). Note that the velocities have resulted from the same excitations used to determine the mobilities. As expected, the two are in near-perfect agreement over a multi-kHz range. This demonstrates the invariant nature of the velocity-based transmissibility (and their underlying blocked force relation), similar to the validation for the different mobility expressions presented in Sec. 5.2.2.

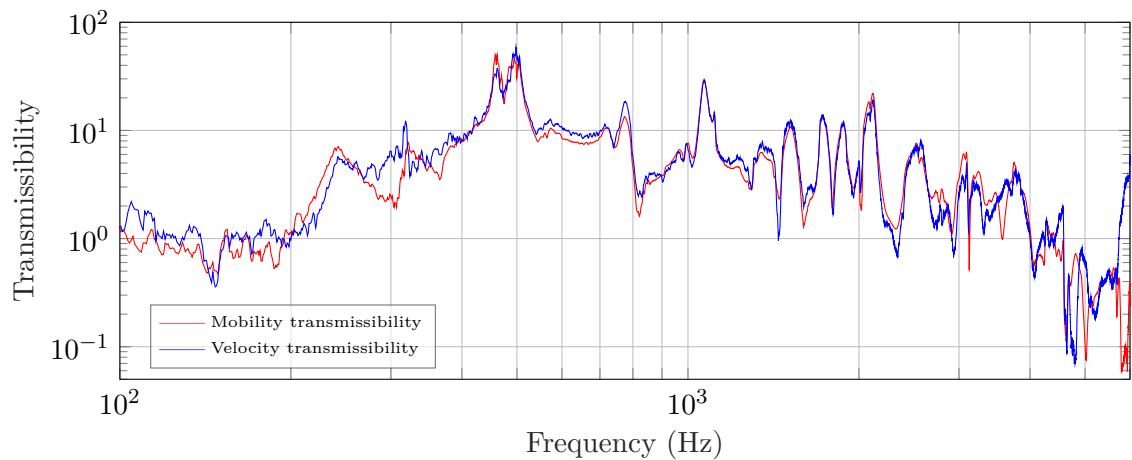


Figure 5.12: Element of the transmissibility matrix relating responses between the DoFs (d) and (b) of two different assemblies. $\mathbf{T}_{C_1,2,db} \in \mathbb{C}^{3 \times 21}$ is determined via conventional mobility measurements (—) and phase referenced velocity matrices (—).

Note that there is some minor disagreement between the transmissibilities around 300 Hz and in the high frequency range (≈ 5.5 -6 kHz). These deviations are somewhat expected, given that the velocity vectors in $\hat{\mathbf{V}}_{C_2,da}$ and $\hat{\mathbf{V}}_{C_1,ba}$ are not normalised to the input force of the shaker. Unlike mobilities, variations in the force amplitude between shaker excitations in (C_1) and (C_2), e.g. due to thermal power loss or back-electromotive force, are left unaccounted in the velocity matrices [156–159]. Hence, the velocity expression in Eq. (4.32) relies on exactly reproduced operational conditions, whilst the mobility-based transmissibility utilised the shaker’s load-cell signal to considers responses due to an (unchanged) unit force excitation.

With these two transmissibility terms in such good agreement, it is no surprise that the transfer FRFs $\mathbf{Y}_{C_2,dc}$ in Fig. 5.13, acquired via the velocity-based (—) approach, is also in near-perfect agreement with those determined from the mobility (—) relation. Compared against the reference (—), the estimated transfer FRFs, $\mathbf{Y}_{C_2,dc}$, for the

z -translation and γ -rotation DoFs at (c_1) are in near-perfect agreement over a multi-kHz range (100 Hz - 6 kHz). This result confirms a successful calibration of the source component (A) and its use as a controlled multi-DoF blocked force exciter. Fig. 5.13 further demonstrates that a roving shaker approach can turn any passive source structure into a blocked force exciter.

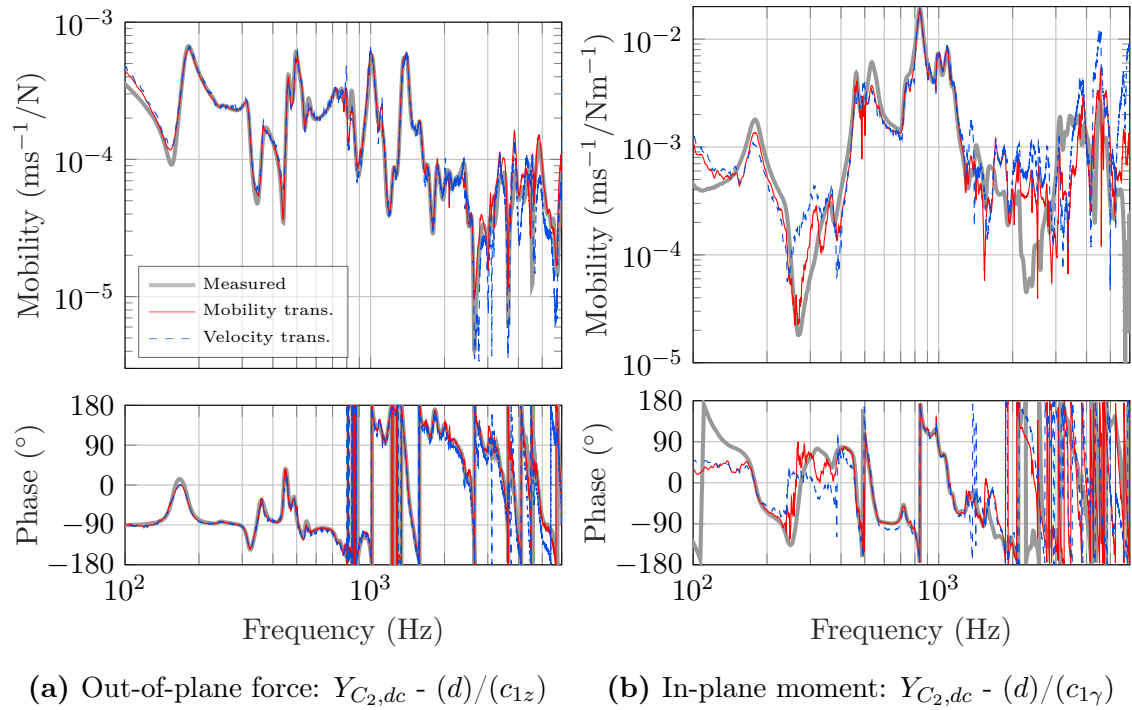


Figure 5.13: Validation of $Y_{C_2,dc}$ using controlled electro-dynamic shakers (see close-up inset in Fig. 5.11b) to turn the source (A) into a blocked force vibration source. Narrowband representation of amplitude (top) and phase spectra (bottom): reference measurement (—); compared to the two-stage estimates using the mobility (—) and velocity approach (--).

Whilst the FRF estimates can be seen to follow the reference measurement, there clearly exist some errors, most noticeable in Fig. 5.13b. That said, deviations may result from experimental errors in the reproduced excitation due to both measurement and operator uncertainty. The latter, for example, is introduced due to an inconsistent excitation position/orientation when repeating the roving shaker measurements in (C_1) and (C_2) . It is interesting to note the improved low frequency estimate in Fig. 5.13b for the mobility approach over the velocity-based transmissibility. This improvement, particularly below 400 Hz, results from normalised responses in the mobility expression. In other words, measurement uncertainty in $\mathbf{Y}_{C_2,dc}$ is reduced by avoiding amplitude variations in the reproduced blocked force excitation.

Also, the two-stage procedure considers the dismantling of assembly (C_1) and subsequent coupling to a different receiver (B_2). The source (A) is connected at multiple contacts, therefore, stiffening effects (e.g. static pre-load or changed interface boundary conditions due to stronger physical constraints from the aluminium plate) may alter the properties of the highly resonant source (beam - (A)). Consequently, the source properties will influence the roving shaker excitation, hence the controlled excitation will vary from one application (C_1) to another (C_2). Note that the blocked force (and therefore the exciter concept) is theoretically invariant to the properties of the connected receiver, however, the passive source properties are assumed to remain unchanged.

Although only a brief experimental investigation has been carried out, the results presented here are sufficient to validate the blocked force exciter concept and, furthermore, demonstrate its potential for fastTPA. Once calibrated, the source can be used to replace conventional FRF measurements whilst avoiding experimental challenges, e.g. moment excitation, measurement of in-plane or inaccessible DoFs and excessive instrumentation in the target assembly, to name but a few. Further experimental investigation of the concept in a more realistic and practical scenario is presented in Part IV.

5.3 Steering Setup – Characterisation of Long Distance Transfer Functions

This study considers the application of the generalised round-trip identity to determine long distance transfer functions in multi-contact assemblies, as proposed in Sec. 3.4.3. The focus is on the measurement quality (i.e. SNR) rather than accessibility problems of certain DoFs encountered by the experimentalist. The experimental setup, shown in Fig. 5.14, considers the long distance transfer functions between the motor mount (a) of a REPS system to the rigidly connected aluminium receiver plate (B). Cross-like elements (see Sec. 5.2.1) at each connection interface (c_1) and (c_2) are designed to fully determine 6 DoFs coupling, including 3 translational and 3 rotational directions. The reciprocal measurement technique in Eq. (3.21) interchanges the excitation and response position of the non-located transfer function DoFs, such that $\mathbf{Y}_{C,ab} = \mathbf{Y}_{C,ba}^T$. Hence, the generalised round-trip measurements to identify the transfer properties between (a) and (b), including any validation FRFs, originate from the passive-side with response measurement on the source at (a).

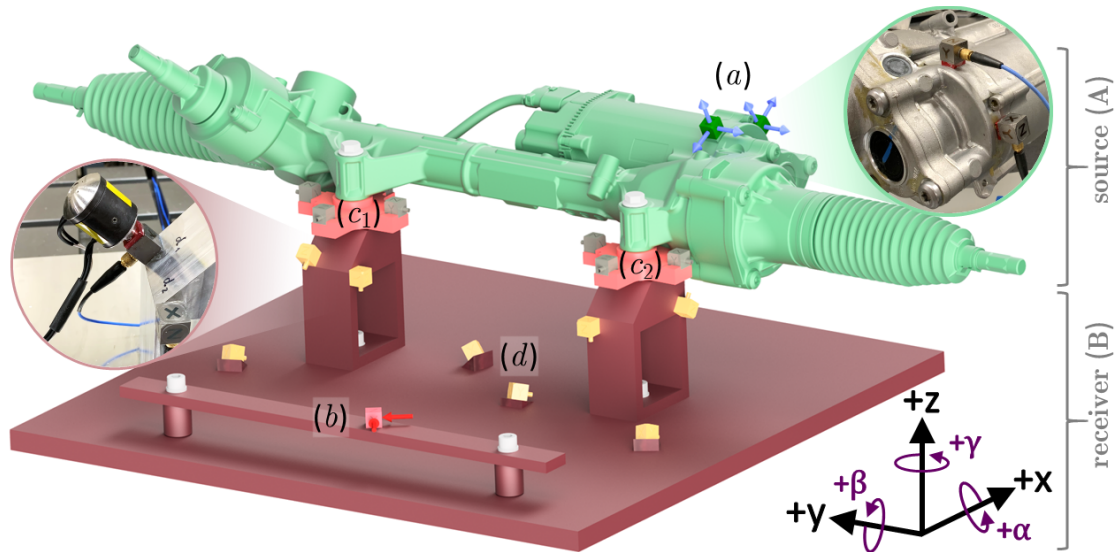


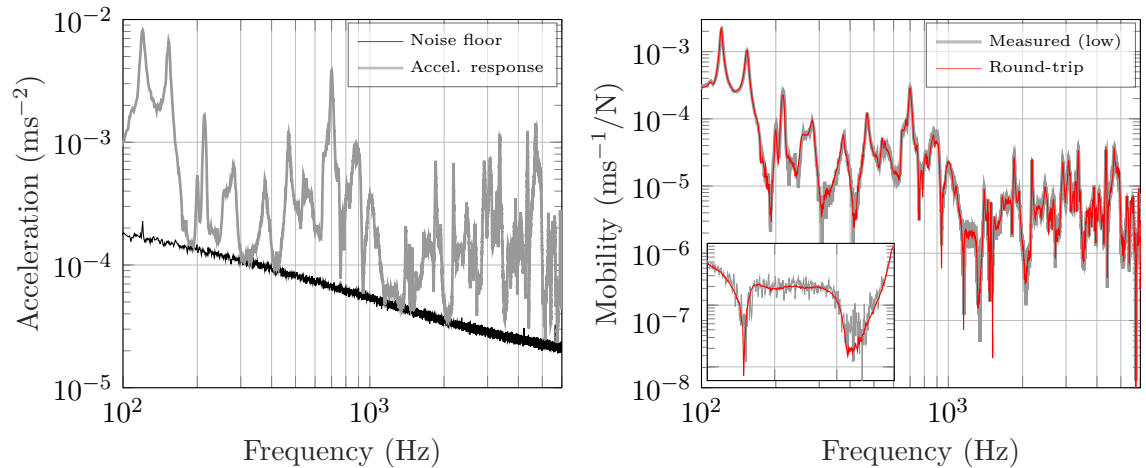
Figure 5.14: Test structure forming a long distance transfer function $\mathbf{Y}_{C,ab}$ from the remote position (b) on the beam to the motor mount (a). Arrows indicate the excitation (red) and response (blue) measurements of the conventional FRF characterisation, whilst the shaker excitation at (d), depicted in the left close-up inset, is part of the generalised round-trip identity. The source-receiver setup contains: REPS - source (A); plate-beam assembly - receiver (B); cross-like elements - coupling interfaces (c_1, c_2); remote locations (d) accessible for direct excitation.

To extend the distance between non-collocated DoFs of the transfer FRFs, the remote force excitations (red arrows) at (b) are applied in the in-plane directions on a steel beam rigidly mounted to the receiver plate. On the source-side, the acceleration responses at (a) (blue arrows) are measured with 2 tri-axial accelerometers positioned at the motor mount. Unlike conventional transfer function measurements, where forces are applied one at a time to determine a single FRF, the generalised round-trip approach solves the MIMO system. However, implementation of the long distance approach in Eq. (3.21) requires additional instrumentation. The receiver-side is instrumented with 8 tri-axial accelerometers (d) (highlighted in yellow in Fig. 5.14) for remote response and excitation measurements ($n_d \geq n_c = 12$). The duality of excitation and response DoFs at (d) requires easy access for roving hammer or shaker testing, which may be realised by practical sensor placement close to the structure's edges. FRF testing of this relatively large structure with stiff support stands in combination with a low in-plane dynamics of the receiver requires considerable excitation energy to achieve an acceptable SNR. Hence, the remote DoFs (d) are located in the vicinity of the support stands to define shorter path segments. As such, noise-sensitive measurements at (a), caused by the too distant force input at (b) and the high stiffness of the receiver sub-structure (B), can be avoided.

In this experimental study, all round-trip FRF elements are measured with a miniaturised shaker (see inset of Fig. 5.14) operated at about 30% of its maximum force output. The lowered shaker output is adjusted at the power amplifier stage to mimic an insufficient excitation scenario for the long transfer functions. However, operated at its full capacity, the ‘high’ excitation energy may be used to provide an appropriate reference measurement of $\mathbf{Y}_{C,ab}$. The generalised round-trip measurement procedure (1.-3.) at reduced shaker output, followed by the validation process (*) at full shaker output, may be outlined as follows:

1. The full distance FRFs $\mathbf{Y}_{C,ab} \in \mathbb{C}^{6 \times 2}$ are measured at ‘low’ shaker output for a realistic representation of insufficient excitation. The applied force is adjusted to cause a poor SNR on the acceleration responses at (a), close the sensors’ noise floor (Fig. 5.15a). Keeping the reduced amplifier settings unchanged, the matrix $\mathbf{Y}_{C,cb} \in \mathbb{C}^{12 \times 2}$ is measured from shaker excitations on the accelerometer at (b).
 2. The assembly matrices $\mathbf{Y}_{C,ad} \in \mathbb{C}^{6 \times 24}$ and $\mathbf{Y}_{C,cd} \in \mathbb{C}^{12 \times 24}$ are determined simultaneously by roving shaker excitation, still at reduced energy output. The shaker forces are directly applied to the 24 (yellow) accelerometer surfaces at (d), depicted in the inset of Fig. 5.14.
 3. The shorter transfer path segments are combined to determine the long distance transfer functions $\mathbf{Y}_{C,ab} \in \mathbb{C}^{6 \times 2}$ using the generalised round-trip formulation in Eq. (3.21).
- * The ideal full length reference FRFs are determined at maximum shaker output (‘high power’) by excitation on the remote sensor faces at (b), indicated by red arrows in Fig. 5.14.

Shown in Fig. 5.15a is the narrowband Fourier spectrum of the vibration response $\mathbf{v}_{C,ab}$ in the translational z -direction at the target motor mount (a), recorded during shaker excitation at (b) under reduced power. By scaling the amplification factor of the shaker’s force output, the attenuated vibration response (—) falls near/below the sensitivity threshold (—) of the measurement equipment. The corresponding long distance transfer function $\mathbf{Y}_{C,ab}$ in Fig. 5.15b (—) is, in fact, influenced by uncorrelated measurement noise at frequencies of poor SNR. Maintaining the ‘low’ shaker output, the compared result of the generalised round-trip procedure (—) significantly improves the FRF quality. Anti-resonances are more prominent in the round-trip FRF, aside from noise being attenuated, as depicted in the inset from 1.1 - 1.4 kHz.



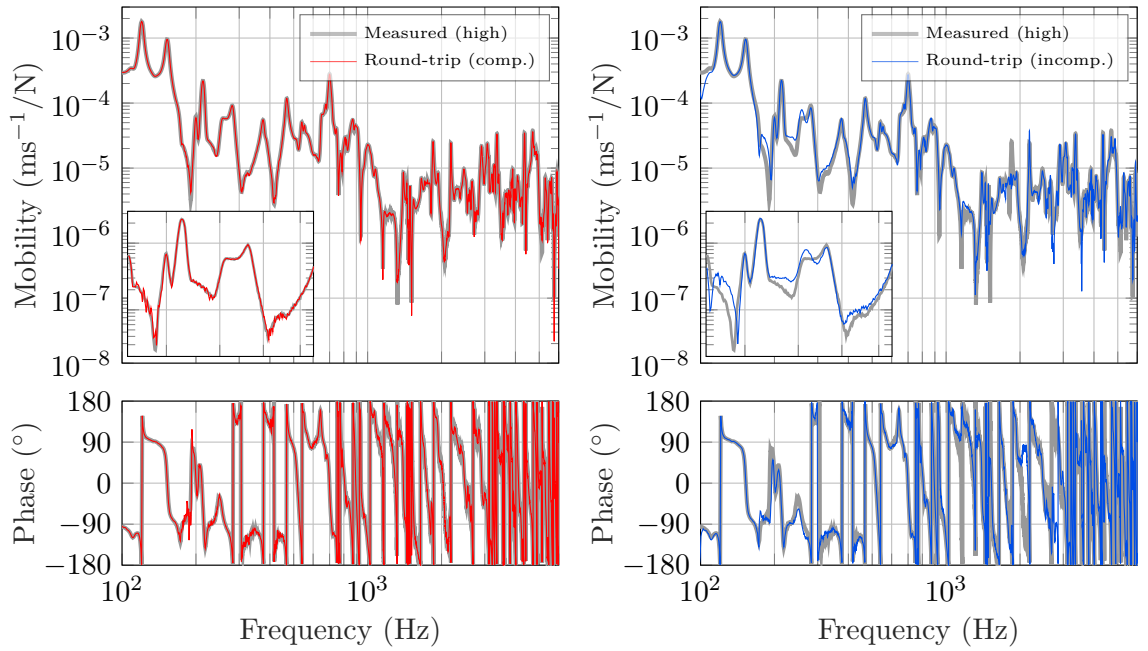
(a) SNR at the motor mount (*a*) due to low level shaker excitation at (*b*). (b) Improvement of the long distance FRF. (Inset covers freq. range from 1.1 - 1.4 kHz)

Figure 5.15: Acceleration response (—) at the motor mount (*a*) with poor SNR, close to the sensor’s noise floor (—), due to ‘low/insufficient’ shaker excitation at (*b*). The directly measured long distance FRF $\mathbf{Y}_{C,ba}$ (—) (Fig. 5.15b) is clearly influenced by noise, whilst the generalised round-trip concept (—) improves measurement quality.

The actual experimental validation of the above round-trip procedure (—) is provided in Fig. 5.16a by comparing the long distance FRF with a direct reference measurement at ‘high’ shaker output (—). The round-trip method provides a convincing agreement, however, some measurement noise still remains, especially at low frequencies between 170 - 370 Hz, highlighted in the inset. The artificially lowered shaker output for the round-trip measurement campaign fails to determine all mobility elements with a sufficient SNR completely free from measurement noise. A relocation of the remote positions (*d*) or, alternatively, a virtual interface (see Fig. 3.5) may be introduced and used in conjunction with the nested round-trip formulation in Eq. (3.24) to improve measurement quality at anti-resonances further.

The result of a more simplistic instrumentation setup with fewer accelerometers and less measurement effort is shown in Fig. 5.16b. The dynamics at the coupling interface, for instance, are characterised by 3 translational DoFs each ($n_c = 6$), which theoretically reduces the finite difference sensor array to a simple tri-axial accelerometer mounted to each foot (c_1, c_2). Clearly, the reduced interface description benefits the receiver-side instrumentation at (*d*), with 12 excitations on 4 sensors providing a 2 fold over-determination of $\mathbf{Y}_{C,cd} \in \mathbb{C}^{6 \times 12}$. The considerably reduced experimental effort comes at the expense of accuracy in the frequency range between

170-370 Hz (see inset of Fig. 5.16b), worsening at higher frequencies. The incomplete representation of the coupling interface dynamics is limited to translational DoFs only, while rotational coupling in the transmissibility term $\mathbf{T}_{C,bd}^{(c)} = \mathbf{Y}_{C,bc} \mathbf{Y}_{C,dc}^+$ (compare Eq. (4.24)) is mathematically omitted. Although the mobility term $\mathbf{Y}_{C,ad}$ (see Eq. (3.21)) implicitly includes the complete set of DoFs through which physical coupling occurs, rotational transfer paths are not included in the propagating transmissibility term.



(a) Complete interface description: $\mathbf{Y}_{C,ab}$ (Inset covers freq. range from 170-370 Hz) (b) Translational coupling at (c): $\mathbf{Y}_{C,ab}$ (Inset covers freq. range from 170-370 Hz)

Figure 5.16: Validation of the long distance FRF $Y_{C,ab}$ based on a complete description of the coupling interface (c) (same as in Fig. 5.15b), including rotations and translations ($n_c = 12$; finite-difference approximation) and simplified translational coupling only ($n_c = 6$; e.g. tri-axial sensor). Narrowband representation of amplitude (top) and phase spectra (bottom): measured reference at ‘high’ shaker output (—); generalised round-trip identity with fully described interface (—); and using an incomplete interface description (—).

Note that care should be taken when certain DoFs are neglected in the system description. Although the simplification in Fig. 5.16b yields a rather accurate result, other structures may be more dependent on rotational coupling causing major deviations. However, the structure’s sensitivity to an incomplete interface description can be assessed with the coherence-style Interface Completeness Criterion (ICC) [1, 46]. Further investigation of the long distance application, for example, using an

operational transmissibility matrix as proposed in Eq. (4.25), is considered beyond the scope of this thesis.

Considering the results in Fig. 5.16, the long distance round-trip relation provides reliable FRFs by combining measurements over shorter distances. In TPA, characterisation of long distance FRFs is not an immediate concern for inverse force identification (e.g. in-situ blocked force or matrix inverse contact force), but becomes relevant for forward response prediction. For example, the transfer FRFs between the steering gear mounts and the distant response at the driver's position are known to be sensitive to measurement errors and poor SNR, particularly in light-duty or commercial vehicles. More than often, the excitation provided by a volume-velocity source is insufficient to achieve an acceptable SNR, whilst impact hammer measurements often provide FRFs only in a narrow frequency range (< 2 kHz). In this case, the presented long distance relation provides a convenient alternative to conventional measurements (probably with an instrumented sledgehammer) for more reliable and realistic prognoses in TPA.

5.4 Summary and Concluding Remarks

This chapter has presented and validated a collection of indirect methods; the generalised round-trip identity for inaccessible and long distance FRFs, the sub-structure form of the round-trip, and the controlled blocked force exciter to characterise FRFs in a different assembly.

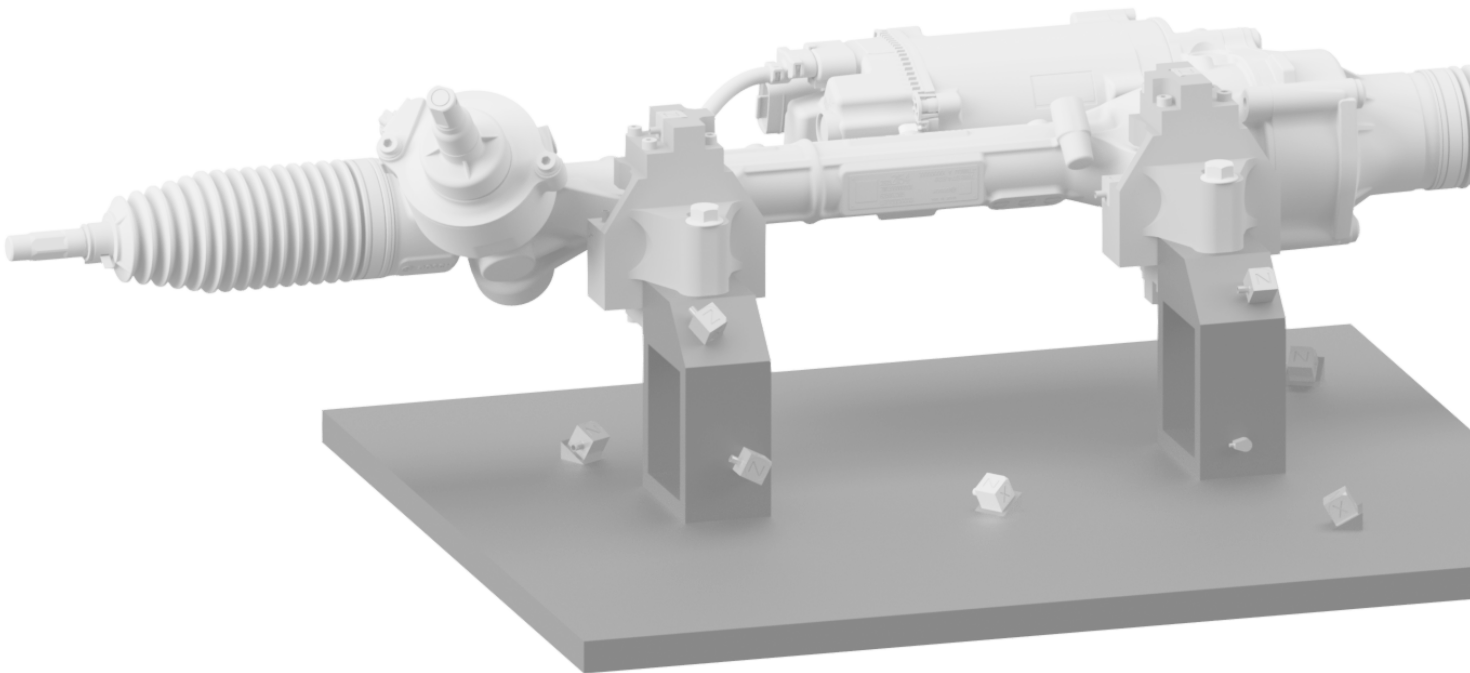
In the context of inaccessible FRFs, the generalised round-trip identity is validated analytically and then experimentally using a single contact rod structure. Later, the indirect approach has been applied to a more complex (multi-contact, multi-DoF) beam-plate assembly, while spaced accelerometer pairs facilitate finite difference approximation to consider rotations. Over a multi-kHz range, it has been shown that driving-point and transfer FRFs of the assembly can be obtained indirectly, that is, from relocated (easy-to-access) remote measurements. Similarly, the receiver's transfer FRFs have been successfully determined using the sub-structure form of the round-trip. With measurements on the assembly (C) and its receiver (B), the invariance of the transmissibility matrix \mathbf{T}_{ab} has been shown, which is used in the derivation of the controlled blocked force exciter approach. Further to the exciter concept, roving shaker excitations are applied to turn the passive source structure

(A) into a calibrated blocked force exciter. Used to determine FRFs in a different assembly, the mobility-based approach has been found to be more reliable than the phase referenced velocity expression, likely due to variations in the controlled excitation.

The rearranged form of the generalised round-trip identity for long distance transfer functions has been experimentally validated for a test bench setup. A set of remote DoFs has been defined on the receiver to divide long-distance FRF measurements into three shorter path segments. In scenarios where conventional FRF testing provides insufficient SNR, the round-trip reconstruction has been shown to improve measurement quality due to a higher SNR, a stronger phase relation, and better coherence of the shorter path segments.

These novel approaches may readily be implemented in place of conventional FRF measurements, avoiding excitations at poorly accessible locations or insufficient SNR. Integrated as part of component-based TPA, these transfer FRFs may be used for; inverse force identification, partial path analysis and source contribution ranking, sound and vibration prediction in physical structures, or virtual assemblies (VAP). The application of the controlled blocked force exciter for fastTPA will be discussed in the following.

PART IV. Application to Steering Gear Vibration



6

Calibration of a Steering System as a Blocked Force Exciter

Part IV demonstrates the application of the blocked force exciter concept for a more realistic scenario, using a steering system as a controlled multi-DoF exciter. In this chapter, we will consider the calibration of the source on a test bench. Two particular strategies to operate the exciter are explored; natural operational excitation controlled by the steering system's electric motor and externally applied roving excitations. Later, in Chapter 7, the calibrated steering system is installed in a vehicle for system identification and fastTPA.

Chapter contents:

6.1	Introduction to Electric Powered Steering	147
6.2	Calibration of the Controlled Exciter	149
6.3	Excitation Strategy	154
6.4	Summary and Concluding Remarks	162

6.1 Introduction to Electric Powered Steering

Whereas in the last few decades, hydraulic power steering systems have been most widely used in passenger cars, nowadays steering assistance is provided by a compact and more efficient electric motor. The electric power steering system shown in Fig. 6.1 is based on a rack-and-pinion principle (also: Rack-and-Pinion Electric Power Steering (REPS) system) and consists of a mechanical steering gear with a steering control unit (SCU) attached to its housing. In the vehicle, the REPS system is connected via 2 (or more) mounting points to the front axle carrier, which

are considered primary transmission paths. Other connections, e.g. the ball-hinged tie rods to the wheels and the steering column, may be important for low-frequency driving dynamics, however, they are not considered vibration transmission paths.

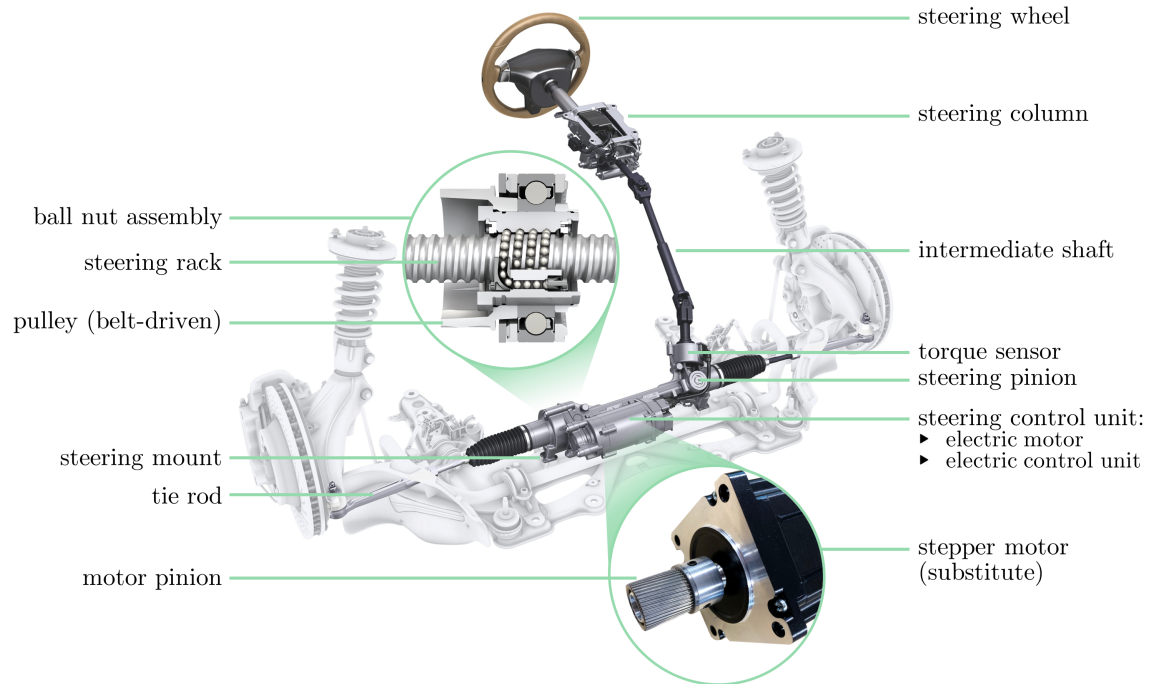


Figure 6.1: Steering system in its intended vehicle installation. The close-up insets show the replaced stepper motor and the ball nut assembly to transform the motor torque into a (side-to-side) rack force [source: bosch-mediaspace.com].

In case dynamic steering input is applied by the driver via the steering wheel, the torque sensor measures the input torque between pinion and steering rack. Dependent on the current driving condition and the measured input torque, the electric control unit (ECU) then calculates the corresponding assist torque, which is generated by the electric motor and superimposed on the rack by the belt-driven ball nut assembly (see inset in Fig. 6.1) [160–162]. In this process, the electric motor emits speed and torque dependent harmonic vibrations related to the number of magnetic poles in the electric machine. These vibrations are mainly caused by electromagnetic forces composed of tangential components, such as cogging torque and torque ripple, and radial forces [163–166]. Other components, such as the toothed belt drive or the pinion, generate tonal vibrations related to the number of meshing teeth. This generates harmonic orders synchronous to the motor/rack speed with a frequency range up to 2.5 kHz [167].

In keeping with the nature of this thesis (that is, in-situ system identification using controlled motors), the REPS system can be actuated by the electrically controlled

motor without mechanical input by the driver. This is comparable with an automated parallel parking manoeuvre. In the following, the electric motor is controlled to utilise the REPS system as an in-situ blocked force vibration source, which is subsequently applied for system identification in a complex multi-DoF assembly. To avoid hardware limitations during this practical study, the steering control unit in Fig. 6.1 is substituted by a (easy-to-control) hybrid stepper motor (86HSE8N-BC38; 8 Nm holding torque). The motor is operated via a closed-loop hybrid servo driver (HSS89) to control the rotor angle by encoder feedback, whilst the input currents of the 2-phase motor are monitored. The substitute motor arguably provides a more straightforward and highly reproducible structure-borne sound excitation, albeit at the expense of a reduced maximum motor speed of 800 min^{-1} . The control logic for the motor speed and rotor position, e.g. number of rotations at constant speed or ramp-up, were programmed into a microcontroller board (Arduino Uno; ATmega328P microchip). It is emphasised that the general approach presented in this thesis is valid for any other type of electric motor and could be implemented with the original steering control unit as well. (The reader is referred to [168–171] for a detailed discussion on external control strategies for permanent-magnet synchronous motors independent from the ECU architecture.)

6.2 Calibration of the Controlled Exciter

Having the blocked force vibration exciter concept validated in Sec. 5.2.3, the following considers its experimental implementation using an active source. This section presents the calibration setup as part of an experimental case study to turn a REPS system into a controlled multi-contact, multi-path blocked force exciter. The purpose of the calibration is to characterise the blocked forces present at the interface DoFs (i.e. the exciter matrix $\bar{\mathbf{F}}_{A,c}$) when the REPS system is operated under controlled and sufficiently reproducible conditions. The calibration considers two measurements steps; the characterisation of the passive properties of the assembly is demonstrated in the following, whereas the operational phase is outlined in Sec. 6.3.

Prior to the calibration, the source-receiver interface has to be defined, that is, the location of the exciter DoFs. In this example, two interfaces (c_1, c_2) are considered at the steering gear mounts, shown in Fig. 6.1. Although typical bench tests require the REPS system to be connected at its pinion and steering rack, these interfaces

are left uncoupled. This allows to maintain equal operational conditions throughout different measurements, e.g. operational loads can change between the bench (C_1) and the vehicle (C_2) measurements due to uncontrolled rack forces when moving the tyres. The two mounts are considered the primary coupling interfaces for transmitting structure-borne steering vibrations, whereas other paths are commonly neglected based on earlier studies [1, 50, 51].

The calibration measurements are performed on a purpose-built test bench, similar to the assembly used in Sec. 5.3. Cocoon-like adapters (see Fig. 6.2b) replace the cross-like elements to facilitate finite difference approximation of 6-DoFs in the centre of the steering gear mount (yellow sphere). Each adapter is instrumented with 4 bi-axial accelerometers, as illustrated in Fig. 6.2b, allowing for spaced response and force (red arrows) measurements at the interfaces (separation distance $\Delta_1 = 60$ mm, $\Delta_2 = 40$ mm). This approach was chosen over the virtual point transformation [78] due to its straightforward implementation and routine employment. The adapters (i.e. the source-receiver interfaces) are designed to allow for unrestricted interface access, simplifying the calibration procedure so that errors related to insufficient excitation positioning are avoided. The adapters and all connected components downstream of the interface are considered part of the receiver (B_1).

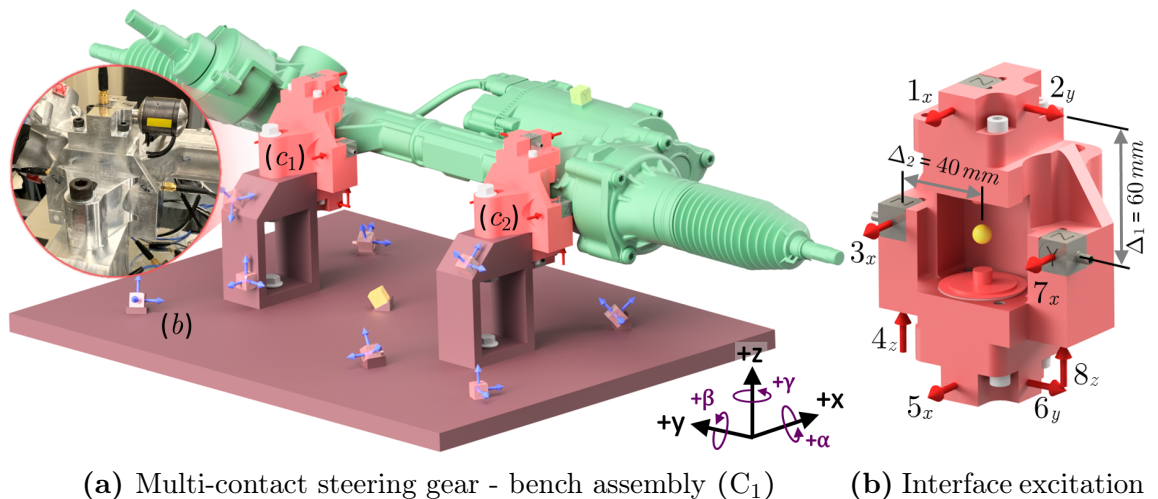


Figure 6.2: Calibration setup (C_1) to turn the REPS system into a controlled blocked force vibration exciter. Arrows indicate excitation (red) and response (blue) measurements as utilised in the FRF measurements. The calibration setup contains: REPS - source (A); plate - receiver (B_1); adapters with the coupling interfaces (c_1, c_2) being positioned exactly in its centre.

For the calibration procedure, only the over-determined solution is considered. In assembly (C_1), responses (blue arrows) are observed downstream of the interface by

8 tri-axial accelerometers (b). The calibration of the REPS system as a blocked force vibration exciter may be outlined as follows:

1. The calibration assembly is instrumented whilst the source is installed, ensuring that all interface DoFs (c_1, c_2) are accounted for. The assembly FRF matrix $\mathbf{Y}_{C_1, bc} \in \mathbb{C}^{24 \times 12}$ is measured using roving shaker excitation at the interface, depicted by red arrows in Fig. 6.2b.
2. In the active measurement phase, the source is operated to generate a controlled excitation. The matrices $\dot{\mathbf{V}}_{C_1, ba}$ or $\mathbf{Y}_{C_1, ba}$ are measured using the remote DoFs on the receiver. Different strategies to generate a reproducible excitation suitable for the exciter concept are outlined in Sec. 6.3.
3. The passive and active measurements are used to calculate the blocked force excitation matrix $\bar{\mathbf{F}}_{A, c}$, as outlined in Eqs. (4.32) and (4.33).

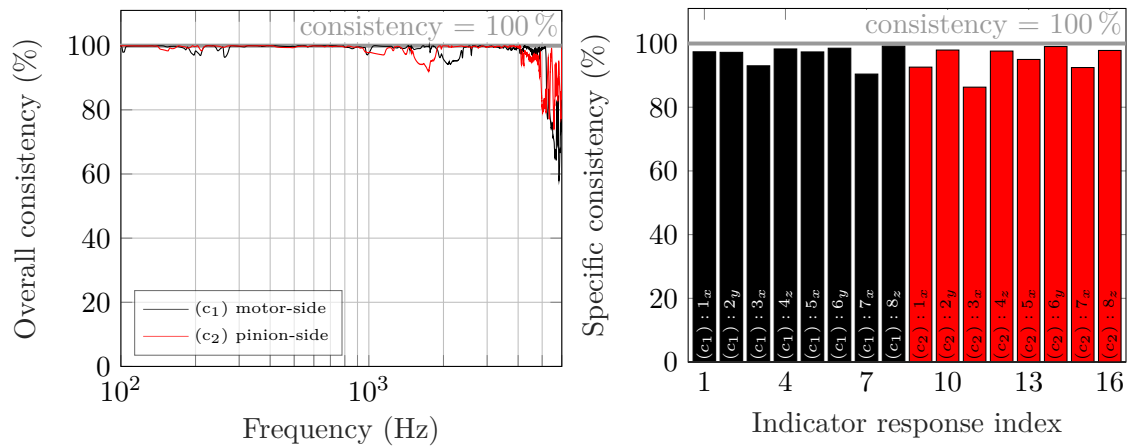
In step 1., the size of the measured FRF matrix is actually 24×16 . Post-multiplication of $\mathbf{Y}_{C_1, bc}$, by the finite difference transformation matrix \mathbf{B} (see Sec. 2.3.2), yields an excitation at (c_1, c_2) that includes both forces and moments, i.e. $[\mathbf{Y}_{C_1, bc} \mathbf{B}] \in \mathbb{C}^{24 \times 12}$. The block diagonal finite difference matrix, $\mathbf{B} = \text{diag}(\mathbf{b}_1, \mathbf{b}_2)$, contains the local transformation matrices \mathbf{b}_1 and \mathbf{b}_2 at each interface. From Fig. 6.2b, it can be seen that 8 excitations (collocated to the response measurements) are considered on the adapter. Here, the indicator excitations ($1_x, \dots, 8_z$) depicted by red arrows are aligned with the positive Cartesian coordinates (x, y, z). For this particular example, the transformation \mathbf{b}_1 for the interface (c_1) takes the form,

$$\mathbf{b}_1 = \begin{bmatrix} \frac{1}{4} & 0 & \frac{1}{4} & 0 & \frac{1}{4} & 0 & \frac{1}{4} & 0 \\ 0 & \frac{1}{2} & 0 & 0 & 0 & \frac{1}{2} & 0 & 0 \\ 0 & 0 & 0 & \frac{1}{2} & 0 & 0 & 0 & \frac{1}{2} \\ 0 & \frac{1}{4\Delta_1} & 0 & \frac{-1}{4\Delta_2} & 0 & \frac{-1}{4\Delta_1} & 0 & \frac{1}{4\Delta_2} \\ \frac{1}{2\Delta_1} & 0 & 0 & 0 & \frac{-1}{2\Delta_1} & 0 & 0 & 0 \\ 0 & 0 & \frac{1}{2\Delta_2} & 0 & 0 & 0 & \frac{-1}{2\Delta_2} & 0 \end{bmatrix} \quad \text{with} \quad \begin{cases} \Delta_1 = 0.06 \text{ m} \\ \Delta_2 = 0.04 \text{ m}. \end{cases} \quad (6.1)$$

Regarding the general construction of \mathbf{b}_1 ; its columns correspond to the measured indicator DoFs ($1_x, \dots, 8_z$), whilst its rows are associated with the target excitation vector $\mathbf{f} = \{f_x, f_y, f_z, \tau_\alpha, \tau_\beta, \tau_\gamma\}^T$ in (c_1). For example, measurements at ($1_x, 3_x, 5_x, 7_x$; first row) are averaged to provide the x -translation in (c_1), whilst the γ -DoF (last row) in the central point is obtained from (3_x) and (7_x) and their separation distance $2\Delta_2$. Due to a shared design, the transformation matrix \mathbf{b}_2 for interface (c_2) takes

the same form as Eq. (6.1). Note that the same matrix \mathbf{B} may be used for the finite difference approximation of responses at (c_1, c_2) .

Potential errors in the FRF measurements and the finite difference approximation matrix \mathbf{B} can be identified with the excitation consistency presented in Sec. 2.4.2. The overall consistency in Eq. (2.36) takes all 8 indicator excitations around (c_1, c_2) , transforms these onto the centre of the adapter and expands the excitations back to their original positions. From Fig. 6.3a, it appears that at frequencies below 4 kHz, a reasonable consistency is obtained (indicated by an overall consistency $\approx 100\%$). In this frequency range, the excitation measurements for the finite difference approximation are dynamically plausible, i.e. all excitations are positioned and configured correctly. A worse agreement is obtained for both (c_1, c_2) at higher frequencies, probably due to flexibility of the adapter. The finite difference approximation assumes rigid body behaviour between the spaced excitations (i.e. over the separation distances $2\Delta_1$ and $2\Delta_2$ in Fig. 6.2b). However, the adapter approximates a rigid structure up to 3-4 kHz, beyond which local flexibilities introduce a finite difference error. For completeness, a more thorough discussion on local flexibilities and a numerical/experimental analysis of the adapter's structural properties are presented in Appendix A.1. Fig. 6.3a also indicates some small inconsistencies around 1.5-2.5 kHz, likely due to flexibilities in the coupling between the adapter and steering mount (not of the adapter itself) or experimental errors.



(a) Overall excitation consistency, $\rho_{f_{C_1, c_2}}(\omega)$ (b) Specific excitation consistency, $\rho_{f_{C_1, c_i}}$

Figure 6.3: Evaluation of the overall and specific excitation consistency for the finite difference approximation of 8 excitations at each coupling point: (c_1) motor-side (—); and (c_2) pinion-side (—).

Experimental uncertainty, particularly due to operator errors in the individual measurements, can be identified using the excitation specific consistency in Eq. (2.37). Deviations in the excitation vector (i.e. position and direction) would appear as ‘outliers’ compared to the consistency score of the remaining interface excitations. The specific consistency is shown in Fig. 6.3b, where the indicator index (1-8) and (9-16) correspond to the measurement positions for the finite difference approximation at (c_1) and (c_2), respectively. A similar score is obtained for all excitations on the adapters, indicating that deviations in Fig. 6.3a are likely due to local flexibilities rather than incorrect placement of one or more excitations on the adapter.

The effect of local flexibilities and measurement error on the completeness of the interface description can further be quantified using the ICC presented in Sec. 2.4.3. Completeness is essential if an operational blocked force vector (i.e. $\bar{\mathbf{f}}_{A,c}$), obtained in the inverse step of fastTPA (see Sec. 4.3.1), is to be characterised correctly and applied with confidence. In the context of the controlled exciter, completeness is not a requirement to identify correct FRFs but indicates if all important exciter-DoFs are (explicitly) included in the calibration process. In other words, the ICC indicates whether enough interface DoFs are considered to determine all FRFs (system identification stage) for the inverse blocked force characterisation.

Based on the 6-DoFs approximation at each steering mount, the ICC in Eq. (2.38) is evaluated for 24 remote receiver DoFs (shown in Fig. 6.2a) and 36 source side excitations. From Fig. 6.4, it appears that at low frequencies, at least below 2 kHz, a reasonable interface description is obtained (indicated by an ICC ≈ 1) when all interface DoFs (—) are included. This indicates that each steering mount behaves like a rigid contact (i.e. sufficiently described by 6 DoFs, 3 translations and 3 rotations) [46]. Even for a ‘complete’ interface description, there exists a notable incompleteness above 2 kHz. For the frequency range above 4 kHz, the local flexibility of the adapter introduces a finite difference error, and therefore the coupling interface is not correctly represented, causing an apparent incompleteness. It is interesting to note that by discarding rotational DoFs (—) in the ICC calculation, little difference is made to the completeness at high frequencies. However, rejecting the rotational coupling can be seen to improve the ICC at frequencies between 1.9-2.5 kHz. This is likely because some rotational coupling DoFs do not significantly contribute to the measured response, introducing noise and further experimental error. This is in contrast to the frequency range below 2 kHz, where the role of rotational DoFs is more evident. Including rotations noticeably improves the interface description,

indicated by the ICC tending towards 1. Whilst this is not an intuitively obvious result, it can be explained from the setup in Fig. 6.2. Both steering mounts are on the same side (opposite to the motor); thus, the source itself is effectively a lever. The one-sided support of the source may create a dominant β -moment contribution at the interfaces also at lower frequencies.

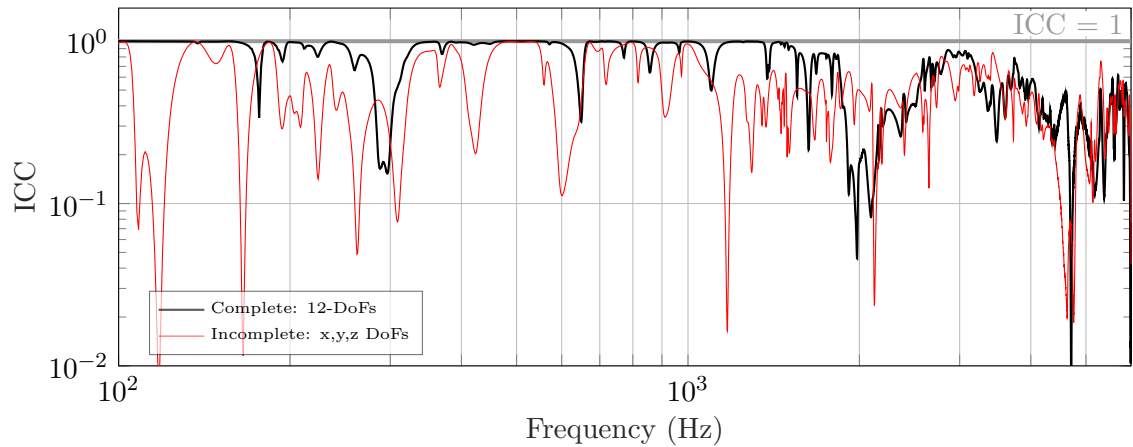


Figure 6.4: ICC for the calibration bench using a ‘complete’ interface description (—) with translational and rotational coupling DoFs and reduced incomplete connectivity accounting for translational-DoFs (—) at (c_1, c_2) only (i.e. x, y, z coupling).

The results presented in Figs. 6.3 and 6.4 suggest that the calibration setup shown in Fig. 6.2 facilitates an accurate calibration up to 4 kHz. Local flexibilities above 4 kHz introduce a finite difference error in $\mathbf{Y}_{C_1, bc}$; this error will also be present in the FRFs determined with the controlled exciter. If the FRFs are used to determine an operational blocked force vector, the defined interface DoFs (i.e. their number and location) are sufficient to describe the active source at least up to 2 kHz (incompleteness between 1.9-2.5 kHz is most likely associated with errors in the rotational driving-point measurements). In practice, the ICC may change when the source is installed in a different assembly. It is recommended to quantify completeness in the target assembly when the REPS system is installed in the vehicle, indicating regions where poor accuracy may be expected. An experimental example of this application is considered in Sec. 7.2.3.

6.3 Excitation Strategy

The measurement configuration described in Sec. 6.2 defines the position of the exciter DoFs at the interface. In this section, different control strategies are considered to operate the source and generate a reproducible excitation at these DoFs.

Together, the excitation matrix $\bar{\mathbf{F}}_{A,c}$ can be calculated, i.e. a set of known blocked force excitations for system identification with the calibrated source in a different assembly.

The requirements for the controlled active state of the REPS system are sufficient reproducibility and enough variation in the excitation for controllability of the interface modes. In the following, two particular active states of the source will be explored; an operational excitation by the active steering system and, for comparison, a series of 36 external excitations using a roving shaker approach. The latter has been successfully implemented in Sec. 5.2.3 and experimentally validated for a similar MIMO assembly (2 contacts, each characterised by 6 DoFs). It will be investigated if the operated REPS system is a suitable source to generate sufficiently independent force contributions at the interface. The challenge herein is that the electric stepper motor is the only controlled source component; thus, enough variation must be generated through different operational states.

6.3.1 Roving Shaker Excitation

If the internal source mechanism is challenging to control, e.g. mechanical sources operated under load, multiple external forces may be applied to represent different operational states of the source (A). The advantages herein are mostly of practical nature: excitations can be placed at accessible locations, whilst mutually independent forces can be added for more variation, e.g. to improve controllability for sources with multiple contacts. The applied external excitations should represent the source's operational state, that is, they should excite the same interface modes. This may be achieved by applying multiple excitations to the source (A) in different directions, for example, using a roving shaker approach.

For the calibration of the REPS system in Fig. 6.2, roving excitation is applied at 36 different source-side DoFs (a) on its housing using an electro-dynamic shaker driven by constant white noise. The force signal of each external excitation is used to determine mobilities between the excitation and response DoFs (b) to calculate a normalised blocked force matrix $\bar{\mathbf{F}}_{A,c}$ given in Eq. (4.33). This provides a more robust and accurate calibration of the exciter than a phase referenced velocity matrix, as shown in Sec. 5.2.3. Each external excitation corresponds to a column in the control matrix $\mathbf{Y}_{C_1,ba} = [\mathbf{Y}_{C_1,ba_1}, \mathbf{Y}_{C_1,ba_2}, \dots, \mathbf{Y}_{C_1,ba_{36}}]$. Note that these excitations will be repeated in the system identification stage whilst the source is installed in the target

assembly (C_2). The excitation DoFs on (A) need to be accessible in both assemblies, ensuring that all measurements are arranged in the same columns.

The calibration considers $n_a = 36$ source-side excitations and $n_b = 24$ remote DoFs on the passive side, i.e. $n_a \geq n_b \geq n_c$, suggesting full controllability and observability at (c). To further investigate the bottleneck effect at the interface, the rank of the excitation matrix $\mathbf{Y}_{C_1,ba} \in \mathbb{C}^{24 \times 36}$ can be analysed through an SVD factorisation, as outlined in Sec. 4.3.3. From the ICC in Fig. 6.4, each interface is fully described by 6 coupling DoFs ($n_c = 12$), at least below 2 kHz. In theory, the resulting responses from all source-side excitations can be represented by 6 forces and 6 moments at the interfaces (c_1, c_2). This suggests that no more than 6 significant singular values shall be present at each interface, corresponding to the rigid coupling DoFs. In Fig. 6.5, the first 12 singular values of $\mathbf{Y}_{C_1,ba}$ are shown.

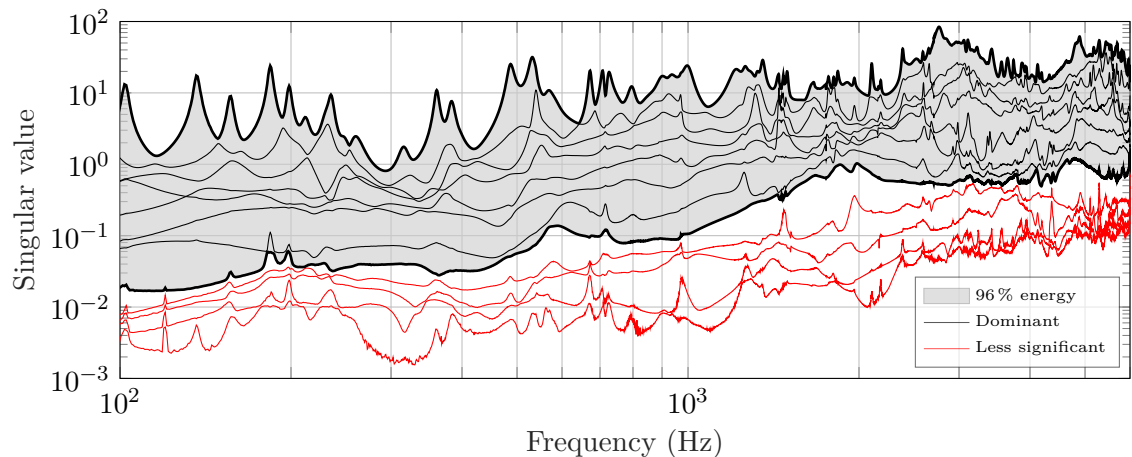


Figure 6.5: Singular values of the bench assembly matrix $\mathbf{Y}_{C_1,ba}$ for 36 roving excitations on the REPS system and 24 remote DoFs (b). The first 8 values (—) are dominant, representing 96% (■) of the energy, indicating a bottleneck effect at the interfaces.

This is confirmed in Fig. 6.5, in fact, the grey area (■) represents the first 8 singular values (—) which together make up more than 96% of the energy in the FRF matrix over the full bandwidth. This means that linear dependencies in $\mathbf{Y}_{C_1,ba}$ result in a rank deficient matrix (effective rank: $n_r = 8$), with the bottleneck effect actively restricting the number of independent excitations passing through the interfaces. The remaining 4 singular values (—) are considered less significant; these lower-order singular values are often composed of noise and measurement error. For example, all four singular values contain a signal distortion at 120 Hz due to electromagnetic interference (data acquisition error: 60 Hz hum).

A rank deficient matrix ($n_r < n_c$) means that either the assembly (C_1) has effectively 8 coupling DoFs or the roving shaker excitations cannot excite more than 8 independent interface modes (not controllable). Additional excitations may be applied to the source to verify this further, whilst the FRF vectors are added to $\mathbf{Y}_{C_1,ba}$ to see if the number of significant singular values increases (compare Fig. 4.3c for partial controllability). For example, 14 additional excitations have been applied to extend the size of the matrix to 24×50 . As expected, the number of significant singular values remained unchanged, indicating full controllability from the roving excitations. Similar considerations apply to the observability on the receiver side (compare Fig. 4.3b for insufficient observability). The number of significant singular values remains unchanged even if the response sensors at (c) (see accelerometers embedded in the adapter in Fig. 6.2b collocated to the excitation DoFs) are considered. Strictly speaking, the control matrix may then be written as a partitioned matrix $[\mathbf{Y}_{C_1,ba} | \mathbf{Y}_{C_1,ca}]^T$ with a size of 40×50 . Note that the responses at the interface account for rotations and translations implicitly, thus providing, in theory, full observability of the rigid interface DoFs. Consequently, the 24 remote DoFs (b) are sufficient to observe the interface dynamics.

Fig. 6.5 implies that the coupling interface of the calibration setup is fully described by 8 DoFs and, furthermore, the external excitations and response measurements provide full controllability and observability. However, this means the calibrated steering system (blocked force exciter) effectively provides an 8-DoFs excitation at the interface, whilst the bottleneck effect limits the throughput. Consequently, using the REPS system to identify a complete set of FRFs (considering 12 coupling DoFs) in a different assembly, the less significant transfer paths may contain errors and noise. In other words, an 8-DoFs blocked force exciter would be utilised to characterise 12-DoFs of the MIMO system. Although this limits the number of paths that can be accurately determined (e.g. in fastTPA), the 4 non-contributing paths will likely appear the least dominant, still allowing a realistic diagnosis (assuming the external excitations represent the source's operational state).

6.3.2 Operational Excitation Using the Electric Motor

Unlike the roving shaker approach, where external forces are applied, this section considers an operational excitation from internal source mechanisms within the REPS system. The operational excitation is controlled by using the electric stepper motor as a vibration source. Connected to the remaining REPS system, the

active motor excites the entire structure of the steering system, thereby moving the steering rack (left-right). The stepper motor can be actuated in steps (increments) of 0.45° to change the steering angle at different speeds. In this case, a controlled operational excitation requires reproducing the operational state at the same rack position.

For enough variation in the operational excitation, the motor may be used as a broadband torque exciter without changing the steering angle or to operate the REPS dynamically between steering end stops [169]. Considering the moving components inside the steering system, the operated source contains multiple vibration generating mechanisms acting in parallel [42]. Alongside the controlled electric motor, other mechanisms are of mechanical nature, e.g. at the ball nut assembly or the pinion (compare Fig. 6.1). These source mechanisms and their internal transfer paths may significantly be affected by the actual position of the steering rack. For example, moving the steering rack from the middle position towards one end changes the transmission paths downstream of the electric motor, particularly in the end stops when the shortened end of the steering rack touches the gear housing (via an end stop damper). Different operational states and rack positions (i.e. steering angles) may be combined for more variation in the operational excitation to provide full controllability. The resulting operational responses are measured on the receiver side at (b) and arranged in columns of the velocity matrix $\dot{\mathbf{V}}_{C_1,ba}$. Note that the setup in Fig. 6.2a prohibits operating the source under an external load applied to the rack bar. Therefore, variation of the internal source mechanisms due to external loading is not considered in this study.

Moving the steering rack for more variation in the excitation may also affect the structural properties of the calibration setup, e.g. due to the shifted mass. In Sec. 6.2, the assembly FRFs were measured with the steering rack in the central position. This raises the question of whether the measured FRFs are valid even for other rack positions. First, we need to quantify how the assembly mobilities, e.g. $\mathbf{Y}_{C_1,cc}$, will change by moving the rack from the middle position towards the end stops. As proven by Bauer in [172], the passive properties measured between different points on the steering housing can be assumed to be invariant to the steering angle. It is shown in Fig. 6.6 that this assumption holds for the assembly FRFs of (C_1). Shown are the driving-point FRFs for the z -translation (Fig. 6.6a) and γ -rotation (Fig. 6.6b) at the interface (c_1) measured for three different rack positions; in the centre and the left/right end stop. Even in the end stop positions (extreme cases),

where the axial joint of the rack touches the gear housing, the variation of the FRFs can be neglected. This may justify that a single FRF matrix (e.g. determined with the rack in the central position) is used during the calibration to represent the passive properties of the experimental setup. However, the altered properties near the end stops may introduce some inconsistency between the operational response and the FRFs (imperfect cancellation between active/passive quantities), which can lead to artefacts in a blocked force calculation [46].

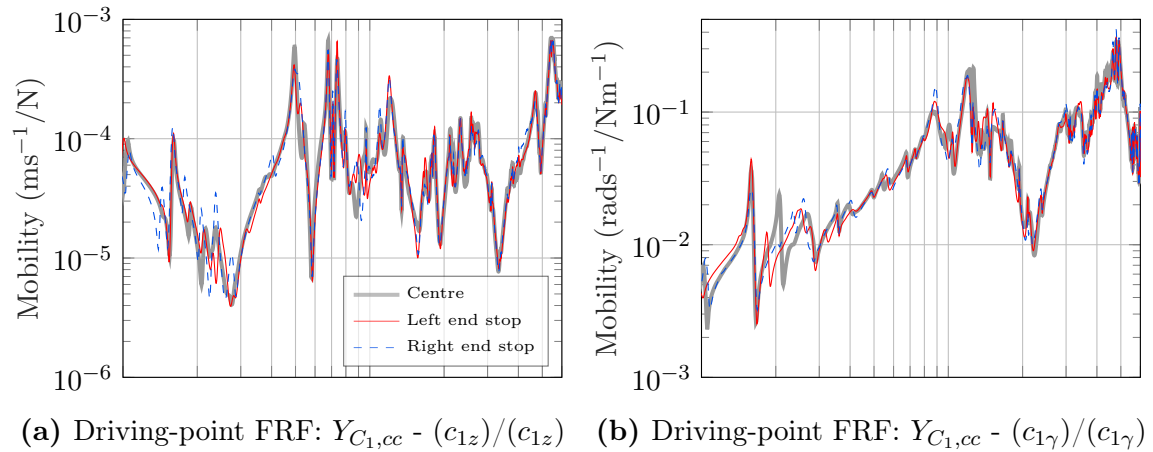


Figure 6.6: Variation in the driving-point FRFs of the calibration setup (C_1) for different steering angles: centre position (—); left end stop (—); and right end stop (--).

Another important consideration is whether a dynamic operational excitation (continuously changing steering angle) can be reproduced in different assemblies. Changes in the source mobilities cause the variation in Fig. 6.6; these are linked to the operational state of the controlled source. Assuming the changes of the source properties are identical in the calibration stage ($\hat{\mathbf{V}}_{C1,ba}$) and the system identification ($\hat{\mathbf{V}}_{C2,da}$), they will cancel in the transmissibility term $\mathbf{T}_{C1,2,db}$ in Eq. (4.32). Recalling the invariant¹ properties of the transmissibility in Sec. 4.13, the term $\mathbf{T}_{C1,2,db} = \hat{\mathbf{V}}_{C2,da} \hat{\mathbf{V}}_{C1,ba}^+$ is only a property of the receiver structure. Consequently, the source can be operated dynamically, assuming changes in the source properties are reproduced in the process.

During the operational excitation, responses are measured on the receiver at the remote DoFs (b). This response signal is separated into discrete time windows. The phase of each window is then reassigned to a reference accelerometer located on the source (see the sensor on the motor housing in Fig. 6.2a). These phase-corrected time

¹ The invariant transmissibility matrix can be used for system identification at multiple steering angles. This requires multiplying the transmissibility term with different FRF matrices $\mathbf{Y}_{C1,bc}$ measured at different rack positions (e.g. the FRFs in Fig. 6.6).

windowed response vectors are then used to construct the velocity matrix $\dot{\mathbf{V}}_{C_1,ba}$. Details on the controlled operational states are listed below:

- ▶ *Torque impulse*: A sudden turn of the stepper motor by 9° generates a torque excitation at the motor shaft, similar to a Dirac function. The motor torque is transmitted over the steering rack onto the housing, therefore, the rack position may alter the internal transmission path. Measurements are performed at 7 different rack positions (centre, half left/right, near the end stops and in the end stop touching the housing) to excite the low to mid frequency range (approximately up to 2 kHz). A velocity vector is obtained at each position from 15 repeated impulses using a rectangular window (as used for impact-based FRF measurements).
- ▶ *White noise*: The stepper motor is connected to a stereo amplifier and operated with a white noise current signal without turning the rotor. This provides a broadband excitation between 500 Hz - 6 kHz, which can be repeated at the different rack positions to extend the frequency range of the impulses. At each position, an averaged velocity vector is determined from a 90 s recording with an window overlap of 50 % (similar to shaker FRF measurements). (Alternatively, the stepper motor can be operated using a sine sweep, e.g. by alternating the motor direction and gradually increasing the stepping frequency.)
- ▶ *Ramp up/down*: The stepper motor is operated to move the steering rack from end stop to end stop. At maximum steering speed ($\approx 200^\circ/\text{s}$), the movement is suddenly brought to a hard stop. Unlike the ‘hard stop’ produced at the end of the range, which is mechanical, this is an electrical hard stop. The fast acceleration and abrupt deceleration of the lateral rack movement exerts moment contributions at the interface. This signal is separated into discrete time windows with an overlap of 50 %. The individual windows (velocity vectors) are arranged in columns of $\dot{\mathbf{V}}_{C_1,ba}$.

For the success of the blocked force exciter approach, the operational excitations need to be replicated in a controlled manner and provide sufficient controllability. Based on the SVD analysis in Sec. 6.3.1, the velocity matrix $\dot{\mathbf{V}}_{C_1,ba}$ needs to contain 8 dominant singular values to provide full controllability of the interface. This is shown in Fig. 6.7, where the first 8 singular values (■) represent 96 % of the energy and that these seem to depart from the noise floor. This means that the matrix $\dot{\mathbf{V}}_{C_1,ba}$ is rank deficient (effective rank: $n_r = 8$), with the bottleneck effect actively constraining the number of independent operational excitations passed onto the

receiver side. Above 2 kHz, there is a well-determined gap in the spectrum of the singular values, separating the dominant from the less significant (—) singular values. This may be related to the characteristics of the broadband operational excitation. Not all operational states are able to excite frequencies up to 6 kHz, e.g. the torque impulses provide an excitation up to 2 kHz. A test for full observability downstream of the interface at (b) was already provided in Sec. 6.3.1.

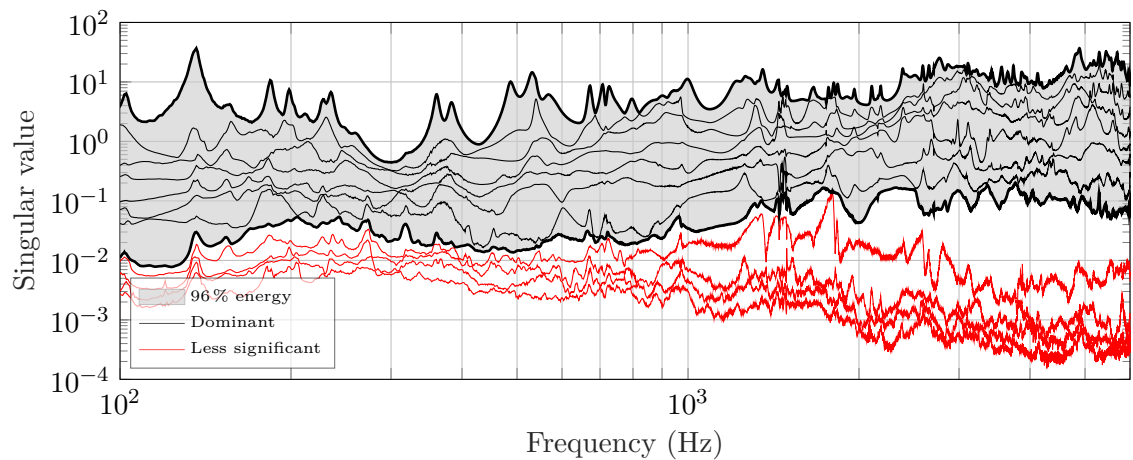


Figure 6.7: Singular values of the bench assembly matrix $\hat{\mathbf{V}}_{C_1,ba}$ for operational excitation of the controlled REPS system and 24 remote DoFs (b). The first 8 values (—) are dominant, representing 96 % (■) of the energy, indicating a bottleneck effect at the interfaces.

It is important to reiterate that the bottleneck effect, in this case, is not caused by insufficient source activity (not controllable) or sensor instrumentation (not observable) but rather results from the physical structure. As shown in Fig. 6.7, the operational excitation provides enough variation to excite the interface DoFs previously identified in Fig. 6.5 and can be performed faster than applying 36 roving excitations. For both (external and operational source excitation), the resulting field of blocked forces at the coupling interface is sufficient to excite the 8 significant interface modes in the frequency range of interest, thus converting the REPS system into a calibrated blocked force shaker.

To verify that the above excitation can be sufficiently reproduced, the concept can be validated in the same installation, where the receiver structure in Fig. 6.3a is modified in some way. For example, the resiliently suspended receiver plate can be clamped to a T-slot bed plate. Although not presented here, FRFs of the modified assembly can be identified with the REPS system and compared to conventional measurements. This form of validation does not require the assembly to physically be dismantled, thus avoiding changes of the source-receiver coupling conditions obtained

when the calibrated source is removed from the calibration setup. That said, this validation indicates errors in the reproduced excitation and the calibration measurements, whilst experimental uncertainty associated with the transfer of the source to a different assembly (e.g. stiffening effects) is avoided.

6.4 Summary and Concluding Remarks

Following its experimental validation in Sec. 5.2.3, the blocked force vibration exciter concept has been applied to an active steering system in a more realistic and practical scenario. The exciter concept considers a calibration and system identification stage; the former has been demonstrated in this chapter. The calibration setup has been presented, consisting of the REPS system (source (A)) rigidly coupled to an aluminium plate (receiver (B)) via two interface adapters. The REPS system is turned into a 12-DoFs (6 translations and 6 rotations) exciter at its two mounts. Two different control strategies have been outlined to operate the exciter: a roving shaker approach and operational excitation.

Roving excitations, already introduced and validated in Sec. 5.2.3, provide a robust and flexible control mechanism using different locations to generate mutually independent excitation. Based on mobilities, the calibration is normalised to the applied shaker force, therefore, easily reproduced. For the operational excitation, the electric stepper motor controls the operational state of the REPS system to generate enough variation in the excitation. The control signals for the operational excitation are highly application-specific and not discussed in detail here; measures to improve controllability and observability have been discussed according to the practical guidelines introduced in Sections 3.6 and 4.3.3. In theory, the operational and roving shaker excitation may also be combined in a mixed fashion to improve controllability, as long as the excitation can be reproduced for system identification.

In the following, the calibrated steering gear will be installed in a vehicle and utilised as a controlled blocked force exciter for fastTPA. The highly reproducible roving shaker excitation provides an ‘ideal’ control mechanism, which is compared to the operational excitation strategy to highlight uncertainties.

7

Vehicle Identification and Steering Noise Prediction

In this chapter, the calibrated steering system, as introduced in the previous Chapter 6, is employed for system identification and diagnostic tests in a vehicle. The controlled excitation is reproduced to predict structural and vibro-acoustic assembly FRFs, which are used for fastTPA and fastVAP of steering noise. The results are compared against an extensive in-situ TPA in the same vehicle; this benchmark study reports on the benefits of the proposed fastTPA in terms of experimental effort and measurement quality. Together, the bench calibration alongside the FRF identification provides a robust fastVAP procedure for steering noise predictions in a virtual vehicle environment. At the same time, experimental hurdles of multi-DoF, multi-paths testing faced in practice are avoided.

Chapter contents:

7.1	Introduction and Outline	164
7.2	Vehicle Subsystem Description	164
7.3	In-Situ TPA Benchmark Study	171
7.4	System Identification with the Controlled Exciter	180
7.5	Case Study I: FastTPA for Vehicle Troubleshooting	190
7.6	Case Study II: FastVAP for Pro-Active Development	202
7.7	Case Study III: System Identification under Realistic Mounting Conditions	206
7.8	Summary and Concluding Remarks	212

7.1 Introduction and Outline

This chapter intends to demonstrate those results that best reflect the implications of the theory developed in Part II. In the previous Chapter 6, calibration procedures have been outlined, turning the REPS system into a controlled blocked force vibration source. In what follows, the same calibrated steering system is installed in a vehicle and used as a 12-DoFs blocked force exciter. The performed system identification, for generality, considers both control strategies (i.e. roving shaker and motor excitation) to determine two sets of vehicle FRFs and for fastTPA and fastVAP (see Sec. 7.5 and 7.6). All steps are, after all, part of a workflow that may be applied to any controllable structure-borne vibration source, not limited to electric motors or steering systems.

TPA and VAP procedures can provide invaluable diagnostic information and impressive predictive capabilities; they are known to be sensitive to measurement and other errors, though. A state-of-the-art benchmark TPA study conducted in the same assembly and under the same ‘industrial environmental conditions’ is presented in Sec. 7.3 to investigate potential errors in the proposed fastTPA and highlight its practical benefits over established methods. In this context, the individual vehicle FRFs are sometimes as insightful as the fastTPA or fastVAP conclusions. The ability to instantly repeat the system identification step is demonstrated in Sec. 7.7, compared to virtual point measurements in a modified vehicle installation. This may prove interesting for applications other than TPA, for example, to validate or design digital twins and evaluate wear and tear events over a lifetime or any type of model-based condition monitoring.

7.2 Vehicle Subsystem Description

Before discussing the applications in the vehicle assembly, let us first introduce the relevant sub-components and their connections. Following the source-interface-receiver model in Sec. 2.5.1 (see Fig. 2.4), the structure-borne transmission from the steering system to the driver’s ear may be described as follows: When operated, the REPS system (A) exerts dynamic forces and moments, through the coupling interfaces (c_1, c_2), onto the vehicle structure (B_2). The following description of the subsystems also considers completeness and consistency primarily from a blocked load perspective, indicating regions that are more susceptible to errors.

7.2.1 Source – Calibrated Steering System

So far, the calibration of the REPS system has been conducted on the test bench. For system identification in the vehicle, the controlled excitation outlined in Sec. 6.3 is repeated to determine structural and vibro-acoustic vehicle FRFs. The controlled excitations to generate known sets of blocked loads $\bar{\mathbf{F}}_{A,c}$ at the interfaces (c_1, c_2) falls into two categories; operational motor excitation ($\dot{\mathbf{V}}_{C_2,da}$) and externally applied forces using a roving shaker approach ($\mathbf{Y}_{C_2,da}$). Note that both variants to operate the multi-DoF exciter are performed in the same in-vehicle installation without dismantling the assembly for consistent testing.

To analyse steering noise in the vehicle, a third operational condition can be distinguished. An automated parallel parking manoeuvre is performed to induce noise and vibrations into the vehicle structure. This is the operational measurement typically conducted during TPA or source characterisation. For the intended operation of the REPS system, the (unknown) operational blocked loads $\bar{\mathbf{f}}_{A,c}$ exerted into the connected vehicle structure are analysed:

- ▶ *EPS-assisted steering cycle*: Steering cycles from end stop to end stop with a constant maximum steering speed of 200 °/s. Each time, five identical cycles have been performed to assess the repeatability of the operational state. The analyses presented throughout this chapter (e.g. fastTPA and fastVAP studies) use the constant-speed steering manoeuvre to address the product's NVH performance in the vehicle, e.g. to troubleshoot the dominant paths for this active state. It is important to reiterate that this steering cycle is independent of the calibration measurements above, which generate a known blocked force excitation $\bar{\mathbf{F}}_{A,c}$ under different operational conditions.

All secondary sources in the vehicle, not of interest for the analysis, are simply turned off during operational testing, thus assuming the vehicle structure being passive.

7.2.2 Receiver – Front Subframe and Vehicle Cabin

In this study, the entire vehicle (without the REPS system) is defined as the passive receiver structure (B_2). The tailored cocoon-like adapters (see Fig. 7.1) are designed to have the same connecting geometry as the original mounts and are used to install the steering system in the vehicle. With the adapter connecting the source to the receiver, the REPS system is mounted to the subframe with an offset to its intended

installation position while allowing direct access to all coupling DoFs (c_1, c_2). Note that the adapters shown in Fig. 7.1 are considered part of the receiver, and may change the dynamic response of the chassis together with the contribution paths due to the shifted source (offset in x-direction: 8 cm). Other than the steering system, the front subframe supports the engine, part of the front wheel suspension assembly, and connects to the vehicle's chassis and bodywork. Further downstream, the propagation of structure-borne sound and vibration becomes quite 'complex'. Steering gear vibrations reach the vehicle interior over multiple dozens of transfer paths, which means that measurements are often preferred to obtain accurate FRFs rather than numerical modelling efforts [10].

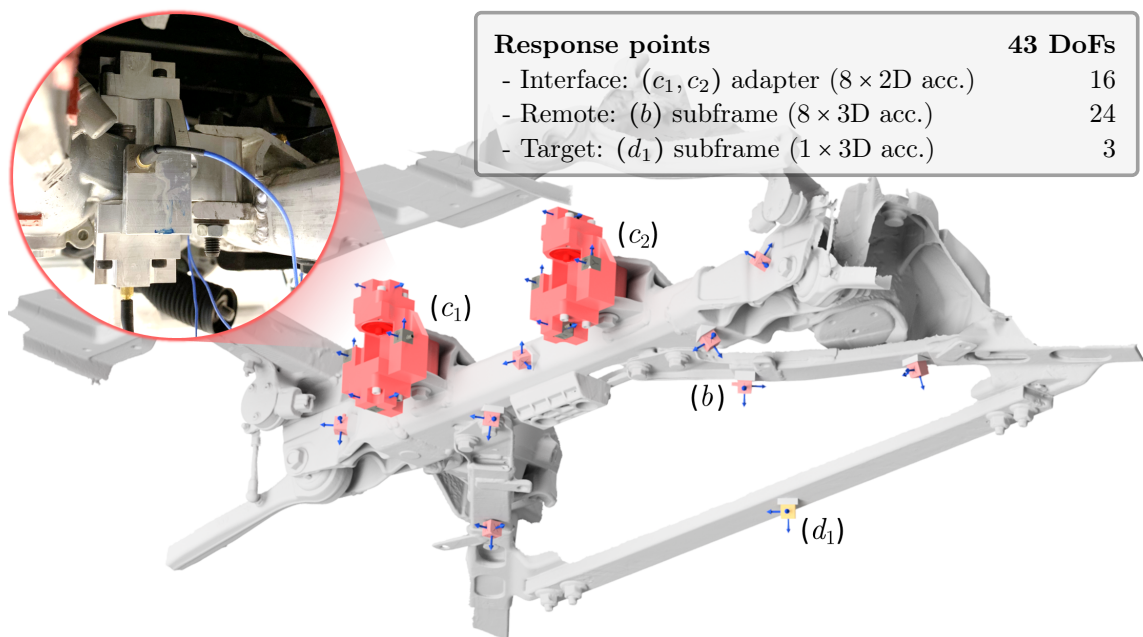


Figure 7.1: Bottom view: Scan of the front subframe, including the target accelerometer (d_1) and the adapters to facilitate access at the coupling interfaces (c_1, c_2). Blue arrows indicate response measurements at the interfaces, the remote DoFs (b) and the target (d).

Both structural and vibro-acoustic propagations are considered in the following validation process by different target DoFs ($d_1 - d_3$) on the receiver. Shown in Fig. 7.1 is the tri-axial sensor to observe the structural response, namely the target (d_1) positioned on the cross-rail connecting the rear ends of the subframe. This validation sensor, indicated in yellow, is located downstream of the interface, somewhat remote yet not too far distant, to establish a consistent phase relationship to the interface DoFs [1]. All remaining accelerometers (red) mounted on the subframe are considered remote DoFs (b) used for inverse force identification in the benchmark in-situ TPA study and fastTPA.

Vibro-acoustic transfer paths are evaluated in the vehicle's cabin and consider the radiation from panels in the interior. Two microphones are positioned at the locations of the driver's ears (d_2), indicated in yellow, next to the dummy head (see Fig. 7.2). Whereas the build-in dummy microphones are well capable for binaural recordings, exact reciprocal measurements are far from trivial. In automotive TPA applications, vibro-acoustic transfer FRFs are often determined by acoustic excitation with a volume-velocity source. Not integrated microphones are preferred to avoid errors related to inaccurate reciprocal conditions, i.e. to achieve proper positioning between microphone and the acoustic centre of the volume-velocity source during reciprocal measurements. In case of reciprocal measurements, the vibration response is measured at the interface (see adapter instrumentation with 4 sensors in Fig. 7.1), whilst the volume-velocity source is attached to the headrest to replace the target microphone, as shown in the close-up in Fig. 7.2.

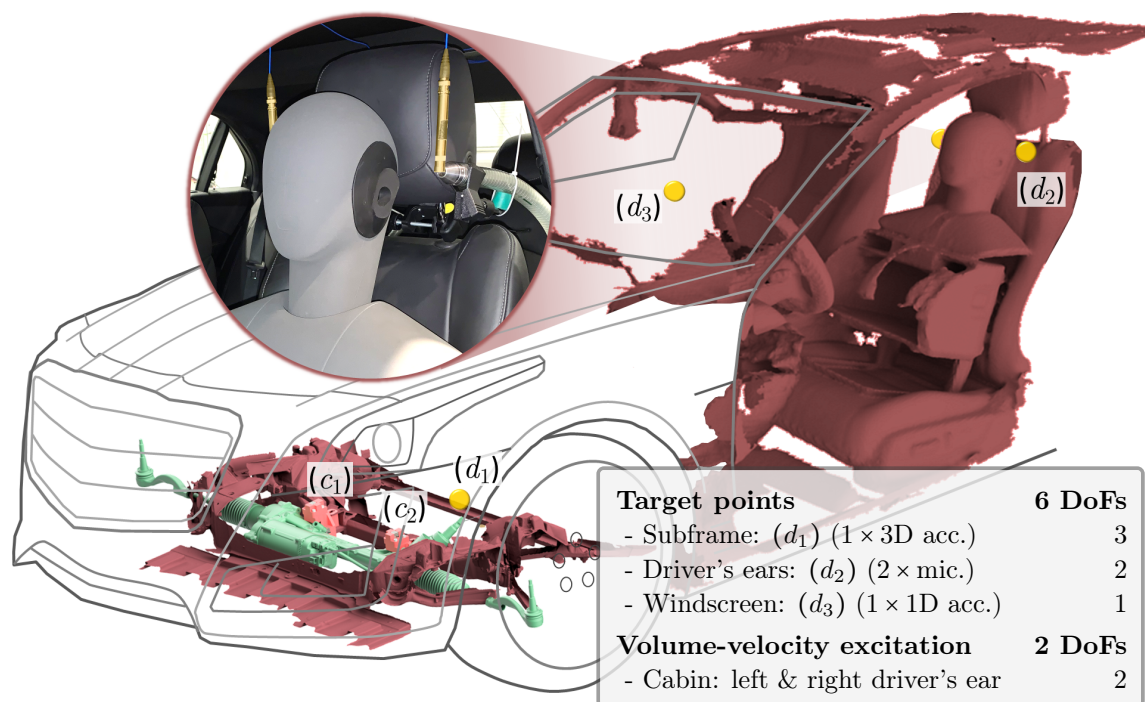


Figure 7.2: Scan of the vehicle cockpit with the target microphones at the driver's ear positions and a windscreen accelerometer at (d_3). The sound pressure probes at (d_2) may be replaced by a volume-velocity source for reciprocal measurements, as shown in the close-up.

Throughout the remainder of this chapter, the accelerometer on the subframe (out-of-plane z -direction) and the microphone at the left driver's ear are used as target and/or validation DoFs. The corresponding structural and vibro-acoustic FRFs used

for validation are, unless otherwise specified, measured with a shaker excitation applied at the interface. A third target DoF (d_3) on the windscreen will be introduced in Sec. 7.7 for reciprocal validation measurements.

7.2.3 Interface – Subsystem Connectivity and Completeness

The REPS system and the adapters are rigidly connected to the front subframe at two bolted connection points, which in turn connects to the vehicle's bodywork. Note that the bench setup is dismantled to install the steering system in the vehicle without having the adapters removed from the source. Hence, the adapters ensure that the interfaces (c_1, c_2) are described by 12-DoFs (matching the calibration setup) in the centre of the mounts, yet facilitating force excitation for consistent FRF measurements. Later (see Sec. 7.7) the adapters will be removed for more representative mounting conditions. Similar to the calibration setup in Sec. 6.2, the input shaft and both tie rods are left uncoupled (i.e. the steering column and the wheels are not connected to the REPS system) to retain consistent coupling conditions, and to some extent, avoid additional loading on the rack bar.

Obviously, all vehicle FRF measurements should meet the basic requirements, e.g. sufficient SNR or proper coherence in the targeted frequency range. Yet, the FRF model as a whole shall, above all, represent the complex MIMO characteristics of the assembly. For an accurate description of the source, experimental testing mostly concentrates on describing the multi-DoF dynamics at the coupling interface. The ICC as evaluated for the calibration setup (C_1) in Fig. 6.4 may be reevaluated for the vehicle assembly (C_2) to verify that the 12 coupling DoFs (i.e. 3 translations and 3 rotations in the centre of each mount) can correctly describe the source activity. It can be seen in Fig. 7.3a that the ICC obtained for the vehicle assembly (—) is similar to the completeness apparent in the calibration setup (—), in part due to the adapter used in both assemblies. It is interesting to note that for a full set of rigid coupling DoFs, even then, there exists a notable incompleteness at approximately 1.5-3 kHz. Looking at both experimental setups, the changed receiver-side mounting of the adapters clamped into the C-shaped bracket of the subframe (see Fig. 7.1) did not affect the sudden drop in the ICC. Instead, the detected incompleteness likely occurs due to flexibility at the source-side coupling where the REPS mount is connected to the adapter. For the source description, this implies that the acquired blocked

loads, $\bar{\mathbf{f}}_{A,c}$, although correct in their own respect, are not the ‘true’ blocked loads¹ at (c_1, c_2) , and may be augmented to include flexible coupling DoFs [46]. Nevertheless, these results suggest high quality blocked force characterisation below 1.5 kHz and consequently indicate regions where the predictions are susceptible to errors.

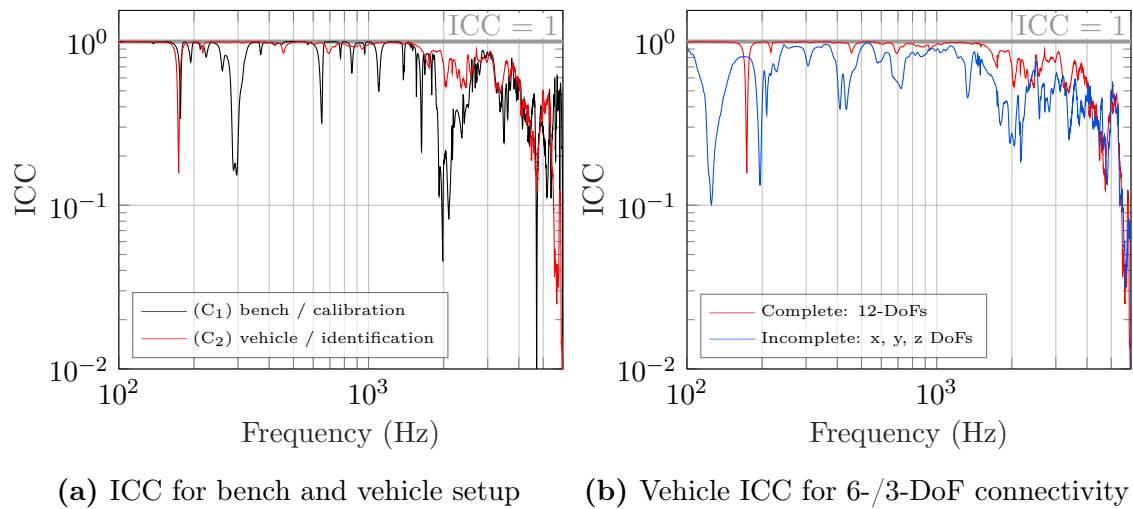


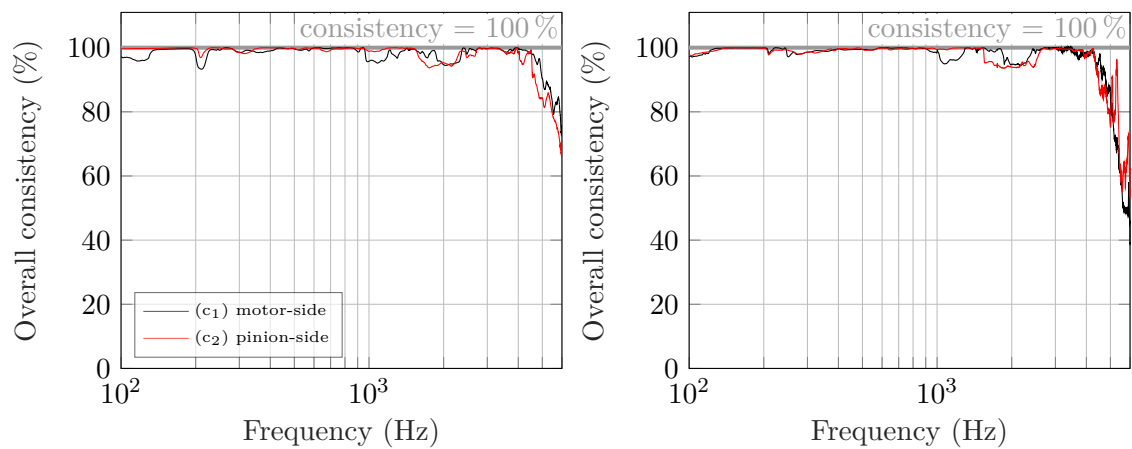
Figure 7.3: ICC for the calibration bench (—) and the vehicle assembly (—), alongside changes between the full (i.e. 3 translations and 3 rotations) and an incomplete interface description (—) using translational DoFs (x, y, z) at each connection point.

The ICC results for the vehicle assembly in Fig. 7.3b indicate that rejection of any DoF worsens the interface description. For the rigidly connected source, it appears that rotational coupling is essential in the frequency range below 4 kHz, whilst higher frequencies are dominated by the breakdown of the local rigid interface behaviour. Although the rotational coupling provides a noticeable improvement this raises the question of whether all coupling DoFs contribute to the receiver-side response. In fact, the SVD analysis in Figures 6.5 and 6.7 suggest that an incomplete interface description with 8 coupling DoFs may be sufficient, however, this may appear speculative and requires further proof by a partial path contribution ranking (see Sec. 7.3.2).

As for the previous calibration setup, evaluating the sensor and excitation consistency is a useful tool to assess measurement quality, troubleshoot errors in the instrumentation and to validate local rigid behaviour at the interface. Here, the consistency analysis for the finite difference approximation complements the ICC, as it may help to justify incompleteness. Analysed for the response measurements at each

¹ By definition, the acquired loads are, in fact, blocked loads and represent the reaction forces/moments of the source (A), blocked at the interface DoFs. However, they are not considered ‘true’ blocked loads, as some contributing coupling DoFs are not mathematically blocked.

adapter, the overall sensor consistency in Fig. 7.4a indicates high values throughout most of the bandwidth, with some small effects of local flexible behaviour around 1.5-2.5 kHz and larger deviations above 4 kHz. Again, errors at high frequencies are associated with the structural properties of the adapter and the breakdown of the rigid body behaviour, shown in Appendix A.1. This means the finite difference error causes an apparent incompleteness in the interface description (see Fig. 7.3) which can be resolved by extending the 6-DoFs description for flexible coupling. However, the relevant frequency range for steering noise prediction and auralisation are mostly limited to 2.5 kHz. Note the ICC (see Sec. 2.4.3) and the response consistency (see Sec. 2.4.2) evaluate completeness/consistency for a set of artificial excitations, which may not be representative of the source's operational state.



(a) Overall response consistency, $\rho_{v_{C,ca}}(\omega)$ (b) Overall excitation consistency, $\rho_{f_{C,c}}(\omega)$

Figure 7.4: Evaluation of the response and excitation consistency for the finite difference approximation of 8 responses/excitations at each coupling point: (c_1) motor-side (—); and (c_2) pinion-side (—).

The consistency analysis can be repeated for the excitations applied on the adapter. The overall excitation consistency in Fig. 7.4b shows a similar frequency characteristic for the force transformation. Although access to the coupling interfaces in the narrow engine compartment is limited, the 8 shaker excitations applied around each coupling point are correctly positioned and properly executed.

Consequently, the source-receiver interface can be correctly represented by point-like contacts with 6-DoFs for steering noise predictions in TPA and VAP. However, the effects of local flexibilities in the interface areas (particularly above 4 kHz) and an apparent incompleteness (1.5-3 kHz) may introduce errors to the in-situ blocked force characterisation.

7.3 In-Situ TPA Benchmark Study

This section reports on a benchmark study; results will be compared against those obtained using fastTPA with respect to reliability, time and experimental effort. There exist many TPA variants to reduce time and complexity (outlined in Sec. 2.5.2), usually at the expense of transparency and the level of confidence in the results [50]. For benchmarking, in-situ TPA (also: iTPA or blocked force TPA) is arguably the most popular and exact diagnostic variant, as it avoids dismantling of the assembly [6]. This means that operational blocked forces at the source-receiver interfaces (c_1, c_2) are characterised in the vehicle and later used to predict total and/or partial operational responses on the connected receiver. The main focus of this study is to provide an accurate model for the propagation of structure-borne noise and vibration in the vehicle, rather than a detailed optimisation of the NVH performance for the installed steering system.

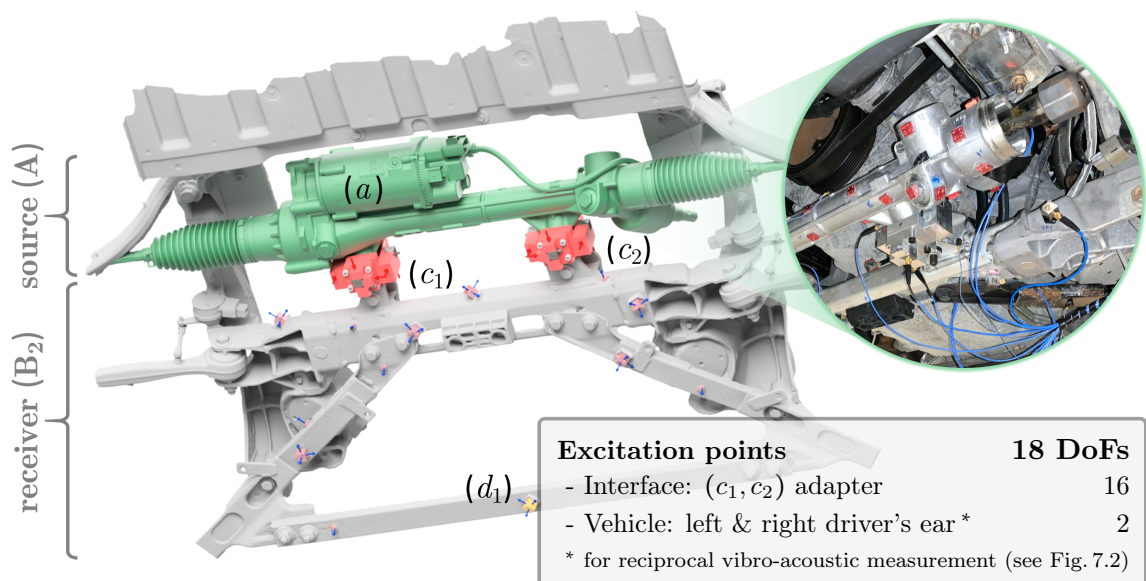


Figure 7.5: Vehicle assembly for in-situ TPA benchmarking and prediction of steering noise. The source-receiver setup contains: REPS - source (A); subframe - receiver (B₂); adapters - coupling interfaces (c_1, c_2); target DoF (d_1).

There are a few important details to note concerning the in-situ TPA study. The aim is to compare TPA results in the full bandwidth from 100 Hz - 6 kHz, which is the operating frequency range of the electro-dynamic shaker used for conventional FRF measurements. This exceeds the frequency range required for accurate steering noise predictions in the driver's cabin. Typically, the interest is in frequencies up to 2.5 kHz to obtain realistic time-domain auralisations for the operational REPS

system. The in-situ TPA results are used as a reference and compared against those of the proposed fastTPA. Unlike the on-board validation for ‘total’ responses, as specified by ISO 20270:2019, partial responses cannot be compared to a directly measured signal. Instead, the partial path contributions of the fastTPA need to be validated against the contributions analysed in the in-situ TPA. In either case, the results will be subject to some degree of uncertainty. However, the in-situ TPA method proved reliable and is up to today one of the most popular state-of-the-art techniques for NVH troubleshooting and thus used as a reference.

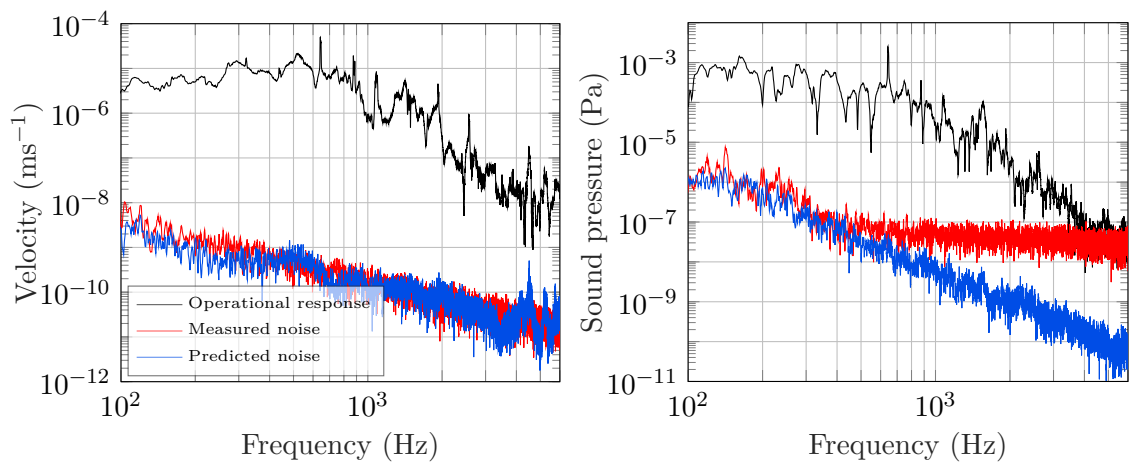
The experimental setup for the in-situ TPA is shown in Fig. 7.5. As before, rotational DoFs at each coupling interface are calculated using a finite difference approximation for full 6-DoF coupling; x , y and z -translations, alongside their corresponding rotations. The transformation and excitation positions on the adapter are essentially the same as in Eq. (6.1) and Fig. 6.2b, respectively. For the inverse blocked force calculation, responses are observed on the passive side by 24 remote DoFs (b) to provide an over-determined solution. The in-situ TPA may be outlined as follows:

1. The matrices $\mathbf{Y}_{C_2,bc} \in \mathbb{C}^{24 \times 12}$ and $[\mathbf{Y}_{C_2,dc} | \mathbf{H}_{C_2,dc}]^T \in \mathbb{C}^{6 \times 12}$ are measured simultaneously using a roving shaker approach (see Fig. 6.2b), with 8 excitations (red arrows) applied to each adapter.
2. Alternatively, by reversing the excitation and response positions, $\mathbf{H}_{C_2,cd} \in \mathbb{C}^{12 \times 2}$ can be measured reciprocally using a volume-velocity source (see Fig. 7.2).
3. The REPS system is operated, and the responses at (b) and (d) are measured during the constant-speed steering manoeuvre.
4. Operational blocked loads (i.e. $\bar{\mathbf{f}}_{A,c}$ for the steering cycle) are determined using Eq. (2.9). The individual contribution paths can be analysed by combining the blocked loads with the corresponding structural/vibro-acoustic FRFs.

Although labelled as in-situ TPA, the steps (**1.-3.**) are part of the in-situ blocked force source characterisation, as specified by ISO 20270:2019 [38]. The workflow described in the ISO standard further outlines a preliminary validation procedure using artificial excitation, that is, a prediction using a simulated operational test. This validation described in Sec. 2.4.1 replaced the tonal nature of the operated source with a broadband excitation to provide a verification check, in which errors in sign convention, ordering data in matrices/vectors, or calculation procedure can be detected. This form of preliminary validation is not presented here; for a practical example, the reader is referred to Ref. [1].

7.3.1 Prediction and On-Board Validation of Steering Noise

This section considers the prediction of noise and vibrations for the operated REPS system. The focus is to validate the complex behaviour of the operated source for a representative load case² to assess the quality of the experimentally determined blocked loads. The actual operational response of the source consists of multiple sharp tonal harmonics (due to periodic mechanisms of various rotational components), whereas excitation levels are relatively low. Due to the source's nature and position far distant from the cabin, the SNR at (d) is analysed to indicate if the operational responses can be resolved from the measurement noise floor. Fig. 7.6a shows the narrowband Fourier spectrum of the operational vibration response $v_{C_2,da}$ (—) measured at the vehicle subframe (d_1), alongside the sensor's noise floor (—). Across the entire frequency range, a sufficient SNR (rule of thumb: $\text{SNR} > 10$ dB [38]) is achieved on the velocity signal. Analogue to the structural response, Fig. 7.6b shows the measured sound pressure response $p_{C_2,da}$ at the left driver's ear (d_2). Above 4 kHz, the sound pressure (—) is dominated by noise, with the limiting factor being the microphone's noise floor (—) rather than the ambient noise of the semi-anechoic test environment. This means the sound pressure signal measured during operation in the vehicle cabin did not exceed the effective sensitivity threshold of approximately 0.01 Pa.



(a) Velocity response on subframe, $v_{C_2,da}$ (b) Sound pressure in vehicle cabin, $p_{C_2,da}$

Figure 7.6: SNR at the target accelerometer/sound pressure probe (d_1, d_2) for the operated REPS (constant speed). Narrowband representation: measured operational response (—); measured noise floor (—); and predicted noise (—) for the vehicle assembly (C_3).

² Artificial shaker excitation (see ISO 20270:2019 [38]) utilises different contribution paths at the interface. Depending on the position, the ‘simulated’ source activity may neglect some translational and/or rotational contribution paths completely, therefore a preliminary validation using artificial excitation will not replace the operational on-board validation.

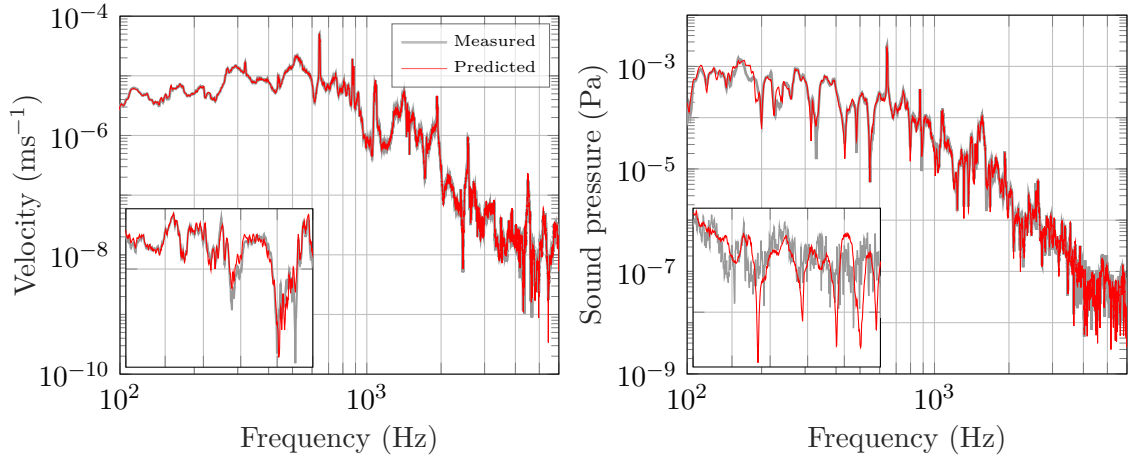
However, if the sound pressure response in Fig. 7.6b is predicted using blocked loads, a remarkably good prediction is obtained not masked by high-frequency noise. This is shown more clearly in the inset of the on-board validation in Fig. 7.7b. The inverse blocked force calculation can be seen to significantly reduce the effect of noise in the sound pressure signal due to employing high quality measurements from different sensor types. For a better understanding of how uncorrelated noise at the remote sensors (b) affects the inverse blocked force calculation, background noise measurements are used to predict the so-called ‘blocked load noise floor’ [173]. While the source is turned off, the noise measured at the response DoFs (b) is converted into blocked loads using the matrix inverse (see Eq. (2.9)), which represents a distorted variant on the measured noise containing errors imposed by the matrix inverse. In other words, the operational velocity $\mathbf{v}_{C_2,ba}$ is replaced by a background noise vector in the blocked force calculation. Physically, one could interpret the ‘blocked load noise’ as the minimum level of source activity which can be resolved by the blocked loads. Propagated onto the target DoFs (d) via Eq. (2.26) allows predicting the effective sensor noise at the validation DoFs after matrix inversion, which defines the lower limit for an accurate prediction [50].

Fig. 7.6b shows the calculated microphone noise (—) is lower than the measured sensitivity threshold (—), for this reason, the on-board validation in Fig. 7.7 is believed to provide reliable SPL estimates even at low levels above 4 kHz. Anti-resonances in Fig. 7.7b are more prominent in the predicted sound pressure, whereas the actual microphone measurement (—) is already masked by unwanted noise. In this benchmark study, the blocked load vector is determined from structural responses³, namely 8 tri-axial accelerometers (sensitivity: 100 mV/g) on the vehicle’s subframe. Propagated into the vehicle cabin, the vibro-acoustic prediction benefits from lower noise floor of the accelerometers, allowing to resolve pressure responses below the microphone’s noise floor.

In contrast, the accelerometer type at (d_1) is the same used at the remote positions (b), which, in principle, share the same sensitivity threshold. This way, the reasonable agreement between the measured and predicted noise floor, shown in Fig. 7.6a, indicates that the matrix inversion was carried out without introducing large numerical errors. Concluding, the level of agreement in the on-board validation

³ Other response types (e.g. sound pressure) are not considered in the inverse blocked force calculation. In theory, different sensors can be used in a mixed fashion to improve the conditioning of the inverse matrix [90].

(see Fig. 7.7) clearly suggests that the interface description provides an accurate representation of the operated REPS system. In spite of the incompleteness detected at 1.5-3 kHz and above 4 kHz (compare Fig. 7.3a), the predicted responses may be more reliable than the actual measurements, as highlighted in the insets.



(a) Velocity response on subframe, $v_{C_2,da}$ (b) Sound pressure in vehicle cabin, $p_{C_2,da}$
(Inset covers freq. range from 3.9 - 4.4 kHz) (Inset covers freq. range from 5 - 5.5 kHz)

Figure 7.7: On-board validation at the target accelerometer/microphone (d_1, d_2) for the operated REPS (steering cycle). Narrowband representation: measured operational response (—); predicted velocity/sound pressure response (—) of the vehicle assembly (C_2).

In theory, the microphone accounts for air-borne transmission from a sound-radiating source and structure-borne contribution caused by radiation from parts on the passive side (e.g. dashboard, windscreen and other panels in the vehicle cabin). The measured sound pressure in Fig. 7.7b may thus be considered a linear combination of the structure-borne excitation $\bar{\mathbf{f}}_{A,c}$ at the interface and the acoustic load generated by the source $\mathbf{q}_{C,a}$, defined by,

$$\mathbf{p}_{C,dc} = \mathbf{H}_{C,dc} \bar{\mathbf{f}}_{A,c} + \mathbf{N}_{C,da} \mathbf{q}_{C,a} \quad (7.1)$$

weighted by their vibro-acoustic and acoustic contributions paths, denoted by $\mathbf{H}_{C,dc}$ and $\mathbf{N}_{C,da}$, respectively. However, the predicted sound pressure in Fig. 7.7b considers only the structure-borne nature of the source, i.e. vibration energy is transmitted over the structural coupling points and radiated downstream of the interfaces. The excellent agreement of the on-board validation implies that the tested REPS system can be considered a source of structure-borne sound and vibration, whereas the air-borne contribution to the vehicle cabin is insignificant (i.e. an air-borne source would manifest itself in an under-prediction in Fig. 7.7b) [172].

7.3.2 Partial Path Analysis and Contribution Ranking

The methods presented throughout this thesis often consider the predicted responses as the result of the TPA. In fact, tools such as on-board validation are applied to quickly assess the error/uncertainty associated with the TPA approach. Instead, the actual purpose is to separate source excitation (i.e. blocked loads) from the structural or vibro-acoustic transfer characteristics to identify the amount of energy transmitted through each path. This indicates if modifications need to be made at the source or the connected receiver structure to troubleshoot the most dominant contribution paths. This section presents the relative contribution of each excitation DoF to the total operational response, i.e. a rank ordering of contributions.

In the so-called partial path analysis, the blocked load DoFs (c_i) are combined with their corresponding propagating transfer paths H_{C,dc_i} , to predict the partial assembly response on receiver side. This procedure allows each contact interface DoF to be assigned a complex partial contribution to the overall target response (d),

$$p_{C_2,dc_i} = H_{C_2,dc_i} \bar{f}_{A,c_i} \quad \text{with} \quad i \in 1, \dots, n_c \quad (7.2)$$

$$p_{C_2,dc} = \sum_{i=1}^{n_c} p_{C_2,dc_i} \cdot \quad (7.3)$$

Summation over i determines which contribution paths are considered in the response $p_{C_2,dc}$. For instance, the total response, used for the on-board validation, is composed of the complex sum of all 12 partial contributions, 6 at each coupling interface. It is this detailed information which makes the method useful for troubleshooting NVH problems.

Fig. 7.8 shows the target sound pressure response at (d_2) split into the individual paths at the motor- (c_1) and pinion-side (c_2) interfaces to allow for visual identification of the dominant contribution path or critical frequency ranges. Typically, the individual paths are arranged in different rows, whereas the operational measurement and the predicted sum (see Eq. (7.3)) are depicted on the top. Mathematically, comparing the measured sound pressure (Target | Measured) with the sum of all partial pressure contributions (Sum | Predicted) corresponds to the on-board validation in Fig. 7.7b and may be used as a quality indicator. The excellent agreement over a wide frequency band in the on-board validation indicates a reliable prediction. This indirectly implies that the dominant partial contributions (that make up the

total response) are correctly determined. Note that validation by comparison to a measured quantity is not possible for the partial responses.

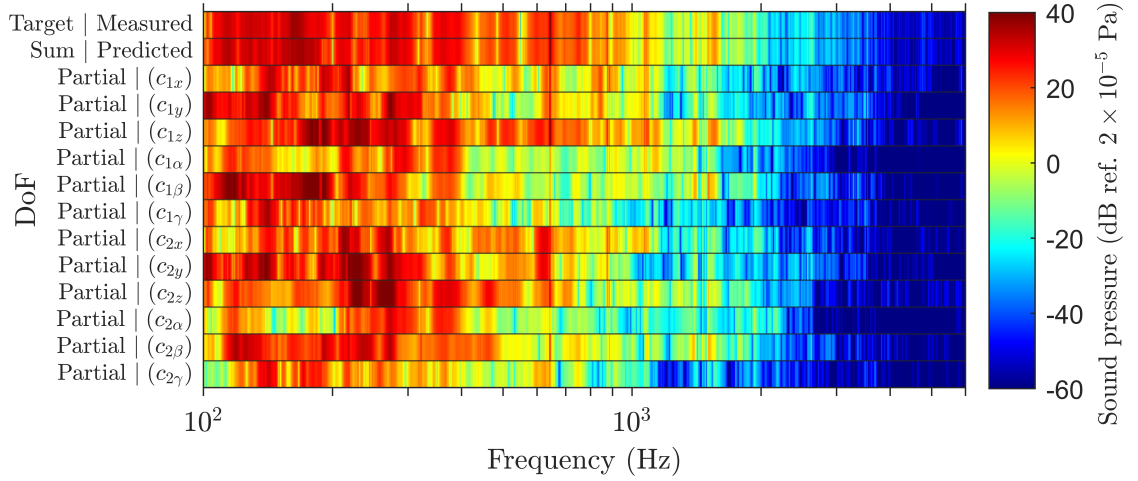


Figure 7.8: Narrowband contribution analysis for the total predicted sum and the partial paths from the coupling DoFs (c_1, c_2) to a target sound pressure probe (left driver's ear) for the operational REPS (constant speed).

In a quick analysis, the sound pressure response in Fig. 7.8 spans an effective frequency range up to approximately 2.5 kHz. A significant contribution, most notably above 400 Hz, can be identified in the translational z -direction at the motor-side interface (i.e. blocked force (c_{1z}) and corresponding vibro-acoustic path). Concerning the practical interpretation, it is mentioned that the illustrated plot offers no insight into whether a significant contribution is caused by a sensitive transmission path or a high dynamic loading at the coupling DoF [1]. For a more detailed analysis, the blocked load spectra may be used to spot interface DoFs with higher source excitation.

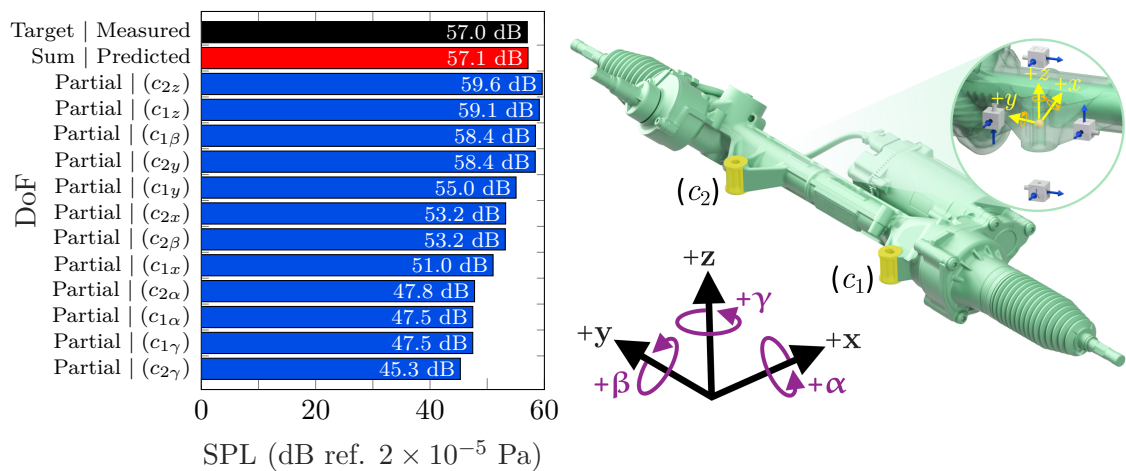
As Fig. 7.8 is not very intuitive, one often considers the contribution ranking of the spectrum levels to identify the dominant partial paths. The root mean square (RMS) values of the total and partial sound pressure represent the overall energy level across a selected frequency range and may be directly derived from the spectrum $X(\omega)$ itself,

$$\text{RMS}(X(\omega)) \triangleq \sqrt{\frac{X(0)^2}{2} + \sum_{i=1}^{k-1} X(i)^2 + \frac{X(k)^2}{2}} \quad (7.4)$$

$$\text{with } \begin{cases} X(0) & \text{lower cutoff for 'high-pass filtering'} \\ X(k) & \text{upper cutoff for 'low-pass filtering'}. \end{cases}$$

This calculation, commonly integrated into commercial software, uses the spectral information (linear format: $X(0), \dots, X(k)$) in the frequency domain to avoid time domain conversion and filtering. This indicates how Fig. 7.8 can be converted into RMS levels for the relevant frequency range from 100 Hz - 2.5 kHz.

The bar graph in Fig. 7.9a provides the contribution ranking (■) of the averaged sound pressure levels in Decibel with a total prediction error (measured (■), predicted (■)) of 0.1 dB. This graphic allows for quick visual troubleshooting (compare Fig. 7.9b) of the most dominant paths: z -translation at both interfaces (c_{2z}, c_{1z}), alongside bending around the y -axis (rocking up-down motion) on the heavier motor-side ($c_{1\beta}$) and y -translation on the pinion-side (c_{2y}), closest to the driver. On the lower end, the partial paths α and γ at both interfaces, although important at low frequencies below 400 Hz (see Fig. 7.8), have no significant contribution to the cabin's SPL. This seems plausible considering the vehicle assembly; the connected structures are fairly rigid in the α and γ -direction, which makes it challenging to excite in the intended rotational directions.



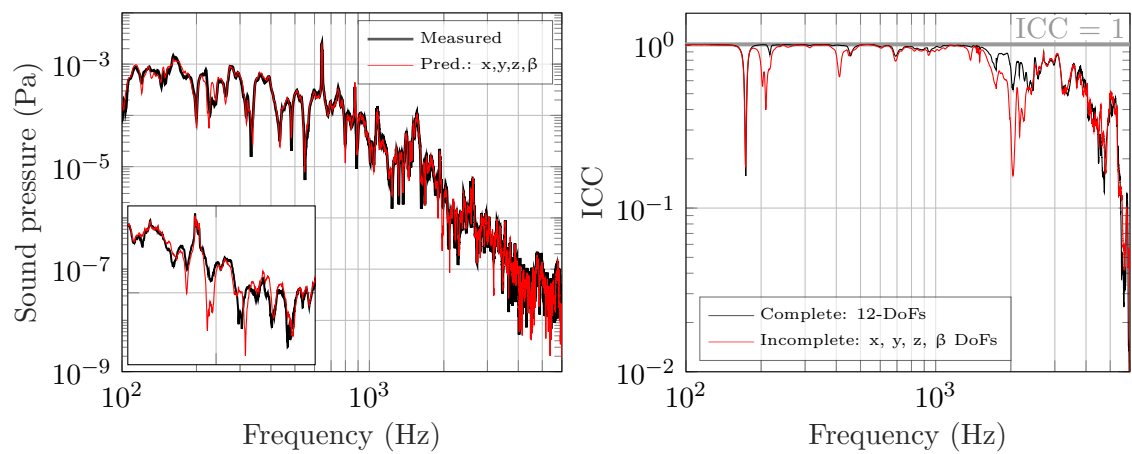
(a) Ranking of the vibro-acoustic paths

(b) Vehicle coordinate system

Figure 7.9: Measured and predicted sound pressure at the left driver's ear (d_2), including a contribution ranking of the partial paths. Sound pressure levels: measured (■); predicted sum (■); and rank ordered partial contributions (■) for the operational REPS system.

For some paths, e.g. (c_{2z}), ($c_{1\beta}$), etc., the partial responses show higher individual levels than the total SPL (predicted: 57.1 dB). This is possible due to phase differences in the complex-valued terms. In the total prediction, partial responses with opposing phases cancel each other. A difference of more than 10 dB to the dominant path (c_{2z}) suggests that an incomplete interface description can be used without rigorously impairing accuracy; 12 interface DoFs have been included (i.e. 6 DoFs per

mount), yet only 8 are physically present. As such, the 4 least dominant paths may be discarded from the assembly FRF matrix $\mathbf{Y}_{C_2,bc} \in \mathbb{C}^{24 \times 8}$ when its inversion is performed, namely; α and γ -DoFs at (c_1) and (c_2) . Fig. 7.10a compares the sound pressure responses for this incomplete representation of the rigid interface dynamics. Although the best response prediction is obtained by using all DoFs (i.e. complete interface), the effect of the incomplete interface description (—) is not evident here. A sufficient source description by 8 coupling DoFs was somewhat expected, given that the source side excitations in Sections 6.3.1 and 6.3.2 contained 8 dominant singular values.



(a) Sound pressure in vehicle cabin, $p_{C_2,da}$ (Inset covers freq. range from 1.7 - 2.4 kHz) (b) ICC for complete/incomplete coupling

Figure 7.10: On-board validation for an incomplete interface description (x , y , z and β) and ICC for the corresponding full 12 DoF (—) and simplified 8 DoF (—) interface coupling.

The corresponding ICC results in Fig. 7.10b indicate that the neglect of any DoF worsens the interface description, however, it appears that the rotational α and γ -DoFs mainly affect the on-board validation between 1.7 - 2.4 kHz (compare inset in Fig. 7.10a). Still, a reasonable prediction can be obtained from the simplified interface description. Although simplifications are feasible, the following studies consider the same 12-DoFs (complete) interface description used throughout the in-situ TPA.

7.4 System Identification with the Controlled Exciter

The in-situ TPA approach presented so far has required roving excitation at the coupling interface, with forces applied one at a time to determine the FRFs (single-input multiple-outputs). Instead, the calibrated REPS system may be used for MIMO identification, assuming the source excitation can be reproduced. This section discusses the system identification with the calibrated REPS system, that is, how to obtain $\mathbf{Y}_{C_2,dc}$ and $\mathbf{H}_{C_2,dc}$ from response measurements due to a controlled excitation.

The controlled vibration source allows, in theory, for simultaneous characterisation of translational and rotational FRFs with the use of minimal additional hardware and experimental effort. Indeed, response measurements are only required at the target DoFs (d), whilst the calibration defines the interface excitation DoFs for the output/input FRF relations. For an overview of the general concept, results are shown for two active states of the multi-DoF exciter; externally applied roving excitations and the natural operational excitation controlled by the motor are reproduced in (C_2). Consequently, interface excitations usually required to measure $\mathbf{Y}_{C_2,dc}$ and $\mathbf{H}_{C_2,dc}$ are avoided entirely. The system identification procedures (**1.-3.**) with the calibrated REPS system as a blocked force vibration exciter, including the validation process (*), may be outlined as follows:

1. The vehicle is instrumented with accelerometers and/or microphones at the target DoFs (d), and the calibrated REPS system is installed.
2. The REPS system applies known (reproduced) blocked loads at the interface using the external roving or operational excitation outlined in Chapter 6. The matrices $\mathbf{Y}_{C_2,da}$ or $\dot{\mathbf{V}}_{C_2,da}$ are measured at the target DoFs (d) on the receiver.
3. The calibration and vehicle (**2.**) measurements are combined in Eqs. (4.32) or (4.33), respectively, to predict the target FRFs $[\mathbf{Y}_{C_2,dc} | \mathbf{H}_{C_2,dc}]^T \in \mathbb{C}^{9 \times 12}$.

* Validation FRFs are obtained from shaker measurements on the adapters or reciprocally with a volume-velocity source.

The remainder of this chapter will be organised as follows. In Sections 7.4.1 and 7.4.2, the predicted structural and vibro-acoustic FRFs will be validated. For vibro-acoustic validations, direct and reciprocal reference measurements (*) are considered

to highlight experimental errors related to inaccurate reciprocal conditions. Later, different practical applications will be demonstrated as part of three experimental multi-contact, multi-DoF examples. The presented FRFs will be used for the proposed fastTPA (Sec. 7.5) and fastVAP (Sec. 7.6), before Sec. 7.7 repeats the system identification and highlights its benefits in a different vehicle setup.

7.4.1 Roving Shaker Excitation

In this section, system identification of $\mathbf{Y}_{C_2,dc}$ and $\mathbf{H}_{C_2,dc}$ is presented for external excitations applied to the steering gear housing. All measurements are performed with an electro-dynamic shaker whilst the source is turned off. Following a similar procedure as in Sec. 6.3.1, responses are measured at the target DoFs (d) due to reproduced roving shaker excitations at 36 source-side DoFs. The REPS system, like other vehicle components, has a highly optimised structure full of curved surfaces that are far from ideal for shaker excitations. Access to these surfaces is even worse when installed in the vehicle, as shown in the close-up inset in Fig. 7.5. The shaker is attached to the red aluminium pads on the housing to repeat the defined excitation sequence. The responses are normalised to the applied shaker force to avoid changes in the force amplitude between calibration and system identification measurements. The roving excitations at (a_1, \dots, a_{36}) are arranged in columns of the control matrix $[\mathbf{Y}_{C_2,da} | \mathbf{H}_{C_2,da}]$, in the same order defined by the calibration measurement. For the assembly considered, transfer mobilities are obtained in terms of FRFs matrices (using Eq. (4.33)) given by,

$$\begin{bmatrix} \mathbf{Y}_{C_2,dc} \\ \mathbf{H}_{C_2,dc} \end{bmatrix} = \begin{bmatrix} \mathbf{Y}_{C_2,da} \\ \mathbf{H}_{C_2,da} \end{bmatrix} \mathbf{Y}_{C_1,ba}^+ \mathbf{Y}_{C_1,bc}. \quad (7.5)$$

The three-fold over-determination of the inverse problem by mutually independent excitations ($n_a > n_c = 12$) provides a robust prediction regarding the controllability of the transfer problem (see Sec. 4.3.3). In a simple TSVD regularisation, the 12 largest singular values of $\mathbf{Y}_{C_1,ba} \in \mathbb{C}^{24 \times 36}$ are retained, since the bottleneck effect limits the effective rank and lower order singular values are likely composed of measurement error and noise. The predicted structural FRFs between DoFs at (c_1) and (d_1) are shown in Fig. 7.11; y and z -translations at the interface, alongside their rotations β and γ . The results are remarkably similar, whilst the best and worst agreement between the predicted FRFs (—) and the reference measurements (—) is shown in Figures 7.11a and 7.11d, respectively. As expected, the roving shaker

measurements on the source's housing are highly reproducible. Using normalised excitation reduces the level of uncertainty, or error, present in the predicted FRFs. Variation in the applied force amplitude is mathematically avoided, whilst some errors may occur due to slight differences in the correct excitation position. Under the present assumption of an exactly reproduced excitation, errors in Fig. 7.11d likely arise due to the bottleneck effect at the interface. The SVD analysis of $\mathbf{Y}_{C_1,ba}$ has shown the assembly contains 8 significant singular values, therefore the controlled REPS system effectively excites 8 DoFs at the interface. The system identification is unable to provide a robust prediction for the less contributing paths (in this case $(c_{1\gamma})$ in Fig. 7.11d).

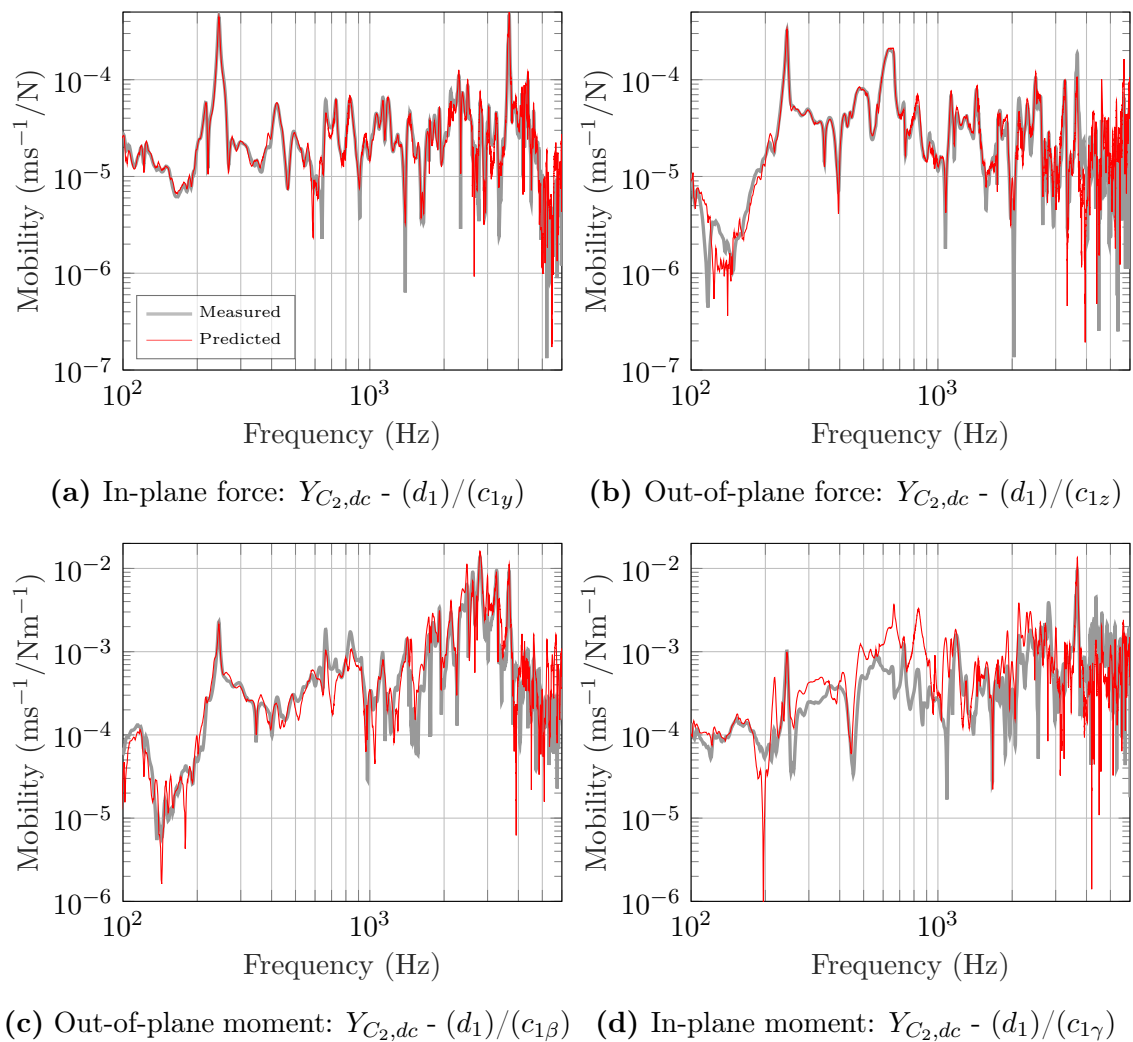


Figure 7.11: Validation of the predicted transfer FRFs $\mathbf{Y}_{C_2,dc}$ between the coupling interface (c_1) and the vibration response on the subframe (d_1). Narrowband representation for force excitation (top) and moment excitation (bottom): shaker measurement (—); and prediction using a roving shaker approach (—).

With regards to vibro-acoustic properties, characterisation of $\mathbf{H}_{C_2,dc}$ is often challenging due to poor SNR in the vehicle cabin. The long transfer paths consider multiple resiliently coupled receiver components, therefore, the controlled exciter needs to exert large enough loads for a response measurement at (d_2) free from noise. In this example, the controlled exciter allows for a robust prediction of $\mathbf{H}_{C_2,dc}$, as shown in Fig. 7.12. Results are compared against direct (shaker) and reciprocal (volume-velocity source) reference FRFs to indicate difficulties involved in the experimental measurement of vibro-acoustic FRFs. Clearly, the predicted FRF (—) for the y -DoF shows a better agreement to the direct (—) and reciprocal (—) measured references than the γ -DoF. This was expected based on the previous contribution analysis (compare Fig. 7.9); the γ -rotation is less significant for the source characterisation. Although most source-side excitations are positioned in the x and z -direction, the stiff source-subframe installation makes it difficult to excite the rotational DoF.

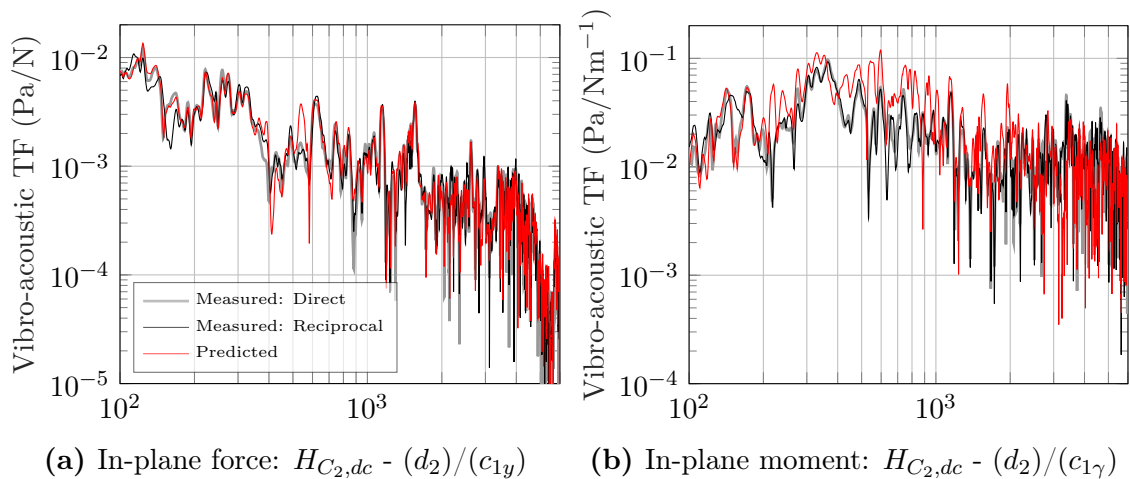


Figure 7.12: Validation of the predicted vibro-acoustic FRFs compared to shaker and volume-velocity source measurements of $\mathbf{H}_{C_2,dc}$ and $\mathbf{H}_{C_2,cd}^T$, respectively. Narrowband representation: direct measurement (—); reciprocal characterisation (—); and prediction using a roving shaker approach (—).

So far, the structural and vibro-acoustic transfer FRFs have been predicted between the interface (c_1, c_2) and the chosen target DoFs (d). Driving-point FRFs at the interface with collocated excitation and response positions have not been considered. However, the notation of the target DoF in Eqs. (7.5) and (7.6) is somewhat arbitrary. The MIMO system identification applies to any DoFs (i.e. (d), (b) or (c)) located at the defined interface or downstream on the receiver. If one chooses the DoF locations of (d) and (c_1) or (c_2) to be collocated, such that (d) = (c), it can be seen that Eq. (7.5) simplifies to a driving-point formulation. The interface driving-point

FRFs at (c_1) are shown in Fig. 7.13 for the x -DoF and its corresponding α -rotation, with a minimum phase between $\angle \mathbf{Y}_{C_2,cc} \in [-90^\circ, 90^\circ]$. Similar to the non-located case in Fig. 7.11, the predicted driving-point FRFs (—) are in good agreement with the reference measurements (—). As such, the controlled exciter concept provides an alternative to the single interface round-trip identity.

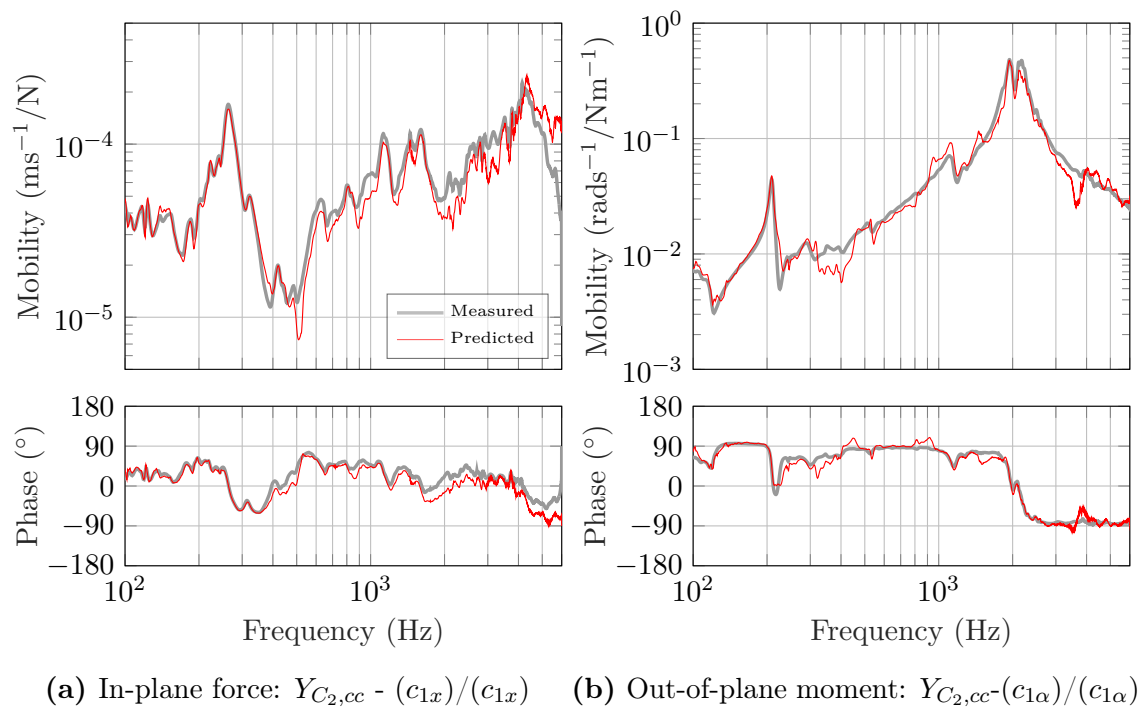


Figure 7.13: Validation of the predicted driving-point FRFs $\mathbf{Y}_{C_2,cc}$ at the coupling interface (c_1) . Narrowband representation of amplitude (top) and phase spectra (bottom): reference measurement (—); and prediction using a roving shaker approach (—).

Together, the driving-point and transfer FRFs characterisation may also be integrated into the FRF based dynamic sub-structuring framework, e.g. to determine the vehicle properties by sub-structure decoupling. However, characterisation of sub-component FRFs (i.e. $\mathbf{Y}_{A,cc}$ and $\mathbf{Y}_{B_2,cc}$) was considered beyond the scope of this work.

7.4.2 Operational Excitation Using the Electric Motor

As outlined in Sec. 6.3.2, the known operational excitation (i.e. torque impulse, white noise excitation, and ramp up/down manoeuvres) controlled by the electric stepper motor is reproduced in the vehicle assembly (C_2). The resulting operational response vectors are measured at the target DoFs (d) and arranged as columns in

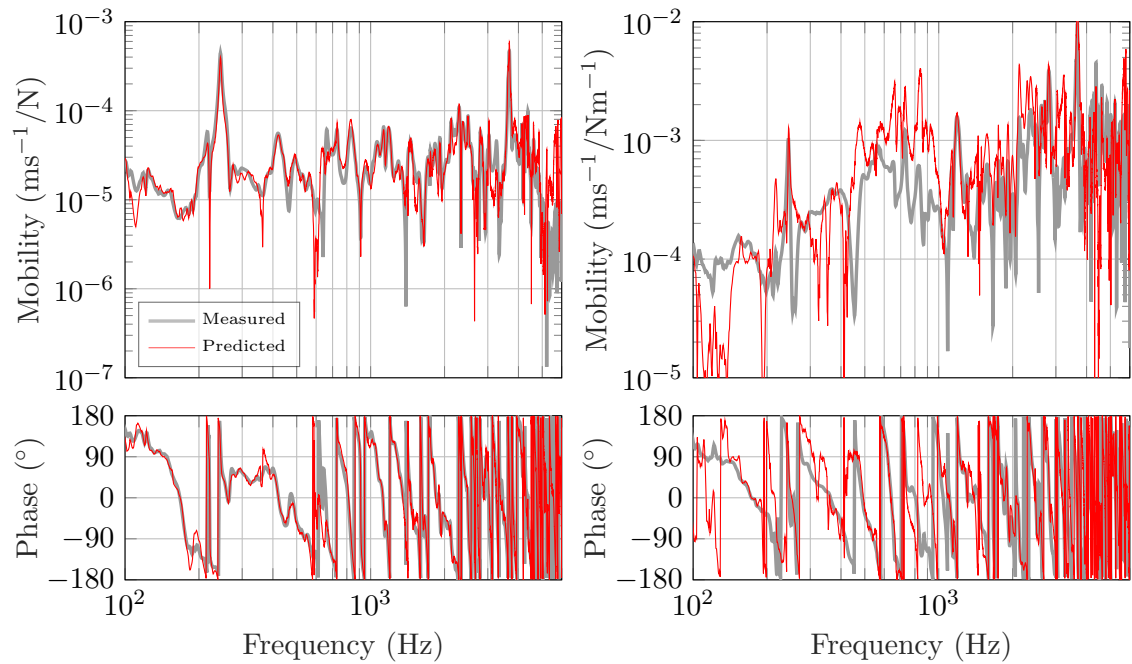
the velocity matrix $\dot{\mathbf{V}}_{C_2,da}$, similar to the construction of $\dot{\mathbf{V}}_{C_1,ba}$. For the MIMO system considered here, the transfer FRFs are given by,

$$\mathbf{Y}_{C_2,dc} = \dot{\mathbf{V}}_{C_2,da} \underbrace{\dot{\mathbf{V}}_{C_1,ba}^+ \mathbf{Y}_{C_1,bc}}_{\bar{\mathbf{F}}_{A,c}^+} . \quad (7.6)$$

In Eq. (7.6), a TSVD regularisation is applied to reduce numerical inversion errors due to rank deficiency (effective rank of $\dot{\mathbf{V}}_{C_1,ba}$: $n_r = 8$) [154]. Only the 12 largest singular values are retained in the velocity matrix $\dot{\mathbf{V}}_{C_1,da}$ when its inversion is performed. Fig. 7.14 shows the predicted transfer FRFs (—) using the electric motor as a controlled blocked force vibration source, compared against conventional FRF measurements (—). The selected transfer functions ($\mathbf{Y}_{C_2,dc} \in \mathbb{C}^{3 \times 12}$) displayed here describe the output/input relation between the in-plane force (see Fig. 7.14a) and in-plane moment (see Fig. 7.14b) excitation at (c_1), whereas the target response is measured on the subframe at (d_1). This target point is probably not of particular interest for TPA or VAP but provides a valuable insight into the method's performance. The two results represent the best (Fig. 7.14a) and least (Fig. 7.14b) accurate matches to indicate the level of accuracy.

Over a multi-kHz range (100 Hz-6 kHz), the reconstructed mobility in Fig. 7.14a is in excellent agreement with the exact measurement, although influenced by undesired noise and larger deviations above 4 kHz. That said, the breakdown of the locally rigid behaviour of the adapters at 4 kHz has introduced a finite-difference error in $\mathbf{Y}_{C_1,bc}$ which also appears in the predicted FRFs. Furthermore, the electric motor provides sufficient (high energy) blocked force output in the lower frequency range. However, at higher frequencies, it becomes particularly difficult to excite all transfer paths due to the relatively weak internal excitation mechanisms of the electric motor for the presented example. Therefore, larger errors are expected in Fig. 7.14 with increasing frequency. Other sources may not even show this behaviour if (hypothetical) broadband excitation can be achieved over the frequency range of interest. Minor deviations at lower frequencies may occur, for example, due to an imperfect reproduced operational excitation in the vehicle. Unlike the external excitations shown in Fig. 7.11, the operational excitation with the controlled motor relies on sufficiently reproduced conditions without a normalisation to the input force via load cells.

Regarding the aims of this thesis, Fig.7.14a demonstrates that it is possible to acquire reasonable estimates of the vehicle FRFs based on reproduced operational excitations controlled by the electric motor. It is stressed that steering induced noise does not govern the frequency range above 2.5 kHz, so errors in the related FRFs at high frequencies will not be noticeable in any subsequent prediction step made thereafter.



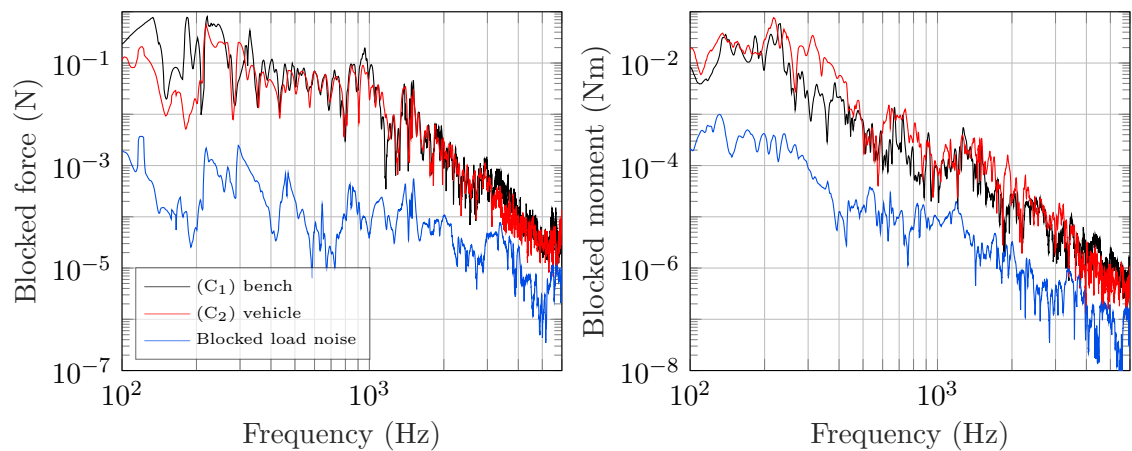
(a) In-plane force: $Y_{C_2,dc} - (d_1)/(c_{1y})$ (b) In-plane moment: $Y_{C_2,dc} - (d_1)/(c_{1\gamma})$

Figure 7.14: Validation of the transfer FRFs between the coupling interface (c_1) and the vibration response on the subframe (d_1). Narrowband representation of amplitude (top) and phase spectra (bottom): reference measurement (—); and prediction using a controlled motor excitation (—).

It should be noted that (c_{1y}) is identified as a dominant excitation/contribution path to the target vibration response on the subframe. Let us consider system identification for a less contributing path, e.g. ($c_{1\gamma}$). Considerably larger deviations are observed between the predicted and true FRF, most likely due to the bottleneck effect and controllability of the rotational DoF. In this example, the bottleneck effect actively restricts the number of independent motor excitations passing through the interface to $n_r = 8$, hence only eight interface modes have been excited. This poses a challenge, as the controlled source is supposed to characterise all 12 interface DoFs, through which rigid coupling can occur. Consequently, not contributing coupling DoFs, such as the γ -DoF shown in Fig.7.14b, are prone to error and sensitive to changes in the reproduced operational excitation.

We are interested in quantifying if the operational excitation calibrated in (C_1) is sufficiently reproduced in (C_2) . The operational activity of the multi-DoF exciter (source) in the different assemblies can be assessed by comparing their blocked loads, which are invariant to the connected receiver structure. The blocked loads for the controlled excitations (e.g. torque impulses, white noise or ramp up/down excitation) may be acquired through the inverse procedure outlined in Eq. (2.10) using FRF measurements from the REPS calibration and in-situ TPA. Using $\{\bar{\mathbf{F}}_{A,c}\}_{(C_1)} = \mathbf{Y}_{C_1,bc}^+ \hat{\mathbf{V}}_{C_1,ba}$ and $\{\bar{\mathbf{F}}_{A,c}\}_{(C_2)} = \mathbf{Y}_{C_2,bc}^+ \hat{\mathbf{V}}_{C_2,ba}$ for the calibration and target assembly, respectively, it is possible to directly compare the underlying blocked force spectra employed to determine the identified FRFs. By doing so, an experimentalist can gain insight into the excited frequency range related to the internal source mechanisms as well as the transferability of these blocked forces. Note that this blocked force comparison requires conventional FRF measurements of $\mathbf{Y}_{C_2,bc}$ in the target assembly (C_2) , which are not part of the fastTPA workflow.

Shown in Fig. 7.15 is a subset of $\bar{\mathbf{F}}_{A,c}$, where the blocked loads (white noise excitation) of the calibration setup (---) are compared to the reproduced excitation (---) in the vehicle assembly. The y -DoF blocked forces (see Fig. 7.15a) are highly reproducible and appear in good agreement with one another across the two assemblies, unlike the γ -moment excitation.



(a) In-plane blocked force: $\bar{f}_{A,c} - (c_{1y})$ (b) In-plane blocked moment: $\bar{f}_{A,c} - (c_{1\gamma})$

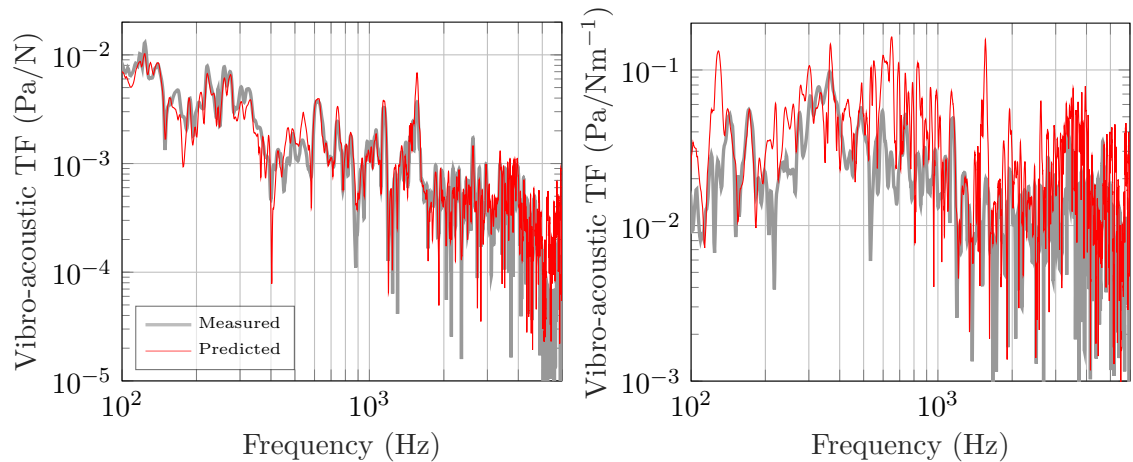
Figure 7.15: Blocked load excitation of the operated REPS system (white noise) in the calibration setup (C_1) (---) and reproduced in the vehicle (C_2) (---). The blocked load noise (---) allows evaluating the effect of noise in the reproduced excitations.

In Fig. 7.15b, the blocked moment obtained in the calibration setup deviates considerably from the reproduced excitation in the vehicle, most notably between 600 – 900 Hz. In the context of system identification, the blocked loads ($\bar{\mathbf{F}}_{A,c}$) from (C_1) are transferred into the target assembly (C_2) and considered the input to the measured velocity response ($\hat{\mathbf{V}}_{C_2,dc}$). These deviations to the applied moment lead to a poor prediction in Fig. 7.14b, repeatedly over and under predicting the measured FRF. The γ -moment also appears close to the blocked load noise (---), which indicates an insufficient operational excitation of this rotational coupling DoF whilst introducing additional errors.

So far, the notation has been based on the mobility concept, whilst modifications to include vibro-acoustic FRFs are straightforward. It should be noted that the proposed system identification in Eq. (7.6) can be amended to include sound pressure signals in the response matrix. Vibro-acoustic FRFs are given by,

$$\mathbf{H}_{C_2,dc} = \hat{\mathbf{P}}_{C_2,da} \hat{\mathbf{V}}_{C_1,ba}^+ \mathbf{Y}_{C_1,bc} \quad (7.7)$$

where $\hat{\mathbf{P}}_{C_2,da}$ contains operational pressure responses. Shown in Fig. 7.16 are the predicted vibro-acoustic transfer FRFs ($\mathbf{H}_{C_2,dc} \in \mathbb{C}^{2 \times 12}$) between the interface (c_1) and the target sound pressure probe (d_2) in the driver's cabin. Also shown are the directly measured FRFs (---), which are obtained from shaker measurements on the adapters. Like the structural case, the predicted vibro-acoustic properties (---) in Fig. 7.16a appear in good agreement with those measured directly. In addition to high-frequency errors encountered previously, some disagreement can be observed in the mid-frequency range. This additional error is likely due to the more complex transfer path involved, which accounts for acoustic radiation. It should be noted that (c_{1y}) is identified in Fig. 7.9a as a dominant excitation/contribution path to the target sound pressure response. Furthermore, it can be seen that the prediction in Fig. 7.16b for a less contributing path tends to over-estimate the measured FRF, most notably between 500 Hz - 1 kHz. An error similar to that can be observed in the structural FRF (compare Fig. 7.14b) and is caused, in part, due to a lower blocked moment in the calibration stage (compare Fig. 7.15b). However, regardless of this error, the level of agreement shown in both Figs. 7.14 and 7.16 suggests that the MIMO system identification with the controlled REPS-system has been successful.



(a) In-plane force: $H_{C_{2,dc}} - (d_2)/(c_{1y})$ (b) In-plane moment: $H_{C_{2,dc}} - (d_2)/(c_{1\gamma})$

Figure 7.16: Validation of the vibro-acoustic transfer FRFs between the coupling interface (c_1) and the sound pressure probe (d_2). Narrowband representation: reference (shaker) measurement (—); and prediction using a controlled motor excitation (—).

Often when dealing with vibro-acoustic measurements, the excitation energy provided by shakers is insufficient to achieve an acceptable SNR in the vehicle cabin. In this scenario, the FRFs may be measured reciprocally, for example, by using a calibrated volume velocity source. The reciprocal measurement of $\mathbf{H}_{C_{2,cd}}$ uses a single shared excitation at (d_2); experimental uncertainties are introduced due to inaccurate reciprocal conditions [2]. That is not to say that the directly measured transfer functions are free from errors. In Fig. 7.17, the spread (\blacksquare) between the direct and reciprocal case is considered to validate the predicted vibro-acoustic FRF (—) for (c_{1y}) (compare Fig. 7.16a). The spread illustrates the variation one would expect from conventional vehicle FRF measurements. The reciprocal variance in Fig. 7.17 is relatively narrow. This is to be expected, given that the volume-velocity source has been positioned with utmost care⁴. Note that the reciprocal variation increases towards the operating limits of the volume-velocity source and shaker, i.e. at frequencies below 200 Hz and above 5 kHz. After all, the validation in Fig. 7.17 indicates that errors in the vehicle FRF obtained with the controlled REPS system (—) are similar to the expected experimental variation. Between the 3 measurements, the proposed system identification with the controlled REPS system is arguably the most practical given its accurate results and minimal experimental effort.

⁴ Proper positioning of the microphone (direct measurement) and volume-velocity source (reciprocal measurement) is essential for the reciprocity of vibro-acoustic transfer FRFs. The nozzle's pressure centre and the microphone (see inset in Fig. 7.2) need to coincide nicely. Inaccurate reciprocal conditions tend to cause significant errors in the FRFs, considering the short acoustic wavelength: approximately 57 mm at 6 kHz. Also, temperature changes may result in node shifts in the complex sound field [20].

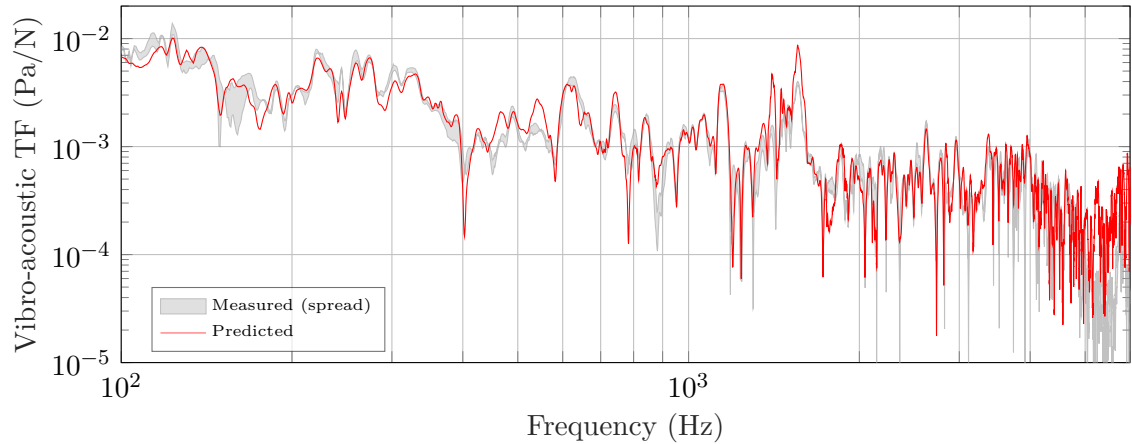


Figure 7.17: Spread (■) between direct (shaker) and reciprocal (volume-velocity source) vibro-acoustic measurements compared to the predicted (—) FRF obtained with the controlled motor approach between the motor-side interface DoF (c_{1y}) to the target microphone (d_2) (see Fig. 7.16a).

Regarding the aims of this thesis, the novel multi-DoF exciter approach bridges existing gaps in direct and reciprocal FRF measurement techniques. For example, MIMO system identification is performed without requiring access to the source-receiver interface while using only standard measurement equipment (e.g. microphones and accelerometers for response measurements). All transfer paths are measured simultaneously, drastically reducing measurement time and preventing other errors related to time-variant problems (e.g. FRF measurements in deep-temperature applications). In the following, the presented FRFs are used for fastTPA in the vehicle.

7.5 Case Study I: FastTPA for Vehicle Troubleshooting

This section focuses on the controlled exciter concept for development, refinement and troubleshooting of existing vehicle assemblies whose vibro-acoustic response is of interest. Using the controlled blocked load excitation in the context of TPA is denoted as ‘fastTPA’ due to the significant time advantage. Like the benchmark study, blocked loads may be determined using in-situ measurements, thus allowing diagnostic tests to be carried out without dismantling the assembly. This study considers the predicted structural FRFs in Sec. 7.4 to determine the operational blocked loads for any arbitrary steering manoeuvre in the vehicle, and therefore in its intended installation. After that, the predicted vibro-acoustic transmission paths may be used to determine the contribution of each blocked load to the total response

and benchmark the fastTPA approach in its capability to identify dominant partial paths.

From a methodological perspective, the independent source description (e.g. ISO 20270:2019) allows, in theory, for a fully bench-based NVH development⁵ as an alternative to in-vehicle measurements. Sometimes, replicating steering noises on a test bench may prove challenging, particularly without knowing the exact steering speed or operational load at which it occurred. Instead, the blocked loads determined in the vehicle via the fastTPA offer a complete source/assembly characterisation whilst under a realistic loading. The general formulation of the fastTPA in Eq. (4.40) is defined for a set of target DoFs (d), where responses are observed in the vehicle assembly (C_2) for the inverse force characterisation. These target DoFs may be located at the interface, so that (d) = (c), or further downstream at some remote DoFs, i.e. (d) = (b). For a consistent notation to that of the benchmark study, the general subscript (d) in Eq. (4.40) is dropped and replaced by the actual measurement location (i.e. (c), (b) or (d)) shown in Fig. 7.1. Therefore, the operational blocked force of the steering system may be determined via the two different DoFs (b) and (c), namely the ‘remote’ and the ‘interface’ blocked force relation (compare Sec. 2.2.2). For clarity, structural FRFs, $\mathbf{Y}_{C_2,bc}$ and $\mathbf{Y}_{C_2,cc}$, are considered for the inverse blocked load characterisation, whereas vibro-acoustic FRFs, $\mathbf{H}_{C_2,dc}$, are used for the forward prediction. The following sections aim to outline the remote (Sec. 7.5.1) and interface relation (Sec. 7.5.2), describe their experimental implementation, alongside an extension to account for flexible sub-structure coupling (Sec. 7.5.3).

7.5.1 FastTPA – Remote Blocked Force Relation

When dealing with real structures, access to the defined contact interface is often limited so that accelerometers to observe the interface dynamics are placed further downstream on the receiver structure. If remote measurement positions (b) shown in Fig. 7.1 are considered in the fastTPA expression in Eq. (4.40), independent source characterisation may be obtained using the ‘remote blocked force relation’. In this case, 24 remote DoFs (b) on the subframe provide a 2-fold over-determination. The instrumentation in the vehicle is, in fact, the same as for the in-situ TPA benchmark study. In the context of structural source characterisation using remote sensors at

⁵ The fastVAP concept to employ blocked loads from one installation (e.g. bench) to predict structure-borne responses in a different source-receiver installation (e.g. vehicle) is discussed in the following case study (see Sec. 7.6).

(b), the fastTPA blocked force relation in Eq. (4.40) may be rewritten as,

$$\bar{\mathbf{f}}_{A,c} = \mathbf{Y}_{C_2,bc}^+ \mathbf{v}_{C_2,ba} \quad \text{for } n_c = 12 \text{ interface DoFs} \quad (7.8)$$

$$\text{with } \begin{cases} \mathbf{Y}_{C_2,bc}^+ = \mathbf{Y}_{C_1,bc}^+ \hat{\mathbf{V}}_{C_1,ba} \hat{\mathbf{V}}_{C_2,ba}^+ & \text{for motor excitation} \\ \mathbf{Y}_{C_2,bc}^+ = \mathbf{Y}_{C_1,bc}^+ \mathbf{Y}_{C_1,ba} \mathbf{Y}_{C_2,ba}^+ & \text{for roving excitation} \end{cases}$$

The measurements in Eq. (7.8) are essentially the same as presented in Sec. 7.4 but include an operational response measurement $\mathbf{v}_{C_2,ba}$ of a realistic steering manoeuvre. For continuity, the fastTPA considers the same operational velocity vector $\mathbf{v}_{C_2,ba}$ used in the benchmark study (i.e. the operational test is not repeated since the remote sensors (b) of the in-situ TPA have not been repositioned), however, any manual steering input may be recorded at (b) to determine the corresponding blocked loads $\bar{\mathbf{f}}_{A,c}$. The matrices $\mathbf{Y}_{C_1,bc}$, $\hat{\mathbf{V}}_{C_1,ba}$ and $\mathbf{Y}_{C_1,ba}$ have been obtained during the source calibration, whilst $\hat{\mathbf{V}}_{C_2,ba}$ and $\mathbf{Y}_{C_2,ba}$ are the reproduced operational and roving excitations for the system identification, respectively. Assuming each mount behaves as a rigid point-like contact (i.e. characterised by 6 DoFs: 3 translations and 3 rotations), full controllability and observability require $n_a \geq n_b \geq n_c = 12$. As such, it is proposed that the 12 largest singular values are considered in $\hat{\mathbf{V}}_{C_2,ba}$ and $\mathbf{Y}_{C_2,ba}$ to perform a truncated inversion.

Shown in Fig. 7.18 are the blocked loads obtained as per Eq. (7.8) (fastTPA using a controlled motor), compared against conventional in-situ measurements as given in Sec. 7.3. The vector $\bar{\mathbf{f}}_{A,c}$ considers 12 coupling DoFs; here, only the y and z -blocked force alongside the β and γ -moment at the interface (c_1) are presented. Although not particularly useful when displayed on their own, a number of observations can be made. It can be seen that the blocked loads determined via fastTPA (—) in Eq. (7.8) are in reasonable agreement with those acquired in the in-situ TPA benchmark study (—). For example, the inset in Fig. 7.18b shows similar z -blocked forces for the 150. and 200. motor harmonics, characteristic for the slotted motor design with 50 ‘teeth’ on the rotor and stator. This in-itself shows that the fastTPA approach is capable of providing suitable blocked loads and, furthermore, suggests that structural FRFs identification with the controlled motor was sufficient for the inverse procedure. However, some large deviations can be observed in Fig. 7.18d, where the fastTPA γ -blocked moment under-estimates the benchmark result. It should be noted that the interface excitation of the γ -DoF is significantly lower than the β -moment in Fig. 7.18c, indicating that ($c_{1\gamma}$) is less excited by the active source and not necessarily

required for a representative source description. At this point, however, we are unable to state which approach in Fig. 7.18 provides the most representative blocked loads (without some form of validation).

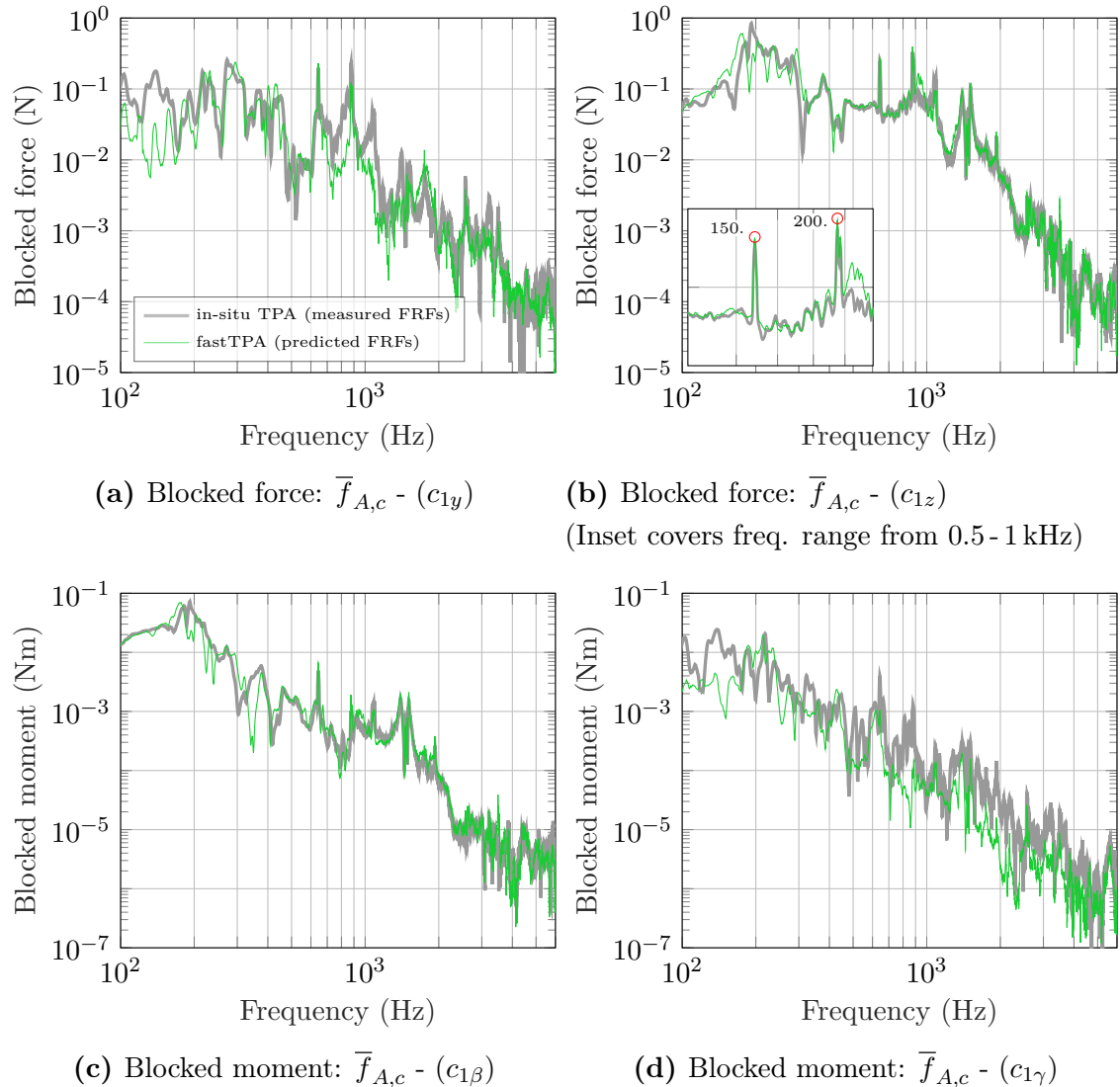


Figure 7.18: Blocked loads at the interface (c_1) for the operated REPS system. Narrowband representation of forces (top) and moments (bottom): results of the benchmark in-situ TPA study (Sec. 7.3) (—); fastTPA using a controlled motor excitation (—).

That said, Eq. (4.44) outlines the fastTPA forward prediction to determine the partial contribution of each blocked load (c_i) on the total response, e.g. the target sound pressure in the vehicle cabin (d_2). Predicting the vibro-acoustic transfer matrix, $\mathbf{H}_{C_2,dc}$, requires no additional effort over and above what would be required as part of Eq. (7.8), provided that responses at (b) and (d) are measured simultaneously during the reproduced controlled excitation. The calculation of the forward FRFs is outlined Sec. 7.4. In the context of fastTPA, the individual contributions

are given by,

$$p_{C_2,dc_i} = H_{C_2,dc_i} \bar{f}_{A,c_i} \quad \text{for partial response of interface DoF } (c_i) \quad (7.9)$$

$$\text{with } \begin{cases} H_{C_2,dc_i} \in \mathbf{H}_{C_2,dc} & \text{and } \bar{f}_{A,c_i} \in \bar{\mathbf{f}}_{A,c} \\ \mathbf{H}_{C_2,dc} = \dot{\mathbf{V}}_{C_2,da} \dot{\mathbf{V}}_{C_1,ba}^+ \mathbf{Y}_{C_1,bc} & \text{for motor excitation} \\ \mathbf{H}_{C_2,dc} = \mathbf{Y}_{C_2,da} \mathbf{Y}_{C_1,ba}^+ \mathbf{Y}_{C_1,bc} & \text{for roving excitation} \end{cases}$$

where p_{C_2,dc_i} is the partial sound pressure contribution of (c_i) . For the forward FRFs (determined as per Sec. 7.4), a TSVD regularisation is performed where the 12 largest singular values are retained in the inversion of $\dot{\mathbf{V}}_{C_1,ba}^+$ and $\mathbf{Y}_{C_1,ba}^+$, respectively.

The bar graph in Fig. 7.19a illustrates the in-situ TPA contribution analysis for the vehicle assembly presented in Sec. 7.3.2. These results, considered as benchmark, are compared in Fig. 7.19b against the fastTPA forward prediction as per Eq. (7.9). Shown are the deviations to the benchmark results ($-$); the predicted sum in the top row, and the partial contributions listed below in descending order. It is important to reiterate that the reliability of fastTPA is determined by its ability to predict the partial responses and, in this respect, identify dominant contributions. That said, a near-exact agreement is achieved for the fastTPA contribution analysis using roving excitations ($-$), with deviation in the dominant partial responses of less than 3 dB. Larger deviations can be observed for the controlled motor excitation ($-$), likely due to errors in the reproduced operational excitation. Note that the disagreement tends to increase towards less contributing paths ($c_{2z} \rightarrow c_{2\gamma}$). These errors are somewhat expected, given that the bottleneck effect at the interface limits the reproduced controlled excitation to 8-DoFs, and so greater errors are observed for the less contributing paths. In other words, this experimental uncertainty causes errors in the forward FRFs and blocked loads (e.g. lower blocked moment of $(c_{1\gamma})$ observed in Fig. 7.18), which are carried forward and propagated onto the target response (d_2). Therefore, the α and γ -predictions in Fig. 7.19b deviate above and below the benchmark responses by a few dB. Although, it is worth noting that the deviations are less of a concern, as the more significant paths (i.e. $(c_{2z}), (c_{1z}), \dots, (c_{2\beta})$) will dominate any eventual auralisation. In industrial TPA applications, it is even common practice to ignore weak contributions entirely if they are 10dB (or more) below the significant partial path contributions. In the presented example, this would relate to the partial path (c_α) and (c_γ) containing the largest errors. Given its simplicity, fastTPA quickly identifies the dominant contribution paths and

provides a reasonable characterisation of the blocked loads and partial responses.

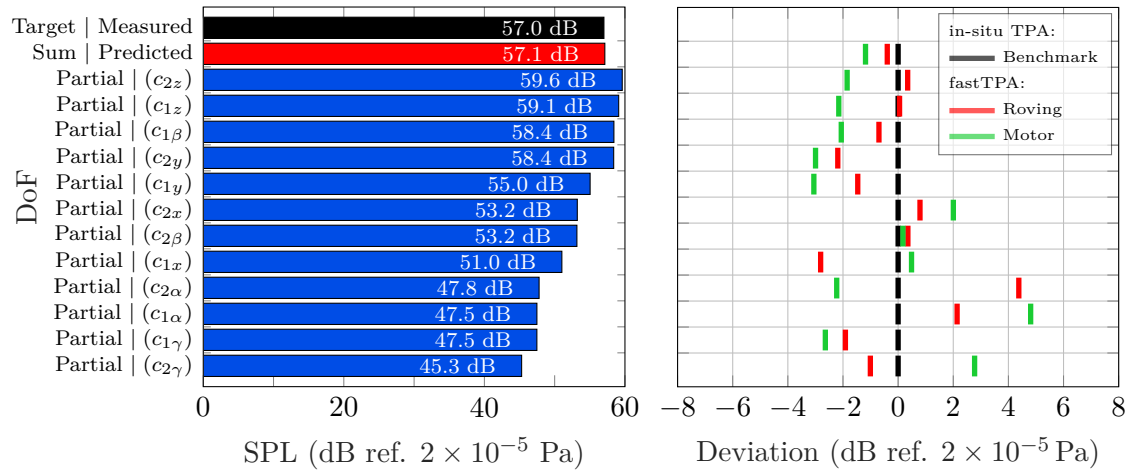


Figure 7.19: Predicted SPL and partial contributions obtained in the benchmark study (in-situ TPA), and deviations for different fastTPA variants: In-situ TPA (—); and fastTPA using a roving shaker approach (—) or operational motor excitation (—).

Note that the predicted sum (top row in Fig. 7.19b) in fastTPA does not provide an on-board validation in a classic sense. Instead, a transferability validation (see Eq. (4.47)) is shown in Fig. 7.20 to assess errors associated with the predicted structural and/or vibro-acoustic transfer FRFs. Blocked loads from assembly (C_1) are transferred into (C_2) and propagated onto the target DoFs (d_2) using the predicted FRFs, $\mathbf{H}_{C_2,dc}$, in Eq. (7.9). The same operational measurement is repeated in the vehicle assembly (C_2), allowing for a comparison to be made. Differences between the measured and predicted responses in Fig. 7.20 indicate frequency regions where the fastTPA predictions are more susceptible to errors. A reasonable agreement is obtained between the two predictions (roving shaker and motor excitation) and the directly measured response. Particularly at low frequencies below 600 Hz, the result obtained with the controlled motor (—) tends to under-predict the measured response (—), whilst the roving shaker approach (—) shows an excellent agreement. Interestingly, a similar trend can be seen in Fig. 7.19b, where the roving shaker approach generally provides better agreement.

Although not an in-depth analysis, the above demonstrates the potential of the transferability validation to identify errors in the FRFs and improve their quality for fastTPA. Note that this validation approach forms the basis of the fastVAP procedure discussed in Sec. 7.6.

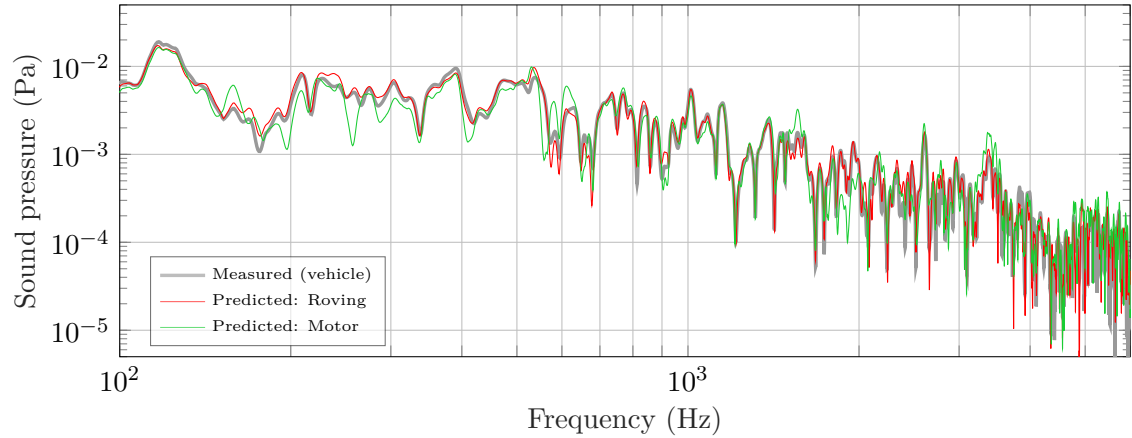


Figure 7.20: Transferability validation to indicate errors in fastTPA. Narrowband representation: measured reference (—); and predicted sound pressure response using a roving shaker approach (—) or operational motor excitation (—) for system identification.

7.5.2 FastTPA – Interface Blocked Force Relation

For the blocked load characterisation, one may only have access to (c), while measurements at (b) are impractical⁶. In such a case, Eq. (4.40) may be rewritten for a set of interface driving-point FRFs, thus providing an ‘interface fastTPA relation’ with the use of minimal additional hardware,

$$\bar{\mathbf{f}}_{A,c} = \mathbf{Y}_{C_2,cc}^+ \mathbf{v}_{C_2,ca} \quad \text{for } n_c = 12 \text{ interface DoFs} \quad (7.10)$$

$$\text{with } \begin{cases} \mathbf{Y}_{C_2,cc}^+ = \mathbf{Y}_{C_1,bc}^+ \hat{\mathbf{V}}_{C_1,ba} \hat{\mathbf{V}}_{C_2,ca}^+ & \text{for motor excitation} \\ \mathbf{Y}_{C_2,cc}^+ = \mathbf{Y}_{C_1,bc}^+ \mathbf{Y}_{C_1,ba} \mathbf{Y}_{C_2,ca}^+ & \text{for roving excitation.} \end{cases}$$

In this example, the operational blocked force vector $\bar{\mathbf{f}}_{A,c}$ is characterised using interface driving-point FRFs (not over-determined). The calibrated source is installed in the target assembly (C_2), whilst responses for the blocked force characterisation are measured at the accelerometers (c_1, c_2) embedded in the adapters. As such, vehicle instrumentation only requires additional target microphones (d_2) placed in the cabin. In Eq. (7.10), the inverse mobility matrix $\mathbf{Y}_{C_2,cc}^+$ is calculated using a TSVD regularisation, using the first 12 singular values of $\hat{\mathbf{V}}_{C_2,ca}^+$ and $\mathbf{Y}_{C_2,ca}^+$, respectively. Once the blocked loads have been obtained, Eq. (7.9) can be used to predict the partial contributions at the target DoFs (d_2).

⁶ The blocked force determination relies on a consistent phase relationship between the interface and the remote DoFs used in the inverse calculation. In practice, if the nearest accessible remote region (b) is too far away from the interface, the implementation of a robust in-situ blocked force characterisation may prove difficult [21].

Fig. 7.21 shows the same contribution analysis presented in the previous section, however, Fig. 7.21b compares the benchmark results to the total and partial responses obtained from the interface fastTPA relation. It can be seen that the partial contributions are predicted with reasonable accuracy, deviating no more than 4 dB. Again, the deviations shown for the controlled motor excitation ($-$) are slightly higher than for the highly repeatable roving excitations ($-$). It is stressed that despite all diligence during the benchmark study, the systematic under-prediction of $(c_{1\beta})$ and the contributions of (c_{1y}, c_{2y}) suggest that the benchmark reference may also contain some experimental errors. Fig. 7.21b demonstrates that the dominant contributions can be identified using the interface relation, however, over-determination in Sec. 7.5.1 can be seen to improve the partial predictions (compare Fig. 7.19b).

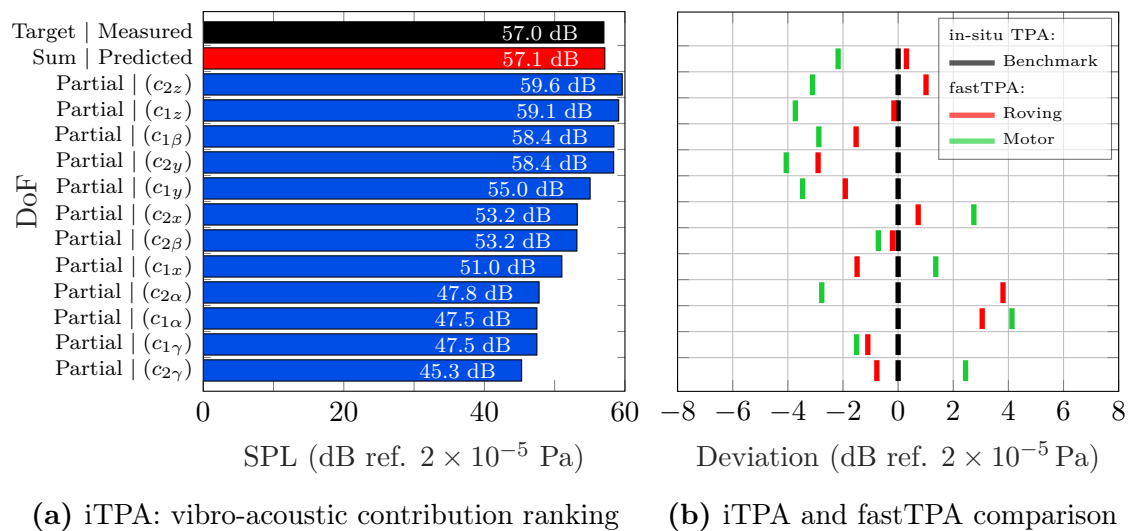
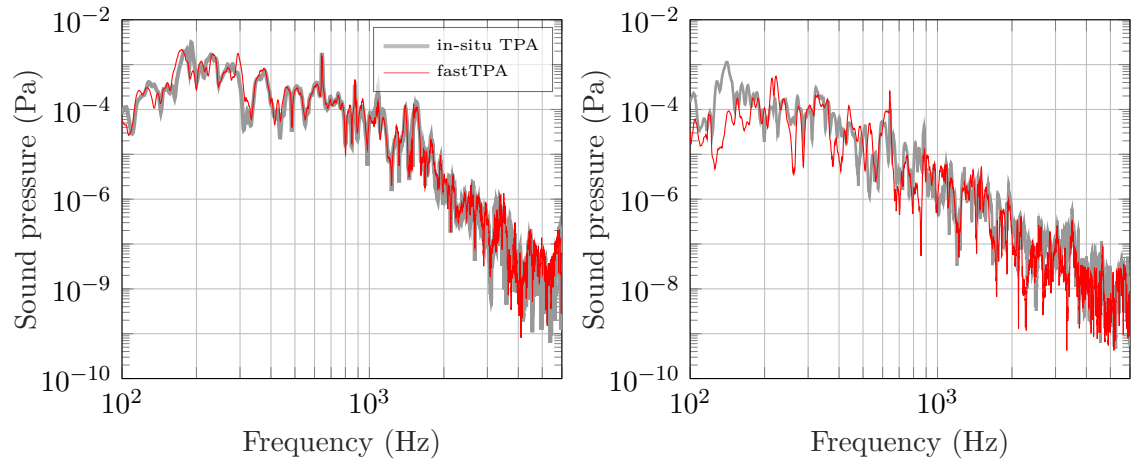


Figure 7.21: Predicted SPL and partial contributions obtained in the benchmark study (in-situ TPA), and deviations for interface fastTPA relation: In-situ TPA ($-$); and fastTPA using a roving shaker approach ($-$) or operational motor excitation ($-$).

Although fastTPA contributions ($-$) for (c_{2z}) and $(c_{2\gamma})$ show similar deviations of 1 dB and 0.7 dB, respectively, the prediction error increases toward lower contributions. For a clearer indication of this error, Fig. 7.22 shows the partial response of the fastTPA (controlled roving excitations ($-$)) compared to the in-situ TPA benchmark ($-$) results. Fig. 7.22a shows an excellent agreement for the contribution of (c_{2z}) , suggesting that the fastTPA approach correctly identifies the dominant contribution. In contrast, differences become more apparent for the less contributing path $(c_{2\gamma})$, shown in Fig. 7.22. The bottleneck effect clearly introduces errors in the blocked force characterisation and the forward FRFs, resulting in an unrealistic partial response prediction.



(a) Partial contribution: $p_{C_{3,dc}} - (d_2)/(c_{2z})$ (b) Partial contribution: $p_{C_{3,dc}} - (d_2)/(c_{2\gamma})$

Figure 7.22: Partial sound pressure contribution obtained from in-situ TPA (i.e. conventional FRF measurements (—)) and application of the interface fastTPA relation (—) using controlled roving excitations.

Note that the fastTPA remote relation in Fig. 7.19 and contact interface relations presented in Fig. 7.21 provide, with some accuracy, a similar result and indicate dominant contributions. Which sensor configuration (interface or remote fastTPA relation) is chosen in practice depends on the complexity of the target assembly and perhaps personal preference.

7.5.3 FastTPA – Extension to the Flexible Modal Regime

In previous examples, the steering system was correctly characterised in a frequency range up to 4 kHz, indicated by the ICC/consistency in Sec. 7.2.3. Pushing the frequency limit of fastTPA up to 6 kHz would allow for more realistic diagnostic tests. This is particularly useful for applications with fast-spinning electric motors, which require a multi-kHz range to analyse harmonic orders. In the presented case, the incomplete interface description (see Fig. 7.3a) becomes a limiting factor at higher frequencies unless we account for local flexibility not captured by the 6-DoFs contact points. In this section, flexible interface coupling is introduced to the fastTPA remote relation (Sec. 7.5.1) to compensate for local flexibilities in the interface area, whilst errors associated with the finite difference approximation are reduced. An important consideration is that of which interface DoFs should be accounted for (i.e. mathematically blocked), particularly without modifying the existing measurement setup tailored for spaced excitations.

In its current form, the fastTPA remote relation presented in Eqs. (7.8) and (7.9) accounts for rigid coupling. Flexible DoFs may be introduced by changing the right-sided force transformation, $\mathbf{Y}_{C_1, bc} \mathbf{B}_f^T$, outlined in Sec. 6.2. That said, the transformation is applied to the FRFs of the bench assembly (C_1), reducing the eight excitations at each adapter, indicated by red arrows in Fig. 7.23b, to 7-DoFs (6 rigid modes as before plus one additional flexible extension mode) in (c_1, c_2) . The interface description may be augmented in a post-processing step by replacing the finite difference approximation with the more versatile virtual point transformation (see Sec. 2.3.3). In Fig. 7.23b, the excitations in x -direction on opposite sides of the defined virtual point (i.e. $1_x, 5_x$ and $3_x, 7_x$; excitation 3_x is shown in Fig. 6.2b) allow accounting for flexible coupling along the x -coordinate, namely χ -extension (also: χ -strain). Mathematically, a force IDM matrix \mathbf{R}_f can be constructed to project the applied excitations on a set of rigid and flexible DoFs in the virtual point; the reader is referred to [81] for a more detailed discussion on how to obtain \mathbf{R}_f .

To evaluate completeness of the updated interface description, the excitation consistency may be used as an indicator for potential flexible loading by the excitations $(1_x, \dots, 8_z)$ applied in the proximity of the interface. As shown in Fig. 7.23a, the consistency for each 7-DoFs virtual point is high throughout the measurement range, with the added χ -DoF compensating local flexibilities above 4 kHz (see Fig. 7.4b and mode shape in Appendix A.1). Note that the ICC is the preferred method to identify completeness, however, Eq. (2.38) would require an alternative sensor configuration at (c_1, c_2) to account for the χ -extension DoF in the driving-point FRFs, $\mathbf{Y}_{C, c_i c_i}$.

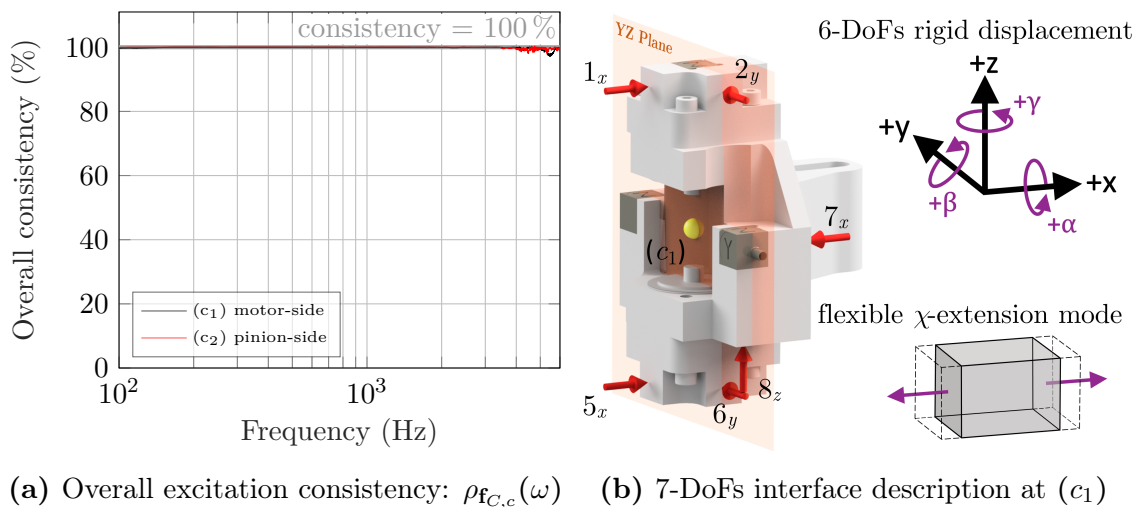


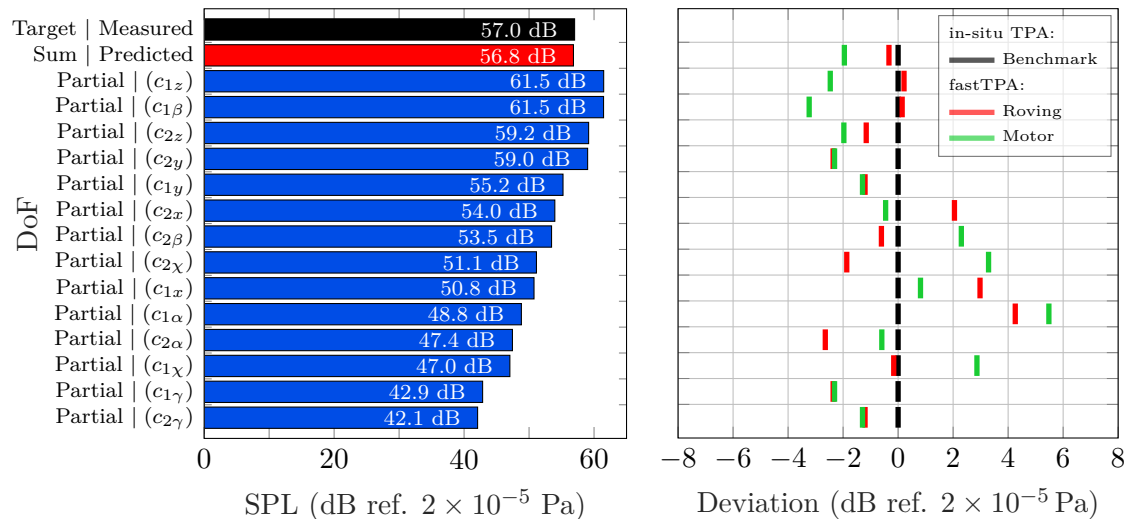
Figure 7.23: Excitation consistency for the virtual point transformation of 8 excitations (red arrows) to a 7-DoFs interface description (6 rigid DoFs + flexible χ -extension DoF) at each coupling point: (c_1) motor-side (\blackrightarrow); and (c_2) pinion-side ($\color{red}\blackrightarrow$).

To extend the fastTPA remote formulation (Sec. 7.5.1) by the χ -extension, the 6-DoFs finite difference approximation may be replaced by the virtual point transformation matrix $\mathbf{B}_f \in \mathbb{R}^{16 \times 14}$ (see Eq. (2.22)). Subsequently, the blocked load vector ($\bar{\mathbf{f}}_{A,c} \in \mathbb{C}^{1 \times 14}$) obtained from Eq. (7.8) contains two 2 additional DoFs, i.e. translational forces, moments and flexible loads at the interface (c_1, c_2) . Similarly, post-multiplication of $\mathbf{Y}_{C_1,bc}$ by \mathbf{B}_f in Eq. (7.9), yields the forward FRFs to determine the partial sound pressure response of the flexible DoFs. Note that a TSVD regularisation is used to calculate the inverse of $\hat{\mathbf{V}}_{C_2,ba}$ or $\mathbf{Y}_{C_2,ba}$ and $\hat{\mathbf{V}}_{C_1,ba}$ or $\mathbf{Y}_{C_1,ba}$ in Eqs. (7.8) and (7.9), respectively, where the first 14 singular values are retained (accounting for 14 coordinate-DoFs). The updated transformation matrix calibrates the REPS system as a 14-DoFs blocked load exciter for system identification of rigid and flexible coupling. Note that the same transformation is employed in the vehicle benchmark study to consider flexible coupling in the in-situ TPA results. It is also noted that the same bench and vehicle measurement raw data is used as in the previous examples but that different geometric transformations are applied to that data in order to extend into the flexible mode regime.

The bar graph in Fig. 7.24a shows the contribution ranking of the benchmark in-situ TPA for the updated 7-DoFs interface description. Including $(c_{1\chi}, c_{2\chi})$ alters the vibrational energy transmitted in the remaining paths; consequently, the blocked loads and their partial contributions in the 7-DoFs and 6-DoFs (compare Fig. 7.21a) studies differ from one another. Although the flexible DoFs compensate for the finite difference error and thus extend the working frequency range of the in-situ TPA, improvements of the total prediction are not expected for the tested REPS system. The operational response of the relatively slow actuated steering gear spans an effective frequency range up to 2.5 kHz, whilst the flexible extension targets frequencies above 4 kHz. As before, the total prediction error (Sum | Predicted) for the updated in-situ TPA is less than 1 dB compared to the true measured response (Target | Measured).

Apart from the updated in-situ TPA, Fig. 7.24b shows the fastTPA partial contributions. The fastTPA results are in good agreement with the altered benchmark analysis. Although the flexible extension accounts for the finite difference error, fastTPA predictions for 7-DoFs at each interface are expected to be somewhat less accurate than its 6-DoFs counterpart (compare Fig. 7.19b). Improvements due to flexible coupling are not evident here due to the low-frequency nature of the source. Instead, two additional columns are added to $\mathbf{Y}_{C_1,bc} \in \mathbb{C}^{24 \times 14}$, effectively reducing

the degree of over-determination. Second, full controllability requires sufficient excitation of 14 interface DoFs (instead of 12 DoFs) to guarantee accurate system identification of all paths in other assemblies. In this example, the controlled REPS system is effectively calibrated as an 8-DoFs exciter (demonstrated in the SVD analysis in Figures 6.5 and 6.7), whilst the less significant contributions (including $(c_{2\chi})$ and $(c_{1\chi})$) include errors.



(a) iTPA: vibro-acoustic contribution ranking (b) iTPA and fastTPA comparison

Figure 7.24: In-situ TPA (benchmark) contribution analysis (—) for the updated 7-DoFs interface connectivity and deviations for fastTPA (remote relation) using a roving shaker approach (—) or operational motor excitation (—).

The flexible extension forms the basis for more complex interface problems, e.g. larger contact surfaces, where simplified point-like contacts are no longer acceptable. In this case, the trivial interface description by 6-DoFs can be augmented to include flexible coupling. In fastTPA, these interface DoFs are defined during the bench calibration procedure (i.e. remote from the vehicle). Interestingly, including the χ -interface DoFs in the calibration stage turns the controlled REPS system into a MIMO exciter for rigid and flexible applied loads. The extended fastTPA may prove useful in practical applications where a fast-spinning motor is controlled as a blocked force exciter for high-frequency analysis.

7.6 Case Study II: FastVAP for Pro-Active Development

The fastTPA concept, based on an inverse blocked force characterisation in the vehicle, considers the transmission of vibrations to the connected passive sub-component for troubleshooting NVH problems in existing designs. Alternatively, the vehicle responses may be predicted without operating the steering system in the actual vehicle by means of virtual acoustic prototyping, outlined in Sec. 4.3.2 [92]. In this second case study, we consider the predicted vehicle FRFs in Sec. 7.4 to propagate operational blocked loads from bench measurements through the vehicle model to construct a fully compatible and therefore more robust fastVAP.

The calibration to turn the steering system into a controlled vibration exciter is typically performed on a test bench. In an additional step, operational blocked loads $\bar{\mathbf{f}}_{A,c}$ of the device can simply be obtained from response measurements $\mathbf{v}_{C_1,ba}$ in (C_1) , as indicated in Eq. (7.11) ($\mathbf{Y}_{C_1,bc}$ is measured during calibration). For example, the steering cycles are conducted on the bench, mimicking those of the vehicle. Next, the calibrated REPS system is installed in the target assembly (C_2) whilst the unknown FRFs $\mathbf{H}_{C_2,dc}$ are determined as outlined in Sec. 7.4. Eq. (7.12) is then used as a predictive tool, providing a response prediction in a virtual assembly. In other words, the vehicle FRFs in Sec. 7.4 are used to construct a fastVAP,

$$\bar{\mathbf{f}}_{A,c} = \mathbf{Y}_{C_1,bc}^+ \mathbf{v}_{C_1,ba} \quad \text{for } n_c \text{ interface \& } n_b \text{ remote DoFs} \quad (7.11)$$

$$\mathbf{p}_{C_2,da} = \mathbf{H}_{C_2,dc} \bar{\mathbf{f}}_{A,c} \quad \text{for } n_d \text{ target DoFs} \quad (7.12)$$

$$\text{with } \begin{cases} \mathbf{H}_{C_2,dc} = \dot{\mathbf{P}}_{C_2,da} \dot{\mathbf{V}}_{C_1,ba}^+ \mathbf{Y}_{C_1,bc} & \text{predicted for fastVAP} \\ \mathbf{H}_{C_2,dc} \text{ or } \mathbf{H}_{C_2,cd}^T & \text{measured for conventional VAP} \end{cases}$$

where the only difference to a conventional VAP (see Eq. (7.12)) lies in the characterisation of the assembly matrix $\mathbf{H}_{C_2,dc}$ for the forward prediction. Apart from the operational runs, which are highly product and problem-specific, all measurements to construct the fastVAP are already part of the calibration procedure outlined in Chapter 6.

Combining blocked loads with FRFs from different assemblies to construct a conventional VAP is, in a practical sense, feasible when both measurements are carefully planned beforehand. Often, the source-receiver interface is defined on the test bench,

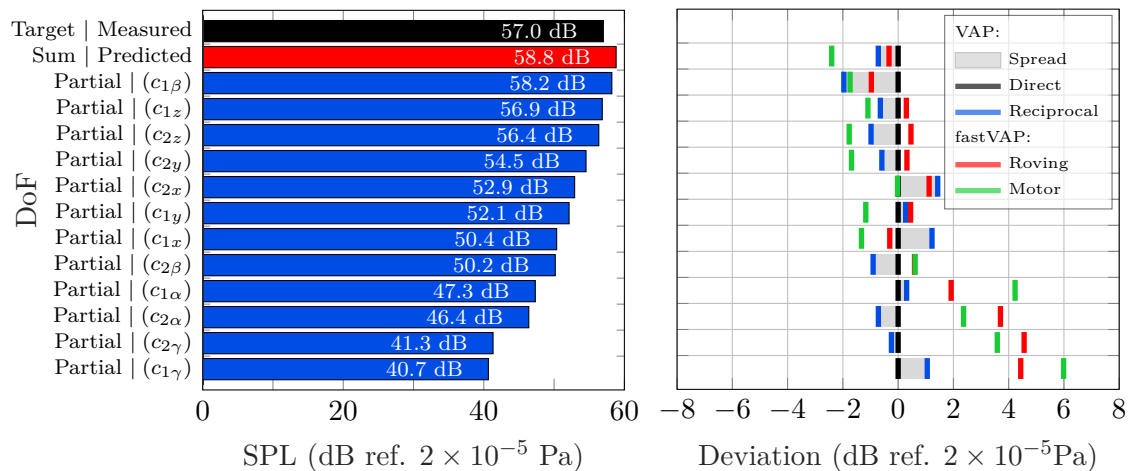
however, the same coupling DoFs may be inaccessible in the target assembly, and the required measurements of $\mathbf{H}_{C_2,dc}$ cannot be undertaken. Instead, if the forward FRFs (vehicle) are determined using a calibrated blocked force exciter, interface compatibility between assemblies is enforced through the method itself. The coupling DoFs used to characterise the operational blocked loads in (C_1) are the same defining the input DoFs of the controlled blocked force excitation in (C_2). Therefore, coordinates at the vehicle interface match the blocked load DoFs of the bench setup and yield a quicker and more robust fastVAP prediction.

This experimental case study compares the different VAP predictions, categorised as either conventional VAPs (**1.-2.**) or fastVAPs (**3.-4.**). In either case, the same operational blocked load vector $\bar{\mathbf{f}}_{A,c} \in \mathbb{C}^{12 \times 1}$ is used to predict the sound pressure response at the driver's left ear. In the forward prediction step, as given in Eq. (7.12), different measured and predicted vibro-acoustic FRFs are considered:

1. *Direct* measurement, $\mathbf{H}_{C_2,dc}$: Shaker excitations applied at the interface DoFs.
 2. *Reciprocal* measurement, $\mathbf{H}_{C_2,cd}$: All forward FRFs share a volume-velocity excitation at (d_2).
 3. *Roving shaker approach*: Predicted FRFs using external excitations (Sec. 7.4.1).
 4. *Controlled motor*: Predicted FRFs using operational excitation (Sec. 7.4.2).
- * To provide a validation reference, the steering system is operated in the vehicle to record the actual sound pressure response $\mathbf{p}_{C_2,da}$.

For benchmarking, the conventional VAP (**1.**) with directly measured forward FRFs is perhaps the most common approach, and used for comparison against (**2.-4.**). The bar graph in Fig. 7.25a shows the predicted partial sound pressure levels in the vehicle cabin with a total prediction error of 1.8 dB. Note that the operational reference measurement (Target | Measured) and the VAP prediction (Sum | Predicted) are evaluated from two different operational runs, i.e. the steering manoeuvre to characterise $\bar{\mathbf{f}}_{A,c}$ on the bench is repeated in the vehicle (*) for validation. Hence, this over-prediction of the target SPL is due, in part, to differences in the source's operational state. The transfer of blocked loads between assemblies makes VAP predictions more susceptible to experimental error than their TPA counterpart (TPA: $\bar{\mathbf{f}}_{A,c}$ is obtained from the same assembly in which a prediction is made). Like in TPA (compare Fig. 7.9a), the same four dominant and least contributing paths can be identified in the VAP contribution ranking, however, their order has slightly changed.

Shown in Fig. 7.25b are the deviations of the VAP variants (2.-4.) compared to the benchmark (1.-) in Fig. 7.25a. Let us first focus on the differences between conventional VAPs. The result of the forward prediction changes in the case that ($\mathbf{H}_{C_2,dc} = \mathbf{H}_{C_2,cd}^T$) is measured reciprocally (2.-). With either set of forward FRFs (direct or reciprocal), deviations in the total prediction (top row) or the partial contributions (listed below) lie within 2 dB. The grey area (■) indicates the experimental uncertainty associated with forward FRFs in a conventional VAP. In a practical situation, where measurements are obtained without adapters at the source-receiver interface, less reliable predictions may be expected. In this case, the transferred blocked loads may be inconsistent with the coupling DoFs defined in the target assembly.



(a) VAP: vibro-acoustic contribution ranking. (b) VAP and fastVAP comparison.

Figure 7.25: Predicted SPL and partial contributions for a conventional VAP (1.) and deviations between different variants: Variation between conventional VAP (■) using direct (—) and reciprocal (—) forward FRFs measurements; and fastVAP using the roving shaker approach (—) or operational motor excitation (—) to predict the forward FRFs.

A similar level of agreement is obtained for the proposed fastVAP (3.-), highlighting the potential use of the calibrated source concept within acoustic prototyping. However, the partial sound pressure of the least contributing paths ($c_{2\alpha}$, $c_{2\gamma}$, and $c_{1\gamma}$) can be seen to over-predict the reference responses by approximately 4 dB. This is expected, given that the corresponding rotational vehicle FRFs are also over-predicted (compare Fig. 7.12b). Nevertheless, these over-predicted partial contributions are not causing an apparent error in the overall sum of 58.4 dB (i.e. the sum for the roving shaker fastVAP prediction lies within the spread of the conventional VAPs) due to their negligible contribution, which is 7 dB lower than the dominant paths (e.g. $c_{1\beta} = 57.2$ dB; $c_{2\alpha} = 50.1$ dB). If vehicle FRFs are predicted using the controlled

motor (4. —), deviations in Fig. 7.25b tend to increase. That said, the partial contributions of the α and γ -coordinate DoFs are over-predicted, whilst the more significant paths can be seen to under-predicted the actual sound pressure responses by approximately 2 dB. The prediction errors are directly related to the vibro-acoustic FRFs in Sec. 7.4.2 and uncertainties in the reproduced operational excitation. In spite of the errors encountered, Fig. 7.25b illustrates the application of fastVAP to a multi-contact assembly and, furthermore, show that dominant contributions can be identified to provide an engineer with the information necessary to make informed design changes.

By listening to an auralisation of the virtual sound pressure (using an inverse FFT of sequential frequency spectra to time signals), both fastVAP predictions provide a realistic representation of the REPS system virtually operated in the vehicle, with some noticeable differences at low frequencies [126]. This is shown in the time-averaged spectrum of the predicted total sound pressure in Fig. 7.26 compared with the directly measured signal (—). The mid to high frequency characteristics is predicted with reasonable accuracy, as shown in the inset in Fig. 7.26, the sound pressure response below 700 Hz less so. This is likely due to errors in the forward FRFs, particularly the dominant contribution paths. The validation also requires a second, repeated operational measurement in the target assembly, introducing some errors (imperfect repeated operational measurement, static pre-load, etc.) in the measured reference signal. It is worth noting that the deviations at frequencies above 3 kHz are less of a concern, as the low frequency response dominates the auralisation. Fig. 7.26 may also be considered a transferability validation outlined in Eq. (4.47) to assess the quality of the predicted vehicle FRFs.

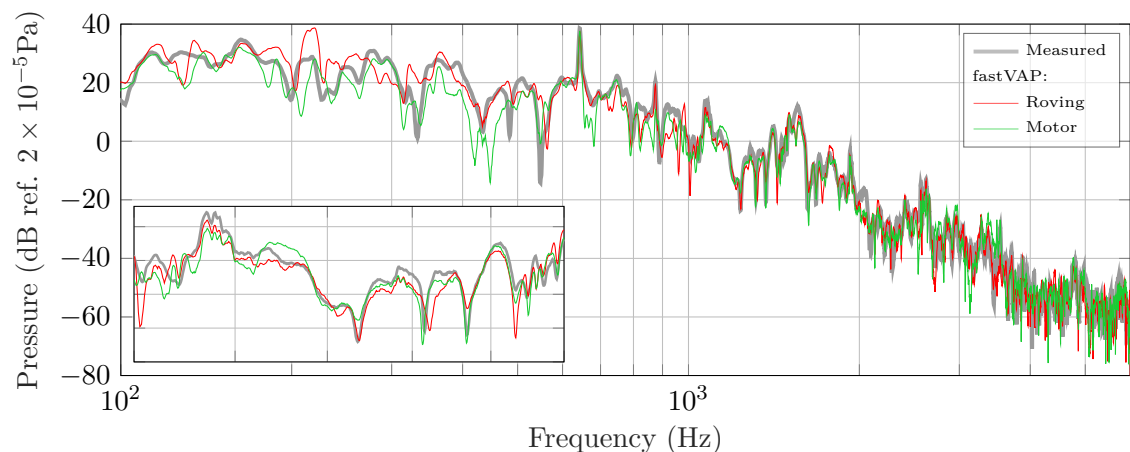


Figure 7.26: Transferability validation of the predicted sound pressure response $\mathbf{v}_{C_2,da}$ in the vehicle cabin. Narrowband representation: reference measurement (—); and fastVAP predictions (3. —) and (4. —). (Inset covers freq. range from 1 - 1.5 kHz).

As demonstrated in this case study, incorporating the controlled exciter concept within the VAP approach allows for quick and robust diagnostic predictions in a virtual vehicle, including translational and rotational contribution paths. The fastVAP approach avoids practical challenges often encountered in conventional prototyping methods, e.g. inconsistent interface DoFs, restricted access, or time-consuming measurements. The same calibrated exciter (REPS system) can be connected to different receivers to determine new forward FRFs. This allows quickly updating the predicted responses for modifications of the receiver. FastVAP enables bench-based development strategies such as product optimisation through iterative testing remote from the vehicle and design evaluation through virtual acoustic prototyping. Hence, fastVAP can convert any multi-DoF, multi-contact blocked load vector measured on a bench into a (single value) virtual response $\mathbf{v}_{C_2,da}$, for example, to define production limit values or virtual acoustic release.

7.7 Case Study III: System Identification under Realistic Mounting Conditions

All previous examples considered either cross-like elements or cocoon-adapters between the source and receiver sub-components to facilitate easy access to the coupling interfaces. These structures were permanently installed and part of the receiver in both the calibration and identification stage. This is considered an ideal case, where the coupling conditions in the target assembly are similar to those during calibration. Such modifications downstream of the interface may be applied without affecting the blocked loads, however, changes in the local dynamic behaviour at the interface may affect the transfer of blocked loads between assemblies. For example, installation without these adapters may introduce a stiffening effect at the source-receiver contact. This raises the question to what extent are the previous predictions and the validation measurements influenced by the installed adapters.

For a more realistic application (industrial test case), the calibrated REPS system is installed in the vehicle (C_3) in its intended position without adapters and, therefore, under representative mounting conditions. The vehicle FRFs $\mathbf{Y}_{C_3,dc}$ are then predicted using the calibrated source by repeating the operational excitation with the controlled stepper motor (see Section 7.4.2). Without the adapters, the interfaces are inaccessible for excitation to validate the FRFs. Instead, reference FRFs may be determined reciprocally, however, minor deviations from the correct excitation

vector may have a significant effect on the measured FRFs. Hence, this example considers the target vibration response on the vehicle's windscreen inside the cabin to reduce off-positioning and misalignment to a minimum. The validation FRFs are measured reciprocally from the windscreen (d_3) with the shaker positioned on the opposite side of the windscreen, as indicated in Fig. 7.27b. The resulting responses at the coupling interfaces (c_1, c_2), on the other hand, are measured on each side by 13 response channels (see Fig. 7.27a) and projected into the centre of each mount using the virtual point transformation⁷ due to restricted access and the complex geometry.

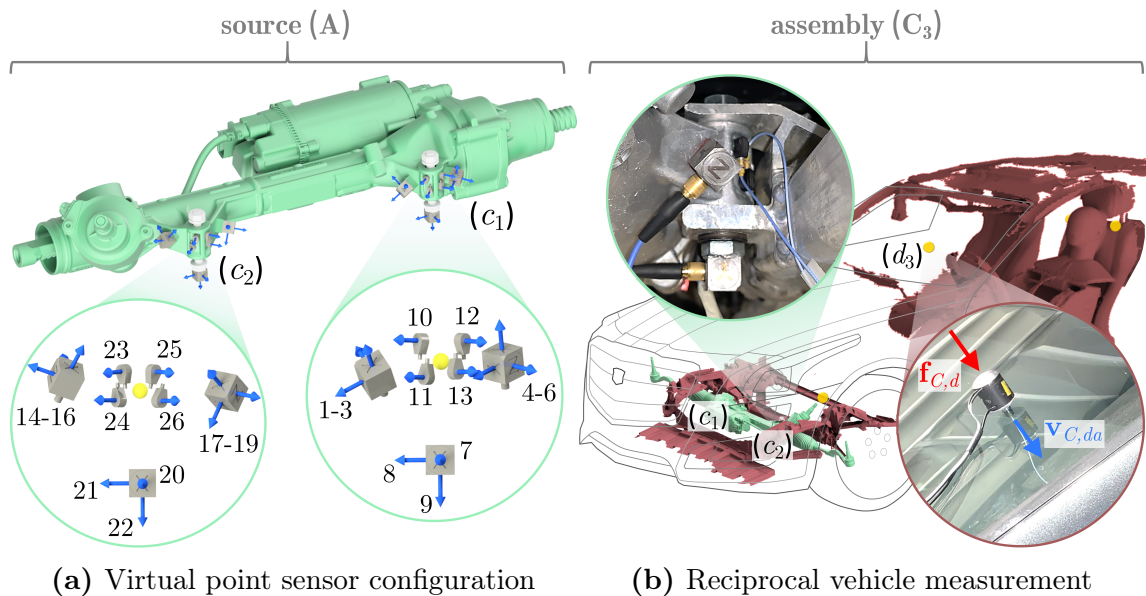


Figure 7.27: Interface sensor array indicating the response index (see Fig. 7.28a) at each virtual point (yellow) and remote shaker excitation on the windscreen (d_3) for reciprocal measurement of the virtual point FRFs $\mathbf{Y}_{C_3,cd}$.

7.7.1 Virtual Point Transformation at the REPS Mounts

Once installed in the vehicle, access to the coupling interfaces between the REPS mounts and the subframe is particularly challenging (see close-up inset in Fig. 7.27b). This section considers the implementation of the virtual point transformation to include translational and rotational DoFs at the partially accessible interfaces. It is important to reiterate that this transformation is not part of the proposed system identification, however, it is used as a means to an end that allows validation FRFs to be measured in-situ.

⁷ Application of the finite difference approximation seems impractical, as it requires spaced sensor pairs around the centre point. This is clearly not achievable or would require temporary fixtures at the curved surfaces for the sensor placement, which are likely to introduce locally flexible behaviour.

For the transformation, 3 tri-axial and 4 single-DoF accelerometers are grouped in the rigid area around each REPS mount, as shown in Fig. 7.27a. Each coupling interface is considered a separate virtual point, indicated by a yellow sphere. After instrumentation, the interface geometry has been captured with a laser scanner and reconstructed in a CAD model (also used for the subframe models). This allows determining the position and orientation of the sensors and the virtual points to construct the sensor IDM matrix \mathbf{R}_v . The virtual point DoFs are defined in the centre of each REPS mount, compatible with the previous finite difference setup.

Let us review some of the virtual point theory presented in Sec. 2.3.3. The reciprocal measured FRFs ($\mathbf{Y}_{C_3,cd} \in \mathbb{C}^{26 \times 1}$) require a one-sided transformation, i.e. $\tilde{\mathbf{Y}}_{C_3,cd} \in \mathbb{C}^{12 \times 1}$ for remote excitation on the windscreen (d_3) to virtual responses measured at (c_1, c_2). More specifically, the 13 response channels at each interface are projected onto the 6 rigid IDMs (x, y and z translations, alongside their corresponding rotations) through pre-multiplication by the transformation matrix \mathbf{B}_v ,

$$\tilde{\mathbf{Y}}_{C_3,cd} = \mathbf{B}_v \mathbf{Y}_{C_3,cd} \quad \text{with} \quad \mathbf{B}_v = [\mathbf{R}_v^T \mathbf{R}_v]^{-1} \mathbf{R}_v^T. \quad (7.13)$$

Together, the 13 response DoFs allow for a more than 2-fold over-determination of the 6-DoFs in the virtual point. It is good practice to include three tri-axial sensors (9 response channels) per virtual point, however, some sensors cannot be positioned as accurately as others. By evaluating the sensor consistency, incorrect channels can be spotted and corrected, as they appear as outliers in the sensor-specific consistency. This is shown in Fig. 7.28a for the 13 indicator DoFs at the motor-side (c_1 – ■), and pinion-side (c_2 – ■) virtual point, respectively, whilst the response indices are specified in Fig. 7.27a. That said, the tri-axial sensors placed under the virtual point show a significantly lower consistency in the z -directions (response index: 9 for (c_1); and 22 for (c_2)) compared to the x and y -directions (i.e. response index: 7, 8 for (c_1); and 20, 21 for (c_2)). Here, the mounting positions on the bolts are fairly rigid, however, the problematic z -direction points straight into the virtual point. Physically, the z -responses (index: 9 and 22) only contribute to the z -translations in the virtual points without a contribution along the rotational axes. These measurement positions are susceptible to inconsistency, for example, due to slight variations between the measured (CAD model) and actual sensor positions. A few other outliers can be observed, most notably the single-axis accelerometers (response index: 10-13 and 23, 26). It is challenging to capture the correct orientation (i.e. surface normal) of the small teardrop sensors on the complex geometry.

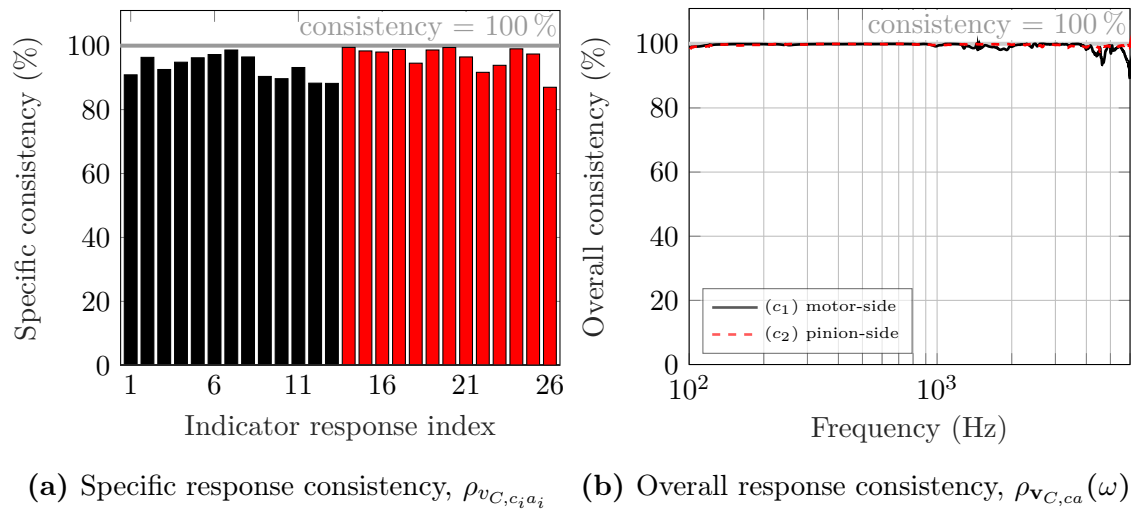


Figure 7.28: Evaluation of the frequency-averaged sensor specific consistency for the 13 channels at each coupling point: (c_1) motor-side (■); (c_2) pinion-side (■), and improved overall consistency for the 9 best response DoFs selected at each virtual point.

Fig. 7.28b shows the corresponding overall sensor consistency for the 9 best responses selected at each virtual point for the transformation. The virtual point transformation is based on the assumption of a rigid body behaviour in the interface area, where the response sensors are mounted. Even at higher frequencies, the effect of local flexibility is considered negligible compared to the consistency of the previous adapter setup (compare Fig. 7.4a; consistency drops: 1.5-3 kHz and above 4 kHz). The virtual point transformation for the selected channels is dynamically plausible; thus, reliable validation FRFs can be obtained in the entire bandwidth up to 6 kHz.

7.7.2 Repeated Vehicle Identification

In this section, vehicle FRFs obtained with the controlled exciter are compared against the previously outlined virtual point measurements, without a specific application (e.g. fastTPA or fastVAP) in mind. After the one-sided transformation to a $\tilde{\mathbf{Y}}_{C_3,dc}^T \in \mathbb{C}^{1 \times 12}$ virtual point matrix, the reciprocal agreement ($\tilde{\mathbf{Y}}_{C_3,dc}^T = \mathbf{Y}_{C_3,dc}$) to the predicted exciter FRFs is shown in Fig. 7.29. Here, the reciprocally measured virtual point results (—) are considered the reference, describing the actual input-output behaviour between the DoFs. The predicted results (—) are obtained through the repeated operational excitation from the controlled REPS system in the modified assembly and a response measurement at the target DoF (d_3) on the windscreen.

Looking at the FRFs individually, a quite reasonable agreement is achieved considering the differences commonly encountered in reciprocal measurements. The largest errors are observed for the γ -rotation DoF (see Fig. 7.29d), where the predicted structural FRF can be seen to over-predict the measured virtual point reference over a wide frequency range (300 Hz-3 kHz). This is to be expected, considering errors previously encountered for less contributing paths (compare Sec. 7.4.2). In spite of the errors encountered in the γ -DoF, the good level of agreement shown in Figs. 7.29a-7.29c indicates that the system identification can be performed in the vehicle assembly without the adapters.

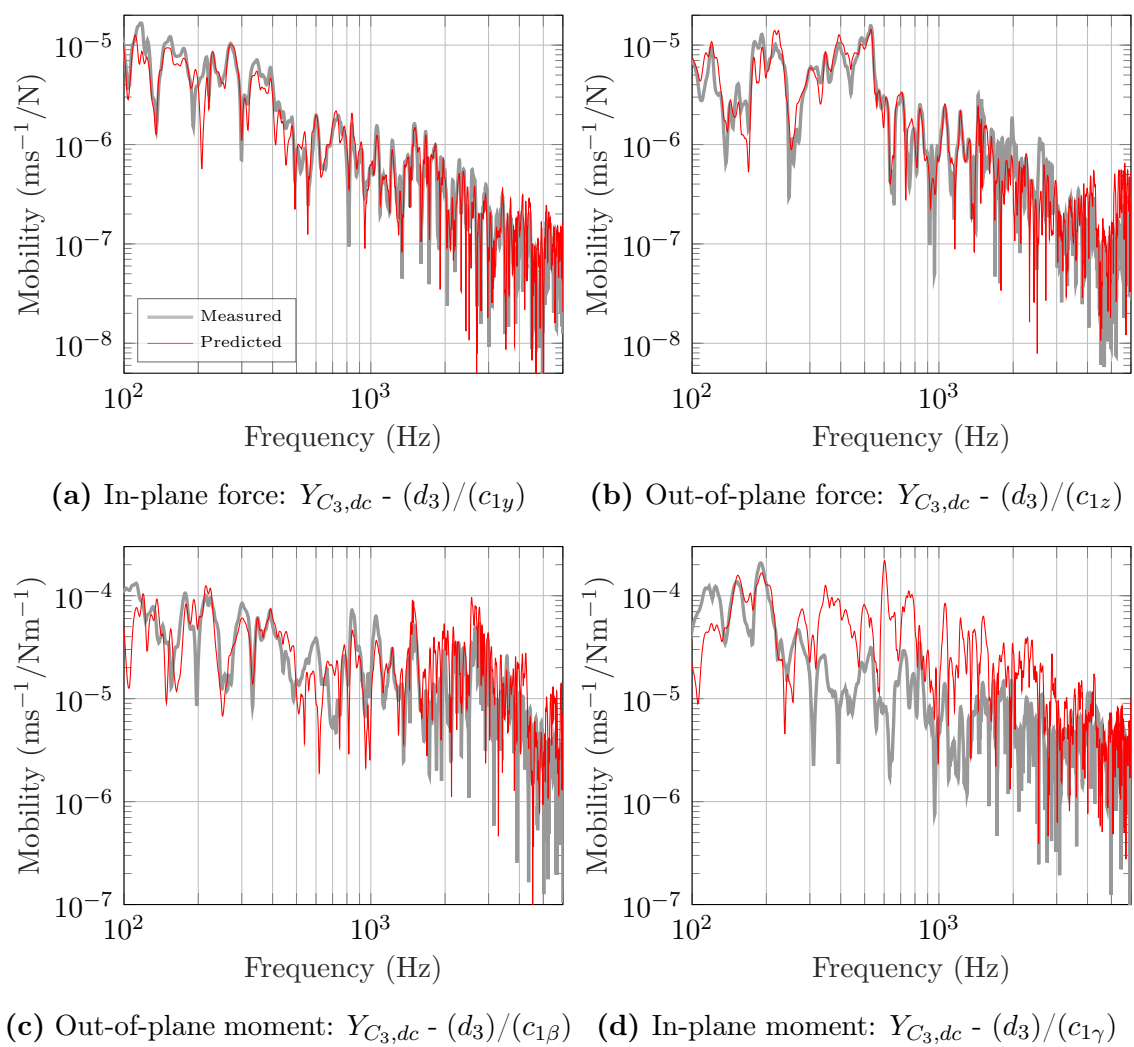


Figure 7.29: Reciprocal transfer FRFs $Y_{C3,dc}$ between the coupling interface at the sub-frame and the vibration response at the vehicle's windscreen. Narrowband representation for translational force excitation (top) and moment excitation (bottom): reciprocal shaker measurement (—); and prediction (--) using the controlled motor.

Errors in the predicted FRFs due to changes in the source-receiver coupling conditions (e.g. stiffening effects or different local interface dynamics) are not noticeable. That said, the adapters can be included as part of the receiver structure without significant influence on the controlled exciter or validation measurements. Clearly, the modification of the receiver structure at the interface will influence the true transfer function of the vehicle; the blocked force defined at the interface, however, remains unchanged. This is perhaps the main advantage of the controlled exciter concept; the interface needs no explicit (manual) excitation or measurement, yet pertains correct excitation properties for system identification. Hence the calibrated source can be connected to other receivers to obtain meaningful FRFs. The results further suggest that the exciter DoFs (without adapter) at (c_1, c_2) are collocated to the interface DoFs of the independent virtual point measurements. In other words, the finite difference approximation (bench calibration) and the virtual point transformation (independent vehicle validation) define the point-like coupling interface in the centre of the REPS mounts. After all, the adapters facilitate interface access during the calibration procedure to predefine the interface DoFs of the controlled blocked force exciter without introducing noticeable error when removed in the subsequent system identification step.

For implementing the virtual point transformation, the main challenge to overcome is the precise measurement of the correct sensor positions and orientation. Key in the experimental setting is to carefully define the measurement locations beforehand, whilst indicators such as consistency may help to assess the quality of the transformation matrix. Instead, the same multi-DoF and multi-contact FRFs can be obtained from a repeated operational excitation with the controlled REPS system and simple response measurements at the target DoFs. The foremost reason for using the exciter concept is that the correct interface DoFs are already defined (bench calibration), and conventional FRF measurements in the vehicle are avoided. This reduces testing time to a fraction of what would be required for the virtual point measurement. The ability to repeat the system identification step once the source is calibrated enables new applications, which otherwise have been considered too time-consuming.

For instance, a major concern in the automotive industry, which, to some extent, is often ignored and not explicitly addressed in this thesis, is the uncertainty of production spread. This is the variation of acoustic properties between different assemblies due to production tolerances. Although conventional methods (e.g. virtual point

FRF measurements) can indicate, with some accuracy, structural differences between complex assemblies, they currently lack practicability as they are not scalable. Instead, the controlled exciter concept (e.g. roving shaker or motor excitation) may be applied to quickly identify NVH uncertainty associated with production spread. A calibrated source repeatedly operated in different assemblies or over the product's lifespan can help evaluate and control production tolerances. With the vehicle assembly in mind, prototypes during the pre-production development can be compared and selected by their FRFs to avoid the occasional 'lemon' in NVH testing [10]. Additionally, the results from various vehicles and trim levels can be combined to define ensemble FRFs (i.e. averaged FRFs from multiple assemblies), whilst deviations (outliers from these ensemble FRFs) may be used to define uncertainty filters. In a novel sound design application, such filters could be applied in a VAP to predict the effect of production spread or to auralise the best/worst case encountered in a practical scenario.

7.8 Summary and Concluding Remarks

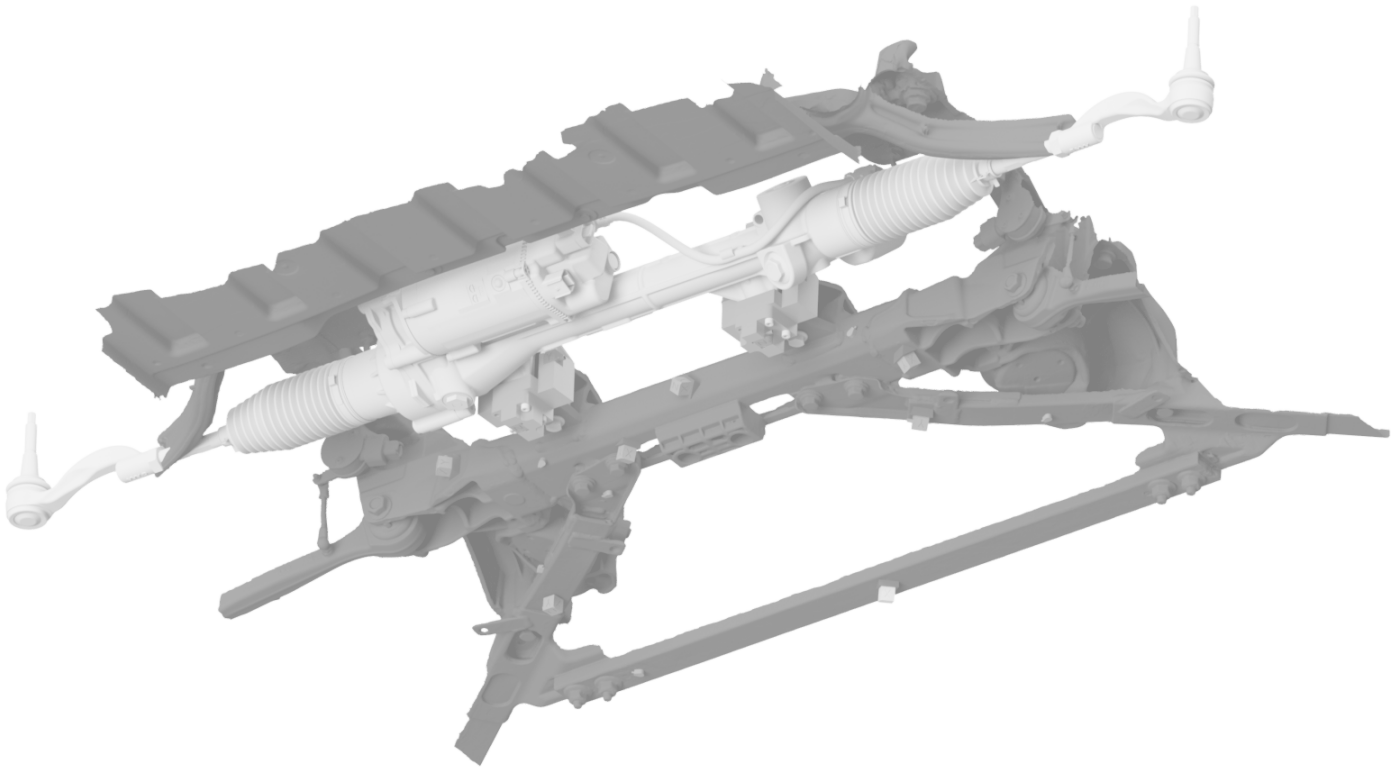
This chapter has presented a collection of applications in the field of source characterisation and diagnostic prediction of structure-borne sound and vibration, based on a novel 'faster' FRF identification procedure. The controlled REPS system (calibrated in Chapter 6) is used as a multi-DoF blocked loads exciter for system identification in a new assembly.

The steering system has been installed in the vehicle to identify dominant contributions paths for steering noise in the passenger compartment. In detail, two different criteria: interface completeness and transformation consistency, have been discussed to indicate uncertainties in the interface description. The source-receiver coupling can be described by 6-DoF point-like contacts to provide robust characterisation of the active REPS system, which was later extended to higher frequencies by including flexible coupling DoFs. The assembly FRFs for the inverse force identification and forward response prediction in the vehicle are determined simultaneously using the controlled exciter concept. Accurate results are obtained for interface driving-point FRFs (including in-planes and rotations) and transfer FRFs (considering structural and vibro-acoustic FRFs), even though access to the measurement points is restricted.

Following the system identification (i.e. prediction of vehicle FRF matrices), the practical implementations of fastTPA and fastVAP have been discussed, with each case study compared against conventional (benchmark) methods. Using the controlled exciter for fastTPA and fastVAP is considered a novel application of the concept, where operational quantities replace conventional FRF measurements in the vehicle. As such, the controlled exciter concept reduces the experimental effort and avoids many challenges commonly involved in TPA, e.g. the near-routine neglect of inaccessible transfer paths. Furthermore, the contribution ranking and the partial results determined via the fastTPA (remote blocked force relation) were in excellent agreement with those acquired via the well established in-situ TPA benchmark study. Repeatable results were obtained via the alternative fastTPA interface relation and a 7-DoF flexible extension of the remote relation; application of the latter extension for a real structure is considered a novelty on its own. Although deviations were encountered in the contribution analysis for some rotational DoFs (expected considering their negligible contribution and the bottleneck effect at the interface), the results clearly demonstrate the method's potential advantages, particularly for constructing an experimental fastVAP with compatible coupling DoFs.

Part three of the case study has been concerned with repeated FRF measurements in a modified and more realistic (without interface adapters) vehicle assembly. The vehicle FRFs obtained with the controlled exciter showed a good agreement with the reciprocal reference measurement, indicating that the blocked load excitation at the interface can be reproduced independent of the adapters. From a practical point of view, the exciter concept outperforms conventional measurements by its ability to conduct MIMO FRFs studies in a shorter time, enabling new applications, e.g. monitoring production spread.

PART V. Conclusions, Bibliography and Appendices



Conclusions and Future Work

In response to ever-increasing demands on NVH attributes in the automotive industry, quick diagnostic methods are required to analyse the propagation of sound and vibration in coupled assemblies. In this thesis, experimental methods have been explored in the fields of system identification and transfer path analysis, which together provide practical tools for the development and refinement of complex built-up structures. Emphasis is on indirect measurement procedures, as it was identified that practical challenges encountered in state-of-the-art TPA methods have led to near-routine neglect of transmission paths.

In particular, the aim was to develop techniques for quick yet reliable characterisation of assembly properties (i.e. system identification) and their implementation in a faster TPA approach, providing engineers with realistic prognoses to make informed design changes.

As an introduction, Chapter 2 highlights state-of-the-art experimental techniques for structure-borne source characterisation. Starting with the definition of passive and active system properties, the in-situ blocked force relation (specified in ISO 20270:2019) was presented for an independent description of active source vibrations. A workflow for source characterisation has been outlined, considering all steps from measurement preparation and instrumentation to post-processing and quality assessment. It was indicated how one could obtain a representative interface description using point-like contacts, including translational and rotational coordinate-DoFs. The equivalent multi-point connection, finite difference approximation and virtual point transformation were outlined as different means to describe rotational behaviour, either implicitly or explicitly. Dimensionless notations for the sensor and excitation transformation consistency were presented to trace back potential errors due to non-consistent dynamics, alongside the Interface Completeness

Criterion (ICC) to evaluate whether enough DoFs have been included for source characterisation. In addition, an on-board and transferability validation can assess errors in the operational blocked force vector as a final evaluation of quality.

Source characterisation is an essential part of most state-of-the-art TPA approaches. Apart from the time-consuming nature of the measurements, practical challenges in TPA are the impracticality to include particular paths (e.g. in-plane), the inability to measure rotational dynamics (e.g. moment excitation), insufficient signal-to-noise ratios (SNR), or simply restricted access. A brief overview of different TPA categories has been presented to highlight popular variants differing in their implementation and interpretation. Conceptually, the novel fastTPA concept is similar to other component-based TPA approaches, where blocked forces characterise active vibrations, but there are potential advantages in terms of convenience and speed.

The concept of round-trip identity has been reviewed in Chapter 3 in a framework for indirect measurement of structural dynamic properties for linear, time-invariant systems. The round-trip identity provides mobilities (or any similar FRFs such as admittances) at ‘passive’ locations, that is, at locations where no excitation is applied. Instead, measurements are relocated to some remote points (easy-to-access) on the source and receiver sub-structures. According to their interface characteristics, classification of round-trip variants has been proposed: single interface-, dual-, and substructure relation. A novel generalised round-trip expression for coupled systems has been introduced to provide a formulation for transfer FRFs between a coupling interface and some selected points on the receiver-side. Apart from similarities within the derivation, it was demonstrated that the generalised expression combines both special cases of the single- and dual-interface round-trip scenario. The generalised round-trip identity can readily be implemented in TPA for system identification of inaccessible transmission paths in any complex built-up structure.

For this purpose, the round-trip relations presented in the framework have been applied in Chapter 5 for indirect system identification, with particular emphasis on in-plane and rotational DoFs. Analytical and experimental validation of the generalised expression for driving-point and transfer FRFs have been presented on a simple rod assembly. A second study demonstrated its application for a multi-contact, multi-DoF assembly, where a cross-like sensor configuration is used at the interface to consider rotational coupling via finite difference approximation. In the preferred

case that more remote DoFs are considered on either side of the interface than coupling DoFs are present, the generalised round-trip relation takes the form of a least-squares problem. It has been shown that the above form of over-determination can reduce errors and the effect of noise, most noticeable in the rotational FRF terms, yet similar improvements have been achieved by using a TSVD regularisation. It was concluded that the generalised round-trip identity provides a full mobility matrix (including in-plane and rotational DoFs) and can readily be implemented in TPA, e.g. for inverse force identification. In case only some matrix elements need to be measured indirectly, correct round-trip FRFs terms can be obtained for a subset of paths (i.e. incomplete instrumentation of the interface coupling DoFs) considered in the experiment.

Indirect methods apply not only to inaccessible FRF measurements involved in TPA, but also to considerably large transmission paths which are susceptible to insufficient SNR. Manipulation of the generalised round-trip identity yielded a novel formulation for long distance transfer FRFs by combining measurements over shorter distances. A nested formulation has been introduced to extend the characterisation for extensively long transfer FRFs by recursively adding shorter path segments, useful for applications such as railroad vibration analysis. Its application has been presented on a test bench - steering system assembly. The round-trip relation improved the measurement quality of the long transfer FRFs compared against a conventional single-excitation measurement in a bandwidth of 6 kHz. This concept can be applied to estimate forward transmission paths in TPA, such as vibro-acoustic FRFs in commercial vehicles where the excitation energy provided by impact hammers is often insufficient to achieve an acceptable SNR on the response measurement.

Common practicalities and considerations of the generalised round-trip identity have been discussed, such as how many remote excitation and response measurements need to be considered on either side of the interface. In particular, the concepts of controllability and observability of the vibrations that occur at the interfaces has been presented to provide practical guidelines. It was concluded that the interface could be regarded as a bottleneck, imposing constraints on the number of source excitations that are transmitted over the interface onto the passive side. These concepts have been discussed in the context of the round-trip framework but generally apply to system identification and to TPA, including fastTPA.

The generalised round-trip approach was further investigated, particularly with regards to its practical implementation. Consequently, Chapter 4 introduced the generalised transmissibility concept to replace excitations that have been relocated on the source substructure by operational forces. In this case, operational excitation from the active source is used to perform part of the round-trip measurements, in fact, the source is considered an exciter that applies blocked force excitation at the interface. The invariance of the blocked force allowed to split the round-trip measurements and perform them on two different assemblies. A novel two-stage procedure has been proposed, where a controllable structure-borne vibration source is calibrated on a test bench and later installed in a target assembly for system identification. In essence, a controllable source is converted into a multi-DoF blocked force vibration exciter to determine translational and rotational FRFs simultaneously. The two-stage system identification provides a convenient and quick alternative to single-excitation FRF measurements with an instrumented hammer or (single-DoF) shaker. The determined FRFs have been used for inverse force identification and response prediction, in other words, to provide diagnostic (fastTPA) or predictive (fastVAP) tools. As a diagnostic tool, the relative contribution of each interface DoF to the total operational response is predicted for troubleshooting of dominant paths in existing assemblies. As a predictive tool, concern is placed on predicting noise and vibration in complex structures that do not necessarily exist physically, based on the measurement of each individual sub-structure.

In Chapters 6 and 7, the fastTPA workflow has been demonstrated to characterise steering vibrations and predict the experienced noise in a vehicle. Starting with the steering gear calibration on a bench, two concepts to operate the multi-DoF blocked force exciter have been outlined: operational excitation controlled by the electric motor and externally applied roving excitations. The above control strategies have been used to exert known blocked loads at two steering gear mounts, comprising 12-DoFs (3 translations and 3 rotations at each interface). It has been demonstrated how singular value decomposition, ICC and excitation consistency can be utilised to better understand the exciter's dynamics, i.e. 8 excitation DoFs can effectively be controlled due to the bottleneck effect. In the vehicle, system identification has been outlined using reproduced controlled excitations. Similar to conventional single-excitation measurements, the steering system used as a calibrated exciter provides accurate estimates for both structural and vibro-acoustic FRFs in a bandwidth of 6 kHz. Fast and convenient system identification was achieved by controlling the

electric motor, whilst errors in the obtained vehicle FRFs are similar to the experimental variation in conventional measurements, e.g. if the vibro-acoustic FRFs are measured with a shaker and reciprocally using a volume-velocity source. It was shown that external excitations provide highly accurate FRFs estimates, with a general improvement over measurements with the controlled motor, since a load cell was used to normalise the applied forces for better reproducibility.

The primary aim of this project was to incorporate the estimated FRFs within a faster TPA approach. To investigate this for an industrial case, the fastTPA approach has been benchmarked against the well-established in-situ TPA methodology. It was concluded that the experimental uncertainty associated with the reproduced excitation is low, even in the multi-kHz range. Dominant contributions have been correctly predicted and identified, while others show worse agreement for reasons traced back to the bottleneck effect at the interface. This again indicates that controllability and observability are key concepts for system identification with the controlled exciter and TPA. It was concluded that fastTPA can be adapted to a wide range of applications and provides a thorough (i.e. all interface loads and their contributions are determined) yet quick analysis. Therefore, fastTPA is an engineering tool for troubleshooting (calibrated) sources in their intended installation, whilst interface measurements (which often lead to the neglect of some paths) are avoided.

For pro-active NVH development, the determined vehicle FRFs have been used to construct a fastVAP. It was shown that the exciter measurements provide a compatible vehicle model to predict the operational responses in a virtual environment. FastVAP is quicker and more reliable (assuming full controllability and observability) than conventional VAP concepts since errors due to inconsistent (not matching) coupling DoFs between source characterisation and propagation model are avoided.

This thesis has introduced novel concepts for system identification and tools for diagnostic and predictive tests. Based on the case studies presented through Chapters 5-7, the following topics have been identified as potentially interesting directions for future research:

- ▶ *Application of the controlled exciter concept to mechanical sources.* For sources that are challenging to control, a roving shaker approach has been proposed to apply reproducible excitations in different assemblies. Similarly, the presented case studies considered a modified steering system with an (easy-to-control)

stepper motor. In order to clearly demonstrate the potential of the fastTPA methodology, the concept may be applied to a steering system without any component modifications. Perhaps the electric motor's input current or voltage signal can be utilised to compensate for variations when the REPS system is operated in different assemblies (similar to the normalisation with a load cell used for external excitations), e.g. by defining vibro-electric FRFs between the operational responses and the controlled electric excitation. It is also suggested to investigate other active components, particularly to evaluate if mechanical mechanisms are suitable for reproducible excitation.

- ▶ *FastTPA quality assessment.* It was demonstrated in Chapter 7 that fastTPA allows identifying dominant contributions to provide an engineer with the information necessary to make informed design changes. In this sense, it appears essential that a measure of its experimental uncertainty accompanies such information. The transferability validation has briefly been discussed in Sec. 4.3.2, however, it only indicates over which frequency range the estimated FRF matrix should be considered with care. In order to apply fastTPA with confidence, alternative validation techniques may be investigated to assess uncertainties in the blocked force and the forward prediction step. Similarly, a linear covariance-based approach could be used to analyse the uncertainty contribution of each term in fastTPA. The experimental uncertainty can be propagated through the inverse procedure onto the blocked force or the predicted response identifying significant error terms. Here, regularisation techniques to minimise noise-induced errors in the inverse of an ill-conditioned matrix complicate the propagation of uncertainty and require further research.
- ▶ *Automatisation of the calibration procedure.* To simplify the calibration of the REPS system as a multi-DoF exciter on the bench, multiple electro-dynamic shakers can be embedded in the specificity designed fixture for automatised FRF measurements. Operated one at a time, these shakers facilitate measurements of the mobility matrix $\mathbf{Y}_{C1,bc}$ in a relatively short time. This would allow for fastTPA and fastVAP predictions without requiring a special skill set on how to perform manual excitations (plug-and-play ready). Assuming linearity and time invariance of this bench assembly, operational tests with the REPS system may be performed while the shakers (turned off) are attached to the fixtures to reduce instrumentation effort further.

- ▶ *Investigation of measurement inconsistency in the generalised round-trip identity.* Regarding the practical side, the experimental validation of the long distance round-trip relation has been kept brief; the concept provides robust system identification, yet not fast. Its application to a real-life structure, e.g. ground vibration testing of aircraft, could provide more in-depth proof of the theory. It is probably worth investigating the effects of inconsistency between the shorter FRF segments due to them being obtained from separate tests. This may lead to an imperfect cancellation and artefacts in the reconstructed long distance FRFs, particularly for a nested formulation with multiple virtual interfaces.



Appendices

A.1 Local Flexibilities at the Adapter

The experimental studies presented in Chapters 6 and 7 consider translational and rotational coupling at each interface using the finite difference approximation. The approximation is based on the assumption of a rigid body behaviour over the distance (i.e. 2Δ), whilst local flexibilities introduce errors at higher frequencies. Due to the relatively large spacing of the force and response measurements on the cocoon-like adapter (see Fig. 6.2b), the rigidity assumption was analysed numerically during its design.

The adapter's design is based on a numerical model using a truncated modal summation, similar to the free-free rod in Sec. 5.1.2. The material properties of the model are the same as in Table 5.1. Translational (x, y, z) mobilities are calculated at the actual excitation and response positions on the adapter (see Fig. 6.2b) to approximate translations and rotations in its centre. A matrix $\mathbf{Y}_{A,cc} \in \mathbb{C}^{6 \times 6}$ is obtained for free boundary conditions of the adapter to analyse its resonant behaviour without being connected to the source or receiver. Fig. A.1 shows the diagonal elements of this mobility matrix (driving-point FRFs) of the numerical simulation (—), compared against an experimental validation measurement (—) of the freely suspended part. A spacer was mounted/modelled inside the adapter to account for stiffening effects when connected to the steering system.

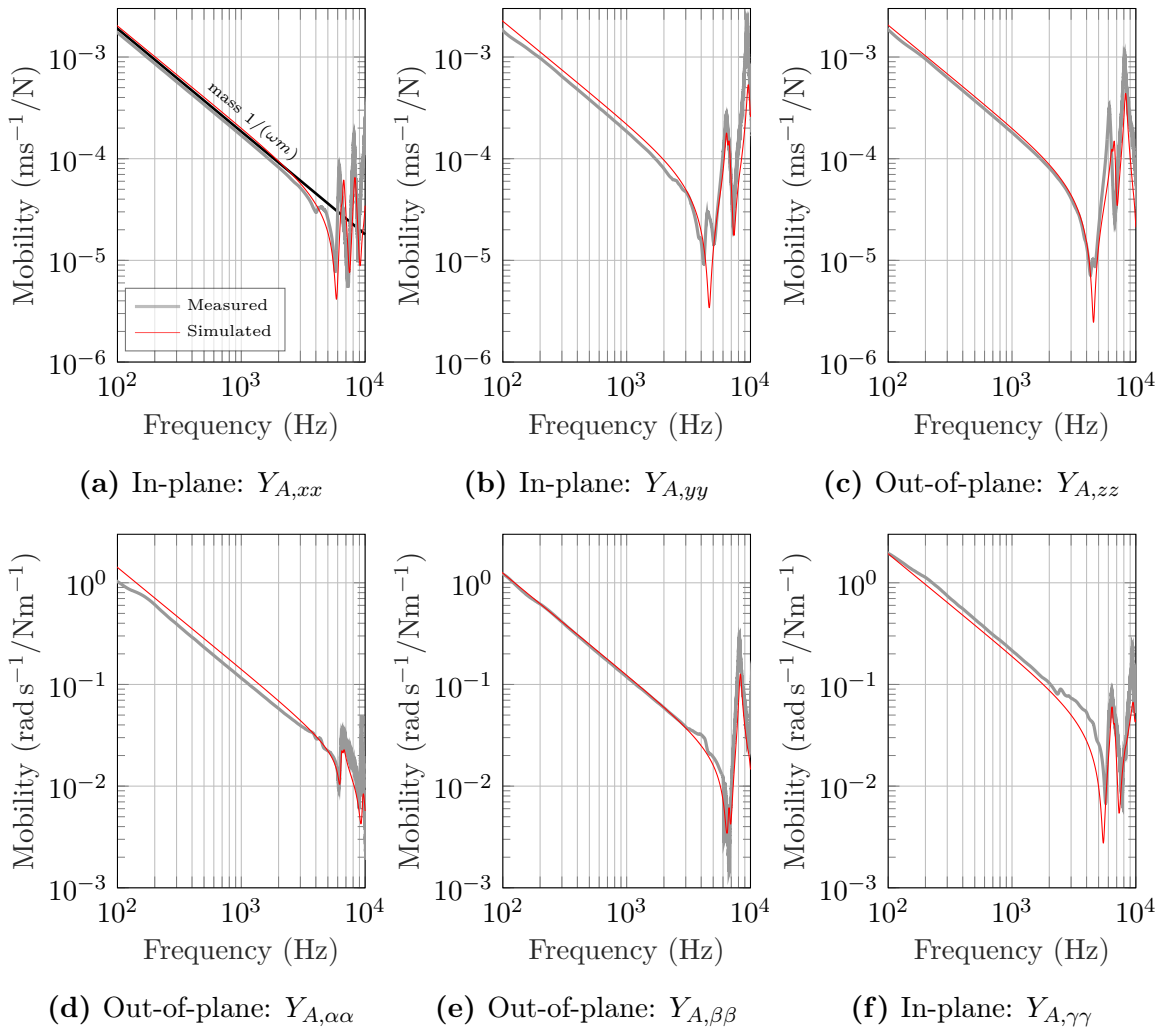
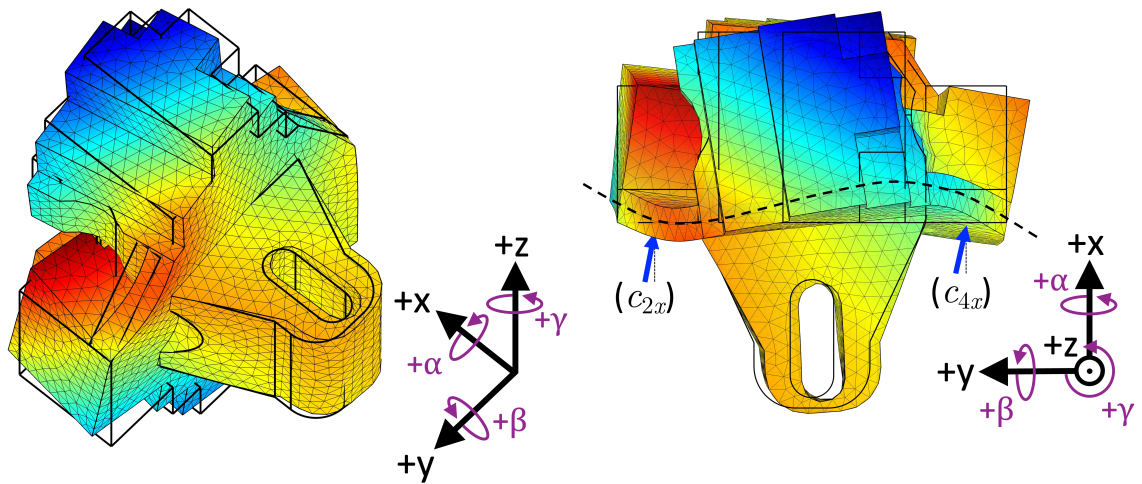


Figure A.1: Translational and rotational driving-point mobilities of the resiliently suspended cocoon adapter using finite difference approximation. Narrowband representation for translational (top) and rotational (bottom) DoFs: experimentally obtained reference (—); numerical FE simulation (—) used during the design.

The mobilities are dominated by mass inertia at low frequencies, indicated by a negative slope of -6 dB/octave ($1/(\omega m)$) [144, 174]. Above approximately 3-4 kHz, the mobilities in Fig. A.1 are not longer asymptotic to the mass line (—). This analysis confirms that the cocoon-like structure might be considered rigid up to 3-4 kHz. At higher frequencies, the effects of local flexibility between the spaced measurements will result in a finite difference error. A smaller force and sensor spacing may extend the upper frequency range, however, installation on the bench (Chapter 6) and in the vehicle (Chapter 7) with access for excitations place restrictions on the adapter’s design. In addition, steering induced noise in realistic scenarios is usually limited to a frequency range below 2.5-3kHz [167], making the cocoon-fixture well suited for most steering related applications.

Further to the breakdown of the locally rigid behaviour, Fig. A.2 shows the corresponding mode shape to the first resonance frequency at 6.2 kHz. Note that the red and blue colour scheme indicates opposite structure deformations, while a colourmap is omitted in these purely qualitative schematics. Local flexibilities in the connection area can be included in the interface description, e.g. the χ -extension DoF may be added to the 6-DoFs coupling, as outlined in Sec. 7.5.3.



(a) Mode shape of the adapter at 6.2 kHz (b) Top view: Bending at the cross section

Figure A.2: Mode shape of the first non-rigid mode (bending along the x-axis) of the interface adapter. The locally flexible behaviour, for example, between the response channels (c_{2x}) and (c_{4x}) at the interface, limit the frequency range of the finite difference approximation.

Bibliography

- [1] K. Wienen, M. Sturm, A. T. Moorhouse, and J. W.R. Meggitt. ‘Robust NVH engineering using experimental methods - Source characterization techniques for component Transfer Path Analysis and Virtual Acoustic Prototyping’. In: *SAE International*, Tech. paper: 2019-01-1542, pp. 1766–1778, 2019.
- [2] J. W.R. Meggitt, A. T. Moorhouse, K. Wienen, and M. Sturm. ‘A framework for the propagation of uncertainty in Transfer Path Analysis’. In: *Journal of Sound and Vibration*, 483, Article 115425, 2020.
- [3] K. Wienen, M. Sturm, A. T. Moorhouse, and J. W. R. Meggitt. ‘Generalised round-trip identity - for the determination of structural dynamic properties at locations inaccessible or too distant for direct measurement’. In: *Journal of Sound and Vibration*, 511, Article 116325, 2021.
- [4] M. V. van der Seijs, D. de Klerk, and D. J. Rixen. ‘General framework for Transfer Path Analysis: History, theory and classification of techniques’. In: *Mechanical Systems and Signal Processing*, 68-69, pp. 217–244, 2016.
- [5] J. W. Verheij. ‘Multi-path sound transfer from resiliently mounted shipboard machinery’. PhD thesis, Delft University of Technology, Netherlands, 1982.
- [6] A.S. Elliott, A.T. Moorhouse, T. Huntley, and S. Tate. ‘In-situ source path contribution analysis of structure borne road noise’. In: *Journal of Sound and Vibration*, 332(24), pp. 6276–6295, 2013.
- [7] D. de Klerk and D. J. Rixen. ‘Component Transfer Path Analysis method with compensation for test bench dynamics’. In: *Mechanical Systems and Signal Processing*, 24, pp. 1693–1710, 2010.
- [8] D. de Klerk and A. Ossipov. ‘Operational Transfer Path Analysis: Theory, guidelines and tire noise application’. In: *Mechanical Systems and Signal Processing*, 24(7), pp. 1950–1962, 2010.
- [9] A. T. Moorhouse, T. A. Evans, and A. S. Elliott. ‘Some relationships for coupled structures and their application to measurement of structural dynamic properties in situ’. In: *Mechanical Systems and Signal Processing*, 25(5), pp. 1574–1584, 2011.
- [10] M. V. van der Seijs. ‘Experimental dynamic substructuring: Analysis and design strategies for vehicle development’. PhD thesis, Delft University of Technology, Netherlands, 2016.
- [11] D. de Klerk, D. J. Rixen, and S. N. Voormeeren. ‘General framework for dynamic substructuring: History, review and classification of techniques’. In: *AIAA Journal*, 46(5), pp. 1169–1188, 2008.

- [12] G. Kerschen, K. Worden, A. F. Vakakis, and J.-C. Golinval. ‘Past, present and future of nonlinear system identification in structural dynamics’. In: *Mechanical Systems and Signal Processing*, 20, pp. 505–592, 2006.
- [13] G. J. O’Hara. ‘Mechanical impedance and mobility concepts’. In: *The Journal of the Acoustical Society of America*, 41(5), pp. 1180–1184, 1967.
- [14] R. B. Randall. ‘Frequency analysis’. K. Larsen & Son, Glostrup, 3rd edition, 1987.
- [15] J. W. Verheij. ‘Inverse and reciprocity methods for machinery noise source characterization and sound path quantification: Part 2: Transmission paths’. In: *Journal of Sound and Vibration*, 2(3), pp. 103–112, 1997.
- [16] R. J. Allemang. ‘The modal assurance criterion - twenty years of use and abuse’. In: *Sound and Vibration Magazine*, (37), pp. 14–23, 2013.
- [17] International Organisation for Standardisation. ‘Mechanical vibration and shock - Experimental determination of mechanical mobility - Part 1: Basic terms and definitions, and transducer specifications: ISO 7626-1:2011’, 2011.
- [18] International Organisation for Standardisation. ‘Mechanical vibration and shock - Experimental determination of mechanical mobility - Part 2: Measurements using single-point translation excitation with an attached vibration exciter: ISO 7626-2:2015’, 2011.
- [19] International Organisation for Standardisation. ‘Mechanical vibration and shock - Experimental determination of mechanical mobility - Part 5: Measurements using impact excitation with an exciter which is not attached to the structure: ISO 7626-5:2019’, 2019.
- [20] F. Fahy. ‘Some applications of the reciprocity principle in experimental vibroacoustics’. In: *Acoustical Physics*, 49(2), pp. 262–277, 2003.
- [21] J. W. R. Meggitt. ‘On in-situ methodologies for the characterisation and simulation of vibro-acoustic assemblies’. PhD thesis, University of Salford, UK, 2017.
- [22] P. Gardonio and M. J. Brennan. ‘Mobility and impedance methods in structural dynamics: An Historical Review’. In: *ISVR Technical Report No. 289*, , 2000.
- [23] R. Penrose and J. A. Todd. ‘A generalized inverse for matrices’. In: *Mathematical Proceedings of the Cambridge Philosophical Society*, 21(3), pp. 406–413, 1954.
- [24] D. J. Rixen, A. Boogaard, M. V. van der Seijs, G. van Schothorst, and T. van der Poel. ‘Vibration source description in substructuring: A theoretical depiction’. In: *Mechanical Systems and Signal Processing*, 60-61, pp. 498–511, 2015.
- [25] J. W. R. Meggitt and A. T. Moorhouse. ‘In-situ sub-structure decoupling of resiliently coupled assemblies’. In: *Mechanical Systems and Signal Processing*, 117, pp. 723–737, 2019.
- [26] M. Haeussler, S. W. B. Klaassen, and D. J. Rixen. ‘Experimental twelve degree of freedom rubber isolator models for use in substructuring assemblies’. In: *Journal of Sound and Vibration*, 474, Article 115253, 2020.

- [27] A. T. Moorhouse. ‘On the characteristic power of structure-borne sound sources’. In: *Journal of Sound and Vibration*, 248(3), pp. 441–459, 2001.
- [28] International Organisation for Standardisation. ‘Acoustics - Determination of sound power levels and sound energy levels of noise sources using sound pressure - Precision methods for reverberation test rooms: ISO 3741:2010’, 2010.
- [29] International Organisation for Standardisation. ‘Acoustics - Determination of sound power levels and sound energy levels of noise sources using sound pressure - Precision methods for anechoic rooms and hemi-anechoic rooms: ISO 3745:2012’, 2012.
- [30] M. M. Späh and B. M. Gibbs. ‘Reception plate method for characterisation of structure-borne sound sources in buildings: Assumptions and application’. In: *Applied Acoustics*, 70, pp. 361–368, 2009.
- [31] M. M. Späh and B. M. Gibbs. ‘Reception plate method for characterisation of structure-borne sound sources in buildings: Installed power and sound pressure from laboratory data’. In: *Applied Acoustics*, 70, pp. 1431–1439, 2009.
- [32] European Standardisation. ‘Acoustic properties of building elements and of buildings - Laboratory measurement of airborne and structure borne sound from building equipment: EN 15657-1:2009’, 2009.
- [33] J. Plunt. ‘Finding and fixing vehicle NVH problems with Transfer Path Analysis’. In: *Sound and Vibration*, 39(11), pp. 12–17, 2005.
- [34] B. J. Dobson and E. Rider. ‘A review of the indirect calculation of excitation forces from measured structural response data’. In: *Proceedings of the Institution of Mechanical Engineers, Part C: Journal of Mechanical Engineering Science*, pp. 69–75, 1990.
- [35] M. H. A. Janssens and J. W. Verheij. ‘A pseudo-forces methodology to be used in characterization of structure-borne sound sources’. In: *Applied Acoustics*, 61, pp. 285–308, 2000.
- [36] J. M. Mondot and B. Peterson. ‘Characterisation of structure-borne sound sources: The source descriptor and the coupling function’. In: *Journal of Sound and Vibration*, 114(3), pp. 507–518, 1987.
- [37] A. T. Moorhouse, A. S. Elliott, and T. A. Evans. ‘In situ measurement of the blocked force of structure-borne sound sources’. In: *Journal of Sound and Vibration*, 325(4), pp. 679–685, 2009.
- [38] International Organisation for Standardisation. ‘Acoustics - Characterization of sources of structure-borne sound and vibration - Indirect measurement of blocked forces: ISO 20270:2019’, 2019.
- [39] M. V. van der Seijs, E. A. Pasma, D. de Klerk, and D. J. Rixen. ‘A robust Transfer Path Analysis method for steering gear vibrations on a test bench’. In: *Proceedings of the International Conference on Noise and Vibration Engineering (ISMA)*, Leuven, Belgium, 2014.

- [40] D. D. van den Bosch, M. V. van der Seijs, and D. de Klerk. ‘Validation of blocked-force Transfer Path Analysis with compensation for test bench dynamics’. In: *Dynamics of coupled structures*, Vol. 6 Proceedings of the 32nd IMAC, A Conference and Exposition on Structural Dynamics. Springer, New York, 2014.
- [41] A. T. Moorhouse, R. D. Cookson, and G. Seiffert. ‘Measurement of operating forces of an electric motor’. In: *Proceedings of Noise Control (NOISE-CON)*, Baltimore (MD), USA, pp. 64–75, 2004.
- [42] M. Sturm. ‘Identification and quantification of transient structure-borne sound sources within electrical steering systems’. PhD thesis, University of Salford, UK, 2013.
- [43] A. S. Elliott and A. T. Moorhouse. ‘Characterisation of structure borne sound sources from measurement in-situ’. In: *Proceedings of Euro-Noise*, Paris, France, 2008.
- [44] A. S. Elliott. ‘Characterisation of structure borne sound sources in-situ’. PhD thesis, University of Salford, UK, 2009.
- [45] Y.I. Bobrovnikskii. ‘A theorem on the representation of the field of forced vibrations of a composite elastic system’. In: *Acoustical Physics*, 47(5), pp. 586–589, 2001.
- [46] J.W.R. Meggitt and A.T. Moorhouse. ‘On the completeness of interface descriptions and the consistency of blocked forces obtained in-situ’. In: *Mechanical Systems and Signal Processing*, (145), 2020.
- [47] A. N. Thite and D. J. Thompson. ‘The quantification of structure-borne transmission paths by inverse methods. Part 1: Improved singular value rejection methods’. In: *Journal of Sound and Vibration*, 264, pp. 411–431, 2003.
- [48] A. N. Thite and D. J. Thompson. ‘The quantification of structure-borne transmission paths by inverse methods. Part 2: Use of regularization techniques’. In: *Journal of Sound and Vibration*, pp. 433–451, 2003.
- [49] M. Thivant, A. Carbonelli, and P. Bouvet. ‘Derivation of the force interaction within strongly coupled systems - application to diesel engine oil pumps’. In: *Proceedings of the International Conference of Noise and Vibration Engineering (ISMA)*, Leuven, Belgium, 2010.
- [50] M. Sturm, T. Alber, A.T Moorhouse, D. Zabel, and Z. Wang. ‘The in-situ blocked force method for characterization of complex automotive structure-borne sound sources and its use for virtual acoustic prototyping’. In: *Proceeding of the International Conference on Noise and Vibration Engineering (ISMA)*, Leuven, Belgium, pp. 3647–3661, 2016.
- [51] T. Alber, M. Sturm, and A. T. Moorhouse. ‘Independent characterization of structure-borne sound sources using the in-situ blocked force method’. In: *Proceedings of INTER-NOISE*, Hamburg, Germany, 2016.
- [52] D. Zabel, M. Sturm, T. Alber, and A. Moorhouse. ‘Embedded MEMS accelerometers for the in-situ measurement of blocked forces in coupled structures’. In: *Proceedings of DAGA*, Kiel, Germany.

- [53] D. Lennström, M. Olsson, F. Wullens, and A. Nykänen. ‘Validation of the blocked force method for various boundary conditions for automotive source characterization’. In: *Applied Acoustics*, 102, pp. 108–119, 2016.
- [54] A. S. Elliott and A. T. Moorhouse. ‘In-situ characterisation of structure borne sound from a building mounted wind turbine’. In: *Proceedings of the International Conference on Noise and Vibration Engineering (ISMA)*, Leuven, Belgium, pp. 2055–2068, 2010.
- [55] A. T. Moorhouse, A. S. Elliott, T. E. Eastwick, A. Ryan, S. von Hunerbein, V. Le Bescond, and D. Waddington. ‘Structure-borne sound and vibration from building-mounted wind turbines’. In: *Environmental Research Letters*, 6, 2011.
- [56] A. S. Elliott, A.T Moorhouse, N. Sanei, M. Glessner, J. Sapena, and S. Ferella. ‘Structure borne noise characterization of an air generation and treatment unit (AGTU) for a train using the mobility method and sub-structuring’. In: *Proceedings of Inter-Noise*, Madrid, Spain, 2019.
- [57] N. Sanei, M. Glessner, J. Sapena, S. Ferella, and A. S. Elliott. ‘Structure borne noise characterization of an air generation and treatment unit (AGTU) for a train by using blocked forces method.’ In: *Proceedings of Inter-Noise*, Madrid, Spain, 2019.
- [58] M. Haeussler, D. C. Kobus, and D. J. Rixen. ‘Parametric design optimization of e-compressor NVH using blocked forces and substructuring’. In: *Mechanical Systems and Signal Processing*, 150, Article 107217, 2021.
- [59] F. Fahy and J. Walker, editors. ‘Advanced applications in acoustics, noise and vibration’. Spon Press, London, 2004.
- [60] International Organisation for Standardisation. ‘Acoustics - Characterization of sources of structure-borne sound with respect to sound radiation from connected structures - Measurement of velocity at the contact points of machinery when resiliently mounted: BS ISO 9611:1996’, 1996.
- [61] A. T. Moorhouse and B. M. Gibbs. ‘Prediction of the structure-borne noise emission of machines: Development of a Methodology’. In: *Journal of Sound and Vibration*, 167(2), pp. 223–237, 1993.
- [62] A. T. Moorhouse and B. M. Gibbs. ‘Measurement of structure-borne sound emission from resiliently mounted machines in situ’. In: *Journal of Sound and Vibration*, 180(1), pp. 143–161, 1995.
- [63] A. T. Moorhouse and A. S. Elliott. ‘The “round trip” theory for reconstruction of Green’s functions at passive locations’. In: *Acoustical Society of America*, 134(5), pp. 3605–3612, 2013.
- [64] M. A. Sanderson and C. R. Fredö. ‘Direct measurement of moment mobility, Part I: A theoretical study’. In: *Journal of Sound and Vibration*, 179(4), pp. 669–684, 1995.
- [65] A. T. Moorhouse and A. S. Elliott. ‘Indirect measurement of frequency response functions applied to the problem of substructure coupling’. In: *Proceeding of Noise and Vibration: Emerging Methods (NOVEM)*, Sorrento, Italy, pp. 1001–1107, 2012.

- [66] A. S. Elliott, G. Pavić, and A. T. Moorhouse. ‘Measurement of force and moment mobilities using a finite difference technique’. In: *Proceeding of EURONOISE*, Paris, France, pp. 1807–1812, 2008.
- [67] M. A. Sanderson. ‘Direct measurement of moment mobility, Part II: An experimental study’. In: *Journal of Sound and Vibration*, 179(4), pp. 685–696, 1995.
- [68] L. H. Ivarsson and M. A. Sanderson. ‘MIMO technique for simultaneous measurement of translational and rotational mobilities’. In: *Applied Acoustics*, 61, pp. 345–370, 2000.
- [69] B. Petersson. ‘On the use of giant magnetostrictive devices for moment excitation’. In: *Journal of Sound and Vibration*, 116(1), pp. 191–194, 1987.
- [70] S. Jianxin and C. M. Mak. ‘Direct measurement of moment mobility and a moment excitation system’. In: *Applied Acoustics*, 63, pp. 139–151, 2002.
- [71] Y. Champoux, V. Cotoni, B. Paillard, and O. Beslin. ‘Moment excitation of structures using two synchronized impact hammers’. In: *Journal of Sound and Vibration*, 263, pp. 515–533, 2003.
- [72] J. E. Mottershead, M. G. Tehrani, D. Stancioiu, S. James, and H. Shahverdi. ‘Structural modification of a helicopter tailcone’. In: *Journal of Sound and Vibration*, 298, pp. 366–384, 2006.
- [73] D. de Klerk. ‘Solving the RDoF problem in experimental dynamic substructuring’. In: *Proceedings of the XXVI International Modal Analysis Conference (IMAC)*, Orlando (FL), USA, 2007.
- [74] S. N. Voormeeren. ‘Coupling procedure improvement & uncertainty quantification in experimental dynamic substructuring’. Master thesis, Delft University of Technology, Netherlands, 2007.
- [75] A. S. Elliott, A. T. Moorhouse, and J. W. R. Meggitt. ‘Identification of coupled degrees of freedom at the interface between sub-structures’. In: *Proceedings of Noise and Vibration: Emerging Methods (NOVEM)*, Ibiza, Spain, 2018.
- [76] S. S. Sattinger. ‘A method for experimentally determining rotational mobilities’. In: *Master thesis, Massachusetts Institute of Technology, USA, 1978*.
- [77] A. S. Elliott, A. T. Moorhouse, and G. Pavić. ‘Moment excitation and the measurement of moment mobilities’. In: *Journal of Sound and Vibration*, 331(11), pp. 2499–2519, 2012.
- [78] M. V. van der Seijs, D. D. van den Bosch, D. J. Rixen, and D. de Klerk. ‘An improved methodology for the virtual point transformation of measured frequency response functions in dynamic substructuring’. In: *Proceedings of the 4th Thematic Conference on Computational Methods in Structural Dynamics and Earthquake Engineering (ECCOMAS)*, Kos, Greece, pp. 4334–4347, 2013.
- [79] M. V. van der Seijs, D. de Klerk, D. J. Rixen, and S. Rahimi. ‘Validation of current state frequency based substructuring technology for the characterisation of steering gear - vehicle interaction’. In: *Proceedings of the XXXI International Modal Analysis Conference (IMAC)*, Garden Grove (CA), USA, 2013.

- [80] M. Haeussler and D. J. Rixen. ‘Optimal transformation of frequency response functions on interface deformation modes’. In: *Proceedings of the XXVI International Modal Analysis Conference (IMAC)*, Garden Grove (CA), USA, 2017.
- [81] E. A. Pasma, M. V. van der Seijs, S. W. B. Klaassen, and M. W. van der Kooij. ‘Frequency based substructuring with the virtual point transformation, flexible interface modes and a transmission simulator’. In: *Proceedings of the XXXVI International Modal Analysis Conference (IMAC)*, Orlando (FL), USA, 2018.
- [82] M. W.F. Wernsen, M. V. van der Seijs, and D. de Klerk. ‘An indicator sensor criterion for in-situ characterisation of source vibrations’. In: *Proceedings of the XXXV International Modal Analysis Conference (IMAC)*, Los Angeles (CA), USA, 2017.
- [83] M. W. F. Wernsen. ‘Observability and transferability of in-situ blocked force characterisation’. Master thesis, Delft University of Technology, Netherlands, 2017.
- [84] J. W.R. Meggitt, A. T. Moorhouse, and A. S. Elliott. ‘A covariance based framework for the propagation of uncertainty through inverse problems with an application to force identification’. In: *Mechanical Systems and Signal Processing*, 124(1), pp. 275–297, 2019.
- [85] J.W.R. Meggitt, A. T. Moorhouse, and A. S. Elliott. ‘On the problem of describing the coupling interface between sub-structures: an experimental test for ‘completeness’’. In: *Proceedings of the XXXVI International Modal Analysis Conference (IMAC)*, Orlando (FL), USA, 2018.
- [86] M. Haeussler, T. Mueller, E. A. Pasma, J. Freund, O. Westphal, and T. Voehringer. ‘Component TPA: benefit of including rotational degrees of freedom and overdetermination’. In: *Proceedings of the International Conference on Noise and Vibration Engineering (ISMA)*, Leuven, Belgium, 2020.
- [87] J. W. R. Meggitt, A. S. Elliott, A. T. Moorhouse, A. Jalibert, and G. Franks. ‘Component Replacement TPA: a transmissibility based structural modification method for in-situ Transfer Path Analysis’. In: *Journal of Sound and Vibration*, 499, Article 115991, 2020.
- [88] A. N. Thite and D. J. Thompson. ‘Selection of response measurement locations to improve inverse force determination’. In: *Applied Acoustics*, 67, pp. 797–818, 2006.
- [89] P. van de Ponsele, H. van der Auweraer, and K. Janssens. ‘Source-transfer-receiver approaches: a review of methods’. In: *Proceedings of the International Conference on Noise and Vibration Engineering (ISMA)*, Leuven, Belgium, 2012.
- [90] S. Dom, T. Geluk, K. Hanssens, and H. van der Auweraer. ‘Transfer Path Analysis: Accurate load prediction beyond the traditional mount stiffness and matrix inversion methods’. In: *Proceedings of the SAE International Noise and Vibration Colloquium*, Sao Paulo, Brazil, 2014.
- [91] D. J. Thompson. ‘Developments of the indirect method for measuring the high frequency dynamic stiffness of resilient elements’. In: *Journal of Sound and Vibration*, 213(1), pp. 169–188, 1998.

- [92] A. T. Moorhouse. ‘Virtual Acoustic Prototypes: listening to machines that don’t exist’. In: *Proceedings of ACOUSTICS*, Busselton, Australia, 2005.
- [93] M. V. van der Seijs, E. A. Pasma, D. D. van den Bosch, and M. W. F. Wernsen. ‘A benchmark structure for validation of experimental substructuring, Transfer Path Analysis and source characterisation techniques’. In: *Dynamics of Coupled Structures, Conference Proceedings of the Society for Experimental Mechanics Series 4*, pp. 295–305, 2017.
- [94] F. X. Magrans. ‘Method of measuring transmission paths’. In: *Journal of Sound and Vibration*, 74(3), pp. 321–330, 1981.
- [95] F. X. Magrans. ‘Path analysis’. In: *Proceedings of DAGA*, Rotterdam, Netherlands, 2009.
- [96] P. Gajdatsy, K. Janssens, L. Gielen, P. Mas, and H. van der Auweraer. ‘Critical assessment of Operational Path Analysis: effect of coupling between path inputs’. In: *Proceedings of Euro-Noise*, Paris, France, 2008.
- [97] K. Janssens, P. Gajdatsy, L. Gielen, P. Mas, L. Britte, W. Desmet, and H. van der Auweraer. ‘OPAX: A new Transfer Path Analysis method based on parametric load models’. In: *Mechanical Systems and Signal Processing*, 25, pp. 1321–1338, 2011.
- [98] K. Janssens, P. Mas, P. Gajdatsy, L. Gielen, and H. van der Auweraer. ‘A novel path contribution analysis method for test-based NVH troubleshooting’. In: *Proceedings of Acoustics*, Geelong, Australia, 2008.
- [99] D. Zabel, T. Alber, M. Sturm, and A. T. Moorhouse. ‘Internal Transfer Path Analysis based on in-situ blocked forces and transmissibility functions’. In: *Proceedings of the 24th International Congress on Sound and Vibration (ICSV)*, London, UK, pp. 3085–3092, 2017.
- [100] D. Zabel. ‘Structure-borne sound transmission within electric power steering systems’. PhD thesis, University of Salford, UK, 2018.
- [101] H. van der Auweraer, P. Mas, S. Dam, A. Vecchio, K. Janssens, and P. van de Ponselee. ‘Transfer Path Analysis in the critical path of vehicle refinement: The role of fast, hybrid and operational path analysis’. In: *SAE International*, Tech. paper: 2007-01-2352, 2007.
- [102] H. van der Auweraer, P. Gajdatsy, K. Janssens, P. Mas, and L. Gielen. ‘Innovative approaches to fast Transfer Path Analysis’. In: *Proceedings of DAGA*, Rotterdam, Netherlands, 2009.
- [103] K. Janssens, P. Mas, L. Gielen, P. Gajdatsy, and H. van der Auweraer. ‘A novel Transfer Path Analysis method delivering a fast and accurate noise contribution assessment’. In: *SAE International*, Tech. paper: 2009-26-047, 2009.
- [104] A. P. V. Urgueira, R. A. B. Almeida, and N. M. M. Maia. ‘On the use of the transmissibility concept for the evaluation of frequency response functions’. In: *Mechanical Systems and Signal Processing*, 25, pp. 940–951, 2011.

- [105] J. W. R. Meggitt, A. S. Elliott, A. T. Moorhouse, and K. H. Lai. ‘In-situ determination of dynamic stiffness for resilient elements’. In: *Journal of Mechanical Engineering Science*, 230(6), pp. 986–993, 2016.
- [106] A. M. R. Ribeiro, J. M. M. Silva, and N. M. M. Maia. ‘On the generalisation of the transmissibility concept’. In: *Mechanical Systems and Signal Processing*, 14(1), pp. 29–35, 2000.
- [107] A. Clot, J. W.R. Meggitt, R. S. Langley, A. S. Elliott, and A. T. Moorhouse. ‘Development of a hybrid FE-SEA-experimental model’. 452(21), pp. 112–131, 2019.
- [108] A. Preumont. ‘Vibration control of active structures: An Introduction’. Springer Science + Business Media, 1997.
- [109] S. W. B. Klaassen, M. V. van der Seijs, and D. de Klerk. ‘System equivalent model mixing’. In: *Mechanical Systems and Signal Processing*, 15, pp. 90–112, 2018.
- [110] S. W. B. Klaassen and D. J. Rixen. ‘Using SEMM to identify the joint dynamics in multiple degrees of freedom without measuring interfaces’. In: *Proceedings of the XXXVII International Modal Analysis Conference (IMAC)*, Orlando (FL), USA, 2019.
- [111] S. W. B. Klaassen and M. V. van der Seijs. ‘Introducing SEMM: A Novel Method for Hybrid Modelling’. In: *Proceedings of the XXXVI International Modal Analysis Conference (IMAC)*, Orlando (FL), USA, 2018.
- [112] E. Pasma, S. Klaassen, L. Nieuwenhuijse, M. van der Seijs, and D. Lennström. ‘Application of System Equivalent Model Mixing (SEMM) to model the structural dynamic properties of a complex vehicle component using numerical and experimental data’. In: *Proceedings of the International Conference on Noise and Vibration Engineering (ISMA)*, Leuven, Belgium, 2018.
- [113] A. M. R. Ribeiro, N. M. M. Maia, and J. M. M. Silva. ‘Experimental evaluation of the transmissibility matrix’. In: *Proceedings of the XVII International Modal Analysis Conference (IMAC)*, Orlando (FL), USA, pp. 1126–1129, 1999.
- [114] P. Gajdatsy, K. Janssens, W. Desmet, and H. van der Auweraer. ‘Application of the transmissibility concept in Transfer Path Analysis’. In: *Mechanical Systems and Signal Processing*, 24(7), pp. 1963–1976, 2010.
- [115] C. Devriendt and P. Guillaume. ‘Identification of modal parameters from transmissibility measurements’. In: *Journal of Sound and Vibration*, 314, pp. 343–356, 2008.
- [116] G. Steenackers, C. Devriendt, and P. Guillaume. ‘On the use of transmissibility measurements for finite element model updating’. In: *Journal of Sound and Vibration*, 303, pp. 707–722, 2007.
- [117] J. Jové and O. Guasch. ‘Direct response and force transmissibilities in the characterization of coupled structures’. In: *Journal of Sound and Vibration*, 407, pp. 1–15, 2017.

- [118] Y. E. Lage, M. M. Neves, N. M. M. Maia, and D. Tcherniak. ‘Force transmissibility versus displacement transmissibility’. In: *Journal of Sound and Vibration*, 333, pp. 5708–5722, 2014.
- [119] N. M. M. Maia, M. Fontul, and A. M. R. Ribeiro. ‘Transmissibility of forces in multiple-degree-of-freedom systems’. In: *Proceedings of the International Conference on Noise and Vibration Engineering (ISMA)*, Leuven, Belgium, 2006.
- [120] N. M. M. Maia, J. M. M. Silva, and A. M. R. Ribeiro. ‘The transmissibility concept in multi-degree-of-freedom systems’. In: *Mechanical Systems and Signal Processing*, 15(1), pp. 129–137, 2001.
- [121] N. M. M. Maia, A. P. V. Urgueira, and R. A. B. Almeida. ‘Whys and wherefores of transmissibility’. In: *Vibration Analysis and Control – New Trends and Development*, chapter 10, Intechopen, 2011.
- [122] J. W. R. Meggitt and A. T. Moorhouse. ‘Finite element model updating using in-situ experimental data’. In: *Journal of Sound and Vibration*, 489, 2020.
- [123] Q. Leclère, C. Pezerat, B. Laulagnet, and L. Polac. ‘Indirect measurement of main bearing loads in an operating diesel engine’. In: *Journal of Sound and Vibration*, 286(1-2), pp. 341–361, 2005.
- [124] L. Barton, A. S. Elliott, A. T. Moorhouse, and J. Smith. ‘In-situ Transfer Path Analysis of multiple vibration sources in a complex source-receiver assembly’. In: *Proceedings of the 23rd International Congress on Acoustics (ICA)*, Aachen, Germany, 2019.
- [125] S. M. Price and R. J. Bernhard. ‘Virtual coherence: A digital signal processing technique for incoherent source identification’. In: *Proceedings of the IX International Modal Analysis Conference (IMAC)*, Los Angeles (CA), USA, pp. 1256–1262, 1986.
- [126] J. W. R. Meggitt, A. S. Elliott, A. T. Moorhouse, G. Banwell, H. Hopper, and J. Lamb. ‘Broadband characterisation of in-duct acoustic sources using an equivalent source approach’. In: *Journal of Sound and Vibration*, 442, pp. 800–816, 2019.
- [127] M. Haeussler. ‘Modular sound & vibration engineering by substructuring: Listening to machines during virtual design’. PhD thesis, Technical University of Munich, Germany, 2021.
- [128] M. Sturm, A. T. Moorhouse, W. Kopp, and T. Alber. ‘Robust calculation of simultaneous multi-channel blocked force signatures from measurements made in-situ using an adaptive algorithm in the time domain’. In: *Proceedings of the 20th International Congress on Sound and Vibration (ICSV)*, Bangkok, Thailand, 2013.
- [129] M. Sturm, A. T. Moorhouse, T. Alber, and F. F. Li. ‘Force reconstruction using an adaptive algorithm in time’. In: *Proceedings of the International Conference on Noise and Vibration Engineering (ISMA)*, Leuven, Belgium, 2012.
- [130] M. Fontul, A. M. R. Ribeiro, J. M. M. Silva, and N. M. M. Maia. ‘Transmissibility matrix in harmonic and random processes’. In: *Shock and Vibration*, 11, pp. 563–571, 2004.

- [131] N. B. Roozen and Q. Leclère. ‘On the use of artificial excitation in operational Transfer Path Analysis’. In: *Applied Acoustics*, 74(1167-1174), 2013.
- [132] D. J. Ewins. ‘Modal testing: Theory, practice and application’. John Wiley & Sons, New York, 2009.
- [133] Q. Leclère, N. B. Roozen, and C. Sandier. ‘Experimental estimation of transmissibility matrices’. In: *Proceeding of the International Conference on Noise and Vibration Engineering (ISMA)*, Leuven, Belgium, 2012, pp. 3563–3569, 2012.
- [134] Q. Leclère, B. Roozen, and C. Sandier. ‘On the use of the Hs estimator for the experimental assessment of transmissibility matrices’. In: *Mechanical Systems and Signal Processing*, 43, 2014.
- [135] R. J. Allemang, D. L. Brown, and R. W. Rost. ‘Experimental modal analysis and dynamic component synthesis: Measurement techniques for experimental modal analysis’. In: *Technical Report*, 1987.
- [136] U. Konnerth. ‘A hydraulic high-speed tryout press for the simulation of mechanical forming processes’. In: *Journal of Materials Processing Technology*, 111, pp. 159–163, 2001.
- [137] F. Bianciardi, K. Janssens, and L. Britte. ‘Critical assessment of OPA: Effect of coherent path inputs and SVD truncation’. In: *Proceedings of the 20th International Congress on Sound and Vibration (ICSV)*, Bangkok, Thailand, 2013.
- [138] J. W. R. Meggitt. ‘On the treatment of uncertainty in experimentally measured frequency response functions’. In: *Metrologia*, 66(806), 2018.
- [139] A. T. Moorhouse, J. W.R. Meggitt, and A. S. Elliott. ‘Evaluation of uncertainties in classical and component (blocked force) Transfer Path Analysis (TPA)’. In: *SAE International Journal of Advances and Current Practices in Mobility*, pp. 1777–1787, 2019.
- [140] S. N. Voormeeren, D. de Klerk, and D. J. Rixen. ‘Uncertainty quantification in experimental frequency based substructuring’.
- [141] P. Gajdatsy, K. Janssens, L. Gielen, P. Mas, and H. van der Auweraer. ‘Critical assessment of Operational Path Analysis: effect of neglected paths’. In: *Proceedings of the 15th International Congress on Sound and Vibration (ICSV)*, Deajeon, Korea, 2015.
- [142] J. Putner, M. Lohmann, and A. Kaltenhauser. ‘Operational Transfer Path Analysis predicting contributions to the vehicle interior noise for different excitations from the same sound source’. In: *Proceedings of INTER-NOISE*, New York (NY), USA, 2012.
- [143] M. Petyt. ‘Introduction to finite element vibration analysis’. Cambridge University Press, New York, 1990.
- [144] T. D. Rossing and N. H. Fletcher. ‘Principles of vibration and sound’. Springer Science + Business Media, New York, 2004.

- [145] L. Cremer, M. Heckl, and B.A.T. Petersson. ‘Structure-borne sound: Structural Vibrations and Sound Radiation at Audio Frequencies’. Springer-Verlag, Heidelberg, 2005.
- [146] L. L. Beranek. ‘Acoustics’. Acoustical Society of America, New York, 1996.
- [147] S. J. Xin. ‘Simplified characterisation of structure-borne sound sources with multi-point connections’. PhD thesis, University of Liverpool, UK, 2003.
- [148] A. A. Shabana. ‘Theory of vibration: An introduction’. Springer International Publishing, New York, 2019.
- [149] F. Fahy and P. Gardonio. ‘Sound and structural vibration: Radiation, Transmission and Response’. Academic Press, Amsterdam, 2007.
- [150] R. Pintelon and J. Schoukens. ‘System identification: A frequency domain approach’. John Wiley & Sons, Hoboken, 2012.
- [151] A. Liljerehn and Abrahamsson, T. J. S. ‘Dynamic sub-structuring with passive state-space components’. In: *Proceeding of ISMA2014 including USD2014*, Leuven, Belgium, 2014, pp. 3879–3890, 2014.
- [152] R. H. Lyon. ‘Machinery noise and diagnostics’. Butterworth, Boston, 1986.
- [153] C. Höller and B. M. Gibbs. ‘Indirect determination of the mobility of structure-borne sound sources’. In: *Journal of Sound and Vibration*, 344(1), pp. 38–58, 2015.
- [154] A. T. Moorhouse. ‘Compensation for discarded singular values in vibro-acoustic inverse methods’. In: *Journal of Sound and Vibration*, 267(3), pp. 245–252, 2003.
- [155] H. W. Engl, M. Hanke, and A. Neubauer. ‘Regularization of Inverse Problems’. Springer Science + Business Media, Dordrecht, 2000.
- [156] G. F. Lang. ‘An introduction to shaker thermodynamics’. In: *Sound and Vibration Magazine*, (August 2004), pp. 14–17.
- [157] G. F. Lang. ‘Electrodynamic Shaker fundamentals’. In: *Sound and Vibration Magazine*, (April 1997), pp. 1–8.
- [158] G. F. Lang and D. Snyder. ‘Understanding the physics of electrodynamic shaker performance’. In: *Sound and Vibration Magazine*, (October 2001), pp. 2–10.
- [159] P. S. Varoto and L. P. R. de Oliveira. ‘On the force drop off phenomenon in shaker testing in experimental modal analysis’. In: *Shock and Vibration*, 9, pp. 165–175, 2002.
- [160] ZF Lenksysteme. ‘ZF Servoelectric: Electric power steering system for passengers cars and light commercial vehicles’. 2009.
- [161] M. Harrer and P. Pfeffer, editors. ‘Steering handbook’. Springer Science + Business Media, Heidelberg, 2017.
- [162] U. Poestgens. ‘Power steering systems for passenger cars and commercial vehicles: Safe and comfortable steering through intelligent assist and control functions’. Sueddeutscher Verlag onpact GmbH, Munich, 2014.

- [163] S. Zuo, F. Lin, and X. Wu. ‘Noise analysis, calculation, and reduction of external rotor permanent-magnet synchronous motor’. In: *IEEE transactions on industrial electronics*, 62(10), 2015.
- [164] F. Lin, S. Zuo, W. Deng, and S. Wu. ‘Modeling and analysis of electromagnetic force, vibration, and noise in permanent-magnet synchronous motor considering current harmonics’. In: *IEEE transactions on industrial electronics*, 63(12), 2016.
- [165] R. Islam, I. Husain, A. Fardoun, and K. McLaughlin. ‘Permanent magnet synchronous motor magnet designs with skewing for torque ripple and cogging torque reduction’. In: *Proceedings of the IEEE Industry Applications Annual Meeting*, New Orleans (LA), USA, 2007.
- [166] P. Mattavelli, L. Tubiana, and M. Zigliotto. ‘Torque-ripple reduction in PM synchronous motor drives using repetitive current control’. In: *IEEE Transactions on Power Electronics*, 20(6), 2005.
- [167] Perneder. ‘Handbuch Zahnriementchnik: Grundlagen, Berechnung, Anwendungen’. Springer-Verlag, Heidelberg, 2009.
- [168] K. Wienen. ‘Experimental determination of electro-magnetic forces in the air gap of a permanent magnet synchronous motor’. Master thesis, University of Stuttgart, Germany, 2016.
- [169] T. Kimpián and F. Augusztinovicz. ‘Multiphase multisine signals: Theory and practice’. In: *Proceedings of the International Conference of Noise and Vibration Engineering (ISMA)*, Leuven, Belgium, pp. 2241–2250, 2016.
- [170] T. Kimpián and F. Augusztinovicz. ‘Torsional modal analysis of single shaft systems containing permanent magnet synchronous motors using novel broadband torque excitation’. In: *Proceedings of the International Conference on Noise and Vibration Engineering (ISMA)*, Leuven, Belgium, pp. 2081–2090, 2012.
- [171] T. Kimpián and F. Augusztinovicz. ‘Universal broadband torsional exciter from a permanent magnet synchronous motor’. In: *Proceedings of the International Conference on Noise and Vibration Engineering (ISMA)*, Leuven, Belgium, pp. 1101–1110, 2014.
- [172] M. Bauer. ‘Virtual acoustic prototyping: Characterisation of a steering system and prediction of structure-borne sound’. PhD thesis, University of Salford, UK, 2011.
- [173] M. Sturm, M. Yankonis, C. Merchand, S. Sherman, J. Hirscher, M. Priebe, S. Parikh, and A. T. Moorhouse. ‘Robust NVH development of steering systems using in-situ blocked forces from measurements with low-noise driver simulators’. In: *Proceedings of Noise Control (NOISE-CON)*, Grand Rapids (MI), USA, 2017.
- [174] N. M. M. Maia and J. M. M. Silva, editors. ‘Theoretical and experimental modal analysis’. Research Studies Press LTD., Baldock, 1998.